frontiers | Research Topics

Innovative pharmacometric approaches to inform drug development and clinical use

Edited by
Zinnia P. Parra-Guillen, Victor Mangas Sanjuan, Maria Garcia-Cremades and Hugo Geerts

Published in
Frontiers in Pharmacology

ISSN 1664-8714
ISBN 978-2-8325-4503-4
DOI 10.3389/978-2-8325-4503-4

About Frontiers

Frontiers is more than just an open access publisher of scholarly articles: it is a pioneering approach to the world of academia, radically improving the way scholarly research is managed. The grand vision of Frontiers is a world where all people have an equal opportunity to seek, share and generate knowledge. Frontiers provides immediate and permanent online open access to all its publications, but this alone is not enough to realize our grand goals.

Frontiers journal series

The Frontiers journal series is a multi-tier and interdisciplinary set of open-access, online journals, promising a paradigm shift from the current review, selection and dissemination processes in academic publishing. All Frontiers journals are driven by researchers for researchers; therefore, they constitute a service to the scholarly community. At the same time, the *Frontiers journal series* operates on a revolutionary invention, the tiered publishing system, initially addressing specific communities of scholars, and gradually climbing up to broader public understanding, thus serving the interests of the lay society, too.

Dedication to quality

Each Frontiers article is a landmark of the highest quality, thanks to genuinely collaborative interactions between authors and review editors, who include some of the world's best academicians. Research must be certified by peers before entering a stream of knowledge that may eventually reach the public - and shape society; therefore, Frontiers only applies the most rigorous and unbiased reviews. Frontiers revolutionizes research publishing by freely delivering the most outstanding research, evaluated with no bias from both the academic and social point of view. By applying the most advanced information technologies, Frontiers is catapulting scholarly publishing into a new generation.

What are Frontiers Research Topics?

Frontiers Research Topics are very popular trademarks of the *Frontiers journals series*: they are collections of at least ten articles, all centered on a particular subject. With their unique mix of varied contributions from Original Research to Review Articles, Frontiers Research Topics unify the most influential researchers, the latest key findings and historical advances in a hot research area.

Find out more on how to host your own Frontiers Research Topic or contribute to one as an author by contacting the Frontiers editorial office: frontiersin.org/about/contact

Innovative pharmacometric approaches to inform drug development and clinical use

Topic editors

Zinnia P. Parra-Guillen — University of Navarra, Spain
Victor Mangas Sanjuan — University of Valencia, Spain
Maria Garcia-Cremades — Complutense University of Madrid, Spain
Hugo Geerts — Certara UK Limited, United Kingdom

Citation

Parra-Guillen, Z. P., Sanjuan, V. M., Garcia-Cremades, M., Geerts, H., eds. (2024). *Innovative pharmacometric approaches to inform drug development and clinical use*. Lausanne: Frontiers Media SA. doi: 10.3389/978-2-8325-4503-4

Table of contents

frontiers | Frontiers in Pharmacology

TYPE Editorial
PUBLISHED 04 October 2023
DOI 10.3389/fphar.2023.1274139

OPEN ACCESS

EDITED AND REVIEWED BY
Alastair George Stewart,
The University of Melbourne, Australia

*CORRESPONDENCE
Hugo Geerts,
hugo-geerts@in-silico-biosciences.com

RECEIVED 07 August 2023
ACCEPTED 14 September 2023
PUBLISHED 04 October 2023

CITATION
Garcia-Cremades M, Parra-Guillen ZP, Mangas-Sanjuan V and Geerts H (2023), Editorial: Innovative pharmacometric approaches to inform drug development and clinical use.
Front. Pharmacol. 14:1274139.
doi: 10.3389/fphar.2023.1274139

Editorial: Innovative pharmacometric approaches to inform drug development and clinical use

Maria Garcia-Cremades[1,2], Zinnia P. Parra-Guillen[3,4], Victor Mangas-Sanjuan[5,6] and Hugo Geerts[7]*

[1]Department of Pharmaceutics and Food Technology, School of Pharmacy, Complutense University of Madrid, Madrid, Spain, [2] Institute of Industrial Pharmacy, Complutense University of Madrid, Madrid, Spain, [3]Pharmaceutical Science Department, School of Pharmacy and Nutrition, University of Navarra, Pamplona, Spain, [4]IdiSNA, Navarra Institute for Health Research, Navarra, Spain, [5]Department of Pharmacy and Pharmaceutical Technology and Parasitology, Faculty of Pharmacy, University of Valencia, Valencia, Spain, [6]Interuniversity Research Institute for Molecular Recognition and Technological Development, Valencia, Spain, [7]Certara, Princeton, NJ, United States

KEYWORDS

pharmacometrics, quantitative systems pharmacology, clinical trials, machine learning, POPPK

Editorial on the Research Topic
Innovative pharmacometric approaches to inform drug development and clinical use

A successful Drug Development is driven by many factors, but ultimately it is often dependent upon the weakest part. Therefore, it is necessary to utilize all tools available to support the complete journey for a successful development program. Model-informed drug development (MIDD) in which crucial information is generated from mathematical analysis or modeling, is rapidly becoming a powerful tool in pharmaceutical R&D and in the regulatory environment. Appropriate use of modeling can contribute to more rational and efficient decision-making in drug development, leading to substantial resource savings and shortened timelines.

MIDD can broadly be divided in data- and mechanism-driven modeling and the manuscripts in this Research Topic are good examples of the diversity of applied algorithms. In addition, the large range of disease indications is testimony to the impact of these modeling techniques in clinical drug development and clinical practice.

Data-driven approaches include more traditional statistical bio-informatics analyses of large datasets or machine learning algorithms to derive predictive insights (Ribba et al.). The quality of these predictions is heavily dependent upon the nature of the training sets and issues of generalizability need to be addressed.

Two articles look to derive estimates of drug exposure using more advanced Physiologically-based Pharmacokinetic models (PBPK) to predict drug exposure in other populations (Zazo et al.). An interesting combination of traditional PopPK modeling with machine learning aims to understand the role of covariates (Zhu et al.). Finally, PK modeling can also be used to derive the quantitative pharmacokinetics trajectory of biomarkers which can clarify the contribution of these biomarkers in clinical development (Michelet et al.).

Mechanism-driven modeling on the other hand can be helpful in those cases where data are lacking or noisy. This is often the case in CNS disorders, where robust quantitative biomarkers are scarce, functional scales are often based on structured interviews and biomarkers are often not strongly related to clinical outcomes. This section includes a contribution, using computational neuroscience to gain insights in the mechanisms of catatonia (Roberts and Conour) and a position paper on computational psychiatry, especially with regard to reward physiology (Ribba), a field in full development. This underscores the power of combining the academic discipline of computational neurosciences with Quantitative Systems Pharmacology.

Another paper describes the powerful prediction capability for combination therapy and virtual patient modeling in oncology (Anbari et al.). Here the authors use a mechanistic modeling of different therapeutic modalities, each calibrated with their own clinical dataset, to explore the optimal conditions for combination therapy and to estimate the variability that can provide estimates for power calculations.

In summary, Model-Informed Drug Development (MIDD) is rapidly becoming an essential tool for quantitatively assessing the relevance of data- and knowledge-based information to support not only clinical trial development but also clinical practice. From estimation of effective doses over combination therapy to personalized medicines, this approach has matured to the point that they can make the difference between a successful and a failed clinical development project.

Author contributions

MG-C: Writing–review and editing. ZP-G: Writing–review and editing. VM-S: Writing–review and editing. HG: Writing–original draft.

Conflict of interest

Author HG was employed by the company Certara.

The remaining authors declare that the research was conducted in the absence of any commercial or financial relationships that could be construed as a potential conflict of interest.

The author(s) declared that they were an editorial board member of Frontiers, at the time of submission. This had no impact on the peer review process and the final decision.

Publisher's note

frontiers | Frontiers in Pharmacology

TYPE Original Research
PUBLISHED 10 August 2022
DOI 10.3389/fphar.2022.951480

OPEN ACCESS

EDITED BY
Victor Mangas Sanjuan,
University of Valencia, Spain

REVIEWED BY
Jorge Duconge,
University of Puerto Rico, Puerto Rico
Bo Zheng,
Naval Medical Center, China

*CORRESPONDENCE
Gong-Hao He,
gonghow@hotmail.com

†These authors have contributed equally to this work and share first authorship.

SPECIALTY SECTION
This article was submitted to Translational Pharmacology, a section of the journal Frontiers in Pharmacology

RECEIVED 24 May 2022
ACCEPTED 13 July 2022
PUBLISHED 10 August 2022

CITATION
Zhou T, Qian K, Li Y-Y, Cai W-K, Yin S-J, Wang P and He G-H (2022), The pyroptosis-related gene signature predicts prognosis and reveals characterization of the tumor immune microenvironment in acute myeloid leukemia.
Front. Pharmacol. 13:951480.
doi: 10.3389/fphar.2022.951480

The pyroptosis-related gene signature predicts prognosis and reveals characterization of the tumor immune microenvironment in acute myeloid leukemia

Tao Zhou[1,2†], Kai Qian[1,2†], Yun-Yun Li[3†], Wen-Ke Cai[4], Sun-Jun Yin[1], Ping Wang[1] and Gong-Hao He[1,5*]

[1]Department of Clinical Pharmacy, 920th Hospital of Joint Logistics Support Force of People's Liberation Army, Kunming, China, [2]College of Pharmacy, Dali University, Dali, China, [3]Department of Pharmacy, The Second People's Hospital of Quzhou Zhejiang, Quzhou, China, [4]Department of Cardiothoracic Surgery, 920th Hospital of Joint Logistics Support Force of People's Liberation Army, Kunming, China, [5]Research Center of Clinical Pharmacology, Yunnan Provincial Hospital of Traditional Chinese Medicine, Kunming, China

Background: Pyroptosis is a novel inflammatory form of programmed cell death and a prospective target for cancer therapy. Nevertheless, little is known about the association between pyroptosis-related genes (PRGs) and acute myeloid leukemia (AML) prognosis. Herein, we systematically investigated the specific functions and clinical prognostic value of multiple PRGs in AML.

Methods: Univariate and LASSO Cox regression analyses based on TCGA and GTEx databases were used to generate the PRG signature, whose predictive efficacy of survival was evaluated using survival analysis, ROC, univariate and multivariate Cox analyses as well as subgroup analysis. The BeatAML cohort was used for data validation. The association between risk score and immune cell infiltration, HLA, immune checkpoints, cancer stem cell (CSC), tumor mutation burden (TMB), and therapeutic drug sensitivity were also analyzed.

Results: Six -PRG signatures, namely, *CASP3*, *ELANE*, *GSDMA*, *NOD1*, *PYCARD*, and *VDR* were generated. The high-risk score represented a poorer prognosis and the PRG risk score was also validated as an independent predictor of prognosis. A nomogram including the cytogenetic risk, age, and risk score was constructed for accurate prediction of 1-, 3-, and 5-year survival probabilities. Meanwhile, this risk score was significantly associated with the tumor immune microenvironment (TIME). A high-risk score is characterized by high immune cell infiltration, HLA, and immune checkpoints, as well as low CSC and TMB. In addition, patients with low-risk scores presented significantly lower IC50 values for ATRA, cytarabine, midostaurin, doxorubicin, and etoposide.

Conclusion: Our findings might contribute to further understanding of PRGs in the prognosis and development of AML and provide novel and reliable biomarkers for its precise prevention and treatment.

KEYWORDS
pyroptosis, acute myeloid leukemia, prognosis, immune microenvironment, TCGA

Introduction

Acute myeloid leukemia (AML) is the second most common type of leukemia diagnosed in adults and accounted for approximately 30% of all adult leukemia cases (Perna et al., 2017), which is primarily characterized by heterogeneity of molecular abnormalities and aberrant accumulation of immature myeloid progenitors in bone marrow and peripheral blood owing to impaired differentiation of hematopoietic progenitors (Sperlazza et al., 2015). The invasive infiltration of AML is mainly represented by a malignant extramedullary infiltration which involves the skin, lymph nodes, liver, spleen, and even central nervous system, and shows poorer prognosis in clinic (Stölzel et al., 2011). In recent years, although the survival and prognosis of AML patients were relatively prolonged with the development and application of molecular targeted therapy and combination therapy in clinical practice, the 5-year survival rate remained at 27% for AML patients over 20 years old and even 69% for patients younger than 20 partially due to the absence of reliable prognostic biomarkers (Ball and Stein, 2019; Schlenk et al., 2019; Zheng et al., 2020). Thus, identifying novel and effective prognostic biomarkers is crucial for improving the AML prognosis and better understanding the pathogenesis of AML.

Recently, much attention was paid to the influences of the tumor microenvironment (TME) on tumorigenesis and development, and alterations in TME components were found at every stage of malignant development in almost all carcinomas (Wu and Dai, 2017; Arneth, 2019). As an important component of TME, the tumor immune microenvironment (TIME) was also found to play prominent roles in tumor cell proliferation, invasion, and metastasis (Fu et al., 2019). Numerous studies showed that TIME was a key determinant of diagnosis and therapeutic response in tumor patients (Xu B. et al., 2021; Yang et al., 2021; Zeng et al., 2021; Wang et al., 2022). However, TIME is complex and variable mainly because of the multiple interaction networks among tumor, immune, stromal, and mesenchymal cells along with various soluble factors and changes in extracellular matrix (ECM) components as well (Wu and Dai, 2017; Xu B. et al., 2021). Therefore, identification of certain potential biomarkers related to TIME would eventually contribute to better understanding of tumor development and further identification of candidate therapeutic targets.

As a highly specific inflammatory programmed cell death, pyroptosis was reported to be significantly cross-correlated with TIME according to previous studies (Orning et al., 2019; Erkes et al., 2020). When persistent inflammation is present, initial activation and assembly of inflammasome started within host cells (Balahura et al., 2020). Subsequently, the caspase was further activated and produced inflammatory cytokines, eventually resulting in pyroptotic cell death (Broz et al., 2010; Moujalled et al., 2021). In recent years, a growing number of studies demonstrated that pyroptosis played crucial roles in pathogenesis and progression of various types of cancers including AML. It was reported that activation of NLR family pyrin domain containing 1 b (NLRP1b) by small molecule inhibitors of serine dipeptidase 8/9 (DPP8/9) induced caspase-1 dependent pyroptosis, which, in turn, suppressed the development of AML (Johnson et al., 2018). Meanwhile, pyridoxine was also found to induce death of primary AML cell in AML patients and prevent disease progression by activating caspase-3/8 and promoting the release of inflammatory factors (Yang et al., 2020). These findings suggested that pyroptosis provided a tumor-suppressive microenvironment and played an immunomodulatory role in AML. However, the prognostic influence of pyroptosis on AML patients was still largely unknown. Moreover, due to technical limitations, most previous studies were limited to a small number of pyroptosis-related genes (PRGs), whereas the involved PRGs might be far more in numbers and their antitumor effects were very likely to interact with each other in a highly coordinated manner. Therefore, a comprehensive analysis regarding the features of TIME cell infiltration mediated by multiple PRGs may provide a relatively whole profile of the function of PRGs and also further insights into the underlying mechanisms of AML occurrence and progression, which, however, has not been investigated so far as we know.

Based on these backgrounds, we, herein, systematically analyzed the differential expression of PRGs and the prognostic value of these genes in clinical practice between AML and normal samples and established an independent prognostic PRG signature. Subsequently, we also explored the relationship between pyroptosis and TIME as well as evaluated the sensitivity of therapeutic drugs for AML patients according to PRG prognostic signature. This study identified reliable prognostic biomarkers for AML patients and provided a novel scientific basis for future immunotherapy in AML.

Materials and methods

Acquisition of data

The specific analysis process of the present study is illustrated in Supplementary Figure S1. The RNA sequencing (RNA-seq) data of 151 AML patients' bone marrow (BM) samples and 755 normal peripheral whole

blood samples were acquired from The Cancer Genome Atlas (TCGA) database (https://portal.gdc.cancer.gov/) and the Genotype-Tissue Expression (GTEx) database (https://www.gtexportal.org/). Meanwhile, we obtained the corresponding clinical features of 151 AML patients from TCGA and eventually included 132 samples after excluding 19 samples without survival time. Furthermore, the gene expression profile and relevant clinical characteristic data of 91 AML patients were downloaded from the BeatAML database (Tyner et al., 2018) (http://www.vizome.org/aml/) as a validation cohort. All patients' clinical features are detailed in Supplementary Table S1. The RNA-seq data of raw count normalized from the aforementioned databases were utilized for differential expression analysis. Then, the count values were converted to transcripts per kilobase million (TPM) values, which were further transformed to log2 (TPM + 1) for subsequent analysis. In addition, the somatic mutation and copy number variation (CNV) data were also retrieved from TCGA database.

Pyroptosis-related genes

A total of 44 PRGs were retrieved from the GeneCards (https://www.genecards.org/) and previously published literature works (Man and Kanneganti, 2015; Wang and Yin, 2017; Karki and Kanneganti, 2019; Xia et al., 2019), all of which were protein-coding genes. The full details of these genes are listed in Supplementary Table S2. However, as the expression profile of *GSDME* and *PTVK* could not be acquired from the GTEx database, we finally selected 42 PRGs for further analysis. The location of PRGs on the chromosome was plotted by the "RCircos" R package. The "limma" R package was utilized to identify the differentially expressed pyroptosis–related genes (DEPRGs) with a p value <0.05 and $|\log_2 FC| > 0$ between tumor and normal tissues. The PRG somatic mutation landscape was presented *via* the "maftools" R packages. The frequencies of genetic amplification and deletion were also summarized. The univariate Cox regression was performed to identify PRGs significantly associated with overall survival (OS) in TCGA cohort. Simultaneously, the Spearman correlation test was applied to evaluate the associations across all PRGs and the comprehensive results were visualized using the "igraph" R package.

Consensus clustering

Consensus clustering was adopted to identify the distinct pyroptosis-related patterns pertaining to the expression of pyroptosis regulators using k-means algorithms (Hartigan and Wong, 1979). The numbers and stability of clusters were determined by the consensus clustering algorithms of the "ConsensuClusterPlus" R package (Wilkerson and Hayes, 2010). We conducted 1,000 times repetitions to guarantee the classification stability.

Construction and validation of a prognostic gene signature by prognostic DEPRGs

The significant prognostic-related DEPRGs were presented *via* the "VennDiagram" R package. Subsequently, the least absolute shrinkage and selection operator (LASSO) Cox regression analysis using the "glmnet" R package was applied to screen out the optimal candidate gene combination to construct the prognostic gene signature (Tibshirani, 1997). The optimal value of the penalty parameter λ was determined by 10-fold cross-validation based on the minimum criteria. According to the coefficient calculated by LASSO regression and the standardized and normalized TCGA AML expression level, the individual risk score of each AML patient could be calculated using the following formula:

$$Risk\ score = \sum_{i=1}^{n} Exp\,i * Coef\,i.$$

Simultaneously, the TCGA AML patients were separated into high- and low-risk categories according to the median risk score. The principal component analysis (PCA) and t-distributed stochastic neighbor–embedding (t-SNE) analysis were conducted using the "Rtsne" and "ggplot2" R packages to investigate the distribution of various groups in terms of gene expression levels in the constructed model. Thereafter, we performed Kaplan–Meier analysis *via* the "survminer" R package to assess the survival difference between the two categories. The "survival" and "timeROC" R packages were utilized to perform the time-dependent receiver operating characteristic (ROC) curve analysis, which was applied to evaluate the prognostic gene signature's predictive value. The prognostic significances of gene signature and other clinical characteristics were further investigated using univariate and multivariate Cox regression analyses. Moreover, the same formula and statistical methods were used to further validate the prognostic capacity of the gene signature in the BeatAML cohort.

The chi-squared test was adopted to explore the association of gene signature and clinicopathological characteristics, which was visualized with a heatmap using the "pheatmap" R package. The Wilcoxon signed-rank test and Kruskal–Wallis H-test were utilized to compare the risk score among various categories of these clinicopathological characteristics, and the visualization of results was presented *via* the boxplots.

Establishment of the predictive nomogram

The independent clinical features (cytogenetic risk, age, and risk score) validated using univariate and multivariate Cox regression analyses were enrolled to construct a predictive prognosis nomogram using the "rms" and "survival" R packages. Time-dependent ROC curves for 1, 3, and 5 years were used to assess the performance of the nomogram. The calibration curves for 1-, 3-, and 5-year prediction were utilized to depict the consistency between predicted and actual survival. Furthermore, an alluvial diagram was drawn to show the changes in pyroptosis-related clusters, risk score, age, and cytogenetic risk using the "ggalluvial" R package.

Functional enrichment analysis of DEGs based on the high- and low-risk groups

AML patients in TCGA cohort were batched into two groups according to the median risk score, respectively. The same approach was also performed in the BeatAML cohort. Afterward, the differentially expressed genes (DEGs) were extracted by utilizing the "limma" R package with the criteria of FDR <0.05 and $|\log_2 FC| > 1$. Gene ontology (GO) and Kyoto Encyclopedia of Genes and Genomes (KEGG) pathway enrichment analyses of the DEGs were performed using the "clusterProfiler" R package (Wu et al., 2021).

Assessment of the tumor immune environment

We applied the ESTIMATE algorithm to calculate the stromal, immune scores, and ESTIMATE scores of each patient in TCGA and BeatAML cohorts (Yoshihara et al., 2013). Furthermore, considering the significant roles of the immune cell infiltration in the TIME, the infiltrating scores of 22 kinds of human immune cells in each AML sample were computed by the CIBERSORT algorithm with 1,000 permutation. Furthermore, the single-sample gene set enrichment analysis (ssGSEA) algorithm using the "gsva" R package was utilized to calculate infiltration abundance of 29 immune signatures in the AML TIME. Subsequently, we explored the association between the enrichment scores of 22 kinds of immune cells and the risk score or expression levels of the aforementioned identified optimal candidate genes. In addition, the Wilcoxon signed-rank test was applied to estimate the differences in expression of human lymphocyte antigen (HLA) signature and immune checkpoint genes between high- and low-risk groups.

Analysis of CSC, TMB, and drug susceptibility between high- and low-risk groups

The gene expression–based stemness index was acquired from the previous study (Malta et al., 2018). We explored the correlation between risk score and cancer stemness cell (CSC). Simultaneously, we also computed the tumor mutation burden (TMB) score for each AML sample based on the "maftools" R package and analyzed the differences in the TMB score between high- and low-risk groups, as well as the associations between the TMB score and risk score. To investigate the differences in efficacy of therapeutic drugs in patients between high- and low-risk categories, we calculated the semi-inhibitory concentration (IC50) values of drugs commonly used for the treatment of AML *via* the "pRRophetic" R package.

Statistical analysis

All statistical analyses were performed by R software (version 4.0.4). Association coefficients were calculated by the Spearman correlation test. Log-rank tests were used for identifying the significance of differences in Kaplan–Meier analysis curves. p values of less than 0.05 were considered statistically significant ($^*p < 0.05$) in all analyses.

Results

Landscape of expression and genetic alterations of PRGs in AML

This study first summarized the incidence of CNVs and somatic mutations of 42 PRGs in AML. The exploration of CNVs demonstrated prevalent CNV alterations in all 42 PRGs, among which the CNV of *TIRAP* was significantly increased while the CNVs of *CEBPB*, *PLCG1*, and *VDR* were significantly decreased (Figure 1A). Furthermore, the location of CNV variation in the PRGs on their respective chromosomes is displayed in Figure 1B. In the following assessment of the genetic mutation of PRGs in depth, only *CASP3* (1%), *NLRC4* (1%), *NLRP1* (1%), *NLRP2* (1%), *NLRP3* (1%), *TFAM* (1%), and *TXNIP* (1%) showed the genetic mutation in AML patients (Figure 1C). To determine whether these gene variants influence the expression of PRGs in patients with AML, we further calculated the mRNA expression levels of 42 PRG between normal and tumor specimens and then identified the statistically significant DEGs ($p < 0.05$) that correspond to them. As a result, 19 downregulated and 16 upregulated genes were observed in the tumor group (Figure 1D). Subsequently, we discovered that the CNV alteration may be a major factor resulting in perturbations on PRG expression

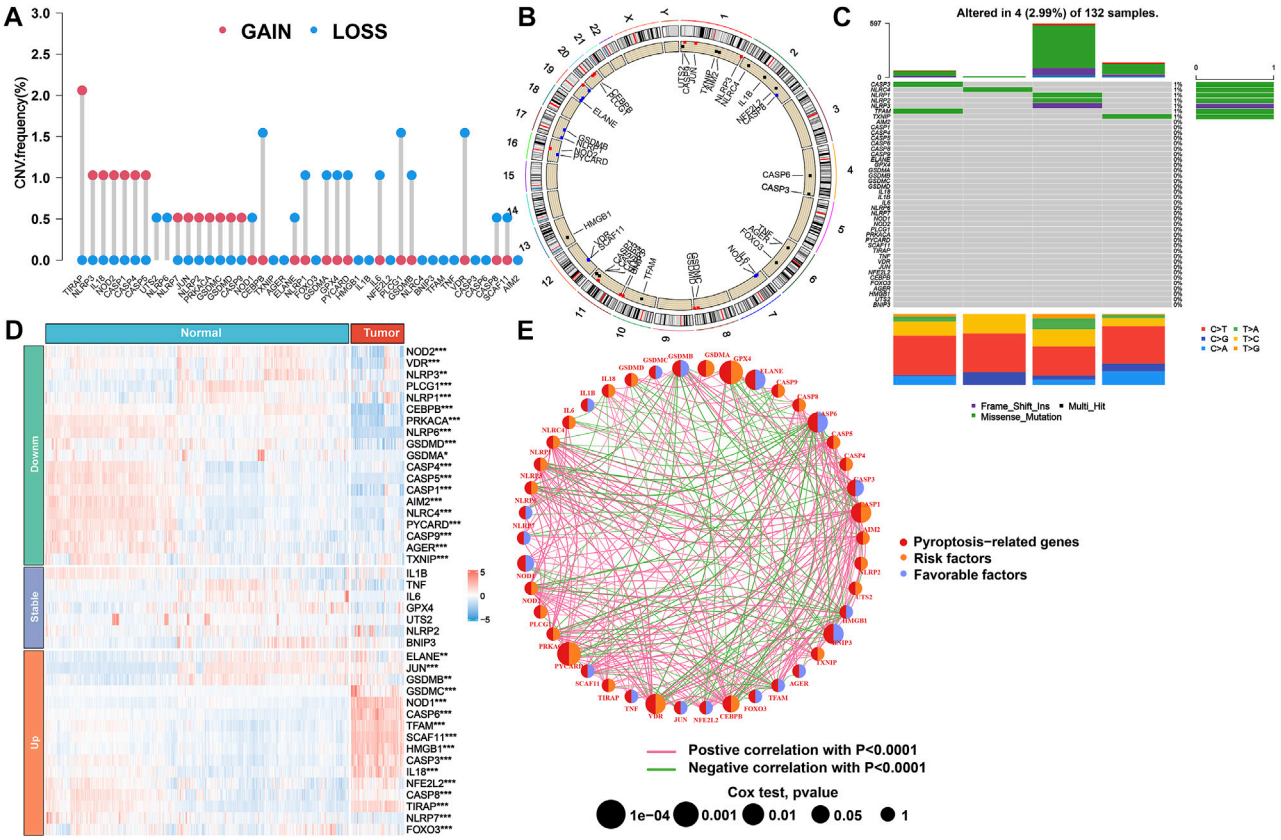

FIGURE 1
Genetic and transcriptional alteration of PRGs in AML. **(A)** Frequencies of CNV gain, loss, and non-CNV for 42 PRGs in TCGA cohort. **(B)** Locations of CNV alterations in PRGs on 23 chromosomes. **(C)** Mutation frequency of PRGs in TCGA cohort. **(D)** Heatmap of expression patterns of PRGs in normal and tumor samples. **(E)** Network of correlations including PRGs in TCGA cohort. PRGs, pyroptosis-related genes; AML, acute myeloid leukemia; CNV, copy number variant; TCGA, The Cancer Genome Atlas.

levels. In comparison to normal samples, the expressions of genes with deleted CNVs were found to be significantly decreased in AML samples (such as *CEBPB*, *PLCG1*, and *VDR*), and vice versa (such as *TIRAP*). Based on the aforementioned results, the composite landscape of interaction and correlation of the 42 PRGs and their prognostic value for AML patients was further comprehensively displayed in a pyroptosis network, which showed that 12 pyroptosis genes exhibited a significant prognostic value (Figure 1E; Supplementary Tables S3, S4).

Tumor classification based on the DEPRGs

To further investigate the expression features of the PRGs in AML, we applied the consensus clustering algorithm to classify the patients with AML according to the expression spectrums of 35 DEPRGs (Supplementary Figures S2A–H). We found that k = 3 seemed to be the optimum alternative for categorizing the entire cohort into three subtypes (Figure 2A and Supplementary Figures S2I–J), based on which satisfied separation across the three clusters was achieved according to the PCA and t-SNE plots (Figures 2B,C). The OS time was also compared between the three groups, but no significant difference was observed ($p = 0.11$, Figure 2D). Furthermore, the heatmap displayed the PRG expression profile and clinicopathological characteristic such as race, gender, age, FAB classification, cytogenetic risk, FLT3-ITD mutation, and NPM1 mutation, with NPM1 mutation (chi-squared test: $p < 0.01$) and FAB classification ($p < 0.001$) demonstrating significant differences among the three groups (Figure 2E).

Gene signature construction and validation from prognostic DEPRGs

To further explore the prognostic value of the DEPRGs in AML patients, the gene signature was constructed. As shown

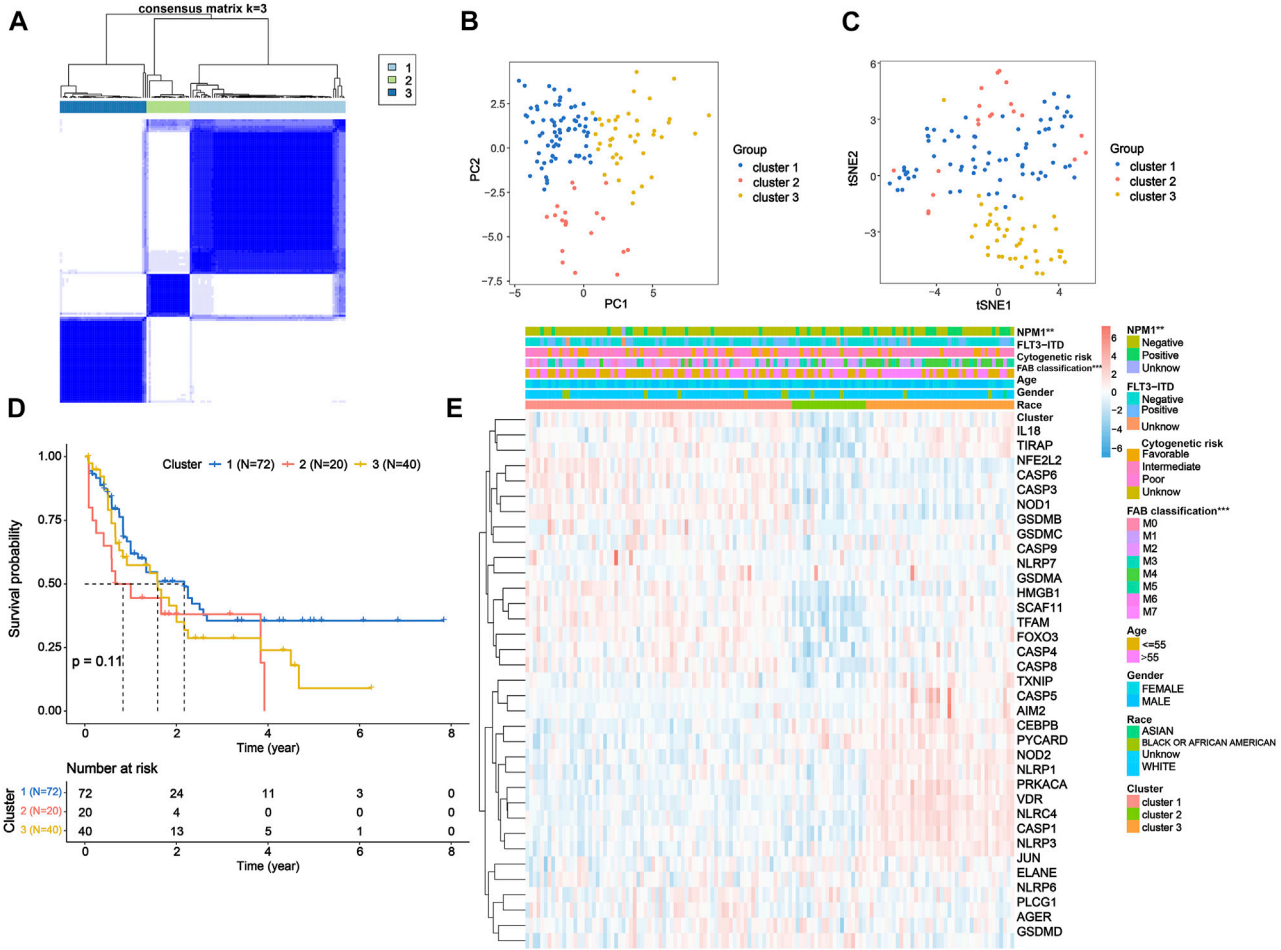

FIGURE 2
Tumor classification based on the DEPRGs. **(A)** 132 AML patients were classified into three clusters according to the consensus clustering matrix (k = 3). **(B)** PCA and **(C)** t-SNE analysis exhibiting a remarkable difference in transcriptomes among three clusters. **(D)** Kaplan–Meier OS curves for three clusters. **(E)** Heatmap and clinicopathological features of three clusters. DEPRGs, differentially expressed pyroptosis-related genes; AML, acute myeloid leukemia; PCA, principal component analysis; t-SNE, t-distributed stochastic neighbor embedding; OS, overall survival.

in Figure 3A, 12 of 42 PRGs showed a significant prognostic value according to univariate Cox regression analysis, among which 10 genes were overlapped between DEPRGs and prognostic genes and were identified as the prognostic DEPRGs. The specific prognostic value of 10 genes is further depicted in Figure 3B and Supplementary Table S5 with five risk and five favorable factors, respectively. Subsequently, based on 1,000 times 10-fold cross-validation in LASSO Cox regression analysis, the minimum of the λ value was selected as the optimum λ value (0.0278). Then, six of 10 genes with not-zero coefficients were screened to construct the gene signature according to the optimum λ (Figures 3C,D). The risk score of each patient is computed as follows: risk score = (−0.0993153386641694 × expression of *CASP3*) + (−0.0669072839409446 × expression of *ELANE*) + (1.29694083393916 × expression of *GSDMA*) + (−0.164405100033389 × expression of *NOD1*) + (0.440274519545682 × expression of *PYCARD*) + (0.00707428724075096 × expression of *VDR*). Then, the patients were separated into the high-risk group (n = 66) and low-risk (n = 66) group according to the median risk score (Figure 4A). The distribution of the risk score indicated that the OS status in the high-risk category was significantly worse than that in the low-risk category (Figure 4B). Further PCA and t-SNE analyses showed identifiable dimensions between the high-risk and low-risk categories (Figures 4C,D). Meanwhile, the Kaplan–Meier survival curves demonstrated significantly superior OS in patients with low scores than those with high scores (p < 0.0001; Figure 4E). Furthermore, time-dependent ROC analysis also revealed that this gene signature exhibited a favorable prognostic performance with AUCs of 0.736, 0.769, and 0.815 at 1-, 3-, and 5-year, respectively (Figure 4F).

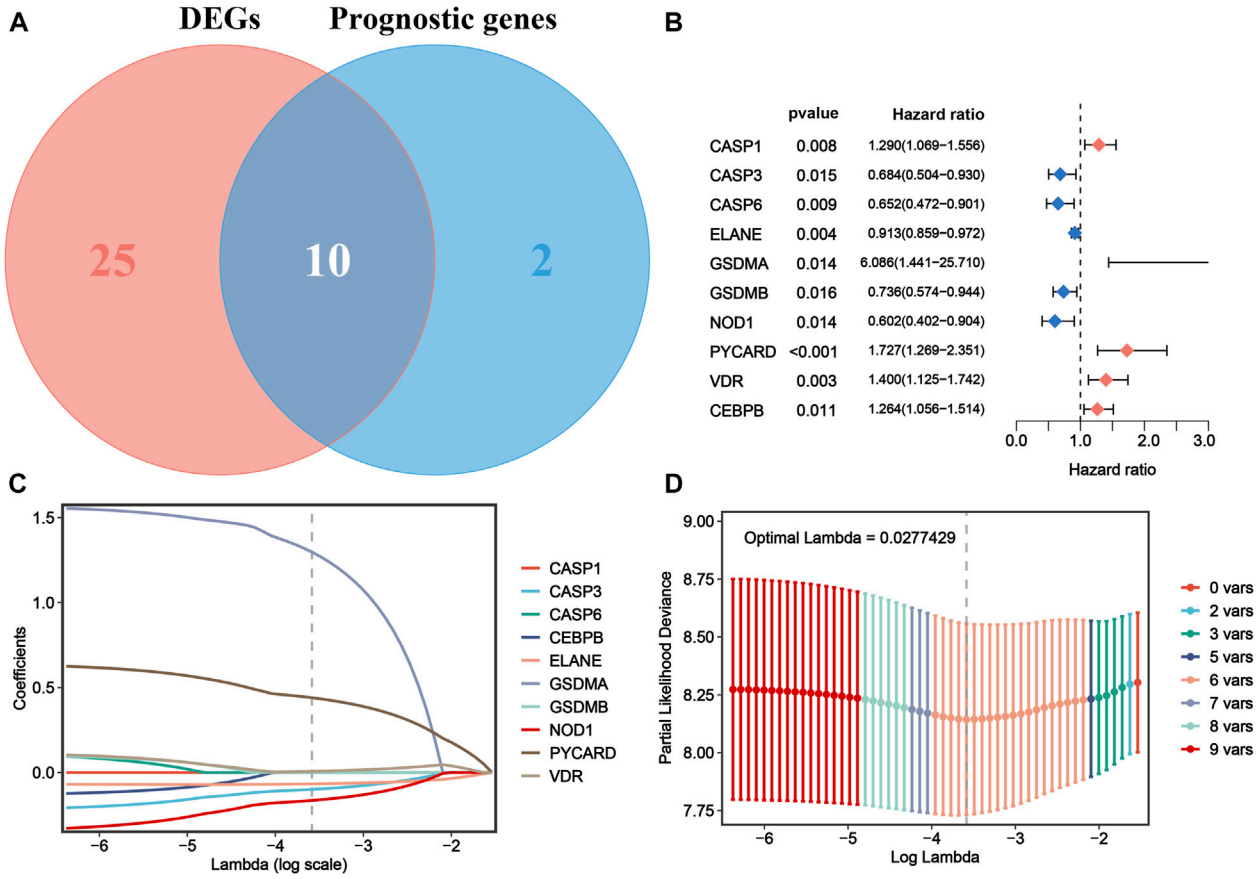

FIGURE 3
Construction of a PRG signature for AML in TCGA cohort. **(A)** Ten prognostic DEPRGs were identified *via* the Venn diagram. **(B)** Forest plots show the results of univariate Cox analysis of OS for 10 prognostic DEPRGs. **(C)** LASSO regression of the 10 prognostic DEPRGs. **(D)** Cross-validation for turning the parameter selection in the LASSO regression. PRG, pyroptosis-related gene; AML, acute myeloid leukemia; TCGA, The Cancer Genome Atlas; DEPRGs, differentially expressed pyroptosis-related genes; OS, overall survival; LASSO, the least absolute shrinkage and selection operator.

To verify the capability of the 6-gene signature, the BeatAML dataset was downloaded as an external validation cohort. We calculated the risk scores of patients with the same formula and stratified patients into high-risk ($n = 45$) and low-risk ($n = 46$) groups (Supplementary Figure S3A). Similarly, patients in the two groups of the BeatAML cohort were distributed in various directions based on the PCA and *t*-SNE analyses (Supplementary Figures S2C–D). Similar to the results of TCGA cohort, patients with low scores were found to have significantly longer OS and a favorable prognostic value ($p = 0.0034$) in the validation cohort (Supplementary Figures S3B,E). In addition, the results of 1-, 3-, and 5-year ROC curves also possessed relatively higher AUC values (0.654, 0.800, and 0.659), indicating that the signature had excellent predictive capability for survival of AML patients (Supplementary Figure S3F).

Independent prognostic value of the 6-gene signature and evaluation of clinical characteristics

We performed univariate and multivariate Cox analyses to assess the possibility of the risk score functioning as an independent prognostic factor. The results of univariate Cox regression analysis demonstrated that the risk score was a significant independent predictor of poor survival in both TCGA ($p < 0.001$, HR = 3.176, 95% CI = 2.122–4.754; Figure 5A) and BeatAML cohorts ($p = 0.005$, HR = 3.108, 95% CI = 1.407–6.867; Figure 5C). Multivariate analysis also revealed that the risk score was a critical prognostic factor for AML patients in both cohorts after accounting for other confounders ($p < 0.001$, HR = 3.356, 95% CI = 1.958–5.753 for TCGA cohort and $p = 0.031$, HR = 2.602, 95% CI = 1.092–6.201 for the BeatAML cohort; Figures 5B,D).

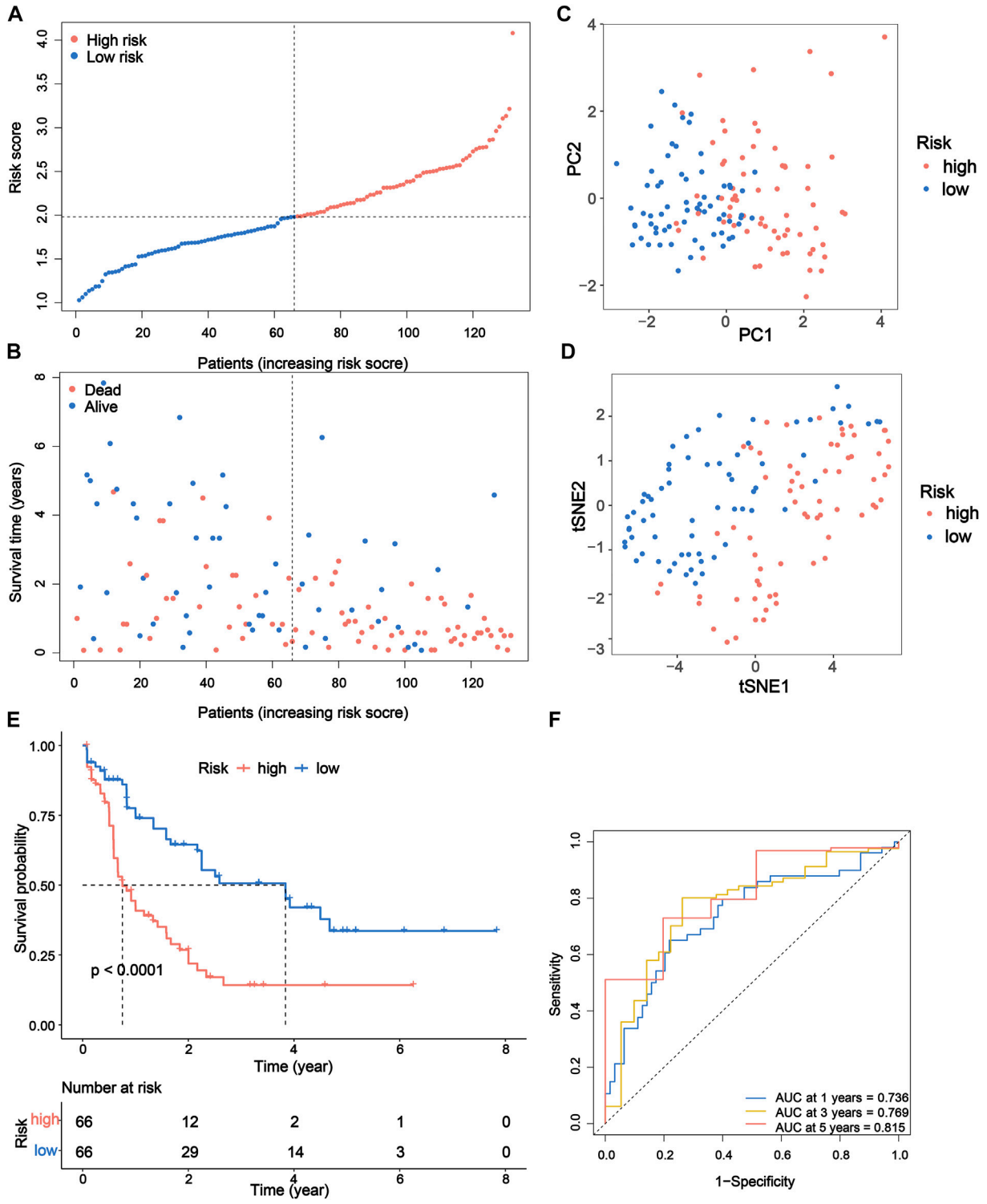

FIGURE 4
Prognostic study of TCGA cohort *via* the PRG signature model. **(A)** Risk scores and **(B)** survival status of AML patients. **(C)** PCA and **(D)** *t*-SNE analysis showing the different gene expression of samples. **(E)** Kaplan–Meier OS curves for high-risk and low-risk groups. **(F)** The 1-, 3-, and 5-year ROC curve to predict the survival status. TCGA, The Cancer Genome Atlas; PRG, pyroptosis-related gene; PCA, principal component analysis; *t*-SNE, *t*-distributed stochastic neighbor embedding; OS, overall survival; ROC, receiver operating characteristic.

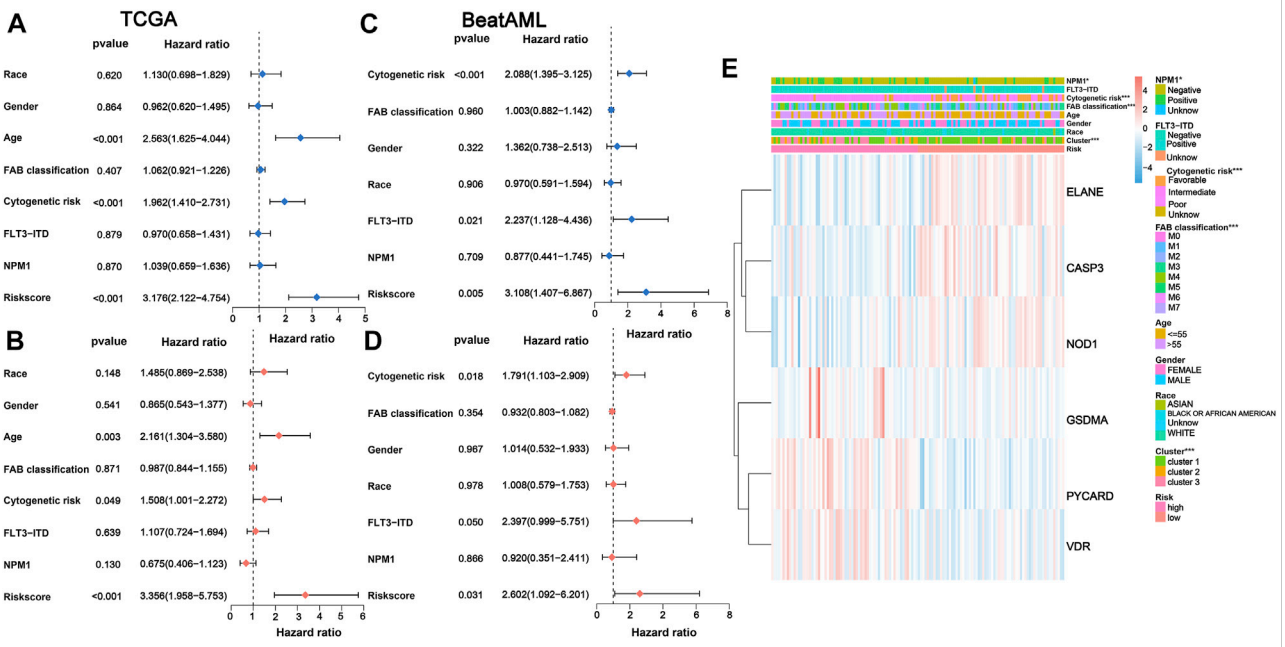

FIGURE 5
Univariate and multivariate Cox regression analyses for the risk score. **(A)** Univariate and **(B)** multivariate Cox regression of the risk score and other clinical characteristics associated with OS in the TCGA cohort. **(C)** Univariate and **(D)** multivariate Cox regression of the risk score and other clinical characteristics associated with OS in the BeatAML cohort. **(E)** Heatmap for association between clinicopathologic characteristics and risk groups. OS, overall survival.

The chi-squared test of correlations between the risk subgroups and clinicopathological features indicated that NPM1 mutation ($p < 0.05$), cytogenetic risk ($p < 0.001$), FAB classification ($p < 0.001$), and PRG clusters ($p < 0.001$) were significantly associated with risk subgroups (Figure 5E). Subsequently, the Wilcoxon signed-rank test was applied to compare the differences in risk scores across respective ;groups of the aforementioned clinicopathological characteristics, also demonstrating a remarkable relationshipof these clinicopathological characteristics with risk scores (Supplementary Figures S4A–D).

In addition, we further assessed whether the risk score could still maintain a good prediction of survival across different subgroups. The results showed that low-risk patients also showed a better prognosis than high-risk patients in all subgroups, with statistically significant results in the following subgroups: race (white: $p < 0.0001$), gender (male: $p = 0.018$; female: $p = 0.0001$), age (≤55 years: $p = 0.024$; >55 years: $p = 0.00045$), FAB classification (M0: $p = 0.017$; M2: $p = 0.011$), cytogenetic risk (intermediate: $p = 0.036$), NPM1 mutation (positive: $p = 0.0051$; negative: $p = 0.0029$), and FLT3-ITD mutation (positive: $p = 0.034$; negative: $p = 0.0019$) (Supplementary Figures S5A–R).

Development of a prognostic nomogram for AML

In consideration of the fact that the risk score alone was not sufficient to predict OS in AML patients, a nomogram incorporating the risk score and clinicopathological features was constructed to forecast 1-, 3-, and 5-year OS of AML patients according to the significant results of multivariate Cox regression analysis (Figure 6A). Furthermore, ROC curves indicated that this nomogram exhibited a good prognostic performance with AUCs of 0.738, 0.768, and 0.815 at 1-, 3-, and 5-year, respectively (Figure 6B). The subsequent calibration plot showed the proposed nomogram operated in a manner consistent with an ideal model (Figure 6C). Moreover, the alluvial diagram was applied to visualize variations in the aforementioned characteristics of AML patients (Figure 6D).

Functional annotation of the 6-gene signature

To further investigate the potential biological functions and pathways of the 6-gene signature, the DEGs across the high-risk and low-risk categories were applied to perform GO and KEGG

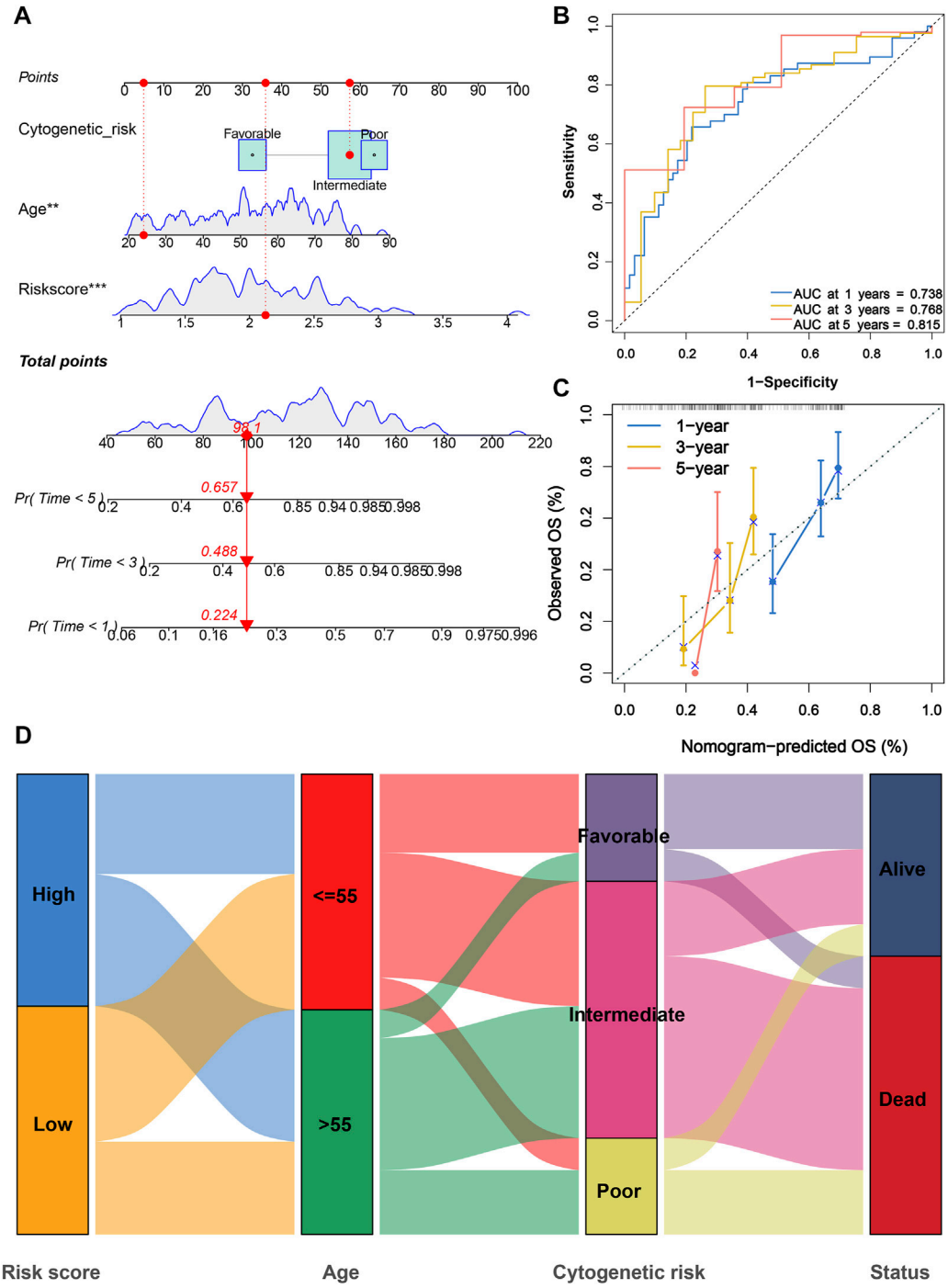

FIGURE 6
Construction and evaluation of a PRG signature-based nomogram. **(A)** Nomogram incorporating cytogenetic risk, age, and risk score was constructed to predict 1-, 3-, and 5-year survival probabilities. **(B)** ROC curves for 1-, 3-, and 5-year were used to assess the performance of nomogram. **(C)** Calibration curves for 1-, 3-, and 5-year prediction were utilized to depict the consistency between predicted and actual survival. **(D)** Alluvial diagram of subgroup distributions with different risk scores and survival outcomes. PRG, pyroptosis-related gene; ROC, receiver operating characteristic.

analyses. The specific details of results were presented in Supplementary Tables S6, S7. Furthermore, these DEGs of TCGA cohort were significantly enriched in biological processes and molecular functions with immunity, such as neutrophil activation involved in the immune response, leukocyte cell–cell adhesion, regulation of leukocyte

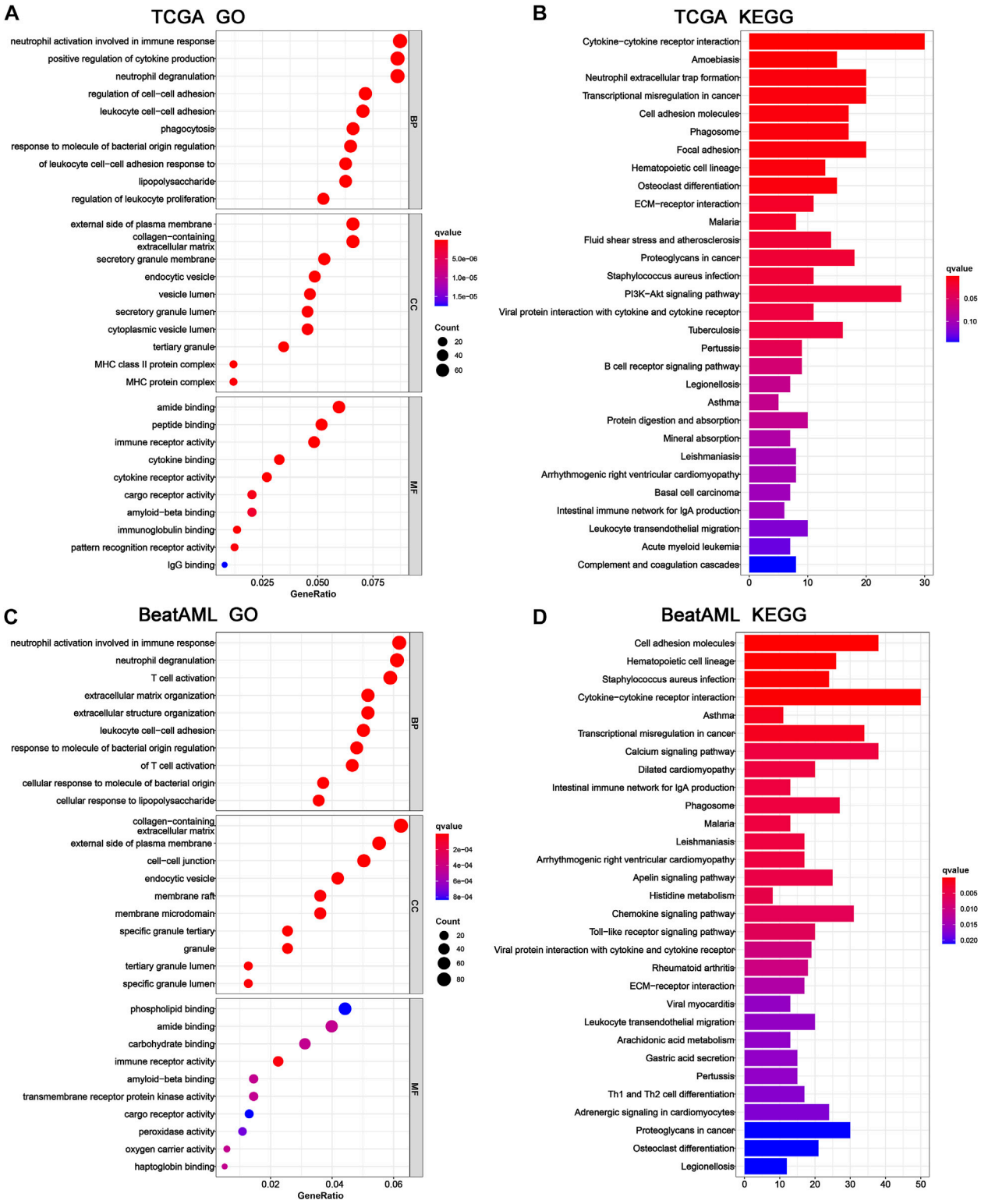

FIGURE 7
GO and KEGG functional enrichment between high- and low-risk groups. Top 10 results of **(A)** GO and **(B)** KEGG pathway enrichment of DEGs among high- and low-risk groups in TCGA cohort. Top 10 results of **(C)** GO and **(D)** KEGG pathway enrichment of DEGs among high- and low-risk groups in the BeatAML cohort. GO, Gene Ontology; KEGG, Kyoto Encyclopedia of Genes and Genomes; DEGs, differentially expressed genes.

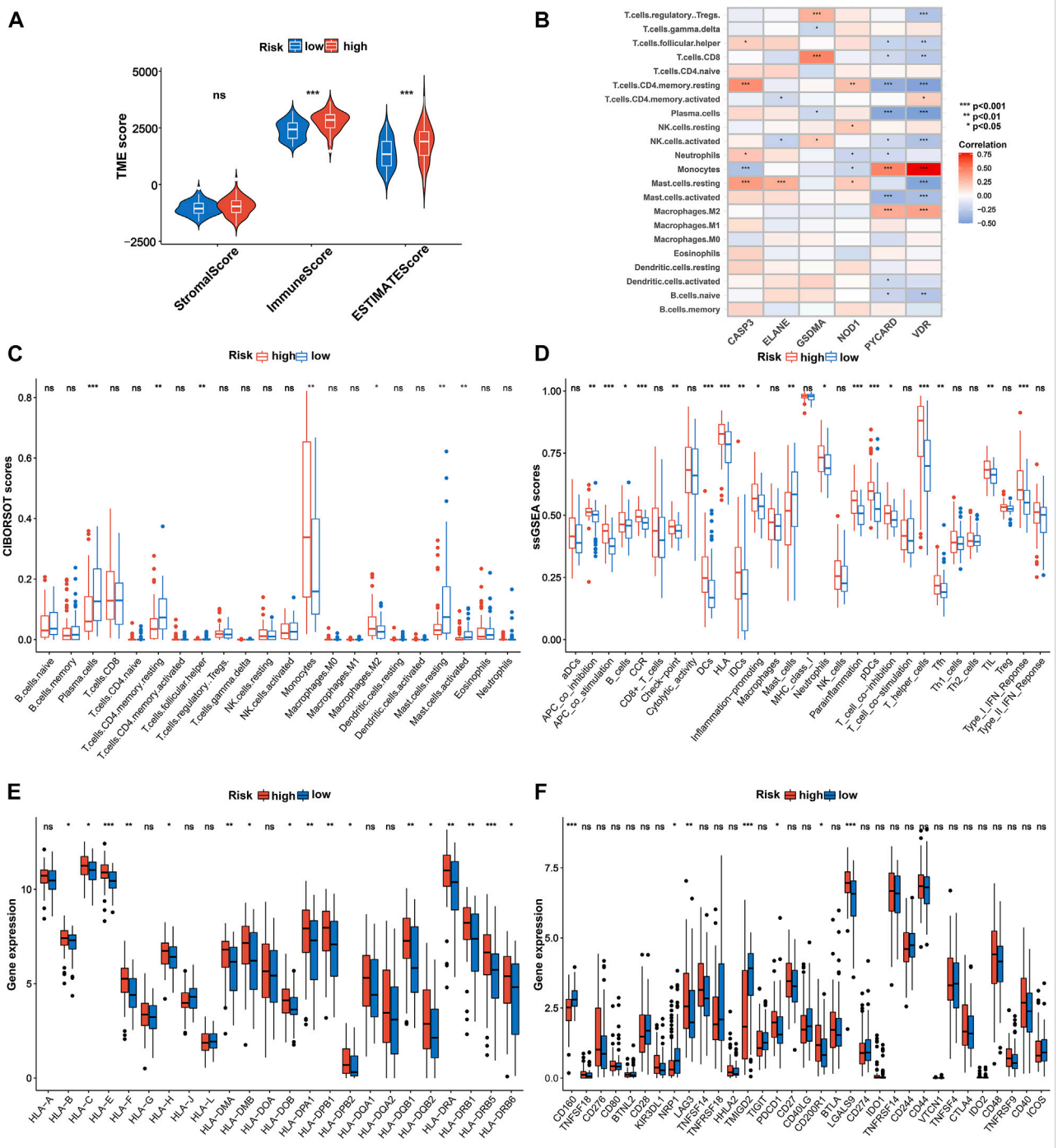

FIGURE 8
Immune characteristics analysis in TCGA cohort. **(A)** Associations between risk score and both immune and stromal scores. **(B)** Correlations between the abundance of immune cells and six genes in the proposed signature. Comparison of the enrichment scores of **(C)** 22 kinds of immune cells and **(D)** 29 types of immune signatures between high- and low-risk groups. **(E)** Expression of HLA in the high- and low-risk groups. **(F)** Expression of immune checkpoints in the high- and low-risk groups. *p* values are shown as: ns, not significant. *$p = < 0.05$; **$p = < 0.01$; ***$p = < 0.001$. HLA, human lymphocyte antigen.

proliferation, immune receptor activity, immunoglobulin binding, and IgG binding (Figure 7A). Several of these biological processes and molecular functions were validated in the BeatAML cohort, including neutrophil activation involved in the immune response, leukocyte cell–cell adhesion, and immune receptor activity (Figure 7C). The results of KEGG analysis also showed enrichment of immune-related pathways, which included cytokine–cytokine receptor interaction, phagosome, viral protein interaction with cytokine and cytokine receptor, intestinal immune network for IgA production, and leukocyte transendothelial migration in both TCGA and BeatAML cohorts (Figures 7B,D). Moreover, pathways regarding B-cell receptor signaling and Th1 and Th2 cell differentiation were also found in TCGA (Figure 7B) and BeatAML cohorts (Figure 7D), respectively. In addition, several cancer-related pathways were simultaneously identified in both cohorts, such as transcriptional misregulation in cancer, hematopoietic cell lineage, ECM-receptor interaction, and proteoglycans in cancer. These results revealed that the pyroptosis-related 6-gene signature was significantly associated with cancer progression and particularly possessed an important influence on the immunoregulation of TME.

Tumor immune microenvironment analysis of 6-gene signature

Next, we further explored the association between the pyroptosis-related gene signature and tumor immune microenvironment and observed that the low-risk patients were significantly correlated with inferior immune and ESTIMATE scores in the TCGA cohort (Figure 8A). Subsequently, based on the CIBERSORT algorithm, we compared the distribution of 22 kinds of immune cells in diverse risk subgroups. A significant difference in the distribution of immune cells was observed in high-risk patients with superior infiltration of monocytes and M2 macrophages, but inferior infiltration of plasma cells, resting memory $CD4^+$ T cells, follicular helper T cells, activated mast cells, and resting mast cells (Figure 8C and Supplementary Table S8). Concurrently, we analyzed the connection between the risk score and the infiltration score of immune cells, which further suggested that the risk score was significantly associated with the six kinds of immune cells (Supplementary Figure S6). We also evaluated the relationship between the six pyroptosis-related genes in the proposed signature and abundance of immune cells. The results showed that partial immune cells were significantly associated with the six genes (Figure 8B). Furthermore, comparisons of 29 immune signatures provided by the ssGSEA algorithm revealed that high-risk patients exhibited higher infiltration scores of APC co-inhibition, APC co-stimulation, B cells, CCR, checkpointa, DCs, HLA, iDCs, increased inflammation , neutrophils, parainflammation, pDCs, T-cell co-inhibition, T helper cells, Tfh, TIL, and type I IFN response, whereas lower infiltration scores of mast cells (Figure 8D and Supplementary Table S9) indicated higher immune infiltration among high-risk AML patients.

Considering that HLA-related genes play a critical role in regulating the immune response, we then compared the expression of HLA-related genes between different subgroups and observed that most of the HLA-related genes were upregulated in the high-risk group (Figure 8E). Furthermore, we investigated the correlation between 33 immune checkpoints and the 6-PRG signature. Figure 8F demonstrated that high-risk patients exhibited significantly higher expression of *PDCD1*, *CD200R1*, *CAG3*, and *LGALS9* as well as lower expression of *CD160*, *NRP1*, and *TMIGD2* compared with low-risk patients. In addition, similar results were also observed in the BeatAML cohort (Supplementary Figures S7, S8; Supplementary Tables S10, S11).

Analysis of CSC index, TMB, and drug susceptibility

Considering that the CSC index and TMB play a critical role in the pathogenesis and immunotherapy of AML (Eppert et al., 2011; Snyder et al., 2014), we further explored the potential correlation between them and the PRG signature. As shown in Figure 9A, the risk score was negatively associated with the CSC index ($R = -0.29$, $p = 0.0011$), suggesting that AML cells with a lower risk score exhibited more significant stem cell characteristics and a lower degree of cell differentiation. Meanwhile, we also found that TMB of the low-risk group was significantly higher than that of the high-risk group ($p = 0.039$; Figure 9B) and was negatively associated with the PRG risk score ($R = -0.25$, $p = 0.019$; Figure 9C). Furthermore, the Kaplan–Meier survival curve for combining the PRG risk score and TMB revealed significant differences in survival outcomes and patients with high TMB and low PRG risk scores exhibited a more pronounced survival advantage (Figure 9D).

Moreover, given the impact of drug susceptibility on patients with AML, we further selected the drugs currently used in the treatment of AML to assess the sensitivity of these drugs to patients in both high-risk and low-risk subgroups. Interestingly, we observed that patients in the low-risk group presented significantly lower IC50 values for ATRA, cytarabine, midostaurin, doxorubicin, and etoposide than those in the high-risk group (Figures 9E–I). Therefore, patients with a low PRG risk score might exhibit better treatment benefits when administrating these drugs. Nevertheless, the effect of these drugs in the treatment of AML patients remains to be further proven in future clinical studies.

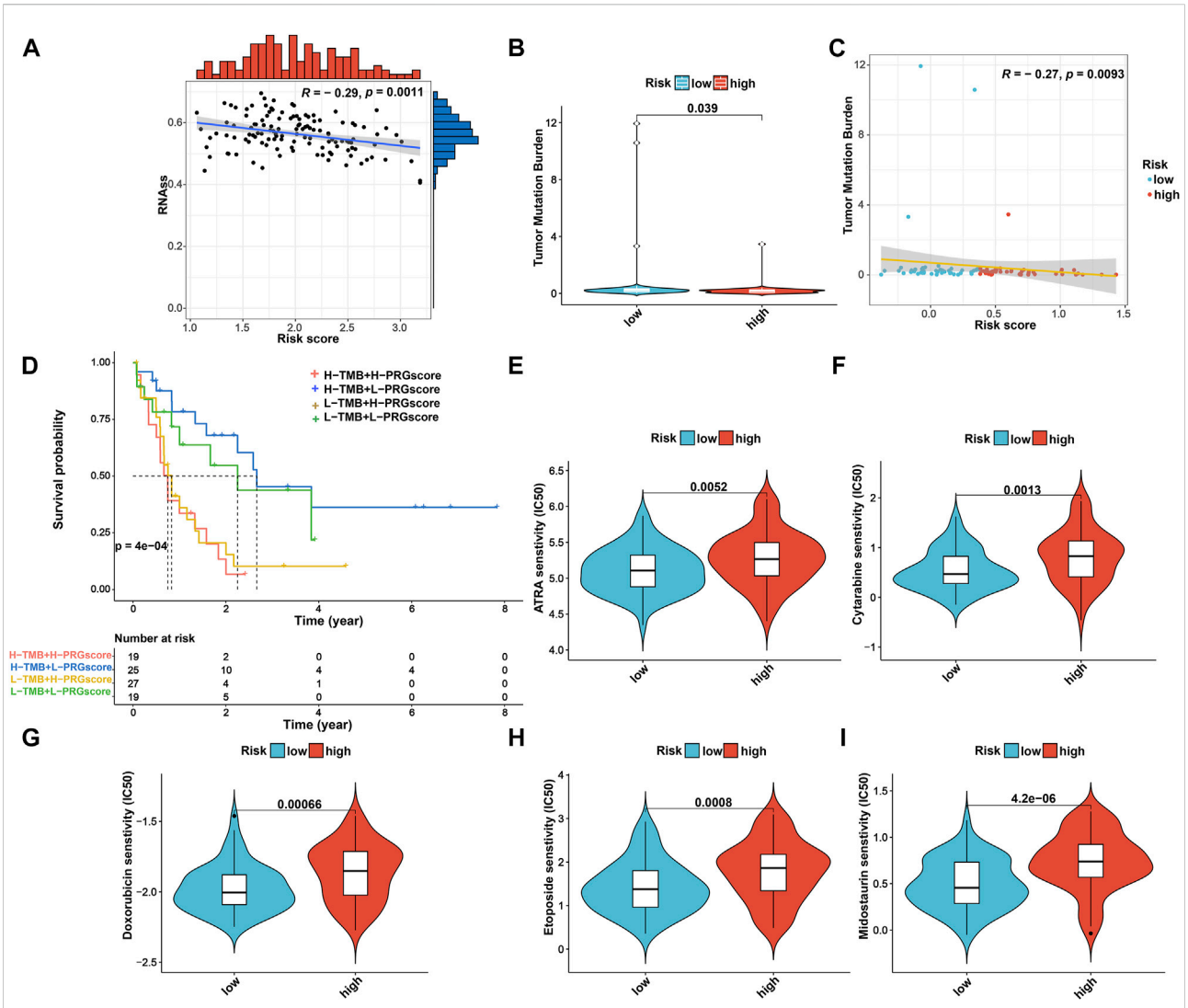

FIGURE 9
Comprehensive analysis of the risk score in AML. **(A)** Associations between the risk score and CSC index. **(B)** Comparison of TMB between high- and low-risk groups. **(C)** Spearman correlation analysis of risk score and TMB. **(D)** Kaplan–Meier OS curves for different TMB and risk score subgroups. **(E–I)** Relationships between risk score and therapeutic drugs of AML sensitivity. AML, acute myeloid leukemia; CSC, cancer stemness cell; TMB, tumor mutation burden; OS, overall survival.

Discussion

AML is a rapidly progressive hematologic tumor with poor prognosis, and its development can be influenced by multiple factors (Coombs et al., 2016), among which genes associated with programmed cell death (PCD), such as autophagy-related genes and ferroptosis-related genes, were demonstrated to serve as reliable prognostic biomarkers for AML (Fu et al., 2021; Shao et al., 2021). However, studies regarding the role of PRGs in AML are restricted to individual PRG and have never been investigated systematically and comprehensively. In this study, we detected the global alterations in PRGs at transcriptional and genetic levels in AML and identified a total of 42 currently available PRGs, the majority of which were differentially expressed between AML and normal samples and were associated with prognostic of this disease. Subsequently, we first constructed a reliable and valid PRG signature for AML based on six PRGs. In both training and validation cohorts, the PRG signature exhibited robust capabilities in predicting survival outcomes in AML patients. Furthermore, patients with low and high PRG scores showed significantly different clinicopathological features. In addition, univariate and multivariate Cox regression analyses also indicated that the PRG signature was an independent prognostic factor. These findings confirm that the present PRG signature can be used as a potentially reliable prognostic biomarker in AML patients with various clinicopathological features.

Pyroptosis, a novel form of PCD, is activated *via* the classical caspase-1 inflammasome or non-classical caspase-4, caspase-5, and caspase-11–mediated pathways (Tang et al., 2020). Recently, the dual roles of pyroptosis in tumor progression gained substantial attention. On one hand, it was reported that inflammatory molecules released from cancer cells underwent pyroptosis and gradually converted the surrounding normal cells into cancer cells by altering the microenvironment, which in turn promoted tumor development. On the other hand, induction of tumor cell pyroptosis was also found to inhibit tumor progression and was demonstrated to be a potential therapeutic target for drug development (Tang et al., 2020). This situation raised great uncertainties regarding the exact functions of pyroptosis in different kinds of tumors. Furthermore, as a matter of fact, previous studies paid much more attention to the roles of PRGs in solid carcinomas [e.g., hepatocellular carcinoma (Deng et al., 2022), breast cancer (Xu D. et al., 2021), lung adenocarcinoma (Lin W. et al., 2021), and colon adenocarcinoma (Luo et al., 2021)] with few studies, however, focusing on non-solid tumor such as AML. Therefore, the present study provided a novel signature featuring six PRGs (*CASP3*, *ELANE*, *GSDMA*, *PYCARD*, *VDR*, and *NOD1*) that exactly and independently predict OS in AML patients, which will further contribute to driving the progress of individualized prevention and treatment of AML.

Among these PRGs, caspase-3 (*CASP3*) is an important member of the caspase family, whose activation degrades structural and functional proteins within cells, thereby inducing cell death (Yuan et al., 1993; Jiang et al., 2020). In the present study, we further revealed that this gene was a favorable predictor of survival outcome and was associated with increased sensitivity to chemotherapeutic drug–induced pyroptosis in AML, which was in accordance with the previous study indicating that *CASP3* activated by chemotherapeutic drugs initiated pyroptosis (Wang et al., 2017). Moreover, as one of the primary serine proteases secreted by neutrophils, *ELANE* is another known promoter of pyroptosis, which activates inflammatory factors such as *TNF-α*, *IL-1β*, and *IL-18*, and induces neutrophils to develop pyroptosis (Kambara et al., 2018; Mirea et al., 2020). Consistently, our study demonstrated that the expression of *ELANE* was significantly higher while the neutrophil infiltration score was remarkably lower in the low-risk group than that in the high-risk group, which was very likely to be ascribed to its pyroptosis activating effect in neutrophils. In addition, the following three genes (*GSMDA*, *PYCARD*, and *VDR*) that were previously identified as possible executors of pyroptosis and usually exhibited tumor-suppressive effects (Ding et al., 2016; Šutić et al., 2019; Ling et al., 2022) were also identified and included in the present PRG signature, further confirming its reliability.

Interestingly, as a cytoplasmic pattern recognition receptor, *NOD1* was initially identified as a cancer-promoting factor and might cause tumor recurrence and metastasis, resulting in a poorer prognosis through pyroptosis (Fernández-García et al., 2022; Nomoto et al., 2022). However, in our research, *NOD1* showed a significant cancer suppressive effect and acted as a protective factor against AML. This discrepancy may be attributed to the specialized tumor microenvironment in non-solid tumors and also the antitumor immune activity generated by the combined action of multiple PRGs although the exact mechanism still needs to be further explored.

Previous studies showed that the pro-inflammatory effects of pyroptosis are strongly associated with the regulation of the TIME (Tsuchiya, 2021). This study hence further evaluated the association between the risk score of PRG signature and TIME and found that patients in the high-risk group showed significantly higher immune scores than those in the low-risk group. The abundance of infiltration of tumor immune cells also differed between the high- and low-risk groups. Compared to the high-risk group, resting $CD4^+$ memory T cells and follicular helper T cells, both of which were well acknowledged to exert an important antitumor immune response (Watanabe, 2021), infiltrated at higher levels in the low-risk group; whereas tumorigenesis-, angiogenesis- and immune suppressing-related cell types, such as M2 macrophages, monocytes, antigen-presenting cells, and dendritic cells (Nahas et al., 2019; Fu and Song, 2021), showed higher infiltration levels in the high-risk group. Furthermore, this study also found that patients with high-risk scores showed a worse prognosis than those with low-risk scores. These findings indicated that the immunosuppressive microenvironment played important roles during the genesis and development of AML. In fact, it was reported that the formation of an immunosuppressive microenvironment usually prevented the clearance of tumor cells by tumor killer cells, resulting in an increased risk of malignant progression and death (Fridman et al., 2022). Therefore, treatment targeting the immunosuppressive microenvironment may be a more effective and feasible strategy for patients with a poor prognosis of AML.

In addition, we found that most HLA-related genes and *PDCD1* expressed at higher levels in the high-risk group, which was in accordance with the current increasing evidence regarding solid tumors suggesting that more HLA presentation increased the recognition of tumor-associated antigens in HLA and in turn increased the success of immune checkpoint inhibitor therapy (Rizvi et al., 2015; Lin W. Y. et al., 2021). Therefore, patients with high-risk scores for AML might benefit more from immunotherapy, especially with immune checkpoint inhibitors PD-1.

Although we analyzed the effects of pyroptosis on the prognosis of AML and the immune microenvironment as comprehensively as possible, the following points remained inadequate. First, all analyses

in this study were performed based on retrospective data from public databases, and large prospective studies and additional *in vivo* and *in vitro* experimental studies are still needed to confirm our findings. Second, the proposed gene signature model was validated only through public databases. Therefore, further clinical trials are still necessary to confirm its clinical utility. In addition, the potential mechanisms of the present six key genes used for model construction need to be further explored in order to better understand the tumorigenesis and development of AML. Finally, subgroup analyses for ethnicity were not performed in our study mainly due to the limited availability of current original data, which should also be validated in future studies based on additional risk models.

In summary, we comprehensively analyzed the expression and genetic changes of PGRs in AML, their prognostic value in the clinic, their important role in TIME, and constructed a signature consisting of six PRGs, which was confirmed to be an independent predictor for OS in AML patients. The results of this study will contribute to further understanding of the important role of pyroptosis in the prognosis and development of AML and provide novel and reliable biomarkers for its precise prevention and treatment.

Data availability statement

The original contributions presented in the study are included in the article/Supplementary Material; further inquiries can be directed to the corresponding author.

Author contributions

G-HH conceived and designed the study, obtained the funding. TZ performed the majority of data analysis and wrote the manuscript. W-KC, S-JY, and Y-YL participated in checking the statistic method and helped to draft the manuscript. KQ and PW prepared the figures. All authors revised and approved the final manuscript.

Funding

This work was supported by the Grants from the National Science Foundation of China (No. 81960664), the Applied Basic Research Program Yunnan Province of China (Joint Special Project of Kunming Medical University) (No. 202101AY070001-300), and the Science and Technology Planning Project of 920th Hospital of Joint Logistics Support Force (No. 2020YGB11).

Acknowledgments

All authors sincerely acknowledge the contributions from the TCGA, GTEx, and BeatAML projects.

Conflict of interest

The authors declare that the research was conducted in the absence of any commercial or financial relationships that could be construed as a potential conflict of interest.

Publisher's note

Supplementary material

The Supplementary Material for this article can be found online at: https://www.frontiersin.org/articles/10.3389/fphar.2022.951480/full#supplementary-material

References

Arneth, B. (2019). Tumor microenvironment. *Med. Kaunas. Lith.* 56 (1), 15. doi:10.3390/medicina56010015

Balahura, L. R., Selaru, A., Dinescu, S., and Costache, M. (2020). Inflammation and inflammasomes: pros and cons in tumorigenesis. *J. Immunol. Res.* 2020, 2549763. doi:10.1155/2020/2549763

Ball, B., and Stein, E. M. (2019). Which are the most promising targets for minimal residual disease-directed therapy in acute myeloid leukemia prior to allogeneic stem cell transplant? *Haematologica* 104 (8), 1521–1531. doi:10.3324/haematol.2018.208587

Broz, P., von Moltke, J., Jones, J. W., Vance, R. E., and Monack, D. M. (2010). Differential requirement for Caspase-1 autoproteolysis in pathogen-induced cell death and cytokine processing. *Cell Host Microbe* 8 (6), 471–483. doi:10.1016/j.chom.2010.11.007

Coombs, C. C., Tallman, M. S., and Levine, R. L. (2016). Molecular therapy for acute myeloid leukaemia. *Nat. Rev. Clin. Oncol.* 13 (5), 305–318. doi:10.1038/nrclinonc.2015.210

Deng, M., Sun, S., Zhao, R., Guan, R., Zhang, Z., Li, S., et al. (2022). The pyroptosis-related gene signature predicts prognosis and indicates immune activity in hepatocellular carcinoma. *Mol. Med.* 28 (1), 16. doi:10.1186/s10020-022-00445-0

Ding, J., Wang, K., Liu, W., She, Y., Sun, Q., Shi, J., et al. (2016). Pore-forming activity and structural autoinhibition of the gasdermin family. *Nature* 535 (7610), 111–116. doi:10.1038/nature18590

Eppert, K., Takenaka, K., Lechman, E. R., Waldron, L., Nilsson, B., van Galen, P., et al. (2011). Stem cell gene expression programs influence clinical outcome in human leukemia. *Nat. Med.* 17 (9), 1086–1093. doi:10.1038/nm.2415

Erkes, D. A., Cai, W., Sanchez, I. M., Purwin, T. J., Rogers, C., Field, C. O., et al. (2020). Mutant BRAF and MEK inhibitors regulate the tumor immune microenvironment via pyroptosis. *Cancer Discov.* 10 (2), 254–269. doi:10.1158/2159-8290.CD-19-0672

Fernández-García, V., González-Ramos, S., Avendaño-Ortiz, J., Martín-Sanz, P., Delgado, C., Castrillo, A., et al. (2022). NOD1 splenic activation confers ferroptosis protection and reduces macrophage recruitment under pro-atherogenic conditions. *Biomed. Pharmacother.* 148, 112769. doi:10.1016/j.biopha.2022.112769

Fridman, W. H., Meylan, M., Petitprez, F., Sun, C. M., Italiano, A., and Sautès-Fridman, C. (2022). B cells and tertiary lymphoid structures as determinants of tumour immune contexture and clinical outcome. *Nat. Rev. Clin. Oncol.* 15, 1–17. Advance online publication. doi:10.1038/s41571-022-00619-z

Fu, D., Zhang, B., Wu, S., Zhang, Y., Xie, J., Ning, W., et al. (2021). Prognosis and characterization of immune microenvironment in acute myeloid leukemia through identification of an autophagy-related signature. *Front. Immunol.* 12, 695865. doi:10.3389/fimmu.2021.695865

Fu, X. W., and Song, C. Q. (2021). Identification and validation of pyroptosis-related gene signature to predict prognosis and reveal immune infiltration in hepatocellular carcinoma. *Front. Cell Dev. Biol.* 9, 748039. doi:10.3389/fcell.2021.748039

Fu, Y., Liu, S., Zeng, S., and Shen, H. (2019). From bench to bed: the tumor immune microenvironment and current immunotherapeutic strategies for hepatocellular carcinoma. *J. Exp. Clin. Cancer Res.* 38 (1), 396. doi:10.1186/s13046-019-1396-4

Hartigan, J. A., and Wong, M. A. (1979). Algorithm as 136: a k-means clustering algorithm. *Appl. Stat.* 28 (1), 100. doi:10.2307/2346830

Jiang, M., Qi, L., Li, L., and Li, Y. (2020). The caspase-3/GSDME signal pathway as a switch between apoptosis and pyroptosis in cancer. *Cell Death Discov.* 6, 112. doi:10.1038/s41420-020-00349-0

Johnson, D. C., Taabazuing, C. Y., Okondo, M. C., Chui, A. J., Rao, S. D., Brown, F. C., et al. (2018). DPP8/DPP9 inhibitor-induced pyroptosis for treatment of acute myeloid leukemia. *Nat. Med.* 24 (8), 1151–1156. doi:10.1038/s41591-018-0082-y

Kambara, H., Liu, F., Zhang, X., Liu, P., Bajrami, B., Teng, Y., et al. (2018). Gasdermin D exerts anti-inflammatory effects by promoting neutrophil death. *Cell Rep.* 22 (11), 2924–2936. doi:10.1016/j.celrep.2018.02.067

Karki, R., and Kanneganti, T. D. (2019). Diverging inflammasome signals in tumorigenesis and potential targeting. *Nat. Rev. Cancer* 19 (4), 197–214. doi:10.1038/s41568-019-0123-y

Lin, W., Chen, Y., Wu, B., Chen, Y., and Li, Z. (2021). Identification of the pyroptosis-related prognostic gene signature and the associated regulation axis in lung adenocarcinoma. *Cell Death Discov.* 7 (1), 161. doi:10.1038/s41420-021-00557-2

Lin, W. Y., Fordham, S. E., Hungate, E., Sunter, N. J., Elstob, C., Xu, Y., et al. (2021). Genome-wide association study identifies susceptibility loci for acute myeloid leukemia. *Nat. Commun.* 12 (1), 6233. doi:10.1038/s41467-021-26551-x

Ling, Y., Xu, F., Xia, X., Dai, D., Sun, R., Xie, Z., et al. (2022). Vitamin D receptor regulates proliferation and differentiation of thyroid carcinoma via the E-cadherin-β-catenin complex. *J. Mol. Endocrinol.* 68 (3), 137–151. doi:10.1530/JME-21-0167

Luo, B., Lin, J., Cai, W., and Wang, M. (2021). Identification of the pyroptosis-related gene signature and risk score model for colon adenocarcinoma. *Front. Genet.* 12, 771847. doi:10.3389/fgene.2021.771847

Malta, T. M., Sokolov, A., Gentles, A. J., Burzykowski, T., Poisson, L., Weinstein, J. N., et al. (2018). Machine learning identifies stemness features associated with oncogenic dedifferentiation. *Cell* 173 (2), 338–354. e15. doi:10.1016/j.cell.2018.03.034

Man, S. M., and Kanneganti, T. D. (2015). Regulation of inflammasome activation. *Immunol. Rev.* 265 (1), 6–21. doi:10.1111/imr.12296

Mirea, A. M., Stienstra, R., Kanneganti, T. D., Tack, C. J., Chavakis, T., Toonen, E., et al. (2020). Mice deficient in the IL-1β activation genes Prtn3, elane, and Casp1 are protected against the development of obesity-induced NAFLD. *Inflammation* 43 (3), 1054–1064. doi:10.1007/s10753-020-01190-4

Moujalled, D., Strasser, A., and Liddell, J. R. (2021). Molecular mechanisms of cell death in neurological diseases. *Cell Death Differ.* 28 (7), 2029–2044. doi:10.1038/s41418-021-00814-y

Nahas, M. R., Stroopinsky, D., Rosenblatt, J., Cole, L., Pyzer, A. R., Anastasiadou, E., et al. (2019). Hypomethylating agent alters the immune microenvironment in acute myeloid leukaemia (AML) and enhances the immunogenicity of a dendritic cell/AML vaccine. *Br. J. Haematol.* 185 (4), 679–690. doi:10.1111/bjh.15818

Nomoto, D., Baba, Y., Liu, Y., Tsutsuki, H., Okadome, K., Harada, K., et al. (2022). Fusobacterium nucleatum promotes esophageal squamous cell carcinoma progression via the NOD1/RIPK2/NF-κB pathway. *Cancer Lett.* 530, 59–67. doi:10.1016/j.canlet.2022.01.014

Orning, P., Lien, E., and Fitzgerald, K. A. (2019). Gasdermins and their role in immunity and inflammation. *J. Exp. Med.* 216 (11), 2453–2465. doi:10.1084/jem.20190545

Perna, F., Berman, S. H., Soni, R. K., Mansilla-Soto, J., Eyquem, J., Hamieh, M., et al. (2017). Integrating proteomics and transcriptomics for systematic combinatorial chimeric antigen receptor therapy of AML. *Cancer Cell* 32 (4), 506–519. doi:10.1016/j.ccell.2017.09.004

Rizvi, N. A., Hellmann, M. D., Snyder, A., Kvistborg, P., Makarov, V., Havel, J. J., et al. (2015). Cancer immunology. Mutational landscape determines sensitivity to PD-1 blockade in non-small cell lung cancer. *Science* 348 (6230), 124–128. doi:10.1126/science.aaa1348

Schlenk, R. F., Jaramillo, S., and Müller-Tidow, C. (2019). What's new in consolidation therapy in AML? *Semin. Hematol.* 56 (2), 96–101. doi:10.1053/j.seminhematol.2018.08.005

Shao, R., Wang, H., Liu, W., Wang, J., Lu, S., Tang, H., et al. (2021). Establishment of a prognostic ferroptosis-related gene profile in acute myeloid leukaemia. *J. Cell. Mol. Med.* 25 (23), 10950–10960. doi:10.1111/jcmm.17013

Snyder, A., Makarov, V., Merghoub, T., Yuan, J., Zaretsky, J. M., Desrichard, A., et al. (2014). Genetic basis for clinical response to CTLA-4 blockade in melanoma. *N. Engl. J. Med.* 371 (23), 2189–2199. doi:10.1056/NEJMoa1406498

Sperlazza, J., Rahmani, M., Beckta, J., Aust, M., Hawkins, E., Wang, S. Z., et al. (2015). Depletion of the chromatin remodeler CHD4 sensitizes AML blasts to genotoxic agents and reduces tumor formation. *Blood* 126 (12), 1462–1472. doi:10.1182/blood-2015-03-631606

Stölzel, F., Röllig, C., Radke, J., Mohr, B., Platzbecker, U., Bornhäuser, M., et al. (2011). ^{18}F-FDG-PET/CT for detection of extramedullary acute myeloid leukemia. *Haematologica* 96 (10), 1552–1556. doi:10.3324/haematol.2011.045047

Šutić, M., Motzek, A., Bubanović, G., Linke, M., Sabol, I., Vugrek, O., et al. (2019). Promoter methylation status of ASC/TMS1/PYCARD is associated with decreased overall survival and TNM status in patients with early-stage non-small cell lung cancer (NSCLC). *Transl. Lung Cancer Res.* 8 (6), 1000–1015. doi:10.21037/tlcr.2019.12.08

Tang, R., Xu, J., Zhang, B., Liu, J., Liang, C., Hua, J., et al. (2020). Ferroptosis, necroptosis, and pyroptosis in anticancer immunity. *J. Hematol. Oncol.* 13 (1), 110. doi:10.1186/s13045-020-00946-7

Tibshirani, R. (1997). The lasso method for variable selection in the Cox model. *Stat. Med.* 16 (4), 385–395. doi:10.1002/(sici)1097-0258(19970228)16:4<385::aid-sim380>3.0.co;2-3

Tsuchiya, K. (2021). Switching from apoptosis to pyroptosis: gasdermin-elicited inflammation and antitumor immunity. *Int. J. Mol. Sci.* 22 (1), 426. doi:10.3390/ijms22010426

Tyner, J. W., Tognon, C. E., Bottomly, D., Wilmot, B., Kurtz, S. E., Savage, S. L., et al. (2018). Functional genomic landscape of acute myeloid leukaemia. *Nature* 562 (7728), 526–531. doi:10.1038/s41586-018-0623-z

Wang, B., and Yin, Q. (2017). AIM2 inflammasome activation and regulation: a structural perspective. *J. Struct. Biol.* 200 (3), 279–282. doi:10.1016/j.jsb.2017.08.001

Wang, S., Yuan, P., Mao, B., Li, N., Ying, J., Tao, X., et al. (2022). Genomic features and tumor immune microenvironment alteration in NSCLC treated with neoadjuvant PD-1 blockade. *NPJ Precis. Oncol.* 6 (1), 2. doi:10.1038/s41698-021-00244-6

Wang, Y., Gao, W., Shi, X., Ding, J., Liu, W., He, H., et al. (2017). Chemotherapy drugs induce pyroptosis through caspase-3 cleavage of a gasdermin. *Nature* 547 (7661), 99–103. doi:10.1038/nature22393

Watanabe, T. (2021). The tumor microenvironment in follicular lymphoma: its pro-malignancy role with therapeutic potential. *Int. J. Mol. Sci.* 22 (10), 5352. doi:10.3390/ijms22105352

Wilkerson, M. D., and Hayes, D. N. (2010). ConsensusClusterPlus: a class discovery tool with confidence assessments and item tracking. *Bioinformatics* 26 (12), 1572–1573. doi:10.1093/bioinformatics/btq170

Wu, T., and Dai, Y. (2017). Tumor microenvironment and therapeutic response. *Cancer Lett.* 387, 61–68. doi:10.1016/j.canlet.2016.01.043

Wu, T., Hu, E., Xu, S., Chen, M., Guo, P., Dai, Z., et al. (2021). clusterProfiler 4.0: a universal enrichment tool for interpreting omics data. *Innovation* 2 (3), 100141. doi:10.1016/j.xinn.2021.100141

Xia, X., Wang, X., Cheng, Z., Qin, W., Lei, L., Jiang, J., et al. (2019). The role of pyroptosis in cancer: pro-cancer or pro-"host" *Cell Death Dis.* 10 (9), 650. doi:10.1038/s41419-019-1883-8

Xu, B., Lu, M., Yan, L., Ge, M., Ren, Y., Wang, R., et al. (2021). A pan-cancer analysis of predictive methylation signatures of response to cancer immunotherapy. *Front. Immunol.* 12, 796647. doi:10.3389/fimmu.2021.796647

Xu, D., Ji, Z., and Qiang, L. (2021). Molecular characteristics, clinical implication, and cancer immunity interactions of pyroptosis-related genes in breast cancer. *Front. Med.* 8, 702638. doi:10.3389/fmed.2021.702638

Yang, J., Hong, S., Zhang, X., Liu, J., Wang, Y., Wang, Z., et al. (2021). Tumor immune microenvironment related gene-based model to predict prognosis and response to compounds in ovarian cancer. *Front. Oncol.* 11, 807410. doi:10.3389/fonc.2021.807410

Yang, W., Liu, S., Li, Y., Wang, Y., Deng, Y., Sun, W., et al. (2020). Pyridoxine induces monocyte-macrophages death as specific treatment of acute myeloid leukemia. *Cancer Lett.* 492, 96–105. doi:10.1016/j.canlet.2020.08.018

Yoshihara, K., Shahmoradgoli, M., Martínez, E., Vegesna, R., Kim, H., Torres-Garcia, W., et al. (2013). Inferring tumour purity and stromal and immune cell admixture from expression data. *Nat. Commun.* 4, 2612. doi:10.1038/ncomms3612

Yuan, J., Shaham, S., Ledoux, S., Ellis, H. M., and Horvitz, H. R. (1993). The *C. elegans* cell death gene ced-3 encodes a protein similar to mammalian interleukin-1 beta-converting enzyme. *Cell* 75 (4), 641–652. doi:10.1016/0092-8674(93)90485-9

Zeng, T., Cui, L., Huang, W., Liu, Y., Si, C., Qian, T., et al. (2021). The establishment of a prognostic scoring model based on the new tumor immune microenvironment classification in acute myeloid leukemia. *BMC Med.* 19 (1), 176. doi:10.1186/s12916-021-02047-9

Zheng, Y., Li, Q., Wu, J., Luo, Z., Zhou, W., Li, A., et al. (2020). All-in-one mitochondria-targeted NIR-II fluorophores for cancer therapy and imaging. *Chem. Sci.* 12 (5), 1843–1850. doi:10.1039/d0sc04727a

frontiers | Frontiers in Pharmacology

TYPE Original Research
PUBLISHED 12 August 2022
DOI 10.3389/fphar.2022.964049

OPEN ACCESS

EDITED BY
Victor Mangas Sanjuan,
University of Valencia, Spain

REVIEWED BY
Matilde Merino Sanjuan,
University of Valencia, Spain
Alicia Rodríguez-Gascón,
University of the Basque Country, Spain

*CORRESPONDENCE
Jung-woo Chae,
jwchae@cnu.ac.kr
Hwi-yeol Yun,
hyyun@cnu.ac.kr

†These authors have contributed equally to this work and share first authorship

SPECIALTY SECTION
This article was submitted to Translational Pharmacology, a section of the journal Frontiers in Pharmacology

RECEIVED 08 June 2022
ACCEPTED 14 July 2022
PUBLISHED 12 August 2022

CITATION
Ryu H-j, Kang W-h, Kim T, Kim JK, Shin K-H, Chae J-w and Yun H-y (2022), A compatibility evaluation between the physiologically based pharmacokinetic (PBPK) model and the compartmental PK model using the lumping method with real cases.
Front. Pharmacol. 13:964049.
doi: 10.3389/fphar.2022.964049

A compatibility evaluation between the physiologically based pharmacokinetic (PBPK) model and the compartmental PK model using the lumping method with real cases

Hyo-jeong Ryu[1†], Won-ho Kang[1†], Taeheon Kim[1], Jae Kyoung Kim[2,3], Kwang-Hee Shin[4], Jung-woo Chae[1*] and Hwi-yeol Yun[1*]

[1]Department of Pharmacy, College of Pharmacy, Chungnam National University, Daejeon, South Korea, [2]Department of Mathematical Sciences, Korean Advanced Institute of Science and Technology, Daejeon, South Korea, [3]Biomedical Mathematics Group, Institute for Basic Science, Daejeon, South Korea, [4]Research Institute of Pharmaceutical Sciences, College of Pharmacy, Kyungpook National University, Daegu, South Korea

Pharmacokinetic (PK) modeling is a useful method for investigating drug absorption, distribution, metabolism, and excretion. The most commonly used mathematical models in PK modeling are the compartment model and physiologically based pharmacokinetic (PBPK) model. Although the theoretical characteristics of each model are well known, there have been few comparative studies of the compatibility of the models. Therefore, we evaluated the compatibility of PBPK and compartment models using the lumping method with 20 model compounds. The PBPK model was theoretically reduced to the lumped model using the principle of grouping tissues and organs that show similar kinetic behaviors. The area under the concentration–time curve (AUC) based on the simulated concentration and PK parameters (drug clearance [*CL*], central volume of distribution [*Vc*], peripheral volume of distribution [*Vp*]) in each model were compared, assuming administration to humans. The AUC and PK parameters in the PBPK model were similar to those in the lumped model within the 2-fold range for 17 of 20 model compounds (85%). In addition, the relationship of the calculated *Vd/fu* (volume of distribution [*Vd*], drug-unbound fraction [*fu*]) and the accuracy of AUC between the lumped model and compartment model confirmed their compatibility. Accordingly, the compatibility between PBPK and compartment models was confirmed by the lumping method. This method can be applied depending on the requirement of compatibility between the two models.

KEYWORDS

pharmacokinetic modeling, physiologically based pharmacokinetic (PBPK) model, lumping method, compartment model, compatibility

1 Introduction

Pharmacokinetic (PK) modeling is a research technique for quantifying and predicting the kinetics of drugs (Daryaee and Tongee, 2019). This technique has contributed to a reduction in failure rate and an increase in success rate in drug discovery and development (Gobburu and Marroum, 2001; Garralda et al., 2017). The main mathematical models used in PK modeling are the compartment model and physiologically based PK (PBPK) model (Lin et al., 2016). The compartment model explains the fate of a drug in the body through compartmentalization of the whole body on the premise of kinetic homogeneity. The number of compartments in the body is determined using the rate of drug distribution in a model body. In general, one- and two-compartment models are used. The compartment models are relatively simple, but they can efficiently predict the concentration of drugs in blood. However, the physicochemical properties of the drug (e.g., solubility, partition coefficient, protein binding) and the physiological properties of tissue and organs (e.g., volume, blood flow) cannot be reflected in the model (Khojasteh et al., 2011a; Jones and Rowland, 2013; Ahmed, 2015; Southwood et al., 2018). In contrast, the PBPK model associates the blood flow with each tissue and organ in the body by expressing the anatomical and physiological characteristics of the body as well as the physicochemical properties of drugs to predict the *in vivo* kinetics of the drug (Edginton et al., 2008; Jones et al., 2009). The PBPK model describes the drug distribution rate through each tissue and organ using models of perfusion rate limited tissue and permeability rate limited tissue. In the perfusion rate limited tissue model, the factors affecting the time for drugs to reach steady state are tissue volume (V_T), tissue blood flow (Q_T), and tissue to plasma partition coefficient (K_{PT}). The permeability rate constant of the drug is a major component to determine the time for drugs to reach steady state in the permeability rate limited tissue model (Espie et al., 2009; Khalil and Läer, 2011; Utembe et al., 2020). The PBPK model allows prediction of the drug blood concentration and tissue distribution for various conditions by reflecting the physicochemical properties of the drug, the physiological properties of tissues and organs, and the PK properties related to the drug (e.g., metabolism, tissue distribution) (Shin et al., 2015; U.S. Food and Drug Administration, 2020). However, the PBPK model is mathematically and structurally more complex than the compartment model, and therefore requires a large amount of varied data to secure sufficient predictive power (Gerlowski and Jain, 1983; Anderson, 1995; Charnick et al., 1995).

The lumped model, a version of the multi-compartment PBPK model with fewer compartments and reduced complexity, was developed to overcome these limitations of the PBPK model. Several methods have been suggested to reduce the complexity of the formulas and structures by simplifying the PBPK model. A lumped model can be created by grouping tissues and organs with similar dynamic patterns to reflect the physiological characteristics of the body (Bernareggi and Rowland, 1991). Alternatively, a mathematical transformation method can be used that groups tissues of the same eigenvalue by matrixing each tissue concentration to ultimately calculate the eigenvalue (Okino and Mavrovouniotis, 1998). It is possible to minimize the errors and bias in the model by simplifying the PBPK model with a mathematical transformation method (Coxson and Bischoff, 1987; Li and Rabitz, 1991). However, this is a simplified method based on the mathematical theory that does not reflect the physiological characteristics of the body and dynamic factors of the drug (Kuo and Wei, 1969; Watson et al., 1996).

Although a few previous studies attempted to enhance model compatibility, including that between the PBPK and lumped models, in terms of mathematical concepts (Coxson and Bischoff, 1987; Li and Rabitz, 1991; Okino and Mavrovouniotis, 1998), an approach to evaluate the theoretical background across PBPK, lumped, and compartment models is still lacking, and no study thus far has shown its application to a real case. Therefore, we focused on evaluating the compatibility of the PBPK and compartment models using the lumping method and demonstrated with 20 real cases. The 20 model drugs were selected based on various ranges of systemic clearance, volume of distribution, therapeutic classification, and the biopharmaceutical drug disposition classification system (BDDCS) (Supplementary Table S1). Additionally, we selected some drugs using the PBPK model code developed for simulation. Although it is important to assess the concentrations of diverse compounds in the tissues and blood, there have been few studies of the PK characteristics of a wide range of compounds using different models. The objective of this study was to simplify of the model and verify of compatibility between the models for various drugs (Figure 1).

2 Materials and methods

2.1 Drugs and software

We selected 20 previously approved drugs for this study. PBPK models for these 20 model compounds were established as described in the literature (Supplementary Tables S2, S3). The R package mrgsolve (version 0.9.2, Metrum Research Group, Tariffville, CT. United States) was used to simulate model compounds, and non-compartment analysis (NCA) was performed using Phoenix WinNonlin (version 8.1; Certara, Princeton, NJ, United States) to calculate the area under the concentration-time curve (AUC).

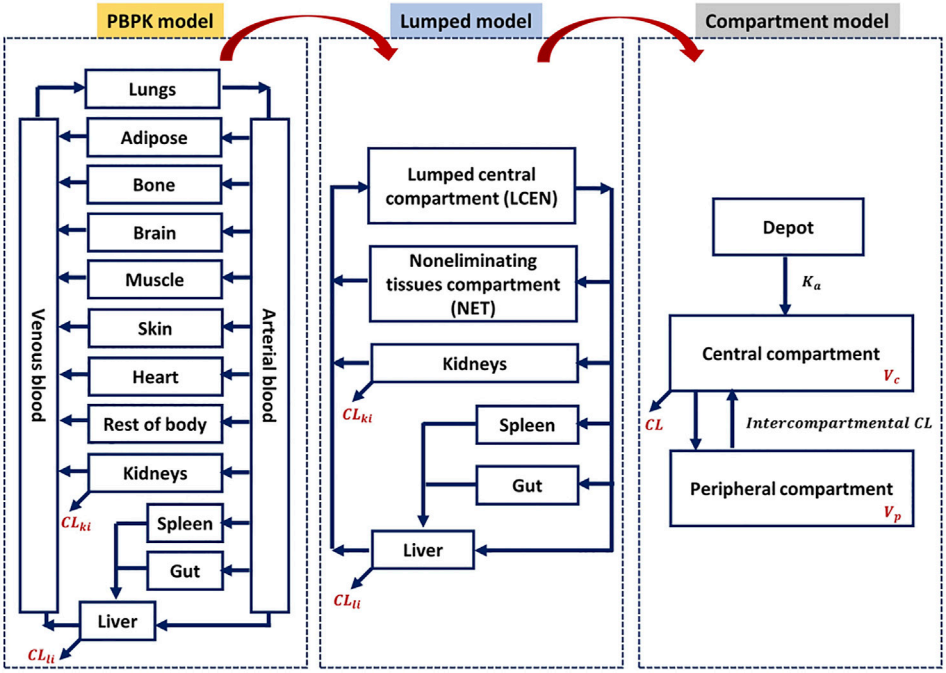

FIGURE 1
Schematic compatibility relationships among PBPK, lumped, and compartment models.

2.2 PBPK modeling approach

This study applied the PBPK models to the model compounds by dividing various tissues and organs into compartments (Figure 2). In general, perfusion rate limited tissue models have been used for the tissue distribution in PBPK models. Therefore, this type of model was used (Jones et al., 2006; Peters and Hultin, 2008; Chen et al., 2012; Sinha et al., 2012). The physiological data (tissue volume, tissue blood flow) and input parameters (hepatic clearance, renal clearance, absorption rate constant, drug-unbound fraction, blood to plasma ratio) used in the model compound PBPK models are summarized in Supplementary Tables S2, S3, respectively. Every model we used was confirmed its validity by the sensitivity analysis and a goodness-of-fit (GOF), reported on relevant literatures. References are listed in Supplementary Table S3.

The following differential equations Eqs 1–3 were used to describe the changes in drug concentrations in arterial blood, venous blood, and lung, respectively:

$$V_A \times \frac{dC_A}{dt} = Q_{lu} \times \left(\frac{C_{lu}}{\frac{K_{Plu}}{BP}} - C_A \right) \quad (1)$$

$$V_V \times \frac{dC_V}{dt} = \sum_T \left(Q_T \times \frac{C_T}{\frac{K_{PT}}{BP}} \right) - Q_{lu} \times C_V \quad (2)$$

$$V_{lu} \times \frac{dC_{lu}}{dt} = Q_{lu} \times \left(C_V - \frac{C_{lu}}{\frac{K_{Plu}}{BP}} \right) \quad (3)$$

where V_A is the arterial volume, C_A is the arterial drug concentration, Q_{lu} is the lung blood flow, C_{lu} is the lung drug concentration, K_{Plu} is the lung to plasma partition coefficient, BP is the blood to plasma ratio, V_V is the venous volume, C_V is the venous drug concentration, Q_T is the tissue blood flow, C_T is the tissue drug concentration, K_{PT} is the tissue to plasma partition coefficient, V_{lu} is the lung volume, and C_{lu} is the drug concentration in the lung. Note that in Eq. 2 for drug concentration in the venous blood, lung tissues that did not take up the drug through venous blood were excluded from calculating the uptake drug concentration (Elmokadem et al., 2019).

In tissues that do not eliminate drugs (e.g., adipose, bone, muscle), drug concentrations can be expressed by differential equations that show the differences between the uptake drug concentrations reflecting the tissue blood flow and output drug concentrations reflecting Q_T and K_{PT} as follows (Elmokadem et al., 2019):

$$V_T \times \frac{dC_T}{dt} = Q_T \times \left(C_A - \frac{C_T}{\frac{K_{PT}}{BP}} \right) \quad (4)$$

where V_T is the tissue volume, C_T is the tissue drug concentration, Q_T is the tissue blood flow, C_A is the arterial drug concentration,

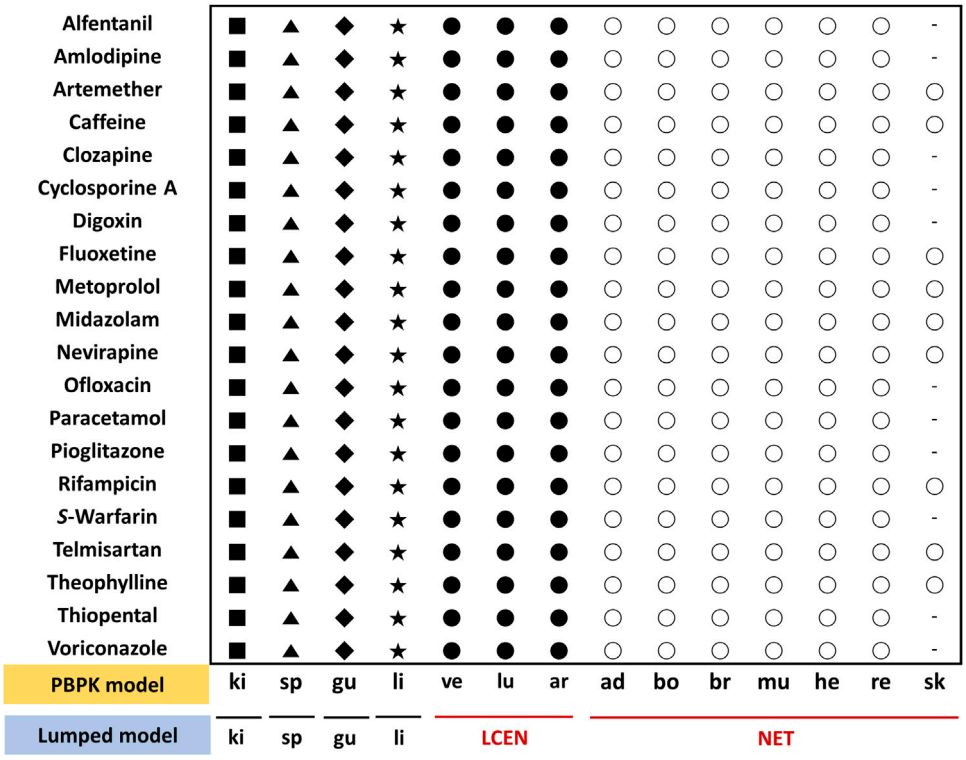

FIGURE 2
Assignment of tissues of the PBPK model to the lumped compartments of the lumped model for 20 model compounds. The lumped central compartment (LCEN) is represented by black circles and the non-eliminating tissues compartment (NET) is represented by white circles. The number of different symbols for a given compound corresponds to the number of compartments in the lumping model. Abbreviations ad, adipose; ar, arterial blood; bo, bone; br, brain; gu, gut; he, heart; ki, kidney; li, liver; lu, lung; mu, muscle; re, rest of body; sk, skin; sp, spleen; ve, venous blood.

K_{PT} is the tissue to plasma partition coefficient, and BP is the blood to plasma ratio.

The changes in drug concentrations in the tissues where drugs are eliminated, such as the liver and kidney, are described as follows (Yanni et al., 2010):

$$V_T \times \frac{dC_T}{dt} = Q_T \times \left(C_A - \frac{C_T}{\frac{K_{PT}}{BP}} \right) - fu \times CL_T \times \frac{C_T}{\frac{K_{PT}}{BP}} \quad (5)$$

where V_T is the tissue volume, C_T is the tissue drug concentration, Q_T is the tissue blood flow, C_A is the arterial drug concentration, K_{PT} is the tissue to plasma partition coefficient, BP is the blood to plasma ratio, fu is the drug-unbound fraction, and CL_T is the total tissue clearance. Hepatic clearance (CL_{hep}) and renal clearance (CL_{ki}) were obtained from the literature as described in Supplementary Table S3.

2.3 Lumped modeling approach

Lumped models were developed as described previously (Nestorov et al., 1998). All tissues and organs compartmentalized in the PBPK model were grouped into six compartments based on similar physiological characteristics (Figure 2). Arterial blood, venous blood, and lungs were lumped into the lumped central compartment (LCEN). The tissues that did not eliminate drugs, such as adipose, bone, brain, muscle, heart, rest of the body, and skin, were lumped into the non-eliminating tissues compartment (NET). However, the tissues that eliminated drugs, such as liver and kidney, as well as the spleen and intestinal tract that are connected to the liver, were not lumped.

As described in Eqs 1–4, the main factors determining drug concentrations in blood and tissues in the PBPK model are V_T, Q_T, and K_{PT}. These factors, therefore, were calculated using the following equations and applied in the lumped model. Volume (V_{Lump}) and blood flow (Q_{Lump}) in the lumped compartments were calculated as the sum of those of the lumped tissues. For the tissue-to-plasma partition coefficient (K_{Lump}) in the lumped compartments, the sum of the partition coefficients reflecting the volume of tissues to be lumped was divided by the volume of the lumped compartment (Supplementary Tables S4, S5) (Nestorov et al., 1998; Pilari and Huisinga, 2010):

$$V_{Lump} = \sum_T V_T \quad (6)$$

$$Q_{Lump} = \sum_T Q_T \quad (7)$$

$$K_{Lump} = \frac{1}{V_{Lump}} \sum_T \left(V_T \times Kp_T\right) \quad (8)$$

where V_{Lump} is the volume in the lumped compartment, V_T is the tissue volume, Q_{Lump} is the blood flow in the lumped compartment, Q_T is the tissue blood flow, K_{Lump} is the tissue to plasma partition coefficient in the lumped compartment, and K_{PT} is the tissue to plasma partition coefficient.

The drug concentrations in LCEN and NET were calculated using Eqs 9, 10, respectively, as follows (Elmokadem et al., 2019):

$$V_{LCEN} \times \frac{dC_{LCEN}}{dt} = \sum_T \left(Q_T \times \frac{C_T}{\frac{K_{PT}}{BP}}\right) - Q_{LCEN} \times C_{LCEN} \quad (9)$$

$$V_{NET} \times \frac{dC_{NET}}{dt} = Q_{NET} \times \left(C_{LCEN} - \frac{C_{NET}}{\frac{K_{PNET}}{BP}}\right) \quad (10)$$

where V_{LCEN} is the volume in the LCEN, C_{LCEN} is the drug concentration in the LCEN, Q_T is the tissue blood flow, C_T is the tissue drug concentration, K_{PT} is the tissue to plasma partition coefficient, BP is the blood to plasma ratio, Q_{LCEN} is the blood flow in the LCEN, V_{NET} is the volume in the NET, C_{NET} is the drug concentration in the NET, Q_{NET} is the blood flow in the NET, and K_{PNET} is the tissue to plasma partition coefficient in the NET. Note that in Eq. 9 for calculation of the drug concentration in the LCEN, the systematic circulation tissues that did not receive blood supply from the venous blood were excluded from the sum for normalization using the V_T, Q_T, and K_{PT} of each tissue.

2.4 Compartment model approach

The one- or two-compartment model was used for model compounds, whereas drug clearance (CL), central volume of distribution (Vc), peripheral volume of distribution (Vp), inter-compartmental clearance (Q), and absorption rate constant (Ka) values were obtained from the literature, as described in Supplementary Table S6. We performed model validation, according to the relevant literature, by checking the GOF plot and conducting a visual predictive check (VPC). References are listed in Supplementary Table S6.

2.5 Theoretical considerations of compatibility among PBPK, lumped, and compartment models

Considering the origin of each PK model, PK models, what it mentioned above, could be expected by compatibility based on meaning of mathematical and biological assumptions.

For instance, the total clearance in the PK model could be represented by Eq. 11 (Cao and Jusko, 2012).

$$CL_T = CL_{hep} + CL_{ki} + CL_{others} \quad (11)$$

where CL_T is the total tissue clearance, CL_{hep} is the hepatic clearance, CL_{ki} is the renal clearance, CL_{others} is the sum of tissue clearances except liver and kidney.

Despite the difference of the way to CL_T among PBPK, lumped, and compartment model, CL_T should be approximated by theoretically true clearance regardless of way of estimation. In general, CL_T could be estimated based on blood concentrations, so we could suppose that CL_T, that is calculated by sum of CL_{hep}, CL_{ki} and CL_{others} obtained by PBPK or lumped model, should be similar with estimation of CL_T value from compartment model.

In addition, above mentioned approaches could be acceptable in case of drug distribution related with volume of distribution to tissue. The rate of drug distribution to liver may be defined in the PBPK and lumped models as Eq. 12 (Cao and Jusko, 2012).

$$V_{li} \times \frac{dC_{li}}{dt} = Q_{li} \times \left(C_A - \frac{C_{li}}{\frac{K_{Pli}}{BP}}\right) - fu \times CL_{hep} \times \frac{C_{li}}{\frac{K_{Pli}}{BP}} \quad (12)$$

where V_{li} is the liver volume, C_{li} is the liver drug concentration, Q_{li} is the liver blood flow, C_A is the arterial drug concentration, K_{Pli} is the liver to plasma partition coefficient, BP is the blood to plasma ratio, fu is the drug-unbound fraction, and CL_{hep} is the hepatic clearance.

Since the lumped model was focused on merging the compartment where it has similar biological characteristics in comparison with PBPK, the compatibility between them could be easily explained.

Moreover, the theoretical compatibility among PBPK, lumped, and compartment model could be explained by additional assumption. For example, the well-stirred assumption of the hepatic compartment may be also applicable. The PBPK and lumped models with hepatic compartment can be related to clearance concepts of compartment model, assuming the well-stirred model as follows (Cao and Jusko, 2012):

$$CL_{hep} = Q_{li} \times \frac{fu \times CL_{int}}{fu \times CL_{int} + Q_{li}} \quad (13)$$

where CL_{hep} is the hepatic clearance, Q_{li} is the liver blood flow, fu is the drug-unbound fraction, and CL_{int} is the intrinsic clearance.

Therefore, CL_T and apparent Vd of drugs, having mainly distributed into liver and eliminated by liver, could be approximately calculated with fu and CL_{hep}.

2.6 Evaluation of compatibility among PBPK, lumped, and compartment models

Simulations were performed 1,000 times to compare the compatibility of the models. The therapeutic dose of each drug

was administered orally in a single dose to adults having similar weight, who were then followed up at various simulation intervals (e.g., 0–48 h or 0–312 h) depending on the drugs and their dosing amounts to determine the drug concentrations under the same experimental conditions in the three models. To compare the drug concentrations in the blood and tissues between each model, the AUC using NCA was utilized as the PK parameter for exposure (Scheff et al., 2011). However, the maximum blood concentration (C_{max}), which is related to absorption, was excluded because this study was performed to examine whether drug distribution, metabolism, and excretion could be lumped. Moreover, it is well known that the variation of C_{max} is 50%–60% higher than that of the AUC (Endrenyi and Yan, 1993). Therefore, key parameters of PK, such as drug *CL*, *Vc*, and *Vp*, were compared (Benet, 1984). To compare the AUC and PK parameters, we used the 2-fold range criteria typically used as the acceptance criteria for the PBPK model (Sager et al., 2015). Additionally, we have performed statistical analysis to compare the AUC and clearance among PBPK, lumped, and compartment model. Those results are described in Tables 1–3. Comparison of AUC and PK parameters was performed according to the following steps:

Step 1. Each model was built based on the parameters described in the literature (e.g., *CL*, *Vc*, *Vp*).

Step 2. Comparison of AUC obtained from drug concentrations in tissues and blood simulated using each model.

Step 3. Comparison of *CL* and *Vc* between models.

Step 4. Comparison of *Vp* between models (*Vp* in PBPK and lumped models were calculated using Eqs 14, 15, respectively).

$$V_{p\ in\ PBPK\ model} = \frac{\overline{V_T \times Kp_T}}{Body\ weight} \tag{14}$$

$$V_{p\ in\ lumped\ model} = \frac{\overline{V_T} \times \overline{Kp_T}}{Body\ weight} \tag{15}$$

where V_p is the peripheral volume of distribution, V_T is the tissue volume, and K_{PT} is the tissue to plasma partition coefficient.

To further approach the compatibility among the three models, we estimated the empirical relationship of the calculated *Vd/fu* and the accuracy of the AUC between the lumped and compartment models.

Step 5. Estimation of empirical relations between lumped and compartment models for the ratio between the volume of distribution (*Vd*, where *Vd* is typically assumed to be the sum of *Vc* and *Vp*) and the drug-unbound fraction (*fu*). Note that the descriptors *Vc*, *Vp*, and *fu* are shown in Supplementary Tables S3, S7, S8, respectively.

Step 6. Estimation of the accuracy of the AUC as follows:

$$Theoritical\ AUC_{last\ at\ central\ compartment} = AUC_{last\ at\ LCEN} \times \frac{CL_{in\ lumped\ model}}{CL_{in\ compartment\ model}} \tag{16}$$

$$The\ accuracy\ of\ AUC = \frac{AUC_{last\ at\ central\ compartment}}{Theoritical\ AUC_{last\ at\ central\ compartment}} \tag{17}$$

3 Results

3.1 Comparison of AUCs

To confirm the model development steps, the performances of all models were confirmed by comparison between simulated and reported PK profiles. The distribution rate in PBPK model is assumed to be governed by rapid equilibrium. Based on this assumption, the average value of each tissue AUC in the PBPK model was compared with each compartment in lumped and the compartment model.

The AUCs in the central compartment of each model are shown in Table 1. Those for arterial blood, venous blood, and lungs in the PBPK model were similar to those in the LCEN of the lumped model within a range of 2-fold for 18 of the 20 model compounds (90%). For clozapine and amlodipine, however, the values for differed considerably between the PBPK model and the LCEN of the lumped model. The AUCs of clozapine and amlodipine of the PBPK model were 130.033 mg h/L and 7.598 mg h/L, respectively. These results differed from the estimates of 12.823 mg h/L and 0.505 mg h/L, respectively, in the lumped model. Furthermore, the AUCs in LCEN of the lumped model were similar to those of the compartment model within the range of 2-fold for 14 of the 20 model compounds (70%); the exceptions were midazolam, telmisartan, paracetamol, artemether, fluoxetine, and theophylline.

The AUCs in the peripheral compartment are shown in Table 2. In adipose, bone, brain, muscle, heart, rest of the body, and skin, where the drugs were not eliminated, the AUCs after lumping were included in the AUCs before lumping for 19 of the 20 model compounds (95%). In the case of metoprolol, however, the AUC of the NET deviated from the 2-fold range between the PBPK and lumped models with values of 5.476 mg h/L and 2.644 mg h/L, respectively. Furthermore, the AUCs in the NET of the lumped model differed from those of the compartment model for most two-compartment model compounds (6 of 9, 66.7%).

3.2 Comparison of PK parameters

Next, we compared the *CL*, *Vc*, and *Vp*.

TABLE 1 Comparison of AUC parameters of central compartment in PBPK, lumped, and compartment models for 20 compounds.

Model	PBPK model	Lumped model	Compartment model
Tissue, compartment	Lungs, arterial blood, venous blood	Lumped central compartment (LCEN)	Central compartment
Parameter (unit) / Compound	Average of tissue AUC_{last} (mg•h/L) (2-fold range)	AUC_{last} at LCEN (mg•h/L) (2-fold range)	AUC_{last} at central compartment (mg•h/L) (2-fold range)
Alfentanil	0.348 (0.174-0.697)	0.351 (0.175-0.702)	0.585 (0.293-1.171)
Amlodipine	7.598 (3.799-15.195)	0.505 (0.253-1.011)*	0.496 (0.248-0.993)#
Artemether	2.608 (1.304-5.216)	2.877 (1.438-5.754)	0.173 (0.087-0.346)+,#
Caffeine	1.349 (0.674-2.698)	1.482 (0.741-2.963)	0.953 (0.477-1.906)
Clozapine	130.033 (65.017-260.066)	12.823 (6.411-25.645)*	14.172 (7.086-28.344)#
Cyclosporine A	21.776 (10.888-43.552)	12.285 (6.143-24.571)	18.363 (9.181-36.726)
Digoxin	0.056 (0.028-0.111)	0.060 (0.030-0.120)	0.030 (0.015-0.060)
Fluoxetine	2.736 (1.368-5.471)	1.926 (0.963-3.851)	4.511 (2.256-9.022)
Metoprolol	0.987 (0.494-1.974)	1.074 (0.537-2.147)	0.630 (0.315-1.260)
Midazolam	1.005 (0.503-2.010)	0.977 (0.489-1.954)	0.098 (0.049-0.196)
Nevirapine	146.303 (73.151-292.605)	164.225 (82.113-328.450)	203.575 (101.787-407.150)
Ofloxacin	50.220 (25.110-100.440)	53.246 (26.623-106.492)	55.173 (27.586-110.345)
Paracetamol	28.650 (14.325-57.300)	33.827 (16.914-67.655)	67.964 (33.982-135.929)
Pioglitazone	2.368 (1.184-4.735)	3.201 (1.600-6.402)	5.529 (2.765-11.058)
Rifampicin	153.468 (76.734-306.937)	79.553 (39.777-159.106)	65.084 (32.542-130.168)
S-Warfarin	28.075 (14.037-56.150)	35.292 (17.646-70.584)	30.006 (15.003-60.012)
Telmisartan	760.097 (380.049-1,520.195)	986.822 (493.411-1973.643)	0.707 (0.353-1.414)+,#
Theophylline	468.329 (234.164-936.658)	554.051 (277.026-1,108.102)	65.239 (32.620-130.479)
Thiopental	1,688.083 (844.042-3,376.166)	1819.869 (909.935-3,639.738)	3,015.313 (1,507.657-6,030.626)
Voriconazole	43.587 (21.794-87.174)	46.360 (23.180-92.720)	63.400 (31.700-126.800)

AUC, area under the concentration-time curve. *,+,# marks are attached after compound name if the AUC, parameters among PBPK, model, lumped model, and compartment model are significantly different ($p < 0.05$) (post-hoc analysis: *PBPK, model and lumped model, #PBPK, model and compartment model, +lumped model and compartment model).

CL is the sum of clearance in the liver and kidneys, which was not significantly different within the 2-fold range between the three models for 19 of the 20 model (95%), the exception being alfentanil for which *CL* deviated from the 2-fold range between the three models with values of 0.555 L/h/kg and 0.209 L/h/kg in the PBPK/lumped models and the compartment model, respectively (Table 3).

Vc where the drug is rapidly and homogeneously distributed was equal to the total tissue volume and was similar between the PBPK and lumped models. However, *Vc* of the lumped model differed from that in the central compartment of the compartment model for most two-compartment model compounds (12 of 20, 60.0%) (Supplementary Table S7).

Vp where the drugs are distributed in a slow and heterogeneous manner was similar within the 2-fold range between the PBPK and lumped models for 19 of 20 model compounds (95%), the exception being metoprolol for which *Vp* deviated from the 2-fold range between the PBPK and lumped models with values of 0.278 L/kg and 0.593 L/kg, respectively (Supplementary Table S8). In addition, the volume of distribution in the peripheral compartment of the lumped model differed from that in the peripheral compartment of the compartment model for most two-compartment model compounds (8 of 9, 88.9%).

The empirical relations of the calculated *Vd/fu* between the lumped and compartment models are shown in Figure 3 (Khojasteh et al., 2011b). The concept of this post hoc analysis which compares with the *Vd/Fu* value between two models was based on the fact that the apparent ideal volume of distribution was close to that of the unbound drug fraction. Furthermore, the protein binding effect on the volume of distribution could be more significant in the peripheral compartment than in the central compartment (Holford and Yim, 2016). Therefore, we had to pay attention that the volume of the peripheral can be distributed to the tissue in inverse proportion to the value of the unbound drug fraction. Using this analysis, the calculated *Vd/fu* in the lumped model was correlated with the calculated *Vd/fu* in the compartment model.

The accuracy of the AUC between the lumped and compartment models was assessed using Eqs 16, 17. The

TABLE 2 Comparison of AUC parameters of peripheral compartment in PBPK, lumped, and compartment models for 20 compounds.

Model	PBPK model	Lumped model	Compartment model
Tissue, compartment	Adipose, bone, brain, muscle, skin, heart, rest of body	Non-eliminating tissues compartment (NET)	Peripheral compartment
Parameter (unit) / Compound	Average of tissue AUC_{last} (mg•h/L) (2-fold range)	AUC_{last} at NET (mg•h/L) (2-fold range)	AUC_{last} at peripheral compartment (mg•h/L) (2-fold range)
Alfentanil	1.772 (0.886-3.544)	0.994 (0.497-1.987)	-
Amlodipine	9.979 (4.989-19.957)	11.920 (5.960-23.840)	-
Artemether	27.217 (13.609-54.435)	19.090 (9.545-38.180)	-
Caffeine	0.901 (0.450-1.801)	0.638 (0.319-1.276)	-
Clozapine	142.308 (71.154-284.617)	134.485 (67.242-268.969)	-
Cyclosporine A	17.777 (8.888-35.553)	12.601 (6.300-25.202)	-
Digoxin	0.077 (0.039-0.154)	0.057 (0.028-0.113)	0.030 (0.015-0.059)
Fluoxetine	20.178 (10.089-40.356)	13.400 (6.700-26.799)	-
Metoprolol	5.476 (2.738-10.952)	2.644 (1.322-5.288)	-
Midazolam	8.860 (4.430-17.720)	5.189 (2.594-10.377)	0.100 (0.050-0.201)$^{+,\#}$
Nevirapine	315.957 (157.979-631.914)	208.837 (104.418-417,674)	202.734 (101.367-405.467)
Ofloxacin	34.537 (17.269-69.074)	29.840 (14.920-59.680)	55.224 (27.612-110.449)
Paracetamol	18.966 (9.483-37.931)	19.120 (9.560-38.240)	68.139 (34.070-136.278)$^{+,\#}$
Pioglitazone	0.348 (0.174-0.696)	0.312 (0.156-0.624)	3.002 (1.501-6.005)$^{+,\#}$
Rifampicin	139.803 (69.901-279.605)	163.653 (81.827-327.307)	-
S-Warfarin	6.697 (3.348-13.394)	5.905 (2.953-11.810)	-
Telmisartan	164.733 (82.367-329.466)	123.565 (61.783-247.130)	0.694 (0.347-1.388)$^{+,\#}$
Theophylline	291.616 (145.808-583.232)	279.114 (139.557-558.228)	-
Thiopental	11,940.270 (5,970.135-23880.540)	7,818.454 (3,909.227-15636.908)	2,773.715 (1,386.858-5,547.430)
Voriconazole	260.225 (130.113-520.450)	273.008 (136.504-546.016)	63.054 (31.527-126.108)

AUC, area under the concentration-time curve. $^{*,+,\#}$ marks are attached after compound name if the AUC, parameters among PBPK, model, lumped model, and compartment model are significantly different ($p < 0.05$) (post-hoc analysis: *PBPK, model and lumped model, $^{\#}$PBPK, model and compartment model, $^{+}$lumped model and compartment model).

approach was based on the fact that the *CL* ratio between two models is used for model-to-model conversion. The compartmental AUC was theoretically calculated using Eq. 16, and the accuracy of the AUC was estimated using Eq. 17. The compatibility between the two models was confirmed when the accuracy of the AUC was approximately one. The accuracy of AUC was found to be within the 2-fold range for 15 of 20 model drugs (75%) (Figure 4).

4 Discussion

Despite the availability of user-friendly software to resolve the technical issues, the barriers to entry for building and understanding full PBPK models have consistently posed difficulties for beginners in pharmacometrics. Therefore, a number of methods have been suggested to simplify full PBPK models, such as simplified PBPK and lumped PBPK modeling approaches. However, there is no precedent for implying or connecting these various PBPK models to traditional compartment models that have been used for many years. Here, we attempted to confirm the relations among the PBPK, lumped, and compartment models. Therefore, in this study, we demonstrated that it is possible to lump tissues and organs with similar physiological characteristics into the PBPK model for 20 model compounds and that the lumped and compartment models are compatible with the PBPK model.

For comparison of compatibility between the models, the AUC was compared between models as the PK parameter for exposure. The AUC in central and peripheral compartments of the PBPK model was similar to that of the lumped model within the 2-fold range for 17 of 20 model compounds (85%), with the exceptions being metoprolol, clozapine, and amlodipine. This indicated that the two models were compatible with regard to drug concentration. As shown in Tables 1, 2, however, the AUCs of metoprolol, clozapine, and amlodipine deviated from the 2-fold range between the PBPK and lumped models. Such AUC

TABLE 3 Comparison of *CL* parameters in PBPK, lumped, and compartment models for 20 compounds.

Parameter (unit)	*CL* (L/h/kg)		
Model / Compound	PBPK model (2-fold range)	Lumped model (2-fold range)	Compartment model (2-fold range)
Alfentanil	0.555 (0.278-1.111)	0.555 (0.278-1.111)	0.209 (0.104-0.417)
Amlodipine	0.408 (0.204-0.816)	0.408 (0.204-0.816)	0.255 (0.127-0.509)
Artemether	13.333 (6.667-26.667)	13.333 (6.667-26.667)	16.436 (8.218-32.873)
Caffeine	0.134 (0.067-0.268)	0.134 (0.067-0.268)	0.094 (0.047-0.189)
Clozapine	0.401 (0.201-0.803)	0.401 (0.201-0.803)	0.313 (0.156-0.626)
Cyclosporine A	0.420 (0.210-0.841)	0.420 (0.210-0.841)	0.459 (0.229-0.918)
Digoxin	0.136 (0.068-0.273)	0.136 (0.068-0.273)	0.222 (0.111-0.444)
Fluoxetine	0.351 (0.175-0.702)	0.351 (0.175-0.702)	0.208 (0.104-0.416)
Metoprolol	3.250 (1.625-6.500)	3.250 (1.625-6.500)	2.821 (1.411-5.643)
Midazolam	0.540 (0.270-1.080)	0.540 (0.270-1.080)	0.896 (0.448-1.791)
Nevirapine	0.022 (0.011-0.044)	0.022 (0.011-0.044)	0.015 (0.008-0.031)
Ofloxacin	0.160 (0.080-0.320)	0.160 (0.080-0.320)	0.132 (0.066-0.265)
Paracetamol	0.270 (0.135-0.540)	0.270 (0.135-0.540)	0.215 (0.108-0.430)
Pioglitazone	0.068 (0.034-0.137)	0.068 (0.034-0.137)	0.035 (0.018-0.071)
Rifampicin	0.142 (0.071-0.283)	0.142 (0.071-0.283)	0.163 (0.081-0.326)
S-Warfarin	0.003 (0.001-0.006)	0.003 (0.001-0.006)	0.002 (0.001-0.004)
Telmisartan	0.800 (0.400-1.600)	0.800 (0.400-1.600)	0.980 (0.490-1.960)
Theophylline	0.045 (0.023-0.091)	0.045 (0.023-0.091)	0.054 (0.027-0.108)
Thiopental	0.189 (0.095-0.378)	0.189 (0.095-0.378)	0.114 (0.057-0.229)
Voriconazole	0.106 (0.053-0.212)	0.106 (0.053-0.212)	0.088 (0.044-0.176)

CL, clearance. $^{*,+,\#}$ marks are attached after compound name if the AUC, parameters among PBPK, model, lumped model, and compartment model are significantly different ($p < 0.05$) (post-hoc analysis: *PBPK, model and lumped model, $^{\#}$PBPK, model and compartment model, $^{+}$lumped model and compartment model).

differences for metoprolol and clozapine have been reported previously due to their high PK variability (Ågesen et al., 2019; Lee et al., 2021). The AUC of central and peripheral compartment differed between lumped and compartment models for 9 of 20 model compounds (45%). This difference may have been attributable to the differences in how these methods reflect the volume of distribution. In the lumped model, the volume of each tissue is an important factor for predicting the drug concentration in tissues and blood. Overall, this volume was accurately reproduced by the model. In contrast, the volume of distribution is calculated based on the blood concentration in the compartment model. In particular, the distribution volume of the peripheral compartment may exhibit greater differences in the AUC due to the difficulties in reflecting the blood concentration. Moreover, the errors due to the lack of inclusion of the tissue to plasma distribution coefficients may also be responsible for these differences. Note that for telmisartan, the difference in the AUC may have been attributable to the non-linear PK characteristics and high individual differences in response to the drug (Stangier et al., 2000; U.S. Food and Drug Administration, 2009). In addition, the difference of C_{max} among the models were compared as well, however, the C_{max} were observed by the difference over 4-fold among the models in comparison with AUC because of reasons (e.g, large variation) as we stated in Section 2.6 (Supplementary Tables S9, S10).

To confirm the compatibility of the models, *CL*, *Vc*, and *Vp*, as the key parameters of PK, were compared between models. *CL* was similar within the 2-fold range between the three models for 19 of 20 model compounds (95%), with the exception being alfentanil. Thus, the three models were compatible for comparison of *CL*. However, the *CL* of alfentanil deviated from the 2-fold range between the three models (0.555 L/h/kg for PBPK model and lumped models and 0.209 L/h/kg for the compartment model). This difference may have been attributable to the high inter-individual differences in clearance of alfentanil; alfentanil is eliminated mainly by hepatic metabolism, and the clearance varied by more than 4-fold, resulting in large inter-individual differences probably due to variation in the hepatic metabolic

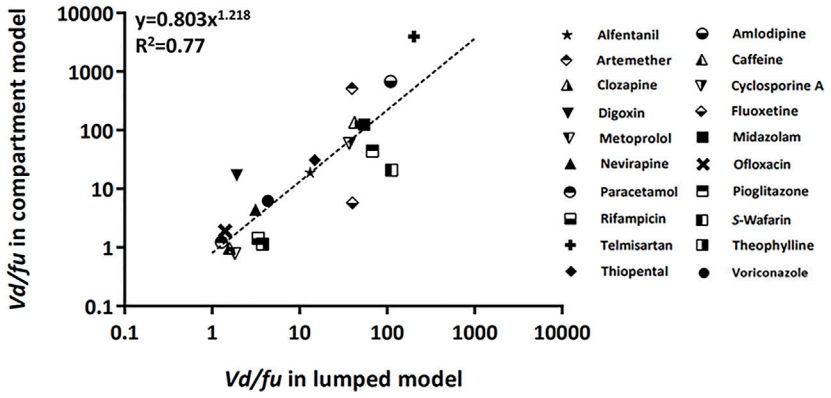

FIGURE 3
Relationship of the calculated *Vd*/*fu* between lumped and compartment models. The dashed line was fitted to the indicated relationship ($y = ax^b$). Abbreviations *fu*, drug-unbound fraction; *Vd*, volume of distribution.

capacity. Furthermore, inter-individual differences in protein binding may also influence clearance (Henthorn et al., 1985; Persson et al., 1988). The volumes of distribution in the central and peripheral compartments were similar between PBPK and lumped models for 19 of 20 model compounds (95%), with the exception being metoprolol for which the volume of distribution in the peripheral compartment deviated from the 2-fold range between the two models (0.278 L/kg for the PBPK model and 0.593 L/kg for the lumped model). As mentioned above, this difference may have been attributable to the high variability of metoprolol PKs (Ågesen et al., 2019). The volumes of distribution in the central and peripheral compartment were different between lumped and compartment models. In interpreting this finding, it is necessary to consider that the deviation in the volume of distribution may be greater than clearance. Furthermore, the compatibility of volume of distribution was not confirmed due to the differences in the tissue to plasma partition coefficients and methods of reflecting blood flow velocity of each tissue organ.

To further assess the compatibility among the three models, we used the empirical relationship of the calculated *Vd*/*fu* and the accuracy of AUC between lumped and compartment models. According to these approaches, the compatibility of PBPK, lumped, and compartment models for 20 model compounds was examined. Although telmisartan is outside the criteria range due to its non-linear PK characteristics and individual differences, the overall results indicated that the three models were compatible in terms of PK parameters (Stangier et al., 2000; U.S. Food and Drug Administration, 2009). Furthermore, the drug concentration of each tissue in the PBPK model could be indirectly estimated by using the drug concentration of the lumped and compartment models when the three models were compatible for drug concentration (e.g., voriconazole). In the PBPK model, the drug movement was determined by V_T, Q_T, and K_{PT}. These parameters were calculated using the lumping equation and further applied to the lumped and compartment models. The drug concentration in each tissue of the PBPK model can be calculated using Eq. 18 (Pilari and Huisinga, 2010).

$$C_T = C_p \times \frac{V_{p\ in\ compartment\ model}}{V_{p\ in\ lumped\ model}} \times \frac{Kp_T}{K_{Lump}} \tag{18}$$

The drug concentration of each tissue in the PBPK model could be predicted by applying Eq. 18. Overall, there were no differences in the AUC of the PBPK model and AUC calculated using Eq. 18 (Supplementary Table S11).

The following limitations must be taken into consideration in interpretation of the findings of this study. Only lumping of the perfusion rate limited tissue model was assessed in the PBPK model based on a single dose of model compounds and a single administration route. In future studies, other administration routes and doses of model compounds, as well as other drugs for permeability rate-limited tissue models, would elucidate new pathways for the lumped model and would help to establish better compatibility between the three models. Moreover, simplification of the model and verification of compatibility between the models for other drugs would facilitate the prediction of drug profiles in tissues using a relatively simple model.

In summary, we evaluated the compatibility between PBPK and compartmental PK models using the lumping method. This study suggested that this lumping method may be useful to provide a simplified PBPK model. Construction of a lumped model may also be possible that can be assessed relative to the compartment model.

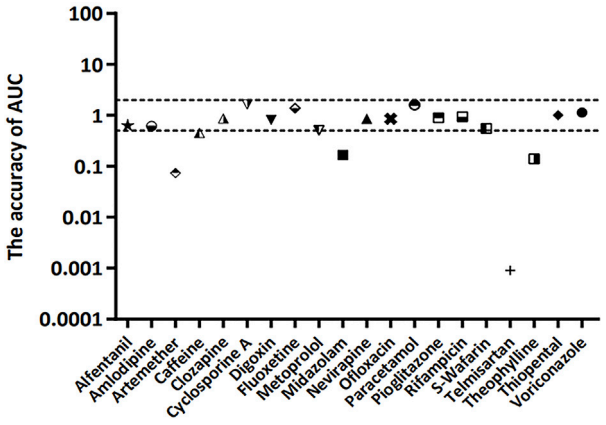

FIGURE 4
Accuracy of AUC for 20 model compounds. The accuracy of AUC was calculated using Eqs 16, 17. The dashed line represents 2-fold deviation.

5 Conclusion

This study evaluated the compatibility between the PBPK and compartment models using the lumping method with 20 model compounds, and further approaches were attempted to determine a theoretical method to establish compatibility between the models. The lumping method is considered to assess the models' compatibility, suggesting the reliability of the PK parameters of the PBPK and compartment models. The lumping method may be further utilized to develop and extend the PBPK and compartment models. Additionally, the lumping method approach with the PBPK model uses a relatively small amount of data and facilitates access to the compartment model. Hence, this approach could help for pharmacometricians gain a deeper understanding of the associations and alignments between the models.

Data availability statement

The original contributions presented in the study are included in the article/Supplementary Material, further inquiries can be directed to the corresponding authors.

Author contributions

H-JR and W-HK contributed equally to this study as the first authors. W-HK, H-JR, J-WC, and H-YY conceptualized the research. H-JR, W-HK, TK, J-WC, and H-YY performed the research. H-JR, W-HK, TK, JK, K-HS, J-WC, and H-YY analyzed the data. H-JR, W-HK, J-WC, and H-YY wrote the original draft of the manuscript. All authors contributed to, reviewed, and approved the manuscript.

Funding

This research was funded by Chungnam National University (CNU), the Institute of Information and Communications Technology Planning and Evaluation (IITP) grant funded by the Korean government (MSIT) (No. 2020-0-01441, Artificial Intelligence Convergence Research Center (Chungnam National University), No. RS-2022-00155857, Artificial Intelligence Convergence Innovation Human Resources Development (Chungnam National University)) and the National Research Foundation of Korea (NRF) grant funded by the Korea government (MSIT) (No. NRF-2022R1A2C1010929). Every author declares that industry and institute, where authors has been employed and funded, was not involved for the study design, collection, analysis, interpretation of data, the writing of this article or the decision to submit it for publication.

Conflict of interest

The authors declare that the research was conducted in the absence of any commercial or financial relationships that could be construed as a potential conflict of interest.

Publisher's note

All claims expressed in this article are solely those of the authors and do not necessarily represent those of their affiliated organizations, or those of the publisher, the editors and the reviewers. Any product that may be evaluated in this article, or claim that may be made by its manufacturer, is not guaranteed or endorsed by the publisher.

Supplementary material

The Supplementary Material for this article can be found online at: https://www.frontiersin.org/articles/10.3389/fphar.2022.964049/full#supplementary-material

References

Ågesen, F. N., Weeke, P. E., Tfelt-Hansen, P., and Tfelt-Hansen, J. (2019). Pharmacokinetic variability of beta-adrenergic blocking agents used in cardiology. *Pharmacol. Res. Perspect.* 7, e00496. doi:10.1002/prp2.496

Ahmed, T. A. (2015). "Pharmacokinetics of drugs following IV bolus, IV infusion, and oral administration," in *Basic pharmacokinetic concepts and some clinical applications*. Editor T. A. Ahmed (London: IntechOpen), 53–55.

Anderson, M. E. (1995). Physiologically based pharmacokinetic (PB-PK) models in the study of the disposition and biological effects of xenobiotics and drugs. *Toxicol. Lett.* 82/83, 341–348. doi:10.1016/0378-4274(95)03487-0

Benet, L. Z. (1984). Pharmacokinetic parameters: Which are necessary to define a drug substance? *Eur. J. Respir. Dis. Suppl.* 134, 45–61.

Bernareggi, A., and Rowland, M. L. (1991). Physiologic modeling of cyclosporin kinetics in rat and man. *J. Pharmacokinet. Biopharm.* 19, 21–50. doi:10.1007/BF01062191

Cao, Y., and Jusko, W. J. (2012). Applications of minimal physiologically-based pharmacokinetic models. *J. Pharmacokinet. Pharmacodyn.* 39, 711–723. doi:10.1007/s10928-012-9280-2

Charnick, S. B., Kawai, R., Nedelman, J. R., Lemaire, M., Niederberger, W., Sato, H., et al. (1995). Perspectives in pharmacokinetics. Physiologically based pharmacokinetic modeling as a tool for drug development. *J. Pharmacokinet. Biopharm.* 23, 217–229. doi:10.1007/BF02354273

Chen, Y., Jin, J. Y., Mukadam, S., Malhi, V., and Kenny, J. Y. (2012). Application of IVIVE and PBPK modeling in prospective prediction of clinical pharmacokinetics: Strategy and approach during the drug discovery phase with four case studies. *Biopharm. Drug Dispos.* 33, 85–98. doi:10.1002/bdd.1769

Coxson, P. G., and Bischoff, K. B. (1987). Lumping strategy. 1. Introductory techniques and applications of cluster analysis. *Ind. Eng. Chem. Res.* 26, 1239–1248. doi:10.1021/ie00066a031

Daryaee, F., and Tonge, P. J. (2019). Pharmacokinetic-pharmacodynamic models that incorporate drug-target binding kinetics. *Curr. Opin. Chem. Biol.* 50, 120–127. doi:10.1016/j.cbpa.2019.03.008

Edginton, A. N., Theil, F.-P., Schmitt, W., and Willmann, S. (2008). Whole body physiologically-based pharmacokinetic models: Their use in clinical drug development. *Expert Opin. Drug Metab. Toxicol.* 4, 1143–1152. doi:10.1517/17425255.4.9.1143

Elmokadem, A., Riggs, M. M., and Baron, K. T. (2019). Quantitative systems pharmacology and physiologically-based pharmacokinetic modeling with mrgsolve: A hands-on tutorial. *CPT. Pharmacometrics Syst. Pharmacol.* 8, 883–893. doi:10.1002/psp4.12467

Endrenyi, I., and Yan, W. (1993). Variation of Cmax and Cmax/AUC in investigations of bioequivalence. *Int. J. Clin. Pharmacol. Ther. Toxicol.* 31, 184–189.

Espie, P., Tytgat, D., Sargentini-Maier, M.-L., Poggesi, I., and Watelet, J.-B. (2009). Physiologically based pharmacokinetics (PBPK). *Drug Metab. Rev.* 41, 391–407. doi:10.1080/10837450902891360

Garralda, E., Dienstmann, R., and Tabernero, J. (2017). Pharmacokinetic/pharmacodynamic modeling for drug development in oncology. *Am. Soc. Clin. Oncol. Educ. Book.* 37, 210–215. doi:10.1200/EDBK_180460

Gerlowski, L. E., and Jain, R. K. (1983). Physiologically based pharmacokinetic modeling: Principles and applications. *J. Pharm. Sci.* 72, 1103–1127. doi:10.1002/jps.2600721003

Gobburu, J. V., and Marroum, P. J. (2001). Utilisation of pharmacokinetic-pharmacodynamic modelling and simulation in regulatory decision-making. *Clin. Pharmacokinet.* 40, 883–892. doi:10.2165/00003088-200140120-00001

Henthorn, T. K., Spina, E., Birgersson, C., Ericsson, O., and von Bahr, C. (1985). *In vitro* competitive inhibition of desipramine hydroxylation by alfentanil and fentanyl. *Anesthesiology* 63, A305. doi:10.1097/00000542-198509001-00305

Holford, N., and Yim, D. (2016). Volume of distribution. *Transl. Clin. Pharmacol.* 24, 74. doi:10.12793/tcp.2016.24.2.74

Jones, H. M., Gardner, I. B., and Watson, K. J. (2009). Modelling and PBPK simulation in drug discovery. *AAPS J.* 11, 155–166. doi:10.1208/s12248-009-9088-1

Jones, H. M., Parrott, N., Jorga, K., and Lave, T. (2006). A novel strategy for physiologically based predictions of human pharmacokinetics. *Clin. Pharmacokinet.* 45, 511–542. doi:10.2165/00003088-200645050-00006

Jones, H., and Rowland, Y. K. (2013). Basic concepts in physiologically based pharmacokinetic modeling in drug discovery and development. *CPT. Pharmacometrics Syst. Pharmacol.* 2, e63. doi:10.1038/psp.2013.41

Khalil, F., and Läer, S. (2011). Physiologically based pharmacokinetic modeling: Methodology, applications, and limitations with a focus on its role in pediatric drug development. *J. Biomed. Biotechnol.* 2011, 907461. doi:10.1155/2011/907461

Khojasteh, S. C., Wong, H., and Hop, C. E. C. A. (2011a). "Pharmacokinetics," in *Drug metabolism and pharmacokinetics quick guide* (New York: Springer), 8–11.

Khojasteh, S. C., Wong, H., and Hop, C. E. C. A. (2011b). "Prediction of human pharmacokinetics," in *Drug metabolism and pharmacokinetics quick guide* (New York: Springer), 139–140.

Kuo, J. C. W., and Wei, J. (1969). A lumping analysis in monomolecular reaction systems: Analysis of approximately lumpable system. *Ind. Eng. Chem. Fund.* 8, 124–133. doi:10.1021/i160029a020

Lee, J., Kim, M., Jeong, H., and Shin, K. (2021). Physiologically-based pharmacokinetic model for clozapine in Korean patients with schizophrenia. *Transl. Clin. Pharmacol.* 29, 33–44. doi:10.12793/tcp.2021.29.e3

Li, G., and Rabitz, H. (1991). New approaches to determination of constrained lumping schemes for a reaction system in the whole composition space. *Chem. Eng. Sci.* 46, 95–111. doi:10.1016/0009-2509(91)80120-N

Lin, Z., Gehring, R., Mochel, J. P., Lavé, T., and Riviere, J. E. (2016). Mathematical modeling and simulation in animal health – Part II: Principles, methods, applications, and value of physiologically based pharmacokinetic modeling in veterinary medicine and food safety assessment. *J. Vet. Pharmacol. Ther.* 39, 421–438. doi:10.1111/jvp.12311

Nestorov, I. A., Aarons, L. J., Arundel, P. A., and Rowland, M. (1998). Lumping of whole-body physiologically based pharmacokinetic models. *J. Pharmacokinet. Biopharm.* 26, 21–46. doi:10.1023/A:1023272707390

Okino, M. S., and Mavrovouniotis, M. L. (1998). Simplification of mathematical models of chemical reaction systems. *Chem. Rev.* 98, 391–408. doi:10.1021/cr950223l

Persson, M. P., Nilsson, A., and Hartvig, P. (1988). Pharmacokinetics of alfentanil in total I.V. anaesthesia. *Br. J. Anaesth.* 60, 755–761. doi:10.1093/bja/60.7.755

Peters, S. A., and Hultin, L. (2008). Early identification of drug-induced impairment of gastric emptying through physiologically based pharmacokinetic (PBPK) simulation of plasma concentration-time profiles in rat. *J. Pharmacokinet. Pharmacodyn.* 35, 1–30. doi:10.1007/s10928-007-9073-1

Pilari, S., and Huisinga, W. (2010). Lumping of physiologically-based pharmacokinetic models and a mechanistic derivation of classical compartmental models. *J. Pharmacokinet. Pharmacodyn.* 37, 365–405. doi:10.1007/s10928-010-9165-1

Sager, J. E., Yu, J., Ragueneau-Majlessi, I., and Isoherranen, N. (2015). Physiologically based pharmacokinetic (PBPK) modeling and simulation approaches: A systematic review of published models, applications, and model verification. *Drug Metab. Dispos.* 43, 1823–1837. doi:10.1124/dmd.115.065920

Scheff, J. D., Almon, R. R., DuBois, D. C., Jusko, W. J., and Androulakis, I. P. (2011). Assessment of pharmacologic area under the curve when baselines are variable. *Pharm. Res.* 28, 1081–1089. doi:10.1007/s11095-010-0363-8

Shin, N., Park, M., and Shin, Y. (2015). Application of physiologically based pharmacokinetic (PBPK) modeling in prediction of pediatric pharmacokinetics. *Yakhak Hoeji* 59, 29–39. doi:10.17480/psk.2015.59.1.29

Sinha, V. K., Snoeys, J., Osselaer, N. V., Peer, A. V., Mackie, C., Heald, D., et al. (2012). From preclinical to human – prediction of oral absorption and drug-drug interaction potential using physiologically based pharmacokinetic (PBPK) modeling approach in an industrial setting: A workflow by using case example. *Biopharm. Drug Dispos.* 33, 111–121. doi:10.1002/bdd.1782

Southwood, R., Fleming, V. H., and Huckaby, G. (2018). "Two-compartment models," in *Concepts in clinical pharmacokinetics*. 7th edn. (Maryland: American Society of Health-System Pharmacists Inc), 81–87.

Stangier, J., Su, C. A., and Roth, W. (2000). Pharmacokinetics of orally and intravenously administered telmisartan in healthy young and elderly volunteers and in hypertensive patients. *J. Int. Med. Res.* 28, 149–167. doi:10.1177/147323000002800401

U.S. Food and Drug Administration (2020). Guidance for industry: *In vitro* drug interaction studies-cytochrome P450 enzyme- and transporter-mediated drug interactions. Available at: http://www.fda.gov/media/134582/download (Accessed January 20, 2021).

U.S. Food and Drug Administration (2009). Micardis (telmisartan) tablets, 20 mg, 40 mg and 80 mg. Available at: http://www.accessdata.fda.gov/drugsatfda_docs/label/2009/020850s022s023lbl.pdf (Accessed January 10, 2021).

Utembe, W., Clewell, H., Sanabria, N., Doganis, P., and Gulumian, M. (2020). Current approaches and techniques in physiologically based pharmacokinetic (PBPK) modelling of nanomaterials. *Nanomaterials* 10, 1267. doi:10.3390/nano10071267

Watson, B. A., Klein, M. T., and Harding, R. H. (1996). Mechanistic modeling of n-heptane cracking on HZSM-5. *Ind. Eng. Chem. Res.* 35, 1506–1516. doi:10.1021/ie950579n

Yanni, S. B., Annaert, P. P., Augustijns, P., Ibrahim, J. G., Benjamin, D. K., Jr, Thakker, D. R., et al. (2010). *In vitro* hepatic metabolism explains higher clearance of voriconazole in children versus adults: Role of CYP2C19 and flavin-containing monooxygenase 3. *Drug Metab. Dispos.* 38, 25–31. doi:10.1124/dmd.109.029769

frontiers | Frontiers in Pharmacology

TYPE Original Research
PUBLISHED 28 September 2022
DOI 10.3389/fphar.2022.977372

OPEN ACCESS

EDITED BY
Victor Mangas Sanjuan,
University of Valencia, Spain

REVIEWED BY
Fan Yang,
Henan University of Science and Technology, China
Belen Perez Solans,
University of California, San Francisco, United States

*CORRESPONDENCE
Jonás Samuel Pérez-Blanco,
jsperez@usal.es
José M. Lanao,
jmlanao@usal.es

†These authors have contributed equally to this work and share last authorship

SPECIALTY SECTION
This article was submitted to Translational Pharmacology, a section of the journal Frontiers in Pharmacology

RECEIVED 24 June 2022
ACCEPTED 12 September 2022
PUBLISHED 28 September 2022

CITATION
Zazo H, Lagarejos E, Prado-Velasco M, Sánchez-Herrero S, Serna J, Rueda-Ferreiro A, Martín-Suárez A, Calvo MV, Pérez-Blanco JS and Lanao JM (2022), Physiologically-based pharmacokinetic modelling and dosing evaluation of gentamicin in neonates using PhysPK.
Front. Pharmacol. 13:977372.
doi: 10.3389/fphar.2022.977372

Physiologically-based pharmacokinetic modelling and dosing evaluation of gentamicin in neonates using PhysPK

Hinojal Zazo[1,2], Eduardo Lagarejos[1], Manuel Prado-Velasco[3], Sergio Sánchez-Herrero[4], Jenifer Serna[4], Almudena Rueda-Ferreiro[4], Ana Martín-Suárez[1,2], M. Victoria Calvo[1,2], Jonás Samuel Pérez-Blanco[1,2*†] and José M. Lanao[1,2*†]

[1]Pharmaceutical Sciences Department, University of Salamanca, Salamanca, Spain, [2]Institute of Biomedical Research of Salamanca (IBSAL), Salamanca, Spain, [3]Multiscale Modelling in Bioengineering Research Group and Department of Graphic Engineering, University of Seville, Seville, Spain, [4]Simulation Department, Empresarios Agrupados Internacional S.A., Madrid, Spain

Each year, infections caused around the 25% of neonatal deaths. Early empirical treatments help to reduce this mortality, although optimized dosing regimens are still lacking. The aims were to develop and validate a gentamicin physiologically-based pharmacokinetic (PBPK) model and then potentially explore dosing regimens in neonates using pharmacokinetic and pharmacodynamic criteria. The PBPK model developed consisted of 2 flow-limited tissues: kidney and other tissues. It has been implemented on a new tool called PhysPK, which allows structure reusability and evolution as predictive engine in Model-Informed Precision Dosing (MIPD). Retrospective pharmacokinetic information based on serum levels data from 47 neonates with gestational age between 32 and 39 weeks and younger than one-week postnatal age were used for model validation. The minimal PBPK model developed adequately described the gentamicin serum concentration-time profile with an average fold error nearly 1. Extended interval gentamicin dosing regimens (6 mg/kg q36h and 6 mg/kg q48h for term and preterm neonates, respectively) showed efficacy higher than 99% with toxicity lower than 10% through Monte Carlo simulation evaluations. The gentamicin minimal PBPK model developed in PhysPK from literature information, and validated in preterm and term neonates, presents adequate predictive performance and could be useful for MIPD strategies in neonates.

KEYWORDS

PBPK, gentamicin, neonates, PhysPK software, dosing evaluation, TDM

1 Introduction

Neonatal population is defined as newborns with less than 1 month of life or postnatal age (PNA). Despite of neonatal mortality has been effectively reduced through early interventions, globally 2.4 million of neonates died in 2019. The 75% of neonatal mortality occurred during the first week of life and around of the 25% of these deaths, both in resource-rich and resource-poor settings, is caused by infections like sepsis, pneumonia or meningitis (Chan et al., 2013; Author Anonymous, 2020). However, there are few information about the appropriate dosing regimens use in the clinical practice for neonates (Lanao et al., 2004). Different physiological maturation, related to the gestational age (GA), and rapid developmental changes of physiological factors affect drug pharmacokinetics (PK), thereby being a hindrance to reaching optimal drug concentrations (Food and Drug Administration (FDA) USD of H and HS, 2020).

Administration of aminoglycosides is recommended for newborns at risk of early-onset sepsis, when it is manifested within 72 h after birth. The empirical therapy recommended is gentamicin, alone or in combination with β-lactam antibiotics, due to the high susceptibility of both gram-positive and gram-negative pathogens (National institute for health and care excellence (NICE), 2021). Gentamicin exhibits a concentration-dependent bactericidal effect and requires high peak concentrations (C_{max}) to exhibit post-antibiotic effect at drug levels below the minimum inhibitory concentration (MIC). Moreover, high trough concentrations (C_{min}) are associated with potential toxicity. Therefore, interactions between pharmacokinetic and pharmacodynamic (PK/PD) parameters should be taken into account for evaluating clinical therapeutic outcomes. PK/PD indexes such as the ratio of C_{max}/MIC, the area under the drug concentration–time curve to the MIC (AUC_{24}/MIC) or the percentage of time of the dosage interval the drug concentration remains above the MIC ($T_{>MIC}$), are considered the best descriptors of clinical efficacy of antibiotics. For aminoglycosides, the most suitable indices are the ratio C_{max}/MIC and the $T_{>MIC}$ (Wicha et al., 2021). In fact, treatment selection is diverging from standard dosing concepts toward the used of PK/PD indexes of each antibiotic for optimal dosing regimen selection, in order to avoid suboptimal drug concentrations which also favour resistance development (Abdul-Aziz et al., 2020). Extended and conventional gentamicin intervals are defined as once-daily or twice-daily in adults, respectively. However, in paediatrics larger dose intervals are suggested due to the lower drug elimination shown in this population (Lanao et al., 2004).

Clinical studies in newborns are rarely performed due to ethical concerns. In fact, the use of *in silico* methods, such as the Physiologically-based pharmacokinetic (PBPK) modelling approach, is recommended for drug development and clinical prescriptions for paediatric populations, in order to reduce the number of child patients in clinical trials (EMA, 2018). PBPK modelling provides the ability to combine maturation and physiological age-related parameters and it has been shown that the predictive performance of a PBPK model is superior to that of empirical/traditional compartmental models (Jones et al., 2006; Jones et al., 2011). Thus, PBPK modelling can be useful for investigating clinical efficacy and safety of current adult treatments in paediatric populations, with this assessment being more accurate than a simple extrapolation based on body weight (Lin et al., 2018). Moreover, model-informed precision dosing (MIPD) is recommended for drugs like gentamicin where adequate exposure is critical, cannot be controlled by easy-to-measure clinical parameters and present large PK variability and a narrow therapeutic index (Wicha et al., 2021). Thus, PBPK models could also be helpful for dosage regimen decision-making in this population.

The aims of this work were to develop a minimal PBPK model of gentamicin in neonates to evaluate potential efficacy and toxicity of the current conventional and extended interval gentamicin dosage regimens in neonates, in order to support MIPD strategies based on PK/PD criteria. This work differs from the previous ones (Abduljalil et al., 2020; Neeli et al., 2021) in several aspects, both in relation to the population study (preterm and term neonates), the methodology and novel PBPK modelling and simulation (M&S) software used (PhysPK), and the used of PK/PD indexes in order to be more comprehensive for clinicians.

2 Materials and methods

2.1 Physiologically based pharmacokinetic model development

2.1.1 Model development

The PBPK model development was based on gentamicin properties such as quickly extracellular water distribution, minimal binding to plasma proteins and low intracellular penetration. Moreover, taking into account that the kidney is a pivotal organ related to gentamicin elimination, a minimal PBPK model was adopted including two flow-limited compartments: kidney and rest of tissues. Both tissues were connected by the circulating blood system and heart chamber, and defined by tissue volume, blood flow and partition coefficient. Since gentamicin undergoes glomerular filtration and tubular reabsorption, this last process has been included in the mathematical description of the kidney compartment by a 21% correction of the initial drug filtered by the kidney (Contrepois et al., 1985).

2.1.2 Model equations

The minimal PBPK model was defined by simulation component relationships and mathematical equations of the mechanism. The following sections define the mathematical equations for each component.

In the PhysPK model, the heart is not modelled as a tissue but as the source of cardiac output (CO). That is, it does not address ADME processes but only the cardiac flow pumping through a well-stirred chamber, governed by Eq. 1:

$$V_h * \frac{dC_h}{dt} = (Q_h * C_b) - (Q_h * C_h) \quad (1)$$

where V_h is the heart chamber volume, C_h is the drug concentration in the heart, C_b is the blood serum drug concentration, and Q_h is the heart flow rate (for which CO value has been used). The equation describes the mechanistic effect of the blood mix with the inertia (C_h tends to C_b with a delay) related to the volume V_h.

Kidney tissue was considered as a flow-limited tissue and gentamicin tissue concentration is derived from blood concentration according to flow limited tissue (FLT) assumption, which is provided by Eq. 2:

$$V_k * \frac{dC_k}{dt} = (Q_k * C_b) - \left(Q_k * \frac{C_k}{P_k}\right) - \left(Q_e * \frac{C_k}{P_k}\right) \quad (2)$$

where V_k is the kidney volume, C_k is the drug concentration in the kidney, C_b is the blood serum drug concentration, Q_k is the kidney flow rate, P_k is the partition coefficient of this tissue and Q_e is the elimination flow rate.

Linear behaviour was assumed in order to model kidney elimination of the drug through the kidney. Tubular reabsorption has been considered in GFR adjustment while tubular secretion is negligible in the case of gentamicin, so GFR x TBW is expressed in mL/min, considering that 21% of the drug has tubular reabsorption (Eq. 3):

$$Q_e = TBW * GFR * 0.79 \quad (3)$$

where Q_e is the elimination flow rate, GFR is the glomerular filtration rate parameter expressed in mL/min/kg and TBW is the total body weight.

Rest tissue includes the remaining body tissues not explicitly considered. It is defined as a flow-limited tissue and gentamicin tissue concentration is provided by Eq. 4:

$$V_r * \frac{dC_r}{dt} = (Q_r * C_b) - \left(Q_r * \frac{C_r}{P_r}\right) \quad (4)$$

where V_r is the volume of the rest tissues (all except heart and kidney), C_b is the blood serum drug concentration, C_r is the drug concentration in this compartment, Q_r is the blood flow rate for this compartment and P_r is the partition coefficient of this compartment.

Serum is defined by the blood system, however, gentamicin binding to plasmatic proteins or cells has not been considered relevant since it was less than 10% (Burton, 2006). Thus, the cells compartment has not been considered in the model development and serum concentration is governed by Eq. 5:

TABLE 1 General physiological parameters values implemented in the gentamicin minimal PBPK model.

	Kidney	Rest of tissues
Organ volumes (ml)	0.03	0.87
Blood flow rates (ml/min/kg)	9.35	217
Partition coefficient	10.0	1.00

$$Vd * \frac{dC_b}{dt} = G * P(t) + (Q_h * C_h) + \sum Q_i \frac{C_i}{P_i} - (Q_h * C_b) \quad (5)$$

where Vd is the volume distribution, C_b is the blood serum drug concentration, C_h is the drug concentration in the heart, G is the dose of gentamicin administered, P(t) is a unitary pulse waveform with period T (equivalent to interval administration) and pulse width of 30 min and C_i, Q_i, P_i are the drug concentration, flow rate and partition coefficient for each compartmental tissue (kidney and rest), respectively.

2.1.3 Model parameters

General physiological parameters such as organ volumes, blood flow rates and partition coefficient were already implemented in the software (Table 1). Partition coefficient of gentamicin in kidney was considered as an approach from previous studies (Thibault et al., 1994). Physiological parameters selected based on previous knowledge in preterm and term neonates, and used during the model-building process were: total body weight (TBW), cardiac output (CO), glomerular filtration rate (GFR), gentamicin volume of distribution (Vd) and kidney flow rate (Qk) (Table 2) (Izquierdo et al., 1992; Jackson et al., 1999; Hayton, 2000; Ali et al., 2012; Encinas et al., 2013; Sulemanji and Vakili, 2013). Monte Carlo simulation methodology was used to take into account the variability of these meaningful physiological parameters. It was assumed that they follow a log-normal distribution, and have coefficients of variation (CV) of 20% for TBW and Qk, 24% for CO and 40% for GFR (Bouillon-Pichault et al., 2011; Wilhelm-Bals et al., 2020).

2.1.4 Model validation

Gentamicin minimal PBPK model-based predictions of concentrations by Monte Carlo Simulation were compared to retrospective gentamicin serum concentrations measured in neonates treated at the University Hospital in Salamanca (Spain). Predictions of drug clearance were compared to the clearance values estimated by Maximum a Posteriori (MAP) Bayesian forecasting routinely performed in the TDM (defined as CL observed). For the prediction performance of the model, the prediction error (PE; Eq. 6) and mean prediction error (MPE; Eq.7) were calculated.

TABLE 2 Physiological parameters values implemented in the gentamicin minimal PBPK model.

Physiological parameter	Preterm population [mean ± SD]	Term population [mean ± SD]
Total body weight (kg)	1.73 ± 0.35	3.56 ± 0.72
Cardiac output (ml/min/kg)	172 ± 50.6	172 ± 50.6
Glomerular filtration rate (ml/min/kg)	1.31 ± 0.53	1.72 ± 0.70
Gentamicin volume of distribution (L/kg)	0.52 ± 0.16	0.46 ± 0.14

SD, standard deviation.

$$PE\ (\%) = \frac{PRED - OBS}{OBS} \times 100 \quad (6)$$

$$MPE = \frac{1}{n}\sum PE \quad (7)$$

The overall predictability of this model was evaluated in terms of bias and precision using the conventional metrics of average-fold error (AFE; Eq. 8) and absolute average-fold error (AAFE; Eq. 9), respectively.

$$AFE = 10^{\frac{1}{n}\sum log\left(\frac{PRED}{OBS}\right)} \quad (8)$$

$$AAFE = 10^{\frac{1}{n}\sum |log\left(\frac{PRED}{OBS}\right)|} \quad (9)$$

If the model predictions reached the criteria of the AFE and AAFE between 0.5 and 2-fold, its predictive performance would be considered to be satisfactory (Puttrevu et al., 2020; Corral Alaejos et al., 2022).

Visual predicted check (VPC) was carried out to evaluate PBPK model performance based on simulations. Observed concentrations were dose-normalized and expressed as the standard dose considered in the Monte Carlo simulations for each group (6 mg/kg q48h for preterm neonates and 6 mg/kg q36h for term neonates). A total of 1,000 virtual patients of each subpopulation were considered to calculate prediction intervals (PI) of 90% and 50%. If observed concentrations were distributed within the 90% PI, the model prediction capability was deemed to be adequate (Rubinstein and Kroese, 2016). Finally, the VPC plots were generated in R version 4.0.2 software from the output of the simulations performed in PhysPK.

2.2 Software

Gentamicin minimal PBPK model was developed using the commercially available PhysPK v.2.4.1 platform as part of EcosimPro 6.2.0® (www.physpk.com). This software is based on first-principles modelling of complex systems with continuous and discrete time equations; which use the Multi-Object-Oriented Modelling (MOOM) paradigm. EcosimPro language is designed to model systems formulated through differential-algebraic equations (DAE) and discrete events, by means of a non-algorithmic code (acausal simulation language). Any EcosimPro model is converted to algorithmic code (C++) through the EcosimPro platform previously being executed. PhysPK is a PBPK M&S software built by means of the EcosimPro language. Simulation component parameters and mechanism variables are defined in the International System of Units (SI), although the user parameter values can be defined with other units and converted to SI with internal functions of PhysPK (Martí et al., 2014).

The gentamicin PBPK model has been created through two categories of mathematical equations. The first one is defined by the physical processes that occur inside each simulation component. These processes are liberation, absorption, distribution, metabolism and excretion (LADME) and other mechanisms for the cardiac output source and drug administrator. Mathematical equations in a simulation component describe these processes through differential - algebraic equations (DAE) to give mass conservation, metabolism, absorption, distribution, excretion, and others (inertial pumping or drug rate infusion) for each chemical compound inside all the spatial regions that pertain to the component (Roa and Prado, 2006). The second category refers to the equations that describe the relationships among the simulation components in the PBPK model. The last equations define the blood convection through the vascular system in our PBPK model. They are generated by PhysPK according to the blood connections. Once a PhysPK model is created, it may be used to predict the evolution of the system starting from the initial conditions for a particular context through a simulation experiment.

A second important issue is that the model's equations are represented by means of a non-algorithmic mathematical formulation. That is, the model is defined in a balanced and complete way (number of variables to solve are equal to number of equations), but it must be previously converted to a flat and algorithmic code in order to be executed in the simulation experiment. The algorithmic code defines the order in which variables are computed and which equations are used to solve them. This methodology for DAE systems is more fully described in the Wiley Encyclopedia of Biomedical Engineering (Roa and Prado, 2006).

EcosimPro also supports Montecarlo simulations, generating a range of possible outcomes considering the *a priori* likelihood

of different variables or scenarios. Moreover, the successive productions of random numbers will also be the same using a seed. The random numbers generated, for this PBPK model, have log-normal probability density function.

2.3 Clinical data

The study was carried out using data from 47 newborn patients admitted between 1999 and 2003 in the Neonatology Unit of the University Hospital in Salamanca (Spain). These data were obtained as part of routine therapeutic drug monitoring (TDM) of aminoglycoside therapy in paediatric patients suspected of suffering from infection due to Gram-negative microorganisms, regardless of whether this had been confirmed in the antibiogram. This data has also been used by our group in a previous publication (Lanao et al., 2004). Patients selected are characterized to be less than one-week of PNA and with GA between 32 and 39 weeks. These patients were subsequently divided into two subgroups due to their different physiological maturation: preterm neonates with GA between 32 and 37 weeks, and term neonates with GA over 37 weeks. Their concentration-time data were used for the model validation.

2.3.1 Gentamicin dosing and sampling schedule

Gentamicin was administered in the form of an intravenous (IV) infusion during 0.5 h, with an initial dose of 6 mg/kg and an administration interval of 36 h or 48 h. Blood serum samples were collected at 2 and 24 h from the start of drug infusion (Lanao et al., 2004).

Serum gentamicin levels were measured by fluorescence polarization immunoassay AXYM (Abbott Laboratories, Chicago, IL, United States) The method was successfully verified for the calibration range of 0.3–10 mg/L. Additional details of the analytical method are provided in a previous publication (Lanao et al., 2004).

2.4 Clearance estimation

In order to check the functionality of the software and the suitability of GFR values selected from literature for the PBPK model developed, this parameter was also estimated using the PhysPK parameter estimation module.

This module allows for the estimation of population parameters of non-linear physiological models. The iterative two-stage (ITS) method was applied to estimate an initial condition of population parameters for each individual subject, without taking into account the population knowledge (Davidian, 2010). After that, the population parameters were estimated using a first-order conditional estimation (FOCE) method, starting with values obtained in ITS.

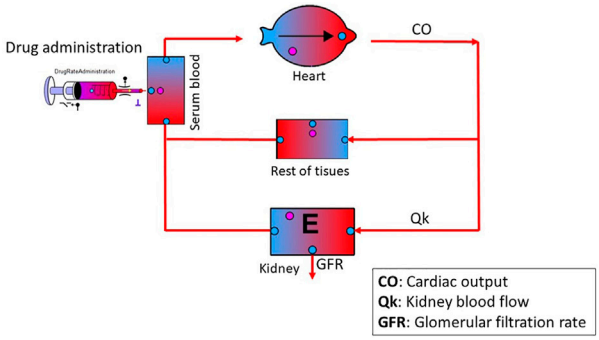

FIGURE 1
Schematic diagram of the minimal PBPK model developed in PhysPK. Black solid circles are Boolean components for activation/deactivation of processes (i.e., dose administration); pink and blue solid circles, are recording components of the system (i.e., drug concentration in a specific region of the system such as plasma, tissue, etc.,). Organ with an E inside means that it has elimination. The purple T next to the syringe means that the administration has a rate and it can be multiple.

2.5 Gentamicin standard dosage evaluation based on PK/PD criteria

Based on PK/PD criteria, conventional and extended interval dosage regimens were evaluated for each subpopulation. For preterm neonates the dosage regimens evaluated were 4 mg/kg/day (q24h) as a conventional regimen, and 6 mg/kg/day (q48h) as an extended interval regimen; while for term neonates the dosages selected were 4 mg/kg/day (q24h) and 6 mg/kg/day (q36), respectively (Lanao et al., 2004). The PTA of different PK/PD indexes were selected for treatment efficacy and toxicity criteria evaluation.

C_{max}/MIC ratio over 8–10 folds, keeping C_{max} lower than 25 mg/L, are necessary to achieve post-antibiotic effect warranting an adequate safety profile related to the maximum drug exposure. Moreover, C_{min} lower than 2 mg/L has been suggested to minimize the potential toxic effects of gentamicin, because it is associated with lower accumulation in both the renal tubule and inner ear (Vučićević et al., 2014). Therefore, the target PK/PD criteria for toxicity were established at Cmin ≥2 mg/L and Cmax ≥25 mg/L. Regarding efficacy criteria, C_{max}/MIC ≥8 and $T_{>MIC}$ (expressed as percentage of the dosing interval) equal to or higher than 60% were selected for both dosage regimens (Zazo et al., 2013). Based on the fact that gentamicin is the treatment recommend against pathogens with MIC values between 0.5 and 2 (O'Connor et al., 2021), MIC value of 1 mg/L was selected for PK/PD criteria calculations. For aminoglycosides, the treatment response was defined as effective when the PTA ≥90% for efficacy PK/PD criteria, and for safety when PTA ≤10% for toxicity criterion (He et al., 2022).

TABLE 3 Demographic baseline characteristics of neonates' patients evaluated.

Parameter	Preterm (GA ≤37 weeks) [mean ± SD (min-max)]	Term (GA >37 weeks) [mean ± SD (min-max)]
Number of patients	31	16
Gestational age (GA) (weeks)	33.7±1.56 (32-37)	38.9± 0.25 (38-39)
Postnatal age (PNA) (days)	3.03±1.02 (2-7)	2.94±0.85 (2-5)
Total body weight (kg)	1.96 ± 0.41 (1.16–3.00)	3.09 ± 0.23 (2.29–3.62)
Dose (mg/kg)	5.74 ± 0.80 (4.01–6.88)	6.64 ± 0.22 (6.99–6.21)
Serum concentration at 2 h	17.7 ± 4.28 (5.06–24.1)	13.8 ± 3.08 (8.17–20.1)
Since drug administration (mg/L)		
Serum concentration at 24 h	2.92 ± 0.79 (1.84–5.50)	1.41 ± 0.41 (0.86–2.32)
Since drug administration (mg/L)		

SD, standard deviation.

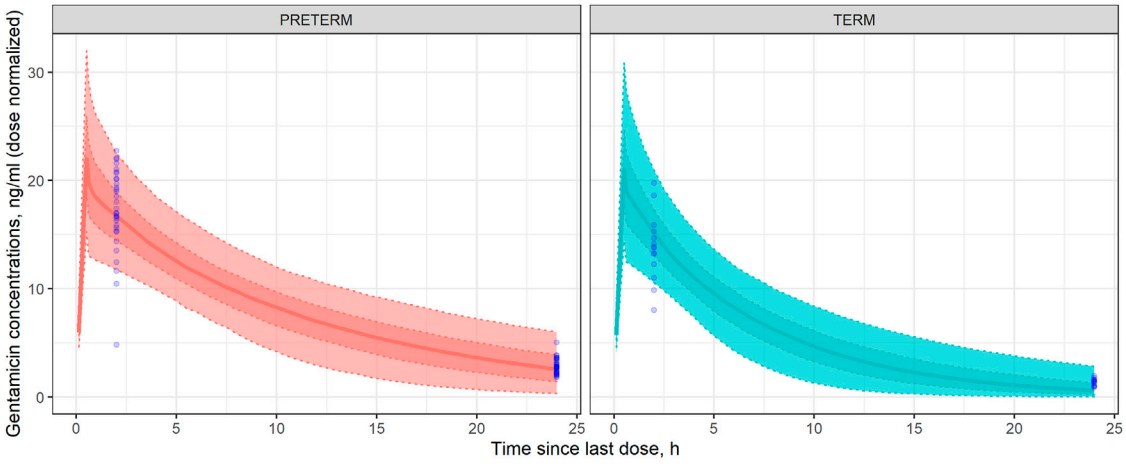

FIGURE 2
Visual Predicted Check (VPC) in preterm (left) and term (right) neonates. Dotted lines represent, from the bottom to the upper panel, the 10th, 25th, 75th, and 90th percentiles of the gentamicin concentrations simulated vs. time. Shaded areas represent, from outside to inside, the 90% and 50% prediction intervals. Solid lines represent the median gentamicin simulated concentration-time profile. Open blue circles represent the observed gentamicin concentrations dose-normalized.

3 Results

The schematic diagram of the minimal PBPK model developed in the interface of PhysPK is shown in Figure 1. It included the two tissues modelled, kidney and rest of tissues, and the heart as the source of CO. The relationships among simulation components are given by the multilevel modelling schematic.

A total of 91 serum samples from 47 subjects, were used for the minimal PBPK model development. Demographic characteristics of patients evaluated are shown in Table 3.

Most of gentamicin observed concentrations (80.6% and 100% for the C_{2h} and $C_{24h,}$ respectively for preterm neonates, and 87.5% and 100% for the C_{2h} and $C_{24h,}$ respectively for term neonates) were within the 90% PI. Therefore, it can be assured that the minimal PBPK model developed for gentamicin in neonates adequately describes the drug concentration-time profile observed, as well as its PK variability, in both the preterm and term neonate populations studied (Figure 2).

Table 4 shows the mean of observed and predicted concentration and clearance values, as well as the bias and precision evaluation for the validation of the model-predictive performance. Both, AFE and AAFE values for all the predictions were between 0.5 and 2. In fact, all AFE values are nearly 1 which is indicative of a lack of significant bias associated with model predictions.

The GFR values obtained by optimization with the PhysPk software were (mean ± SD) 1.176 ± 0.037 ml/min/kg and 1.324 ± 0.054 ml/min/kg for preterm and term neonates, respectively.

TABLE 4 Mean values and precision and bias errors of gentamicin minimal PBPK model developed.

	Preterm			Term		
	C 2 h (mg/L)	C 24 h (mg/L)	CL (L/h)	C 2 h (mg/L)	C 24 h (mg/L)	CL (L/h)
Mean value observed	17.7	2.92	0.09	13.8	1.41	0.19
Mean value predicted	17.4	2.62	0.11	15.4	0.89	0.23
Mpe (%)	8.08	−5.04	26.5	16.3	−28.8	27.7
Afe	1.02	0.92	1.24	1.14	0.68	1.26
Aafe	1.22	1.23	1.26	1.20	1.47	1.29

C, concentration; CL, clearance; MPE, mean prediction error; AFE, average-fold error; AAFE, absolute average-fold error.

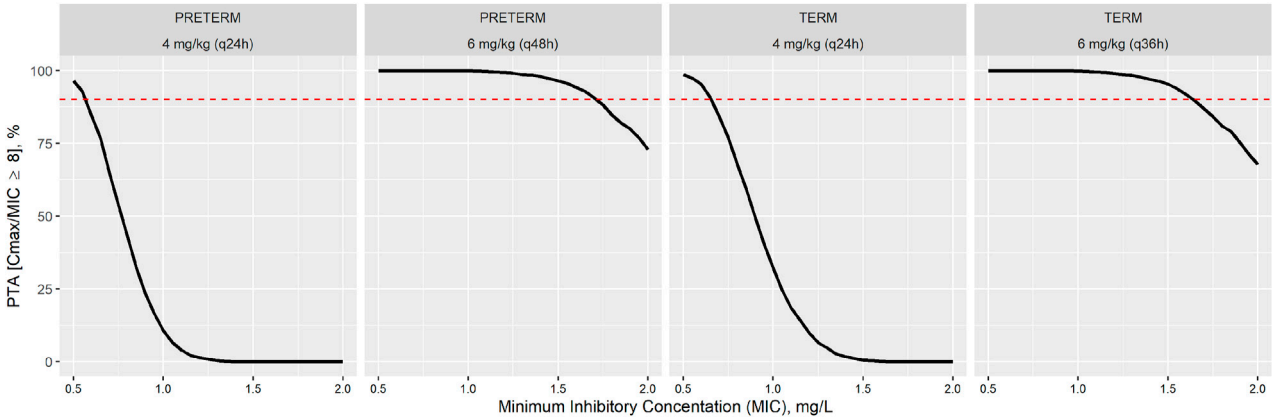

FIGURE 3
Probability of target attainment (PTA) to reach the C_{max}/MIC ≥8 ratio for each gentamicin dosage regimen: conventional (4 mg/kg q24h) and extended interval regimen (6 mg/kg q48h and 6 mg/kg q36h for preterm and term, respectively).

Figure 3 shows that the PTA to reach a C_{max}/MIC was adequate with the extended interval regimen (6 mg/kg q48h and 6 mg/kg q36h for preterm and term, respectively) while PTA reached with the conventional regimen (4 mg/kg q24h) was insufficient to achieve proper treatment efficacy, for any MIC value considered (0–2 mg/L). In fact, the extended interval regimens can be assumed to be effective (PTA≥90%) up to MIC values nearly 2 mg/L (1.7 mg/L for preterm and 1.6 mg/L for term neonates), while conventional regimens can be considered effective until MIC values close to 0.6 mg/L (0.55 mg/L for preterm and 0.65 mg/L for term neonates).

Table 5 show the PTA to reach the efficacy and toxicity criteria (C_{max}/MIC ≥8 and $T_{>MIC}$ ≥60% for efficacy and C_{min} ≥2 mg/L and C_{max} ≥25 mg/L for toxicity) for each gentamicin regimen considered in each specific population. According to the PTA of PK/PD indexes studied, both regimens presented PTA <10% for the toxicity criteria.

4 Discussion

M&S techniques in biomedicine have experienced great advances and impact in drug development and evaluation in recent decades. Consequently, specialized M&S software is now necessary in the pharma, clinical and biomedical engineering industries. Neonates are one of the most vulnerable populations and also require more ethical considerations, so studies designed with M&S methodologies have been highlighted as a useful methodology in drug development, especially for dose selection decision-making.

The software used in this work, PhysPK, is a novel PBPK platform which has already been successfully applied in MIPD of paediatric patients (Prado-Velasco et al., 2020). It is a robust and potent M&S tool allowing easy and efficient implementation of simulations, execution (such as parameter estimation) and dosage optimization algorithms based on PK/PD criteria (efficacy and/or toxicity), which supports the implementation

TABLE 5 Probability of target attainment (PTA) for efficacy and toxicity criteria (%) (MIC = 1 mg/L).

PK/PD criterion	Preterm		Term	
	Conventional Reg. (q24h)	Extended interval (q48h)	Conventional Reg. (q24h)	Extended interval (q36h)
Efficacy				
C_{max}/MIC ≥8	10.8	99.9	32.3	99.8
$T_{>MIC}$ ≥60%	87.9	70.7	61.2	54.9
Toxicity				
C_{min} ≥2 mg/L	5.0	5.9	0.4	1.8
C_{max} ≥25 mg/L	0.0	6.9	0.0	6.5

C_{min}, trough concentrations; C_{max}, peak concentrations; MIC, minimum inhibitory concentration; PK/PD, pharmacokinetic-pharmacodynamic; $T_{>MIC}$, percentage of time of the interval the drug concentration remains above the MIC.

TABLE 6 Comparison of PhysPK and commonly used PBPK software programs.

	PhysPK	Simcyp	GastroPlus	NONMEM	WinNonlin	PK-Sim/MOBI
Company	Empresarios Agrupados Internacional	Certara United States Inc.	Simulations Plus Inc.	ICON plc	Certara United States Inc.	Bayer Technology Services
User friendly software	Yes	Yes	Yes	Yes	Yes	Yes
Model creation and edition	Yes	No	No	Yes	Yes	Yes
Population estimation/ validation module	Yes	Yes	Yes	Yes	No[a]	No[a]
Execution out-of-the-box	Yes	No	No	No	No	No

[a]Estimation/validation module by optimization.

of MIDP strategies in the clinical routine. PhysPK provides a highly intuitive graphics environment that facilitates the PBPK model development process based on object-oriented schematics (Rodrigues Matos et al., 2013). It is based on different multi-flexi libraries which let components' development and reusability (i.e., tissues, membranes, etc.,) increasing model complexity and overcoming the useful of other PBPK tools, like Simcyp, GastroPlus or PK-SIM (Reig-Lopez et al., 2020). The PhysPK modeling approach let also to customized PBPK models, like MATLAB/Berkeley Madonna, but without mathematical causality requirements like others software, as NONMEM or Winnonlin (Prado-Velasco, 2016) (Table 6). Moreover, models and calculations can be encapsulated and encrypted in a standalone application (deck), for example Shiny applications. Then, user can only input any data from external well-known applications like Excel, Matlab, C++, etc., and visualize the outputs in real time.

This work is focused on a neonatal population with less than 1 week of life. This is a critical period of life for newborns where the highest infection mortality rate has been observed (Author Anonymous, 2020). Therefore, patients have been classified based on gestational age (GA), in two important subgroups: 1) Preterm neonates with GA ≤37 weeks and 2) Term neonates with GA >37 weeks. The main differences between these two groups are whole blood volume, physiological maturation, and total body water. Moreover, rapid developmental changes of physiological factors in newborns affect drug PK, so different parameters' values have been used for each subpopulation. Thus, a gentamicin PBPK model was developed and validated in term and preterm neonates. Subsequently, the model was used to evaluate the efficacy and safety, based on PK/PD criteria, of current gentamicin dosages recommended for these population.

Extended interval aminoglycoside regimens are recommended, rather than conventional multiple daily dose regimens, because they allow achievement of higher C_{max} and lower C_{min}, improving therapeutic efficacy and safety (Wicha et al., 2021). These reasons, along with pharmacoeconomic justification, are all sufficient grounds to select extended interval dosing as the gold-standard regimens for gentamicin in adults (Abdul-Aziz et al., 2020). In neonate populations, their use has been suggested by various authors, even the British Medical Association, despite this regimen being off-label (Lanao et al., 2004; National institute for health and care excellence (NICE), 2021; Rao et al., 2011; El-Chaar et al., 2016). However, some guidelines still recommend a once-daily dosage regimen for term neonates instead of extended-interval such as in other populations like preterm ones (ANMF - Australasian Neonatal Medicines Formulary, 2022; Comité de

Medicamentos de la Asociación Española de Pediatríaá, 2022). In fact, according to Neeli et al. 60% of term neonates in intensive care units treated with a once-daily dosage regimen presented potentially toxic concentrations but only around a quarter of them were changed to an extended-interval dosage regimen (Neeli et al., 2021). In order to be a more comprehensive study that encourages clinicians to extended-interval regimen for neonates, specially term ones, this research has been focused on both kinds of neonates, preterm and term, unlike other gentamicin PBPK models published which focus just on preterm populations (Abduljalil et al., 2020; Idkaidek et al., 2020).

The PBPK model development follows a top-down modelling approach. Gentamicin is a hydrophilic drug (logP = −3.1) that mostly distributes in extracellular fluid, eliminating the need for the full PBPK model [16]. It also has low intracellular penetration so it was assumed that the drug distributes instantly in the whole volume of the tissue from the incoming blood flow and a flow-limited model was selected. The kidney is a pivotal organ related to gentamicin elimination. Indeed, 90% of the drug is renally excreted, and it is also directly related to gentamicin nephrotoxicity (Johnson et al., 2006). Thus, due to their PK and toxicity interest, this tissue was the only one included in the minimal PBPK model.

Renal function matures slowly and depends on GA and PNA, as indicated by diuresis, GFR and renal tubular activity (Vučićević et al., 2014). In order to take into account kidney maturation, the studied population has been divided into two subgroups, preterm and term neonates, with different mean GFR values selected for each subgroup based on the available information in the scientific literature. Moreover, 21% of gentamicin that is renally excreted undergoes tubular reabsorption (Contrepois et al., 1985) and this was also reflected in the minimal PBPK model proposed. This is an important point of difference vs. other studies which used adult GFR values (Gastine et al., 2022) or reflected the absence of tubular reabsorption as a limitation (Abduljalil et al., 2020; Neeli et al., 2021).

Based on the critical relevance of the GFR values observed during the model-building stage, this parameter was also optimized using the PhysPK parameter estimation module both in preterm and term neonates. The GFR values obtained by optimization through the PhysPK software (1.176 ± 0.037 ml/min/kg and 1.324 ± 0.054 ml/min/kg for preterm and term, respectively) were well in agreement with those implemented in the PBPK model from the literature [1.21 ml/min/kg and 1.59 ml/min/kg for preterm and term, respectively (Izquierdo et al., 1992; Sulemanji and Vakili, 2013)]. In this way, both the selected values and the functionality of the software has been verified.

In order to evaluate the appropriateness of the model-based predictions, bias and precision metrics (AFE and AAFE) were calculated with results between 0.5 and 2 in all of the cases (Table 4). For concentrations at 2 h after start of drug administration, the AFE value near 1 indicates a lack of bias associated with model predictions. Despite of there are some values under the 10th percentile and an outlier in preterm population. Although, for concentrations at 24 h the MPE results indicate that in the term population, what are lightly underestimated (Table 4). Simulation-based diagnostics (Figure 3) showed an adequate model prediction-capability of the gentamicin minimal PBPK model in term and preterm neonates. The large PK variability of the neonatal population observed in these patients was in agreement with previous studies (Nielsen et al., 2009; Bijleveld et al., 2017). This gentamicin PK variability was also properly captured by the gentamicin minimal PBPK model-based simulations.

PBPK models are useful both for predicting drug concentrations and PK parameters which are difficult to measure properly, such as the drug clearance in neonates. The measurement of creatinine levels in neonates is not precise because of the reflection of maternal creatinine levels and the uncertainty about creatinine renal tubular handling. So, it makes the use of serum creatinine levels unreliable and therefore the use of the Schwarz Bedside equation is not recommended in patients younger than 1 year old (Sulemanji and Vakili, 2013; Go et al., 2018). According to the bias and precision results (Table 4), CL values predicted with this gentamicin minimal PBPK model are suitable.

Because the therapy usually starts empirically, the causative pathogen and then its MIC value are commonly unknown at this clinical stage, so MIC distributions from EUCAST reference laboratories are typically used. The highest MIC breakpoint for gentamicin is 2 mg/L. In such case that the pathogen isolated presents a higher value, administration of a concomitant antibiotic or a change to another treatment would be advisable (Burton, 2006). Therefore, no MIC higher than 2 mg/L was considered when evaluating Cmax/MIC efficacy criterion (Figure 3) and a reference MIC of 1 mg/L has been selected for PTA calculation as the most likely within the standard MIC observed in the clinic for pathogens treated with gentamicin.

The conventional dosing regimen recommended by the AEP-SEIP has been compared with the extended interval dosage regimen recommended by the University Hospital in Salamanca. Figure 3 showed that both gentamicin dosage regimens appear to be potentially effective and safe, according to the PK/PD indexes considered. Peak serum concentrations of gentamicin with the conventional regimen (4 mg/kg q24h for both populations) were not sufficiently high enough to achieve C_{max}/MIC ratio over 8 necessary to achieve post-antibiotic effect, in most cases (Figure 3). Moreover, it could bring on bacterial resistance development despite eliciting a therapeutic response. In contrast, extended interval gentamicin dosing regimens (6 mg/kg q48h and 6 mg/kg q36h for preterm and term neonates, respectively) showed adequate efficacy (PTA higher than 90%) with acceptable safety (PTA for toxicity criteria ≤7% in all cases) through Monte Carlo simulation evaluations (Table 5). Indeed, extended interval regimens reached the

main efficacy criteria (C_{max}/MIC ≥8) up to MIC values of 1.55 mg/L and 1.65 mg/L for preterm and term neonates, respectively (Figure 3). These results are in line with the current clinical decisions of combining gentamicin with an alternative antibiotic or even changing the drug selected to treat a Gram-negative infection caused by pathogens with MIC higher than 2 mg/L (O'Connor et al., 2021). However, the conventional dosing regimen only reaches C_{max}/MIC ≥8 against pathogens with MICs lower than 0.5 mg/L (Figure 3).

Findings in our study are consistent with other published studies like Gastine et al. (2022) whose results show that the conventional regimen would be insufficient to cover most common Gram-negative Enterobacterales (MIC ≤2 mg/L) responsible for many neonatal sepsis, with this regimen being efficacious in only less than one-quarter of neonates treated.

Apart from the important usefulness and potential applications of the gentamicin minimal PBPK model presented in this work, some limitations must be acknowledged such as: 1) The model has been validate with a small sample size, just 2 concentration-time points and retrospective data which might limit precise assessments and additional evaluations of the model; 2) No correlations between the physiological variables simulated were considered in the Monte Carlo simulations (Franchetti and Nolin, 2020). However, the impact of these correlations is not expected to be relevant as most of the parameters were expressed per kg of TBW and specific values observed in the literature were considered for preterm and term neonates.

Finally, gentamicin treatment is limited mainly by its potential toxicity. Thus, this minimal PBPK model will serve as a starting point for future investigations regarding the gentamicin concentrations reached in the kidneys. After a refinement of the minimal PBPK model presented, it will be able to evaluate the potential toxicity of gentamicin dosages proposed in neonates and optimize these dosages based on PK/PD criteria. Moreover, the model presented can be applied to different aminoglycosides in similar populations after model refinement. Similarly, additional information could be valuable for extending the PBPK model applications such as physiological changes in intensive care neonate patients (i.e., fluid shift due to capillary leak and renal dysfunction), kidney and ear accumulation (related to the most-likely drug side effects), or bacteria growth models (considering potential drug resistance) among others.

5 Conclusion

In summary, the gentamicin minimal PBPK model developed in the PhysPK platform adequately described preterm and term neonates' gentamicin PK behaviour. According to the PK/PD criteria, extended interval dosage regimens reached the efficacy criterion with a reduced probability of presenting toxicity even against pathogens with a minimum inhibitory concentration near 2 mg/L. The minimal gentamicin PBPK model presented in this work has shown an adequate model predictive performance with acceptable precision and lack of significant bias. Thus, it could be useful for MIPD strategies in neonates based on PK/PD criteria.

Data availability statement

The original contributions presented in the study are included in the article/Supplementary Material, further inquiries can be directed to the corresponding authors.

Ethics statement

Ethical review and approval was not required for the study on human participants in accordance with the local legislation and institutional requirements. Written informed consent from the participants' legal guardian/next of kin was not required to participate in this study in accordance with the national legislation and the institutional requirements.

Author contributions

Methodology, HZ, JP-B, and JL; software, SS-H, JS, AR-F, EL, and MP-V; formal analysis and evaluation, SS-H, HZ, and JP-B; data curation, MC, AM-S, JL; writing—original draft preparation, HZ, JP-B, JS; conceptualization, writing—review and editing, AM-S, JL; supervision, JL; data visualization, JP-B; All authors have read and agreed to the published version of the manuscript.

Acknowledgments

The authors would like to thank the patients, investigators, and the medical, nursing, and laboratory staff who participated in the clinical routine practice included in the present work.

Conflict of interest

Preliminary results of this research were presented at XIV Jornadas de modelización y simulación en biomedicina, in November 2021 in Barcelona, Spain. SS-H, JS and AR-F were employees of "Empresarios Agrupados SA" at the time the analysis was conducted.

The remaining authors declare that the research was conducted in the absence of any commercial or financial relationships that could be construed as a potential conflict of interest.

Publisher's note

References

Abdul-Aziz, M. H., Alffenaar, J. W. C., Bassetti, M., Bracht, H., Dimopoulos, G., Marriott, D., et al. (2020). Antimicrobial therapeutic drug monitoring in critically ill adult patients: A position paper. *Intensive Care Med.* 46 (6), 1127–1153. doi:10.1007/s00134-020-06050-1

Abduljalil, K., Pan, X., Pansari, A., Jamei, M., and Johnson, T. N. (2020). Preterm physiologically based pharmacokinetic model. Part II: Applications of the model to predict drug pharmacokinetics in the preterm population. *Clin. Pharmacokinet.* 59 (4), 501–518. doi:10.1007/s40262-019-00827-4

Ali, A. S., Farouq, M. F., and Al-Faify, K. A. (2012). Pharmacokinetic approach for optimizing gentamicin use in neonates during the first week of life. *Indian J. Pharmacol.* 44 (1), 36–40. doi:10.4103/0253-7613.91864

ANMF - Australasian Neonatal Medicines Formulary (2022). Anmf - australasian neonatal Medicines formulary. [Internet][citado 17 de marzo de 2022]. Disponible en: Available at: https://www.anmfonline.org/ (Accessed March 17, 2022).

Comité de Medicamentos de la Asociación Española de Pediatríaá, 2022, *Pediamécum. Edición 2015* | Asociación Española de Pediatría [Internet]. [citado 7 de febrero de 2022]. Disponible en: Available at: https://www.aeped.es/comite-medicamentos/pediamecum/gentamicina (Accessed February 7, 2022).

Author Anonymous (2020).Newborns: Improving survival and well-being. Geneva, Switzerland: World Hhealth Organization. [internet]. [citado 3 de diciembre de 2021]. Disponible en:Available at: https://www.who.int/news-room/fact-sheets/detail/newborns-reducing-mortality (Accessed September 19, 2020).

Bijleveld, Y. A., van den Heuvel, M. E., Hodiamont, C. J., Mathôt, R. A. A., and de Haan, T. R. (2017). Population pharmacokinetics and dosing considerations for gentamicin in newborns with suspected or proven sepsis caused by gram-negative bacteria. *Antimicrob. Agents Chemother.* 61 (1), e01304–e01316. doi:10.1128/AAC.01304-16

Bouillon-Pichault, M., Jullien, V., Bazzoli, C., Pons, G., and Tod, M. (2011). Pharmacokinetic design optimization in children and estimation of maturation parameters: Example of cytochrome P450 3A4. *J. Pharmacokinet. Pharmacodyn.* 38 (1), 25–40. doi:10.1007/s10928-010-9173-1

Burton, M. E. (2006). *Applied pharmacokinetics & pharmacodynamics: Principles of therapeutic drug monitoring*. 4th ed. Baltimore: Lippincott Williams & Wilkins.

Chan, G. J., Lee, A. C., Baqui, A. H., Tan, J., and Black, R. E. (2013). Risk of early-onset neonatal infection with maternal infection or colonization: A global systematic review and meta-analysis. *PLoS Med.* 10 (8), e1001502. doi:10.1371/journal.pmed.1001502

Contrepois, A., Brion, N., Garaud, J. J., Faurisson, F., Delatour, F., Levy, J. C., et al. (1985). Renal disposition of gentamicin, dibekacin, tobramycin, netilmicin, and amikacin in humans. *Antimicrob. Agents Chemother.* 27 (4), 520–524. doi:10.1128/aac.27.4.520

Corral Alaejos, Á., Zarzuelo Castañeda, A., Jiménez Cabrera, S., Sánchez-Guijo, F., Otero, M. J., and Pérez-Blanco, J. S. (2022). External evaluation of population pharmacokinetic models of imatinib in adults diagnosed with chronic myeloid leukaemia. *Br. J. Clin. Pharmacol.* 88 (4), 1913–1924. doi:10.1111/bcp.15122

Davidian, M. (2010). "Nonlinear mixed effects models" in *International Encyclopedia of Statistical Science*.Editor M. Lovric (New York: Springer).

El-Chaar, G. M., Supaswud-Franks, T., Venugopalan, L., Kohn, N., and Castro-Alcaraz, S. (2016). Extended-interval gentamicin administration in neonates: A simplified approach. *J. Perinatol.* 36 (8), 660–665. doi:10.1038/jp.2016.37

EMA (2018).Extrapolation of efficacy and safety in paediatric medicine development. Amsterdam, Netherlands: European Medicines Agency. Internet[citado 10 de febrero de 2022]. Disponible en: Available at: https://www.ema.europa.eu/en/extrapolation-efficacy-safety-paediatric-medicine-development (Accessed 10 30, 2018).

Encinas, E., Calvo, R., Lukas, J. C., Vozmediano, V., Rodriguez, M., and Suarez, E. (2013). A predictive pharmacokinetic/pharmacodynamic model of fentanyl for analgesia/sedation in neonates based on a semi-physiologic approach. *Paediatr. Drugs* 15 (3), 247–257. doi:10.1007/s40272-013-0029-1

Food and Drug Administration (FDA) USD of H and HS (2020). General clinical Pharmacology considerations for neonatal studies for drugs and biological products guidance for industry. [Internet]. U.S. Food and Drug Administration. FDA[citado 12 de enero de 2022]. Disponible en: Available at: https://www.fda.gov/regulatory-information/search-fda-guidance-documents/general-clinical-pharmacology-considerations-neonatal-studies-drugs-and-biological-products-guidance (Accessed July, 2022).

Franchetti, Y., and Nolin, T. D. (2020). Dose optimization in kidney disease: Opportunities for PBPK modeling and simulation. *J. Clin. Pharmacol.* 60, S36–S51. doi:10.1002/jcph.1741

Gastine, S., Obiero, C., Kane, Z., Williams, P., Readman, J., Murunga, S., et al. (2022). Simultaneous pharmacokinetic/pharmacodynamic (PKPD) assessment of ampicillin and gentamicin in the treatment of neonatal sepsis. *J. Antimicrob. Chemother.* 77 (2), 448–456. doi:10.1093/jac/dkab413

Go, H., Momoi, N., Kashiwabara, N., Haneda, K., Chishiki, M., Imamura, T., et al. (2018). Neonatal and maternal serum creatinine levels during the early postnatal period in preterm and term infants. *PLoS One* 13 (5), e0196721. doi:10.1371/journal.pone.0196721

Hayton, W. L. (2000). Maturation and growth of renal function: Dosing renally cleared drugs in children. *AAPS PharmSci* 2 (1), E3. doi:10.1208/ps020103

He, S., Cheng, Z., and Xie, F. (2022). Population pharmacokinetics and dosing optimization of gentamicin in critically ill patients undergoing continuous renal replacement therapy. *Drug Des. devel. Ther.* 16, 13–22. doi:10.2147/DDDT.S343385

Idkaidek, N., Hamadi, S., Bani-Domi, R., Al-Adham, I., Alsmadi, M., Awaysheh, F., et al. (2020). Saliva versus plasma therapeutic drug monitoring of gentamicin in Jordanian preterm infants. Development of a physiologically-based pharmacokinetic (PBPK) model and validation of class II drugs of salivary excretion classification system. *Drug Res.* 70 (10), 455–462. doi:10.1055/a-1233-3582

Izquierdo, M., Lanao, J. M., Cervero, L., Jimenez, N. V., Domínguez-Gil, A., and Dominguez-Gil, A. (1992). Population pharmacokinetics of gentamicin in premature infants. *Ther. Drug Monit.* 14 (3), 177–183. doi:10.1097/00007691-199206000-00001

Jackson, M., Abdel-Rahman, S., and Kearns, G. (1999). Pharmacology of antibiotics in the neonate. *Seminars Pediatr. Infect. Dis.* 10, 91–96. doi:10.1016/S1045-1870(99)80039-9

Johnson, T. N., Rostami-Hodjegan, A., and Tucker, G. T. (2006). Prediction of the clearance of eleven drugs and associated variability in neonates, infants and children. *Clin. Pharmacokinet.* 45 (9), 931–956. doi:10.2165/00003088-200645090-00005

Jones, H. M., Gardner, I. B., Collard, W. T., Stanley, P. J., Oxley, P., Hosea, N. A., et al. (2011). Simulation of human intravenous and oral pharmacokinetics of 21 diverse compounds using physiologically based pharmacokinetic modelling. *Clin. Pharmacokinet.* 50 (5), 331–347. doi:10.2165/11539680-000000000-00000

Jones, H. M., Parrott, N., Jorga, K., and Lavé, T. (2006). A novel strategy for physiologically based predictions of human pharmacokinetics. *Clin. Pharmacokinet.* 45 (5), 511–542. doi:10.2165/00003088-200645050-00006

Lanao, J. M., Calvo, M. V., Mesa, J. A., Martín-Suárez, A., Carbajosa, M. T., Miguelez, F., et al. (2004). Pharmacokinetic basis for the use of extended interval dosage regimens of gentamicin in neonates. *J. Antimicrob. Chemother.* 54 (1), 193–198. doi:10.1093/jac/dkh261

Lin, W., Yan, J. H., Heimbach, T., and He, H. (2018). Pediatric physiologically based pharmacokinetic model development: Current status and challenges. *Curr. Pharmacol. Rep.* 4 (6), 491–501. doi:10.1007/s40495-018-0162-1

Martí, R., Rodríguez, T., Pitarch, J. L., Sarabia, D., and de Prada, C. Dynamic Optimization by automatic differentiation using EcosimPro y Casadi. 2014;12. https://www.ecosimpro.com/wp-content/uploads/2015/02/CEA_2014_dynamic_optimization_EcosimPro_CASADI.pdf

National institute for health and care excellence (NICE) (2021). "Neonatal infection: Antibiotics for prevention and treatment," in *Guidance NICE* (NICE). Overview | Internet[citado 1 de abril de 2022]. Disponible en: Available at: https://www.nice.org.uk/guidance/ng195 (Accessed April 20, 2021).

Neeli, H., Hanna, N., Abduljalil, K., Cusumano, J., and Taft, D. R. (2021). Application of physiologically based pharmacokinetic-pharmacodynamic modeling in preterm neonates to guide gentamicin dosing decisions and predict antibacterial effect. *J. Clin. Pharmacol.* 61 (10), 1356–1365. doi:10.1002/jcph.1890

Nielsen, E. I., Sandström, M., Honoré, P. H., Ewald, U., and Friberg, L. E. (2009). Developmental pharmacokinetics of gentamicin in preterm and term neonates: Population modelling of a prospective study. *Clin. Pharmacokinet.* 48 (4), 253–263. doi:10.2165/00003088-200948040-00003

O'Connor, K., Davies, M. W., Koorts, P., Cartwright, D. W., and Whitfield, K. (2021). Gentamicin dosing in neonates with normal renal function: Trough and peak levels. *Eur. J. Drug Metab. Pharmacokinet.* 46 (5), 677–684. doi:10.1007/s13318-021-00708-x

Prado-Velasco, M., Borobia, A., and Carcas-Sansuan, A. (2020). Predictive engines based on pharmacokinetics modelling for tacrolimus personalized dosage in paediatric renal transplant patients. *Sci. Rep.* 10 (1), 7542. doi:10.1038/s41598-020-64189-9

Prado-Velasco, M. (2016). Bridging the gap between open and specialized modelling tools in PBPK/PK/PD with physPK/EcosimPro modelling system: PBPK model of methotrexate and 6-mercaptopurine in humans with focus in reusability and multilevel modelling features. in Proceedings of the Conference: Annual Meeting of the Population Approach Group in Europe (PAGE) 2016, June 2016, Lisboa, Portugal, Internet[citado 17 de marzo de 2022]. Disponible en: Available at: https://www.page-meeting.org/?abstract=5769.

Puttrevu, S. K., Arora, S., Polak, S., and Patel, N. K. (2020). Physiologically based pharmacokinetic modeling of transdermal selegiline and its metabolites for the evaluation of disposition differences between healthy and special populations. *Pharmaceutics* 12 (10), 942. doi:10.3390/pharmaceutics12100942

Rao, S. C., Srinivasjois, R., Hagan, R., and Ahmed, M. (2011). One dose per day compared to multiple doses per day of gentamicin for treatment of suspected or proven sepsis in neonates. *Cochrane Database Syst. Rev.*, CD005091. doi:10.1002/14651858.CD005091.pub3

Reig-Lopez, J., Merino-Sanjuan, M., Mangas-Sanjuan, V., and Prado-Velasco, M. (2020). A multilevel object-oriented modelling methodology for physiologically-based pharmacokinetics (PBPK): Evaluation with a semi-mechanistic pharmacokinetic model. *Comput. Methods Programs Biomed.* 189, 105322. doi:10.1016/j.cmpb.2020.105322

Roa, L., and Prado, M. (2006). "Simulation languages," in *Wiley Encyclopedia of biomedical engineering* (New Jersey, United States: John Wiley & Sons). [Internet] [citado 16 de marzo de 2022]. Disponible en: Available at: https://onlinelibrary.wiley.com/doi/abs/10.1002/9780471740360.ebs1089 (Accessed April 14, 2006).

Rodrigues Matos, T., Prado-Velasco, M., Navarro, J. M., and Vallez, C. (2013). On a reusable and multilevel methodology for modeling and simulation of pharmacokinetic-physiological systems: A preliminary study. *Comput. Biol. Med.* 43 (10), 1512–1522. doi:10.1016/j.compbiomed.2013.07.025

Rubinstein, R. Y., and Kroese, D. P. (2016). *Simulation and the Monte Carlo method*. New Jersey, United States: John Wiley & Sons, 432.

Sulemanji, M., and Vakili, K. (2013). Neonatal renal physiology. *Semin. Pediatr. Surg.* 22 (4), 195–198. doi:10.1053/j.sempedsurg.2013.10.008

Thibault, N., Grenier, L., Simard, M., Bergeron, M. G., and Beauchamp, D. (1994). Attenuation by daptomycin of gentamicin-induced experimental nephrotoxicity. *Antimicrob. Agents Chemother.* 38 (5), 1027–1035. doi:10.1128/aac.38.5.1027

Vučićević, K., Rakonjac, Z., Janković, B., Kovačević, S. V., Miljković, B., and Prostran, M. (2014). Clinical pharmacokinetics in optimal gentamicin dosing regimen in neonates. *Open Med. (Wars).* 9 (3), 485–490. doi:10.2478/s11536-013-0298-7

Wicha, S. G., Märtson, A. G., Nielsen, E. I., Koch, B. C. P., Friberg, L. E., Alffenaar, J. W., et al. (2021). From therapeutic drug monitoring to model-informed precision dosing for antibiotics. *Clin. Pharmacol. Ther.* 109 (4), 928–941. doi:10.1002/cpt.2202

Wilhelm-Bals, A., Combescure, C., Chehade, H., Daali, Y., and Parvex, P. (2020). Variables of interest to predict glomerular filtration rate in preterm newborns in the first days of life. *Pediatr. Nephrol.* 35 (4), 703–712. doi:10.1007/s00467-019-04257-z

Zazo, H., Martín-Suárez, A., and Lanao, J. M. (2013). Evaluating amikacin dosage regimens in intensive care unit patients: A pharmacokinetic/pharmacodynamic analysis using Monte Carlo simulation. *Int. J. Antimicrob. Agents* 42 (2), 155–160. doi:10.1016/j.ijantimicag.2013.04.021

frontiers | Frontiers in Pharmacology

TYPE Original Research
PUBLISHED 17 October 2022
DOI 10.3389/fphar.2022.994665

OPEN ACCESS

EDITED BY
Zinnia P Parra-Guillen,
University of Navarra, Spain

REVIEWED BY
Tingjie Guo,
Leiden University, Netherlands
Eleni Karatza,
University of North Carolina at Chapel Hill, United States

*CORRESPONDENCE
Yuguan Wen,
wenyuguandede@163.com
Dewei Shang,
shang_dewei@163.com

†These authors contributed equally to this work.

SPECIALTY SECTION
This article was submitted to Translational Pharmacology, a section of the journal Frontiers in Pharmacology

RECEIVED 15 July 2022
ACCEPTED 03 October 2022
PUBLISHED 17 October 2022

CITATION
Zhu X, Zhang M, Wen Y and Shang D (2022), Machine learning advances the integration of covariates in population pharmacokinetic models: Valproic acid as an example.
Front. Pharmacol. 13:994665.
doi: 10.3389/fphar.2022.994665

Machine learning advances the integration of covariates in population pharmacokinetic models: Valproic acid as an example

Xiuqing Zhu[1,2†], Ming Zhang[1,2†], Yuguan Wen[1,2*] and Dewei Shang[1,2*]

[1]Department of Pharmacy, The Affiliated Brain Hospital of Guangzhou Medical University, Guangzhou, China, [2]Guangdong Engineering Technology Research Center for Translational Medicine of Mental Disorders, Guangzhou, China

Background and Aim: Many studies associated with the combination of machine learning (ML) and pharmacometrics have appeared in recent years. ML can be used as an initial step for fast screening of covariates in population pharmacokinetic (popPK) models. The present study aimed to integrate covariates derived from different popPK models using ML.

Methods: Two published popPK models of valproic acid (VPA) in Chinese epileptic patients were used, where the population parameters were influenced by some covariates. Based on the covariates and a one-compartment model that describes the pharmacokinetics of VPA, a dataset was constructed using Monte Carlo simulation, to develop an XGBoost model to estimate the steady-state concentrations (C_{ss}) of VPA. We utilized SHapley Additive exPlanation (SHAP) values to interpret the prediction model, and calculated estimates of VPA exposure in four assumed scenarios involving different combinations of *CYP2C19* genotypes and co-administered antiepileptic drugs. To develop an easy-to-use model in the clinic, we built a simplified model by using *CYP2C19* genotypes and some noninvasive clinical parameters, and omitting several features that were infrequently measured or whose clinically available values were inaccurate, and verified it on our independent external dataset.

Results: After data preprocessing, the finally generated combined dataset was divided into a derivation cohort and a validation cohort (8:2). The XGBoost model was developed in the derivation cohort and yielded excellent performance in the validation cohort with a mean absolute error of 2.4 mg/L, root-mean-squared error of 3.3 mg/L, mean relative error of 0%, and percentages within ±20% of actual values of 98.85%. The SHAP analysis revealed that daily dose, time, *CYP2C19*2* and/or **3* variants, albumin, body weight, single dose, and *CYP2C19*1*1* genotype were the top seven confounding factors influencing the C_{ss} of VPA. Under the simulated dosage regimen of 500 mg/bid, the VPA exposure in patients who had *CYP2C19*2* and/or **3* variants and no carbamazepine, phenytoin, or phenobarbital treatment,

was approximately 1.74-fold compared to those with *CYP2C19*1/*1* genotype and co-administered carbamazepine + phenytoin + phenobarbital. The feasibility of the simplified model was fully illustrated by its performance in our external dataset.

Conclusion: This study highlighted the bridging role of ML in big data and pharmacometrics, by integrating covariates derived from different popPK models.

KEYWORDS

machine learning, covariate, population pharmacokinetic, valproic acid, therapeutic drug monitoring, XGBoost, shap, Monte Carlo simulation

1 Introduction

Model-informed precision dosing (MIPD), an emerging, modern approach for individualizing drug therapy, involves various mathematical modeling methods (e.g., pharmacometrics) to integrate multidimensional patient-level data (Darwich et al., 2021). In particular, machine learning (ML), as a new promising data-driven tool in MIPD, has attracted considerable attention recently (Kluwe et al., 2021). For example, a previous study by us proved the feasibility of ML algorithms for predicting the dose-adjusted concentrations of lamotrigine for personalized dose adjustment (Zhu et al., 2021a). Although a lot of related work has been conducted to directly predict drug concentration or drug dose using ML-based strategies (Jovanović et al., 2015; Huang et al., 2021a; Zheng et al., 2021), the integration of model-informed and data-driven approaches is critical (Kluwe et al., 2021).

Fortunately, research collaborations among experts in different fields are advancing the integration of these approaches. Tang et al. (2021) reported a combined population pharmacokinetic (popPK) and ML approach, which had more accurate predictions of individual clearances of renally eliminated drugs in neonates and could be used to individualize the initial dosing regimen. Bououda et al. (2022) also suggested that ML could be used in combination with standard popPK approaches to increase confidence in the predictions of vancomycin exposure. Ogami et al. (2021) developed a model by applying artificial neural networks for predicting the time-series pharmacokinetics of cyclosporine A, which showed higher prediction accuracy than the conventional popPK model. Woillard et al. (2021a) developed an eXtreme gradient boosting (XGBoost) model allowing accurate estimation of the area under the curve (AUC) of tacrolimus based on only two or three concentrations with excellent performance, better than that of deterministic pharmacokinetic models with Bayesian estimation. However, the major limitation to developing such accurate ML models is the availability of large databases on drug concentration-time profiles, which can be solved by using simulation methods such as Monte Carlo (MC) simulation (Woillard et al., 2021b). MC simulation results in estimations of the possible outcomes by expanding the sample size, in light of probability distributions of the relevant parameters as inputs in a model (Zhu et al., 2021b). This technique has been used for popPK models to determine remedial dosing recommendations for non-adherent patients (Wang et al., 2020; Liu et al., 2021). Another study by Sibieude et al. (2021) applied ML as a fast initial covariate screening strategy and then utilized more traditional pharmacometrics approaches to build a final satisfying model to assess the clinical relevance of selected covariates and make predictions in different populations and scenarios. Thus, pharmacometrics can partner with ML to advance clinical data science by strongly decreasing computational costs for analyzing clinical datasets (Koch et al., 2020; Sibieude et al., 2021). Nevertheless, to the best of our knowledge, few studies have explored integrating covariates derived from different popPK models using ML. Our study, therefore, fills this gap.

Valproic acid (VPA) is a widely used drug for the treatment of bipolar disorder, particularly for acute mania, and multiple seizure types such as generalized tonic-clonic seizures (Hakami, 2021; Kishi et al., 2022). As a narrow therapeutic index drug, it is characterized by high pharmacokinetic variability (Johannessen and Johannessen, 2003). Various popPK models of VPA in Chinese patients have been constructed in recent years, to explore personalized VPA dosing and its variability patterns (Xu et al., 2018; Zang et al., 2022a). However, the covariates that influence the VPA pharmacokinetics varied between these models. Therefore, it is necessary to investigate the comprehensive impacts of these potential factors on VPA pharmacokinetics using our established XGBoost model.

The XGBoost algorithm, one of the best-known ensemble techniques, was originally developed by Chen and Guestrin (2016). It is based on the basic idea of boosting and serves as an extension to gradient boosted decision trees (GBDT), where the decision trees are built serially and each tree tries to minimize the error made by the previous one (Yaman and Subasi, 2019). Several innovations have been made to the XGBoost algorithm, including parallel tree boosting and approximate greedy search (Chen and Guestrin, 2016). Therefore, it can simultaneously reduce the model bias and variance (Cao et al., 2010). This state-

of-the-art ML algorithm has been gradually applied to deal with predictions of therapeutic drug monitoring (TDM) values, drug dose, and drug exposure to specific medications (Huang et al., 2021a; Guo et al., 2021; Bououda et al., 2022). The details of the differences between the XGBoost and GBDT algorithms are given in the section titled "An introduction to XGBoost algorithm."

In this study, our objective was to integrate covariates derived from different popPK models of VPA using the XGBoost algorithm, interpret our proposed model based on the SHapley Additive exPlanations (SHAP) analysis (Lundberg and Lee, 2017), and evaluate the combined effects across multiple covariates (i.e., *CYP2C19* genotypes and co-administered enzyme-inducing antiepileptic drugs) in terms of VPA exposure by assuming four scenarios. Furthermore, for easy clinical use, we built a simplified model by using only *CYP2C19* genotypes and some noninvasive clinical parameters, and omitting several features (similar to the practices in the ablation experiment) that were infrequently measured during TDM [e.g., albumin (ALB)], or whose clinically available values were inaccurate [e.g., blood sampling time (t)]. We evaluated this simplified model on our independent external dataset. An easy-to-use web application based on the simplified model was then designed as a real-time tool to support clinical decisions for MIPD.

2 Materials and methods

2.1 Data source and dataset construction

Generally, the predictability of different popPK models when extrapolated to other clinical centers might remain to be compared (Lv et al., 2021). An external validation study based on published VPA models by Zang et al. (2022b) suggested that the absence of children, Asian ethnicity, one-compartment models, and inclusion of the covariates body weight (BW) and VPA dosage, were the most important factors contributing to good performance in their Chinese dataset. This indicates that the selection of published popPK models of VPA is vital in our study, and priority may be given to these models that include the abovementioned factors. Moreover, glucuronidation and β-oxidation in the mitochondria are the major routes of VPA metabolism in humans (Ghodke-Puranik et al., 2013), and cytochrome P450 2C9 (CYP2C9) is the most significant cytochrome P450 (CYP) enzyme that mediates the oxidation of VPA considered a minor route of its metabolism (Ho et al., 2003; Ghodke-Puranik et al., 2013). Nevertheless, cytochrome P450 2C19 (CYP2C19) also participates in VPA metabolism (Hiemke et al., 2018; Song et al., 2022). Multiple studies reported that *CYP2C19* polymorphisms/genotypes significantly influenced the pharmacokinetic variability of VPA in Chinese Han subjects (Jiang et al., 2009; Guo et al., 2020; Wang et al., 2021). Given the limitations of the genetic test items in our hospital (no *CYP2C9* genotype testing), the reported references about the impact of *CYP2C19* polymorphisms on VPA, and the goal of validation of the simplified XGBoost model using our external dataset, we selected two previously published popPK models of VPA in Chinese epileptic patients for simulations [i.e., Model-A including the covariate *CYP2C19* genotypes (Guo et al., 2020) and Model-B including the covariates BW and daily dose of VPA (Daily Dose) (Lin et al., 2015)], both of which involved one-compartment models and Chinese epileptic patients aged 14 years and above. The detailed descriptions of the two studies are listed in Table 1.

A general overview of our implementation of pharmacometric models to ML models in this study is shown in Figure 1. The population parameters, namely, the rate of absorption (k_a), the apparent volume of distribution (V_d), and the total serum clearance (CL), of Model-A and Model-B, were used to simulate the individual steady-state concentrations (C_{ss}) of VPA, whose concentration-time profiles have been described by a one-compartment model, described as follows:

$$C_{ss}\left(k_{a_j}, t_j, V_{d_j}, CL_j, X_{0j}, \tau_j\right) = \frac{k_{a_j} \cdot F \cdot X_{0j}}{V_{d_j} \cdot k_{a_j} - CL_j} \cdot \left(\frac{e^{-\frac{CL_j \cdot t_j}{V_{d_j}}}}{1 - e^{-\frac{CL_j \cdot \tau_j}{V_{d_j}}}} - \frac{e^{-k_{a_j} \cdot t_j}}{1 - e^{-k_{a_j} \cdot \tau_j}} \right)$$

where $C_{ss}\left(k_{a_j}, t_j, V_{d_j}, CL_j, X_{0j}, \tau_j\right)$, k_{a_j}, V_{d_j}, CL_j, X_{0j}, and τ_j are the C_{ss} of VPA (mg/L) at the blood sampling time t_j (h), the k_a (h^{-1}), the V_d (L), the CL (L/h), a single dose (mg), and the dosing interval (h) for an individual j, respectively, F is the absolute bioavailability (%).

To determine a clear relationship between the features and the simulated outcomes without noise, V_{d_j} and CL_j are calculated using the following formulas without considering their inter-individual random effects (Mould and Upton, 2013):

$$V_{d_j} = V_{d_{pop}}$$
$$CL_j = CL_{pop}$$

where $V_{d_{pop}}$ and CL_{pop} represent the typical population values of V_d and CL, respectively.

The parameter k_a is fixed at 2.38 h^{-1} and 1.90 h^{-1} in Model-A and Model-B, respectively; that is to say, k_{a_j} equals k_a. F is assumed to be one because the absolute systemic availability of VPA was found to be complete for all commonly used formulations (Gugler and von Unruh, 1980; Romoli et al., 2019). For Model-A, the covariates acting on $V_{d_{pop}}$ included gender, those acting on CL_{pop} included *CYP2C19* genotypes and ALB, while the covariates included in Model-B were BW, which

TABLE 1 Descriptions of the two studies about Model-A and Model-B.

Items	Model-A (Guo et al., 2020)	Model-B (Lin et al., 2015)
Study design	A prospective study	A prospective study
Subjects	Chinese patients with seizures aged ≥18 years old in General Hospital of Taiyuan Iron and Steel (Group) Corporation (TISCO)	Chinese epileptic patients with normal liver and renal functions and 14 years of age or older in Huashan Hospital (Shanghai), Changzheng Hospital (Shanghai), Children's Hospital (Shanghai), Tiantan Hospital (Beijing), and Brain Hospital (Nanjing)
Sample collection	Steady-state VPA serum concentration data were collected from January to December 2018	VPA serum samples at a steady state before the morning dose were collected between 1 October 1998, and 31 October 2003
Model description	One-compartment model	One-compartment model
Number of patients	60	199
Number of measurements	98	247
Age (years)	60 ± 11.8 (22–88)	26.6 ± 11.7 (14–66)
Gender (male/female)	44/16	114/85
Daily dose of VPA (mg)	500 (200–1,200)	884.5 ± 317.7 (250–1800)
VPA concentration (mg/L)	<150	61.9 ± 26.8 (3.2–140.3)
Formulation of VPA	Standard VPA dosing regimens (i.e., oral: 500 mg [immediate release tablets/solutions], twice per day; intravenous: 400 mg, twice per day)	VPA was prescribed 1–4 times a day and was administered orally in the forms of sustained-release tablets (Depakine, Sanofi-Aventis Pharmaceutical Ltd., Hangzhou, China) or conventional tablets (Hunan Xiangzhong Pharmaceutical Ltd., China)
Concomitant medications	Other medications that affect VPA concentrations were excluded (e.g., phenobarbital, carbamazepine, meropenem, imipenem, etc.)	Carbamazepine, phenytoin, phenobarbital, topiramate, and clonazepam

influences both $V_{d_{pop}}$ and CL_{pop}, the Daily Dose, and cotherapy with enzyme-inducing antiepileptic drugs [including carbamazepine (CBZ), phenytoin (PHT), and phenobarbital (PB)] that influence CL_{pop}. The related parameters in these models for the dataset simulation process are summarized in Table 2.

The constructed dataset combined two simulated datasets, i.e., Dataset-A and Dataset-B, derived from Model-A and Model-B, respectively. For Dataset-A, four scenarios (i.e., *CYP2C19*1/*1* + male, *CYP2C19*1/*1* + female, *CYP2C19*1/*2 or *1/*3 or *2/*3 or *2/*2 or *3/*3* + male, and *CYP2C19*1/*2 or *1/*3 or *2/*3 or *2/*2 or *3/*3* + female) were considered for simulating overall 20,000 virtual patients (in equal proportion, namely, simulating 5,000 virtual patients for each scenario). For each scenario, BW and ALB were simulated using normal distributions with mean ± standard deviation (SD) of (66.5 ± 12.1) kg and (38.9 ± 6.4) g/L, respectively, obtained from Model-A (see Table 2). For Dataset-B, a total of seven scenarios for different types of concomitant medication were simulated, including combinations with CBZ, PHT, PB, CBZ + PHT, CBZ + PB, PHT + PB, and CBZ + PHT + PB, and for each type, 2,000 virtual patients were generated, whose BW (kg) followed a normal distribution with 60.2 mean and an SD of 12.5, taken from Model-B (see Table 2). Dosing regimens were presumed to be the same in both models, as follows:

$$X_{0j} \in \{125, 250, 300, 350, 400, 450, 500, 550, 600, 650, 700, 750, 800, 850, 900\}\,(\text{mg})$$

$$\tau_j \in \{6, 8, 12, 24\}\,(\text{h})$$

where X_{0j} and τ_j were sampled at random with the probability equal to 1/15 and 1/4, respectively. t_j was assumed to have a uniform distribution of values between 0 and τ_j h.

Subsequently, MC simulations resulted in 20,000 and 14,000 individual values of C_{ss} for Dataset-A and Dataset-B, respectively. Notably, types of concomitant medication (i.e., co-administered CBZ/PHT/PB) as a new feature, the values of which were "None," was added in the generated Dataset-A because drugs that affect VPA concentrations had been excluded in Model-A; similarly, *CYP2C19* genotypes, as a new feature with values "Unknown," were added in the generated Dataset-B owing to the unknown distributions of the values of this covariate (i.e., the proportions of the genotypes *CYP2C19*1/*1*, *CYP2C19*1/*2*, *CYP2C19*1/*3*, etc.). This was also not included in Model-B. However, gender and ALB, both of which were not covariates for Model-B, were set to null as new features in the generated Dataset-B due to their missing value imputation. To obtain less noise, filters were applied to both models to remove C_{ss} higher than 150 mg/L to obtain a range of values compatible with observed data reported in the original articles (Woillard et al., 2021b), resulting in 14,509 and 11,664 C_{ss} values retained in the finally generated Dataset-A and Dataset-B, respectively. Moreover, to ensure high-quality data containing as much useful information as possible to facilitate the

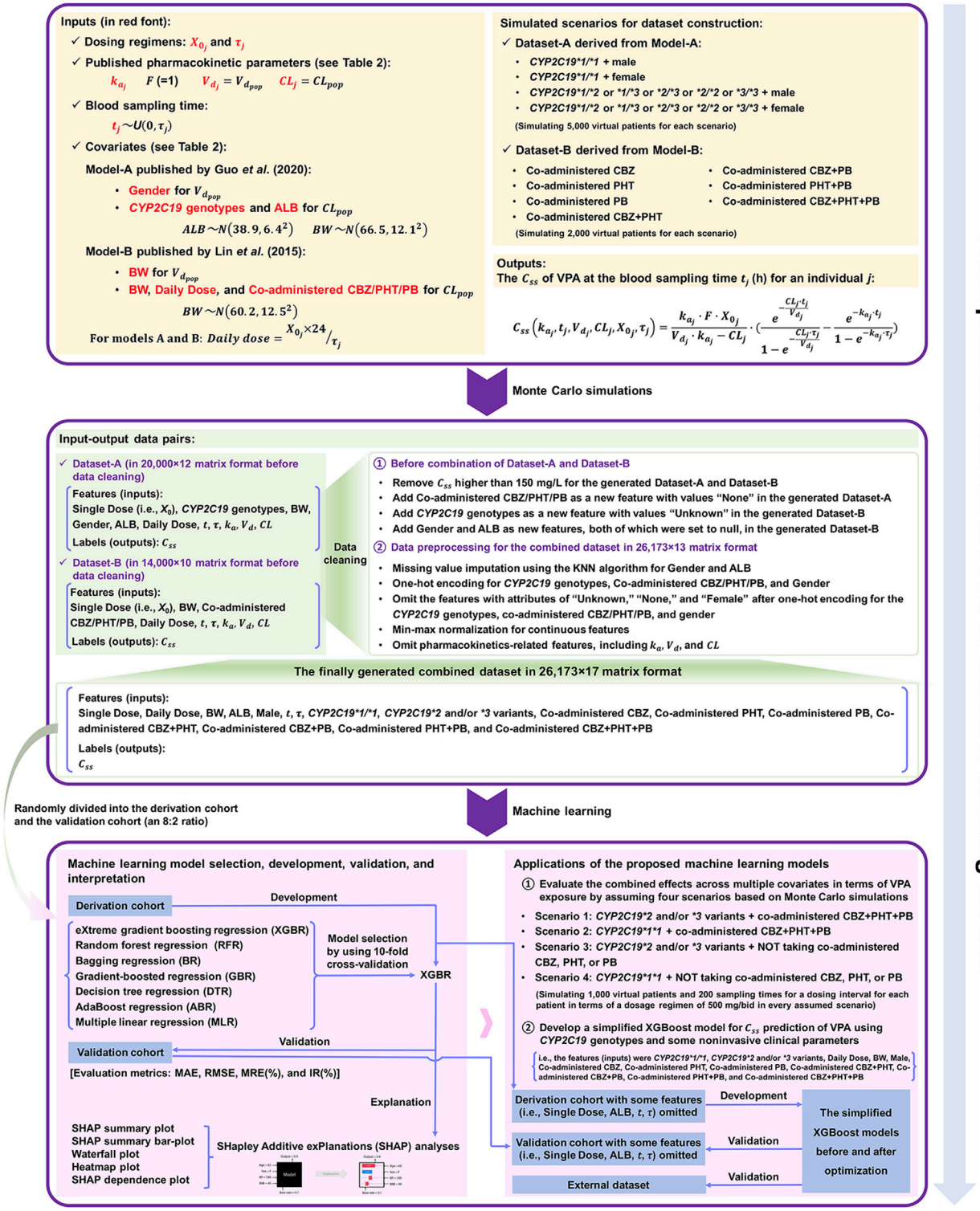

FIGURE 1
The workflow from pharmacometrics models to machine learning (ML) models mainly involves three parts: 1) data acquirement from published pharmacokinetic studies, 2) the construction of the combined dataset via Monte Carlo (MC) simulation and a series of data cleaning process, and 3) ML-based predictive modelling based on the finally generated combined dataset.

TABLE 2 Related parameters in the Model-A and Model-B for the dataset simulation process (in accordance with the original articles).

Models	Pharmacokinetic parameters			Covariates	
	k_a (h^{-1})	$V_{d_{pop}}$ (L)	CL_{pop} (L/h)	BW (kg)	ALB (g/L)
Model-A Guo et al. (2020)	2.38	22.15 (if gender = female) $22.15 \times e^{0.78}$ (if gender = male)	$0.64 \times (ALB/38.7)^{-1.06}$ (if *CYP2C19*1/*1*) $0.64 \times (ALB/38.7)^{-1.06} \times e^{-0.45}$ (if *CYP2C19*1/*2 or *1/*3 or *2/*3 or *2/*2 or *3/*3*)	66.5 ± 12.1	38.9 ± 6.4
Model-B Lin et al. (2015)	1.90	$0.14 \times BW$	$0.1 \times (BW/60)^{0.7} \times Daily\_Dose^{0.2} \times 1.36$ (if cotherapy with *CBZ*) $\times 1.25$ (if cotherapy with *PHT*) $\times 1.11$ (if cotherapy with *PB*)	60.2 ± 12.5	Not available

Note: Model-A had excluded other drugs that affect VPA concentrations (e.g., CBZ, PHT, or PB).

training and test of the ML models, for the combined dataset in 26,173 × 13 matrix format [i.e., 26,173 simulated input–output data pairs (Dataset-A: Dataset-B = 14,509: 11,664)], we used the k-nearest neighbor imputation for gender and ALB. Both had 44.57% (11,664/26,173 × 100%) missing data (Beretta and Santaniello, 2016). We used one-hot encoding for categorical variables (Lopez-Arevalo et al., 2020), and min-max normalization for continuous feature variables, and then omitted the features with attributes of "Unknown," "None," and "Female" after one-hot encoding for the *CYP2C19* genotypes, co-administered CBZ/PHT/PB, and gender (considering the increased dimensionality of the dataset and the issue of collinearity because one of the categories could be completely generated from the others). We also omitted the pharmacokinetics-related features that are not easily available in the clinic (including k_a, V_d, and CL). The combined dataset was finally generated after data preprocessing, including 26,173 C_{ss} values and 16 features (i.e., Single Dose, BW, ALB, t, τ, Daily Dose, *CYP2C19*1/*1*, *CYP2C19*2* and/or **3* variants (i.e., *CYP2C19*1/*2 or *1/*3 or *2/*2 or *2/*3 or *3/*3*), Male, Co-administered CBZ, Co-administered PHT, Co-administered PB, Co-administered CBZ + PHT, Co-administered CBZ + PB, Co-administered PHT + PB, and Co-administered CBZ + PHT + PB). Among these 16 features, the values of the categorical variables were one (=yes) or zero (=no). The process of dataset construction is shown in Figure 1.

2.2 An introduction to the XGBoost algorithm

XGBoost, a gradient-boosting framework, was developed by a team led by Chen Tianqi at the University of Washington (Chen and Guestrin, 2016). It is an effective tool for tackling classification and regression problems using tabular data. Compared with GBDT, XGBoost uses a series of optimizations (Li et al., 2019; Chen et al., 2020). An important aspect is the application of an additional regularization term to the loss function to prevent overfitting. The objective function (L) of XGBoost is calculated as:

$$L = \sum_i l(\hat{y}_i, y_i) + \sum_k \Omega(f_k)$$

where l is the loss function representing the error between the actual values (y_i) and the predicted values ($\hat{y}_i$), and $\Omega(f_k)$ is the regularized term, defined as:

$$\Omega(f_k) = \gamma T + \frac{1}{2}\lambda\|\omega\|^2$$

where T and ω represent the number of leaves in the tree and the corresponding weight of different leaves of each tree, respectively, and γ and λ are the regularized parameters that penalize T and ω, respectively.

Moreover, the second-order Taylor expansion of L can more efficiently fit the error. For the t-th iteration, $L^{(t)}$ is:

$$L^{(t)} \simeq \sum_i \left[l\left(y_i, \hat{y}_i^{(t-1)} + g_i f_t(x_i) + \frac{1}{2} h_i f_t^2(x_i) \right) \right] + \Omega(f_t)$$

where $g_i = \partial_{\hat{y}_i^{(t-1)}} l(y_i, \hat{y}_i^{(t-1)})$ and $h_i = \partial^2_{\hat{y}_i^{(t-1)}} l(y_i, \hat{y}_i^{(t-1)})$ are the first- and second-order gradients, respectively.

Subsequently, other calculations were used to determine the optimal split node by using the information gain of L. This is another algorithmic innovation. *Gain* denotes the gain for each split of the tree. It is used to evaluate the candidate splits, and is given by:

$$Gain = \frac{1}{2} \left[\frac{\left(\sum_{i \in I_L} g_i\right)^2}{\sum_{i \in I_L} h_i + \lambda} + \frac{\left(\sum_{i \in I_R} g_i\right)^2}{\sum_{i \in I_R} h_i + \lambda} - \frac{\left(\sum_{i \in I} g_i\right)^2}{\sum_{i \in I} h_i + \lambda} \right] - \gamma$$

where I_L and I_R represent the instance sets of the left and right nodes after the split, respectively, and $I = I_L \cup I_R$.

XGBoost has a multitude of hyperparameters. The optimal choice of the following key hyperparameters may yield the best performance by the model:

1) n_estimators: This represents the total number of trees. Too small or too large a value of *n_estimators* may lead to underfitting or overfitting, respectively.
2) max_depth: It is the maximum depth of the tree. Increasing *max_depth* will make the model more complex and lends it a stronger fitting ability. However, a large value is likely to cause it to overfit the data.
3) min_child_weight: It represents the minimum number of samples that a node can represent in order to be split further. We can increase this value to reduce overfitting.
4) gamma: It is a regularization parameter that denotes the minimum reduction in loss at every split. The larger *gamma* is, the more conservative the algorithm is, the smaller is the number of leaves that the tree has, and therefore, the lower is the complexity of the model.
5) colsample_bytree: It denotes the subsample ratio of columns (i.e., the rate of feature sampling) when constructing each tree, and controls overfitting.
6) subsample: It is the subsample ratio of the training instances. Increasing this value makes the algorithm more conservative and the model more likely to underfit.
7) learning_rate: It is the shrinkage in step size used in updates to prevent overfitting. Reducing the weight of each step makes the model more robust.

2.3 Model development and evaluation

The finally generated combined dataset in 26,173 × 17 matrix format was randomly divided into two parts, the derivation cohort for model selection and the development of the XGBoost model, and the validation cohort for its evaluation (an 8: 2 ratio). Before using the XGBoost algorithm, 10-fold cross-validation was applied to the derivation cohort to assess the performance of the XGBoost model, and other tree-based and non-tree-based models, including random forest regression (RFR), bagging regression (BR), gradient-boosted regression (GBR), decision tree regression (DTR), AdaBoost regression (ABR), and multiple linear regression (MLR). We used their default settings for the hyperparameters.

K-fold cross-validation involves 1) splitting the derivation cohort into K folds, 2) starting by using K-1 folds as the training set and the remaining one fold as the test set, 3) training the model on the training set and testing it on the test set, 4) saving the test score, 5) repeating steps 2–4 for K iterations, and 6) comparing the performance of the models by using the average cross-validation score [mean absolute error (MAE), used as the evaluation metric in this study] in the test sets across all K folds (Kalagotla et al., 2021).

The metrics used to evaluate the performance of the developed XGBoost model on the validation cohort were the MAE, root-mean-squared error (RMSE), mean relative error (MRE), and ideal rate (IR, i.e., percentages within ±20% of actual values), defined as follows:

$$MAE = \frac{\sum_{i=1}^{N} \left(\hat{y}_i - y_i \right)}{N}$$

$$RMSE = \sqrt{\frac{\sum_{i=1}^{N} \left(\hat{y}_i - y_i \right)^2}{N}}$$

$$MRE(\%) = \frac{\sum_{i=1}^{N} \left(\hat{y}_i - y_i \right) / y_i}{N} \times 100\%$$

$$IR(\%) = \frac{N_{predicted\ values\ within\ \pm 20\%\ of\ actual\ vaules}}{N_{total\ actual\ vaules}} \times 100\%$$

where $\hat{y}_i$ and y_i denote the predicted and actual values, respectively.

2.4 Model interpretation

The SHAP analysis was utilized to provide interpretability to the proposed XGBoost model, which is generally criticized as a 'black-box' model due to its complexity. The main advantages of SHAP inspired by cooperative game theory (Štrumbelj and Kononenko, 2014), are that it is model agnostic, easy to use, and straightforward to interpret the feature contributions at global and local levels, as well as the interactions among these features (Li et al., 2020). The contribution of each feature on the model output associated with each predicted sample is allocated according to their marginal contribution (Shapley, 1953), and can be determined by the Shapley value, defined via the following formula (Yang et al., 2021):

$$\phi_i(\nu) = \sum_{S \subseteq \{1,\ldots,p\} \setminus \{i\}} \frac{|S|!\,(p - |S| - 1)!}{p!} \left(\nu(S \cup \{i\}) - \nu(S)\right)$$

where $\phi_i(\nu)$ is the contribution of feature i, p is the number of features, S is a subset of the features used in the model, and $\nu(S \cup \{i\}) - \nu(S)$ represents the influence of feature i on the improvement of the result (i.e., marginal contribution).

2.5 Applications of the integration of pharmacometrics and ML models

2.5.1 Impacts of the integrated covariates on VPA exposure

To assess the comprehensive impacts of different popPK models-derived covariates–*CYP2C19* genotypes and co-administered enzyme-inducing antiepileptic drugs–on VPA exposure, we used MC simulations to simulate 1,000 virtual patients and 200 sampling times for a dosing interval (i.e., t, uniformly distributed between 0 and 12 h) for each patient in terms of a dosage regimen of 500 mg/bid in every assumed scenario. A total of 16 predictors [Single Dose (set to 500 mg), BW, ALB, t, τ (set to 12 h), Daily Dose (set to 1,000 mg), *CYP2C19*1/*1*, *CYP2C19*2* and/or **3* variants, Male, Co-administered CBZ, Co-administered PHT, Co-administered PB, Co-administered CBZ + PHT, Co-administered CBZ + PB, Co-administered PHT + PB, and Co-administered CBZ + PHT + PB] were simulated based on the proposed XGBoost model. Among them, the BW and ALB were simulated as normal distributions, with mean ± SD described in the finally generated combined dataset (see Table 3), and the male and female patients were simulated with equal probabilities (i.e., the probability of Male = 1 was 0.5).

A total of four scenarios were considered:

Scenario 1: Patients with *CYP2C19*2* and/or **3* variants (feature value = 1) and taking co-administered CBZ + PHT + PB (feature value = 1).

Scenario 2: Patients with *CYP2C19*1*1* genotype (feature value = 1) and taking co-administered CBZ + PHT + PB (feature value = 1).

Scenario 3: Patients with *CYP2C19*2* and/or **3* variants (feature value = 1) and *NOT* taking co-administered CBZ, PHT, or PB (feature values of all co-administered drug predictors = 0).

Scenario 4: Patients with *CYP2C19*1*1* genotype (feature value = 1) and *NOT* taking co-administered CBZ, PHT, or PB (feature values of all co-administered drug predictors = 0).

All predictors except for t were considered to be constant for each virtual patient. Therefore, these static values were replicated across t, resulting in tabular data in which each scenario had 1,000 × 200 samples for predictions of C_{ss} by using our proposed XGBoost model. The concentration-time profiles were then plotted for all scenarios using the two visualization libraries matplotlib and seaborn. The VPA exposures [i.e., $AUC_{0\to12h}$ (mg· h/L)] in the aforementioned scenarios were obtained using the trapezoidal rule by dividing the curve's total area into small trapezoids rather than dividing it into small rectangles (Woillard et al., 2021b), and the average C_{ss} ($\bar{C}_{ss}$) (mg/L) was calculated as follows:

$$\bar{C}_{ss} = AUC_{0\to12h}/12$$

Both $AUC_{0\to12h}$ and $\bar{C}_{ss}$ were calculated in Python by using the numpy package.

TABLE 3 Simulated patient characteristics in the finally generated combined dataset (N = 26,173).

Continuous data	Value [(mean ± SD) or median (min–max)]	Categorical data	Distribution [n (%)]
C_{ss} (mg/L)	73.7 ± 37.2	Male	7,237 (27.65%)
BW (kg)	64.3 ± 12.4	*CYP2C19*1/*1*	8,358 (31.93%)
ALB (g/L)	37.9 ± 5.6	*CYP2C19*2* and/or **3* variants	6,151 (23.50%)
Daily Dose (mg)	900 (125–3,600)	Co-administered CBZ	1,636 (6.25%)
Single Dose (mg)	450 (125–900)	Co-administered PHT	1,529 (5.84%)
t (h)	5.57 (0–24)	Co-administered PB	1,421 (5.43%)
τ (h)	12 (6–24)	Co-administered CBZ + PHT	1,854 (7.08%)
		Co-administered CBZ + PB	1,735 (6.63%)
		Co-administered PHT + PB	1,652 (6.31%)
		Co-administered CBZ + PHT + PB	1,837 (7.02%)

Note: Css denotes the steady-state concentrations of VPA, t denotes the blood sampling time, and τ denotes the dosing interval.

TABLE 4 Descriptions of our external dataset.

Items	Value
Number of patients	56
Total number of measured steady-state VPA concentrations	105
Average TDM measurements per patient	1.88
Age (years, mean ± SD)	34.48 ± 13.10
BW (kg, mean ± SD)	63.82 ± 11.48
Gender	
Male	42
Female	14
The number of patients with the *CYP2C19* genotype of	
*CYP2C19*1/*1*	22
*CYP2C19*1/*2*	26
*CYP2C19*1/*3*	4
*CYP2C19*2/*2*	1
*CYP2C19*2/*3*	3
Daily dose [mg, median (min–max)]	1,000 (250–2000)
C_{ss} (mg/L)	87.3 ± 22.8

Note: All patients did not take co-administered CBZ/PHT/PB.

2.5.2 Model simplification to develop an easy-to-use MIPD tool

In clinical practice, a balance needs to be struck between the performance of the ML model and its ease of use. The ideal ML models are those that have as few predictors as possible (and perhaps should be easily available in the clinic) while delivering high performance. In this study, we aimed to build a simplified XGBoost model to develop an easy-to-use MIPD tool. Considering that the values of some predictors were missing owing to infrequent measurements during TDM (e.g., ALB) or were inaccurate clinical data (e.g., inappropriate sampling time in the TDM practice and irregular single doses or dosing intervals in the prescriptions) (Jakobsen et al., 2017; Firman et al., 2021), we built a simplified model by omitting these types of features (i.e., Single Dose, ALB, t, τ) in the final, combined dataset. We developed an easy-to-use model in the clinic by using only *CYP2C19* genotypes and some noninvasive clinical parameters as predictors, and observed the influence of the omitted predictors on the performance of the proposed XGBoost model. Finally, we optimized the hyperparameters via the sklearn's own grid search approach using the evaluation metric of MAE and tenfold cross-validation (Radzi et al., 2021), and verified this simplified model after optimization in our independent external dataset, which consisted of 105 input-output data pairs retrospectively collected from our routine TDM practice according to guidelines of the Ethics Committee of the Affiliated Brain Hospital of Guangzhou Medical University approval ([2021] NO.027). The inputs to the external dataset were the same as those of the finally generated combined dataset with Single Dose, ALB, t, and τ omitted. They consisted of *CYP2C19*1/*1*, *CYP2C19*2* and/or **3* variants, Daily Dose, BW, Male, Co-administered CBZ, Co-administered PHT, Co-administered PB, Co-administered CBZ + PHT, Co-administered CBZ + PB, Co-administered PHT + PB, and Co-administered CBZ + PHT + *p*B. The external dataset is described in Table 4. We designed an easy-to-use web application based on the simplified optimum XGBoost model to realize real-time estimations of values of C_{ss} of the VPA by automatically crawling information on the model inputs from the electronic health record (EHR) system.

2.6 Implementation

All the analyses were performed in Python using the Jupyter notebook. Libraries sklearn, XGBoost, pandas, numpy, scipy, matplotlib, seaborn, palettable, and shap, were used for implementation.

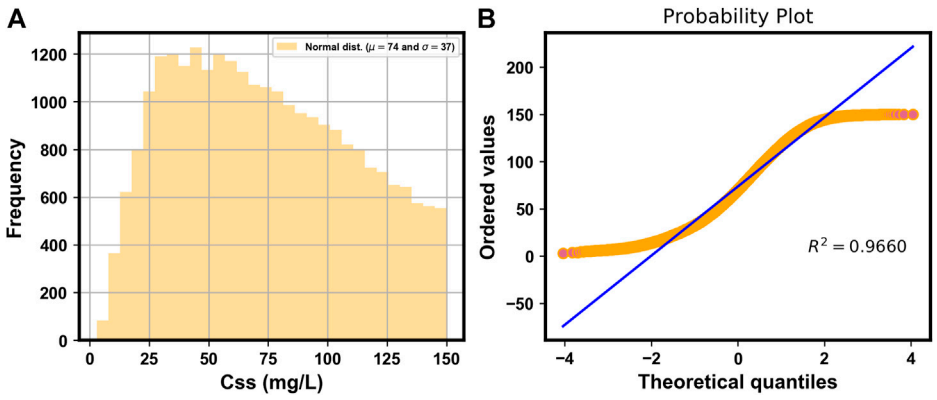

FIGURE 2
Histogram **(A)** and probability plot **(B)** of the simulated C_{ss} of VPA.

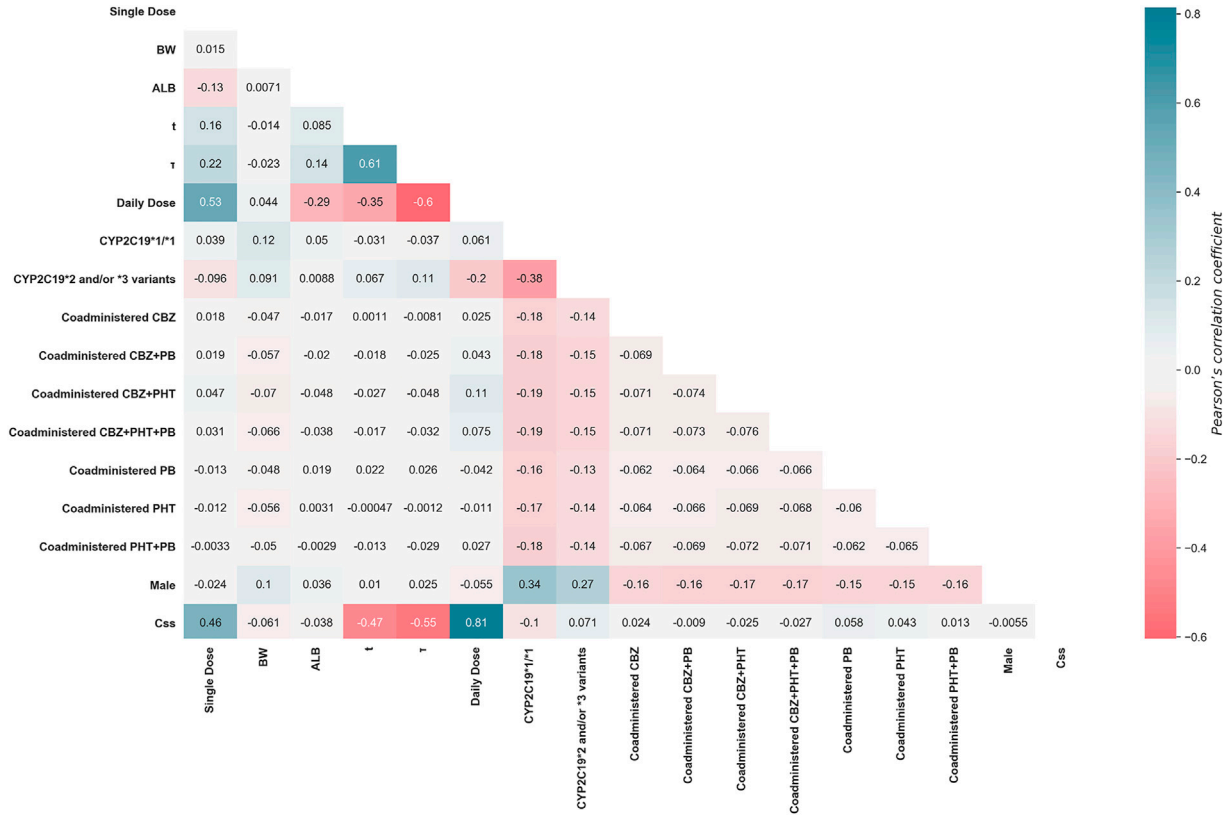

FIGURE 3
Heat map of Pearson's correlations between C_{ss} of VPA and features.

3 Results

3.1 Simulation and data

Figure 2A shows the histogram of the simulated C_{ss} of VPA, whose probability plot indicated a normal distribution (R^2 = 0.9660) (Figure 2B). Figure 3 shows a heat map of the Pearson's correlation coefficients between the C_{ss} of VPA and features, indicating that "Daily Dose" and "τ" were the most important positive and negative predictors correlated with C_{ss}, respectively, and no obvious multi-collinear relationships were observed between the features. The characteristics of the simulated patients in the finally generated combined dataset are shown in Table 3.

3.2 XGBoost model

Table 5 shows the overall comparison of the regression models in the derivation cohort. The lowest average MAE value of the XGBoost model in the test sets indicated that it was superior to the other tree-based and non-tree-based models considered. As is presented in Table 6, the proposed XGBoost model delivered excellent performance on the validation cohort, illustrated by an MAE of 2.4 mg/L, RMSE of 3.3 mg/L, MRE of 0%, and IR of 98.85%, respectively.

3.3 SHAP analysis

Figure 4A shows the SHAP summary plot that orders all predictors according to their feature importance to detect the features which have high contributions to the C_{ss} of VPA. Among these features, Daily Dose was ranked first, followed by *t*, *CYP2C19*2* and/or **3* variants, ALB, BW, Single Dose, and *CYP2C19*1/*1*. Moreover, higher SHAP values of a feature indicated higher C_{ss} of VPA, and *vice versa*. The colored dots determined the direction of influence, i.e., the higher the input value of a feature, the higher the C_{ss} of VPA, when red dots were in the positive range of SHAP values. Likewise, Figure 4B shows the hierarchical feature clustering of the SHAP bar plot that sorts the feature importance values of each cluster and subcluster to show the most important features at the top. The global importance of the predictors was calculated according to the

TABLE 5 The mean absolute error (MAE) at 95% confidence interval (CI) for the prediction of the value of C_{ss} of VPA in the derivation cohort for the XGBoost and other regression models.

Models	Training set		Test set	
	MAE (mg/L)	(+/-) 95% CI of MAE (mg/L)	MAE (mg/L)	(+/-) 95% CI of MAE (mg/L)
XGBR	1.7	0.1	2.5	0.1
RFR	1.2	0	3.1	0.2
BR	1.5	0	3.5	0.2
DTR	0	0	5.1	0.3
GBR	6.0	0.1	6.2	0.2
MLR	10.2	0	10.2	0.4
ABR	14.1	0.3	14.2	0.7

TABLE 6 Comparisons of the performance of the proposed models on the validation cohort and the independent external dataset.

Datasets	Models	Descriptions of models		Evaluation metrics			
		Selected features	Hyperparameters	MAE (mg/L)	RMSE (mg/L)	MRE (%)	IR (%)
Validation cohort (N = 5,235)	XGBoost model	Single Dose, BW, ALB, *t*, *τ*, Daily Dose, *CYP2C19*1/*1*, *CYP2C19*2* and/or **3* variants, Male, Co-administered CBZ, Co-administered PHT, Co-administered PB, Co-administered CBZ + PHT, Co-administered CBZ + PB, Co-administered PHT + PB, and Co-administered CBZ + PHT + PB	Default settings	2.4	3.3	0	98.85
	Simplified XGBoost model	BW, Daily Dose, *CYP2C19*1/*1*, *CYP2C19*2* and/or **3* variants, Male, Co-administered CBZ, Co-administered PHT, Co-administered PB, Co-administered CBZ + PHT, Co-administered CBZ + PB, Co-administered PHT + PB, and Co-administered CBZ + PHT + PB	Default settings	11.2	14.7	5	68.00
	Simplified XGBoost model after optimization	BW, Daily Dose, *CYP2C19*1/*1*, *CYP2C19*2* and/or **3* variants, Male, Co-administered CBZ, Co-administered PHT, Co-administered PB, Co-administered CBZ + PHT, Co-administered CBZ + PB, Co-administered PHT + PB, and Co-administered CBZ + PHT + PB	n_estimators: 20, max_depth: 6, min_child_weight: 5, gamma: 0, colsample_bytree: 1.0, subsample: 1.0, learning_rate: 0.3	11.0	14.4	5	69.11
External dataset (N = 105)	Simplified XGBoost model after optimization	BW, Daily Dose, *CYP2C19*1/*1*, *CYP2C19*2* and/or **3* variants, Male, Co-administered CBZ, Co-administered PHT, Co-administered PB, Co-administered CBZ + PHT, Co-administered CBZ + PB, Co-administered PHT + PB, and Co-administered CBZ + PHT + PB	n_estimators: 20, max_depth: 6, min_child_weight: 5, gamma: 0, colsample_bytree: 1.0, subsample: 1.0, learning_rate: 0.3	16.5	20.1	13	60.00

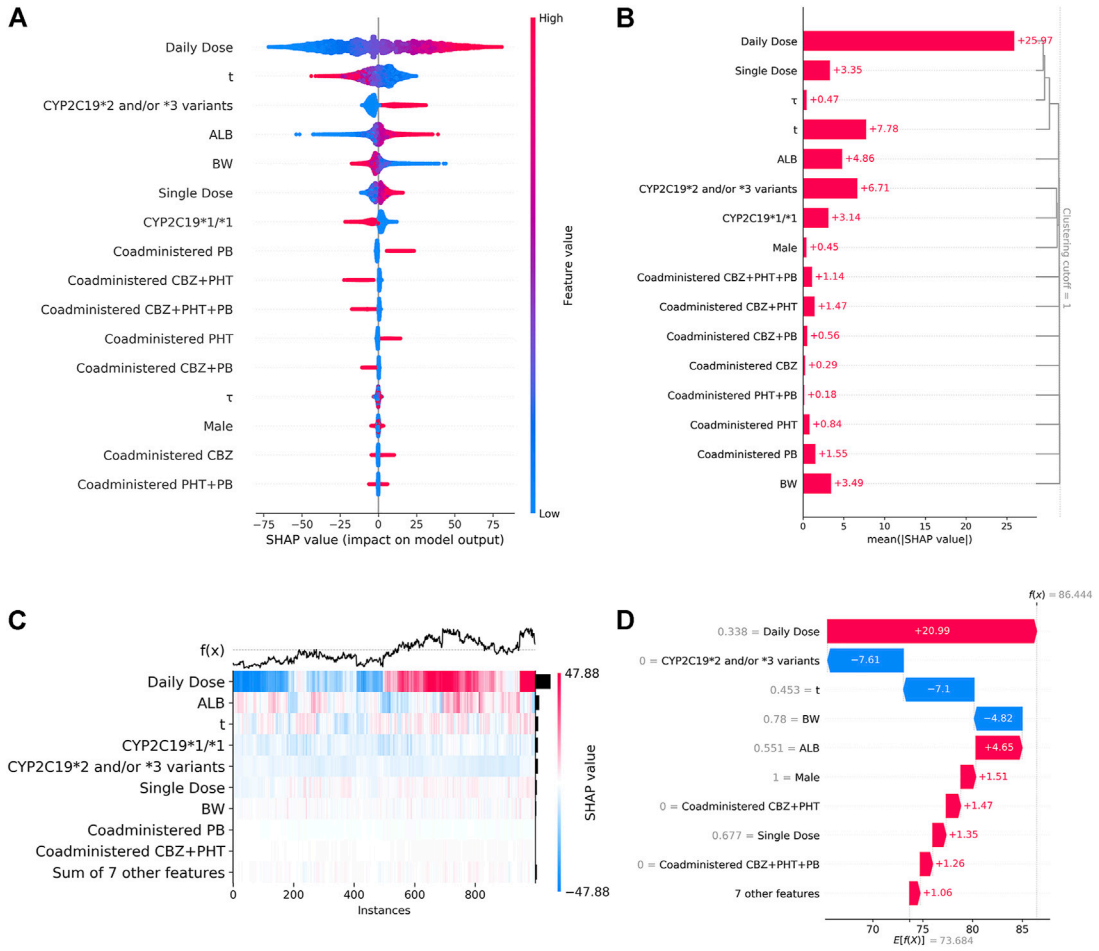

FIGURE 4
(A). SHAP summary plot. From it, we can get an initial sense of the relationship between the value of a certain feature and its impact on prediction. Each point represents an instance and a Shapley value for a feature. Its position on this plot is determined by the feature on the *y*-axis (ordered by feature importance) and the Shapley value on the *x*-axis, while its color is determined by the value of the feature. A higher SHAP value corresponds to a higher C_{ss} of VPA, and *vice versa*. **(B)** SHAP bar plot obtained by using feature clustering, from which we can simultaneously visualize the structure of the clustering and the importance of the features. The numbers on the histograms represent the mean (|SHAP value|) of a feature. SHAP analysis can also explain individual predictions, illustrated by **(C–D)**. **(C)** SHAP heat map, with the top 1,000 instances on the *x*-axis and the model inputs on the *y*-axis. The SHAP values encoded on a color scale. The model outputs are shown above the heatmap matrix and centered around the dotted gray baseline. The global importance of each feature is shown as a black bar plot on the right-hand side of the plot. **(D)** Waterfall plot that explains a single prediction of the sample randomly selected from the 1,000 instances by visualizing how to obtain the final prediction with the SHAP values of each feature. The bottom of the plot starts as expected, and then each row shows how the positive (red) or negative (blue) contribution of each feature moves the value from the expected output of the model, under the background distribution of the dataset, to its final prediction. The value of each feature for this sample appears in gray text before the feature name.

mean absolute SHAP values [mean (|SHAP value|)] of each feature over all instances (rows) of the finally generated combined dataset. SHAP can also explain individual predictions. Figure 4C shows the SHAP heat map of the top 1,000 instances extracted from the dataset. It ordered samples by using supervised clustering, and this resulted in samples that had the same model outputs, for the same reason for which they were grouped together. Figure 4D shows the applicability of the proposed XGBoost model on a single sample randomly selected from these 1,000 instances, where the highest contribution to the C_{ss} of VPA is the Daily Dose (feature value = 0.338) and *CYP2C19*2* and/or **3* variants (feature value = 0), and was generally not in agreement with the results of the global interpretations of the SHAP summary plot analysis. It indicated the potential difference in the rankings of the contributions of the features at the individual level. The SHAP dependence plots of the top seven key features are displayed in Figure 5, to show how a feature affected the C_{ss} of VPA. Nonlinear associations between features (e.g., *t*) and the C_{ss} of VPA were observed. The results showed that higher Daily/Single Dose and ALB, lower BW, and *CYP2C19*2* and/or **3* variants, were related to higher C_{ss} of VPA.

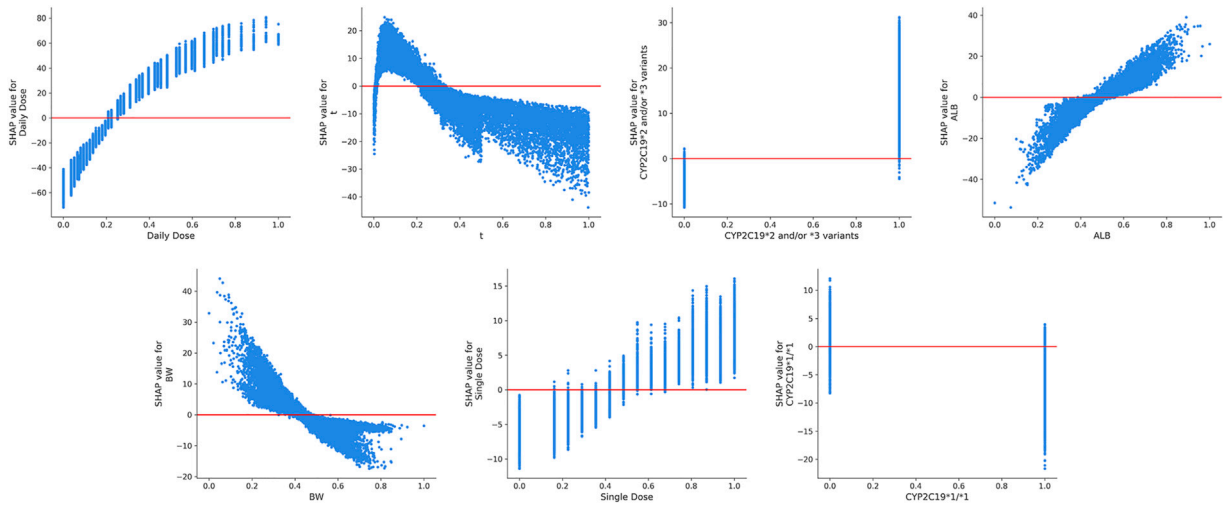

FIGURE 5
The SHAP dependence plots of features that ranked higher according to their importance ranking. From the scatter plots, we can see the exact form of the relationships between a single feature and the predictions made by the model.

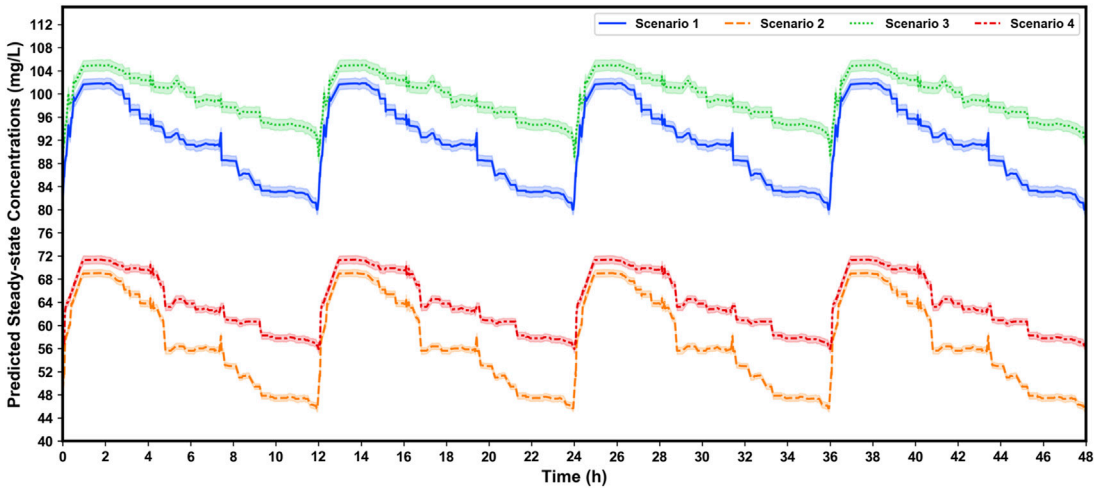

FIGURE 6
Simulated C_{ss} of VPA plotted by using four dosing intervals at the dosage regimen of 500 mg/bid in different scenarios based on the proposed XGBoost model. The numbers of virtual patients at each time point is 1,000. The blue, orange, green, and red line denotes scenario 1 (patients with *CYP2C19*2* and/or **3* variants, and taking co-administered CBZ + PHT + PB), scenario 2 (patients with *CYP2C19*1*1* genotype, and taking co-administered CBZ + PHT + PB), scenario 3 (patients with *CYP2C19*2* and/or **3* variants, and *not* taking co-administered CBZ, PHT, or PB), and scenario 4 (patients with *CYP2C19*1*1* genotype, and *not* taking co-administered CBZ, PHT, or PB), respectively. The shaded area represents the 95% confidence interval.

3.4 Impacts of covariates on VPA exposure

Figure 6 shows the comprehensive impacts of *CYP2C19* genotypes and co-administered enzyme-inducing antiepileptic drugs on the C_{ss} of VPA under the dosage regimen of 500 mg/bid, by simulating four scenarios using the XGBoost model. The simulated $AUC_{0\rightarrow 12h}$ values at a steady-state calculated by the trapezoidal rule and the corresponding $\bar{C}_{ss}$ values are listed in Table 7. Our results showed that patients who had the *CYP2C19*2* and/or **3*

TABLE 7 Simulated steady-state area under the curve from time zero to 12 h ($AUC_{0\rightarrow12h}$) and the corresponding average C_{ss} ($\bar{C}_{ss}$) values of VPA under the dosage regimen of 500 mg/bid in terms of four different scenarios based on the XGBoost model.

Scenarios	$AUC_{0\rightarrow12h}$ (mg·h/L)	$\bar{C}_{ss}$ (mg/L)
Scenario 1	1,093.3 ± 170.2	91.1 ± 14.2
Scenario 2	683.4 ± 103.7	56.9 ± 8.6
Scenario 3	1,187.5 ± 183.5	99.0 ± 15.3
Scenario 4	765.4 ± 117.0	63.8 ± 9.8

Note: Scenario 1 denotes patients with *CYP2C19*2* and/or **3* variants and taking co-administered CBZ + PHT + PB), Scenario 2 denotes patients with *CYP2C19*1*1* genotype and taking co-administered CBZ + PHT + PB, Scenario 3 denotes patients with *CYP2C19*2* and/or **3* variants and *NOT* taking co-administered CBZ, PHT, or PB, and Scenario 4 denotes patients with *CYP2C19*1*1* genotype and *NOT* taking co-administered CBZ, PHT, or PB.

variants and did not receive CBZ, PHT, or PB, had more VPA exposure [$AUC_{0\rightarrow12h}$: (1,187.5 ± 183.5) *versus* (683.4 ± 103.7) mg·h/L, approximately 1.74-fold] and more $\bar{C}_{ss}$ [(99.0 ± 15.3) *versus* (56.9 ± 8.6) mg/L] than those of individuals with *CYP2C19*1/*1* genotype and co-administered CBZ + PHT + PB.

3.5 Performance of the simplified models

The simplified XGBoost model by omitting the features of Single Dose, ALB, t, and τ, yielded reduced performance on the validation cohort, with an MAE of 11.2 mg/L, RMSE of 14.7 mg/L, MRE of 5%, and IR of 68.00%, respectively; whereas, its

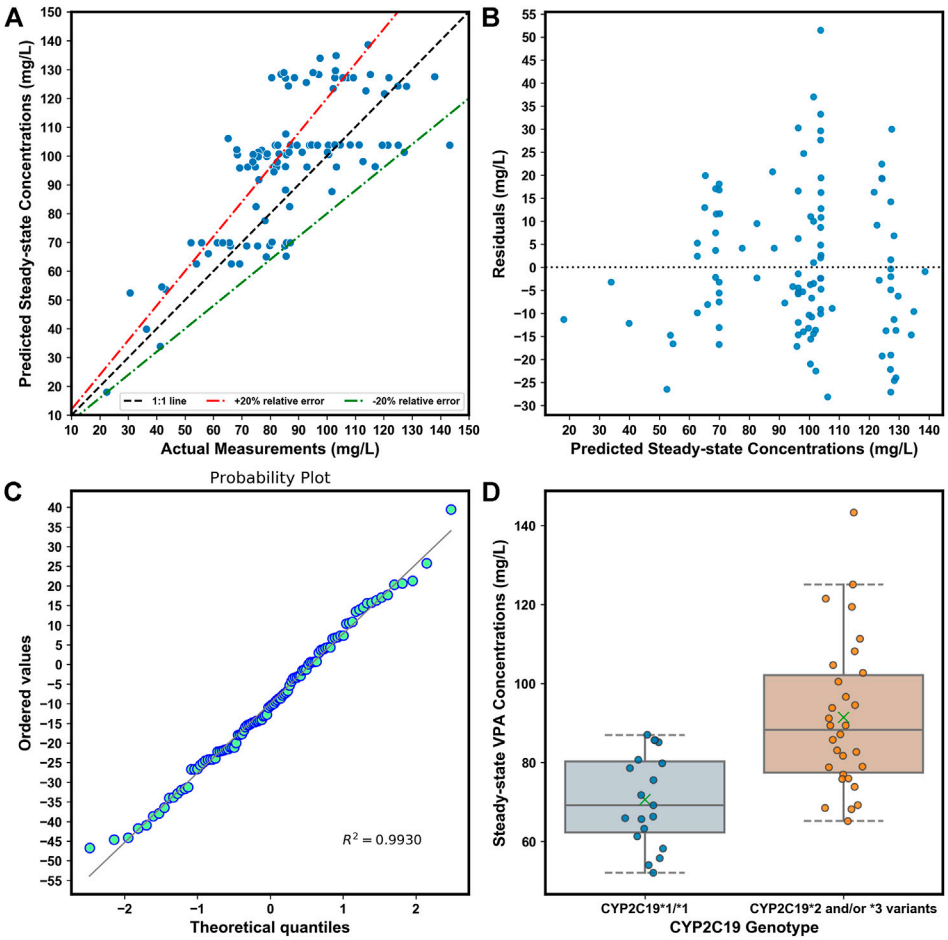

FIGURE 7
(A). Comparison of predicted and observed C_{ss} values of VPA on the independent external dataset based on the simplified optimum XGBoost model. The range between red and green dotted lines represents +20%~-20% relative errors, i.e., the predicted values within ±20% of the observed values. **(B)** Residuals plot of residuals *versus* the predicted C_{ss} values. **(C)** Probability plot of the residuals. **(D)** Comparison of observed C_{ss} of VPA between patients with *CYP2C19*1*1* genotype and *CYP2C19*2* and/or **3* variants at a dosage regimen of 500 mg/bid on our independent external dataset. The green multiplication sign indicates the mean C_{ss} values of VPA.

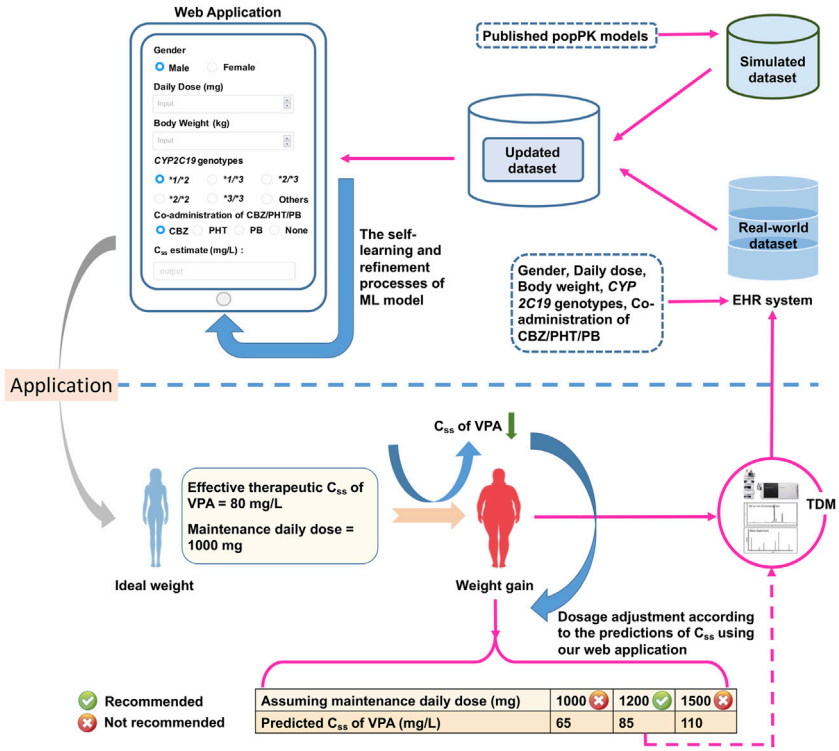

FIGURE 8
The designed web application for real-time estimations of the value of C_{ss} of VPA based on the simplified optimum XGBoost model. The database can be updated by integrating our simulated dataset with empirical data that are automatically crawled from the electronic health record (EHR) system. This may enhance the self-learning and refinement of the ML model.

performance has since been upgraded after optimization (Table 6). The simplified optimum XGBoost model also obtained good performance on our independent external dataset (Table 6). About 60.00% of predicted values fell within ±20% of the empirical values (Figure 7A). Figure 7B illustrates no clear patterns of the distribution of the residuals, and Figure 7C shows the residuals were symmetrically distributed, which meets the assumption of normality (R^2 = 0.9930). In the external dataset (described in Table 4), the mean measured C_{ss} values of VPA in scenarios 3 and 4 were (91.4 ± 18.7) and (70.6 ± 11.3) mg/L, respectively (Figure 7D), which were close to the predicted $\bar{C}_{ss}$ of VPA in these scenarios based on the XGBoost model (see Table 7). A snapshot of the workflow of the designed web application based on the simplified optimum XGBoost model is shown in Figure 8.

4 Discussion

ML can serve as a bridge between big data and pharmacometrics by providing an efficient computational approach, but the effective utilization of ML tools in pharmacometrics modeling is still in its infancy (McComb et al., 2022). Many attempts have been made to combine ML and pharmacometrics to advance MIDP, such as the fast screening of covariates in popPK models using ML. However, the ML-based integration of covariates in different popPK models, to our knowledge, is another potentially interesting but unexplored application of ML in pharmacometrics.

In this work, we have first proposed an innovative approach to integrate covariates in multiple previously published popPK models of VPA in Chinese epileptic patients using MC simulations to construct population-based large datasets for ML modeling. However, several key points need to be addressed before implementation. One is the choice of published popPK models. As mentioned at the beginning of the section "materials and methods," it is important to select suitable popPK models of VPA due to the differing predictability within models. Another point that involves the size ratio of simulated datasets from different popPK models, is also noteworthy. Due to the potential differences in covariate types in different popPK models, missing values of features are inevitable when merging these simulated datasets from different popPK models to construct the combined dataset for the ML task. These features should usually occur in more than 50% of samples; otherwise, they need to be omitted (Meyer et al.,

2018). Hence, it is of crucial importance to determine the partition ratio of different sub-datasets in the combined dataset so as not to remove key covariates. Processing these features with less than 50% missing values usually consists of assigning "Unknown" to categorical variables, or setting them to null for further imputation of the missing values. Furthermore, the proportion of data simulated by using different models, as well as the methods dealing with features with missing values, may have an impact on explaining feature importance and the patterns of influence. For example, an inappropriate proportion of simulated datasets may lead to the learning of an insufficient amount of information on the key factors by ML models. Therefore, the appropriate construction of the combined dataset requires incorporating expert knowledge into the ML modeling process. In this study, we have tried to set the simulated sub-datasets close to the same scale while considering the percentages of missing values of features in the finally generated combined dataset. We also have incorporated our expert knowledge into the construction of the combined dataset and well explained the influence of a predictor in the XGBoost model based on the constructed combined dataset by using explanation methods (e.g., the SHAP analysis). The last point to consider is that, after the data cleaning process including missing data imputation and one-hot encoding, we might have to be concerned about multi-collinearity in features in the finally generated combined dataset before ML modeling because collinearity in the features may affect the performance of ML models. The common method of dealing with this is to remove collinearity from the feature set (Dormann et al., 2013). Nevertheless, the decision regarding whether to retain the features related to each other depends on their interpretation meaning, the severity of multicollinearity, and the performance of XGBoost models.

The ultimate prediction model established with XGBoost achieved a good prediction precision and accuracy in the validation cohort. The prediction behaviors of this "black-box" model were illustrated by SHAP analysis. Our results demonstrated that the daily dosage of VPA was the most important variable. Other variables ranking among the top were as follows: blood sampling time, *CYP2C19*2* and/or **3* variants, ALB, BW, single dosage of VPA, and *CYP2C19*1/*1* genotype. The SHAP dependent plots indicated the nonlinear relationships between the C_{ss} of VPA and blood sampling time and daily/single dosage of VPA. We intuitively found that the time to peak plasma concentration was 1–2 h in line with previous clinical pharmacokinetics reports of VPA (Gugler and von Unruh, 1980). The positive influence of daily/single dosage of VPA on the C_{ss} of VPA tended to be stable along with increased VPA dose, partly explained by a saturable VPA protein binding status, along with a subsequent increase in unbound VPA associated with increased *CL*, as VPA is a high protein-binding drug (Lin et al., 2015; Gu et al., 2021). The SHAP plots also showed that the C_{ss} of VPA was positively correlated with ALB and *CYP2C19*2* and/or **3* variants, and negatively correlated with BW and *CYP2C19*1/*1* genotype, which was generally consistent with the results of our selected popPK models (Lin et al., 2015; Guo et al., 2020). The increased content of ALB in the blood results in less unbound VPA, thereby decreasing the *CL*. *CYP2C19*2* and/or **3* variants are associated with the diminished catalytic activity of CYP2C19. Patients with wild-type alleles for *CYP2C19* are classified as extensive metabolizers associated with lower VPA concentrations, whereas non-extensive metabolizers are those with loss-of-function alleles, resulting in higher VPA exposure (Guo et al., 2020). Regarding the BW, our finding was expected given its association with organ functionality development responsible for drug elimination (Methaneethorn, 2018); this was in accordance with several previous studies that reported an increase in *CL* and V_d with increasing BW (Correa et al., 2008; Methaneethorn, 2017; Xu et al., 2018).

Furthermore, after covariate integration, it was necessary to explore the comprehensive impacts of *CYP2C19* genotypes and co-administered enzyme-inducing antiepileptic drugs on VPA exposure. Our simulations, which were well-verified by our independent external dataset, showed that at the dosage regimen of 500 mg/bid, VPA exposure in patients with *CYP2C19*2* and/or **3* variants and no co-administered CBZ, PHT, or PB, was approximately 1.74-fold compared to those with *CYP2C19*1/*1* genotype and co-administered CBZ + PHT + PB, who would obtain $\bar{C}_{ss}$ of (56.9 ± 8.6) mg/L, close to the lower limit of the therapeutic reference range of VPA (50–100 mg/L) recommended by the consensus guidelines for TDM in neuropsychopharmacology (Hiemke et al., 2018). This indicated that in combination with CBZ + PHT + PB, the VPA concentration was decreased in patients with wild-type alleles for *CYP2C19*, which may lead to the risk of ineffective treatment.

We simplified the XGBoost model by omitting several predictors that were infrequently measured during TDM (e.g., ALB), or whose clinical values were inaccurate (e.g., blood sampling time), to develop a clinically easy-to-use model. Compared with the initially proposed XGBoost model, the reduced performance of our simplified XGBoost model indicated the important influences of these features, particularly the blood sampling time and ALB, on the model output. Nevertheless, a 60.00% IR of the simplified optimum XGBoost model on our external dataset suggested its good forecasting performance, considering the prediction accuracy of the predicted TDM within ±30% of the actual TDM in many similar studies that utilized XGBoost models, ranging from 40% to 75% (Huang et al., 2021b; Guo et al., 2021; Zheng et al., 2021; Ma et al., 2022). Based on the simplified optimum XGBoost model, we designed an easy-to-use web application by using only *CYP2C19* genotypes and some noninvasive clinical parameters as an MIPD tool for personalized dosing adjustments. For instance, VPA is known to have both metabolic and endocrinal side effects, and is likely to induce weight gain, which may influence its value of C_{ss} (Corman et al., 1997). Assuming that the effective therapeutic value of C_{ss} of VPA was 80 mg/L under the maintenance of a daily dose of

1,000 mg for a female patient with the ideal BW, adjusted dosing regimens due to weight gain can be recommended by using our web application to reach the target C_{ss} while ignoring the problems of adherence and drug–drug interactions. Furthermore, compared with the static pharmacometrics that requires new models, ML is capable of dynamic learning and retraining (McComb et al., 2022). The database can be updated by integrating our simulated dataset with empirical data automatically crawled from the EHR system. This promotes the self-learning and refinement of the model (see Figure 8).

Despite these promising results, several limitations should be considered. The first was the relatively small sample size of our independent external dataset for performing model validation. In particular, cases of co-administered CBZ/PHT/PB were lacking due to rather few such cases. The second was that some potential key covariates were not included owing to no related published popPK literature. For example, combination with carbapenems can substantially decrease serum VPA concentrations with a mean difference of -43.98 mg/L (Chai et al., 2021), which might cause a huge prediction bias in our model. Future popPK research is needed to evaluate such covariates. The third was that we could not be able to verify whether the covariates from Model-A and Model-B were (partly) correlated or not in the context of pharmacokinetics since they were not identified in the same study. For example, low ALB concentrations have been proved to be associated with weight gain (Basolo et al., 2021), however, the exact relationship between ALB level and BW level remains unclear among Chinese epileptic patients, thus it is difficult to determine which level of ALB corresponds to which level of BW if considering the covariance of the two covariates when creating a virtual population with both covariates. Notably, our ML-based integration approach assumes the covariates derived from different popPK models are not correlated with each other in the context of pharmacokinetic modeling, considering that this ML method generally requires as many candidate influencing factors as possible. The abundant feature information and the massive volume of data can enhance the performance of the ML because it is data intensive. Moreover, the weight of each feature which presents the contribution of a feature to the final prediction can be updated in the ML model's self-learning and refinement processes by integrating our simulated dataset with the real-world dataset from the EHR system. Finally, as pharmacometrics data are typically limited in size, the methods of model validation in ML are not routinely used in pharmacometrics. There is also a lack of consensus on the relevant definition and approaches (Sherwin et al., 2012; McComb et al., 2022). Nevertheless, a comparison of the predictive performance of the proposed XGBoost model and the two popPK models may be worthy of further examination. Besides, it is difficult to fairly evaluate and quantify the gain of using a combined dataset to develop the XGBoost model compared to a dataset taken from a single popPK model because both the feature dimensions of different datasets and the predictability of different popPK models are different. Whereas, a comparison of the predictive performance of XGBoost models built by using the combined dataset and a dataset derived from a single popPK model may also deserve further research.

5 Conclusion

Various popPK models for VPA have been reported; however, covariates affecting pharmacokinetic variability of VPA varied considerably between different popPK models. We innovatively proposed a method to integrate these covariates from multiple previously published popPK models using MC simulations to construct a large combined dataset for ML modeling. Our proposed XGBoost model exhibited excellent performance, the prediction behaviors of which were well-explained by the SHAP analysis. In short, our study highlighted the role of ML, presented as a computational bridge between big data and pharmacometrics, in integrating covariates derived from different popPK models.

Data availability statement

The original contributions presented in the study are included in the article/supplementary material, further inquiries can be directed to the corresponding authors.

Ethics statement

The studies involving human participants were reviewed and approved by the Ethics Committee of the Affiliated Brain Hospital of Guangzhou Medical University ([2021] NO.027). Written informed consent from the participants' legal guardian/next of kin was not required to participate in this study in accordance with the national legislation and the institutional requirements.

Author contributions

YGW and DWS together conceived and designed the study. MZ performed the data collection and data analyses. XQZ wrote the original draft preparation.

Funding

This work was supported by the Science and Technology Plan Project of Guangdong Province (grant number

2019B030316001), Guangzhou municipal key discipline in medicine (2021–2023), Guangzhou Municipal Science and Technology Project for Medicine and Healthcare (grant numbers 20201A011047 and 20202A011016), Natural Science Foundation of Guangdong Province (grant number 2021A1515011325), and Guangdong Provincial Hospital Pharmaceutical Research Fund (grant number 2022A22).

Acknowledgments

We thank International Science Editing (http://www.internationalscienceediting.com) for editing this manuscript.

Conflict of interest

The authors declare that the research was conducted in the absence of any commercial or financial relationships that could be construed as a potential conflict of interest.

Publisher's note

All claims expressed in this article are solely those of the authors and do not necessarily represent those of their affiliated organizations, or those of the publisher, the editors and the reviewers. Any product that may be evaluated in this article, or claim that may be made by its manufacturer, is not guaranteed or endorsed by the publisher.

References

Basolo, A., Ando, T., Chang, D. C., Hollstein, T., Krakoff, J., Piaggi, P., et al. (2021). Reduced albumin concentration predicts weight gain and higher ad libitum energy intake in humans. *Front. Endocrinol. (Lausanne)* 12, 642568. doi:10.3389/fendo.2021.642568

Beretta, L., and Santaniello, A. (2016). Nearest neighbor imputation algorithms: A critical evaluation. *BMC Med. Inf. Decis. Mak.* 16 (3), 74. doi:10.1186/s12911-016-0318-z

Bououda, M., Uster, D. W., Sidorov, E., Labriffe, M., Marquet, P., Wicha, S. G., et al. (2022). A machine learning approach to predict interdose vancomycin exposure. *Pharm. Res.* 39 (4), 721–731. doi:10.1007/s11095-022-03252-8

Cao, D. S., Xu, Q. S., Liang, Y. Z., Zhang, L. X., and Li, H. D. (2010). The boosting: A new idea of building models. *Chemom. Intell. Lab. Syst.* 100 (1), 1–11. doi:10.1016/j.chemolab.2009.09.002

Chai, P. Y., Chang, C. T., Chen, Y. H., Chen, H. Y., and Tam, K. W. (2021). Effect of drug interactions between carbapenems and valproate on serum valproate concentration: A systematic review and meta-analysis. *Expert Opin. Drug Saf.* 20 (2), 215–223. doi:10.1080/14740338.2021.1865307

Chen, C., Zhang, Q., Yu, B., Yu, Z., Lawrence, P. J., Ma, Q., et al. (2020). Improving protein-protein interactions prediction accuracy using XGBoost feature selection and stacked ensemble classifier. *Comput. Biol. Med.* 123, 103899. doi:10.1016/j.compbiomed.2020.103899

Chen, T., and Guestrin, C. (2016). XGBoost: A scalable tree boosting system. *KDD '16 Proc. 22nd ACM SIGKDD Int. Conf. Knowl. Discov. data Min.* 2016, 785–794. doi:10.1145/2939672.2939785

Corman, C. L., Leung, N. M., and Guberman, A. H. (1997). Weight gain in epileptic patients during treatment with valproic acid: A retrospective study. *Can. J. Neurol. Sci.* 24 (3), 240–244. doi:10.1017/s0317167100021879

Correa, T., Rodríguez, I., and Romano, S. (2008). Population pharmacokinetics of valproate in Mexican children with epilepsy. *Biopharm. Drug Dispos.* 29 (9), 511–520. doi:10.1002/bdd.636

Darwich, A. S., Polasek, T. M., Aronson, J. K., Ogungbenro, K., Wright, D., Achour, B., et al. (2021). Model-informed precision dosing: Background, requirements, validation, implementation, and forward trajectory of individualizing drug therapy. *Annu. Rev. Pharmacol. Toxicol.* 61, 225–245. doi:10.1146/annurev-pharmtox-033020-113257

Dormann, C. F., Elith, J., Bacher, S., Buchmann, C., Carl, G., Carré, G., et al. (2013). Collinearity: A review of methods to deal with it and a simulation study evaluating their performance. *Ecography* 36 (1), 27–46. doi:10.1111/j.1600-0587.2012.07348.x

Firman, P., Whitfield, K., Tan, K. S., Clavarino, A., and Hay, K. (2021). The impact of an electronic hospital system on therapeutic drug monitoring. *J. Clin. Pharm. Ther.* 46 (6), 1613–1621. doi:10.1111/jcpt.13497

Ghodke-Puranik, Y., Thorn, C. F., Lamba, J. K., Leeder, J. S., Song, W., Birnbaum, A. K., et al. (2013). Valproic acid pathway: Pharmacokinetics and pharmacodynamics. *Pharmacogenet. Genomics* 23 (4), 236–241. doi:10.1097/FPC.0b013e32835ea0b2

Gu, X., Zhu, M., Sheng, C., Yu, S., Peng, Q., Ma, M., et al. (2021). Population pharmacokinetics of unbound valproic acid in pediatric epilepsy patients in China: A protein binding model. *Eur. J. Clin. Pharmacol.* 77 (7), 999–1009. doi:10.1007/s00228-020-03080-y

Gugler, R., and von Unruh, G. E. (1980). Clinical pharmacokinetics of valproic acid. *Clin. Pharmacokinet.* 5 (1), 67–83. doi:10.2165/00003088-198005010-00002

Guo, J., Huo, Y., Li, F., Li, Y., Guo, Z., Han, H., et al. (2020). Impact of gender, albumin, and *CYP2C19* polymorphisms on valproic acid in Chinese patients: A population pharmacokinetic model. *J. Int. Med. Res.* 48 (8), 300060520952281. doi:10.1177/0300060520952281

Guo, W., Yu, Z., Gao, Y., Lan, X., Zang, Y., Yu, P., et al. (2021). A machine learning model to predict risperidone active moiety concentration based on initial therapeutic drug monitoring. *Front. Psychiatry.* 12, 711868. doi:10.3389/fpsyt.2021.711868

Hakami, T. (2021). Neuropharmacology of antiseizure drugs. *Neuropsychopharmacol. Rep.* 41 (3), 336–351. doi:10.1002/npr2.12196

Hiemke, C., Bergemann, N., Clement, H. W., Conca, A., Deckert, J., Domschke, K., et al. (2018). Consensus guidelines for therapeutic drug monitoring in neuropsychopharmacology: Update 2017. *Pharmacopsychiatry* 51 (1-02), 9–62. doi:10.1055/s-0043-116492

Ho, P. C., Abbott, F. S., Zanger, U. M., and Chang, T. K. (2003). Influence of CYP2C9 genotypes on the formation of a hepatotoxic metabolite of valproic acid in human liver microsomes. *Pharmacogenomics J.* 3 (6), 335–342. doi:10.1038/sj.tpj.6500210

Huang, X., Yu, Z., Bu, S., Lin, Z., Hao, X., He, W., et al. (2021b). An ensemble model for prediction of vancomycin trough concentrations in pediatric patients. *Drug Des. Devel. Ther.* 15, 1549–1559. doi:10.2147/DDDT.S299037

Huang, X., Yu, Z., Wei, X., Shi, J., Wang, Y., Wang, Z., et al. (2021a). Prediction of vancomycin dose on high-dimensional data using machine learning techniques. *Expert Rev. Clin. Pharmacol.* 14 (6), 761–771. doi:10.1080/17512433.2021.1911642

Jakobsen, M. I., Larsen, J. R., Svensson, C. K., Johansen, S. S., Linnet, K., Nielsen, J., et al. (2017). The significance of sampling time in therapeutic drug monitoring of clozapine. *Acta Psychiatr. Scand.* 135 (2), 159–169. doi:10.1111/acps.12673

Jiang, D., Bai, X., Zhang, Q., Lu, W., Wang, Y., Li, L., et al. (2009). Effects of CYP2C19 and CYP2C9 genotypes on pharmacokinetic variability of valproic acid in Chinese epileptic patients: Nonlinear mixed-effect modeling. *Eur. J. Clin. Pharmacol.* 65 (12), 1187–1193. doi:10.1007/s00228-009-0712-x

Johannessen, C. U., and Johannessen, S. I. (2003). Valproate: Past, present, and future. *CNS Drug Rev.* 9 (2), 199–216. doi:10.1111/j.1527-3458.2003.tb00249.x

Jovanović, M., Sokić, D., Grabnar, I., Vovk, T., Prostran, M., Erić, S., et al. (2015). Application of counter-propagation artificial neural networks in prediction of topiramate concentration in patients with epilepsy. *J. Pharm. Pharm. Sci.* 18 (5), 856–862. doi:10.18433/j33031

Kalagotla, S. K., Gangashetty, S. V., and Giridhar, K. (2021). A novel stacking technique for prediction of diabetes. *Comput. Biol. Med.* 135, 104554. doi:10.1016/j.compbiomed.2021.104554

Kishi, T., Ikuta, T., Matsuda, Y., Sakuma, K., Okuya, M., Nomura, I., et al. (2022). Pharmacological treatment for bipolar mania: A systematic review and network meta-analysis of double-blind randomized controlled trials. *Mol. Psychiatry* 27 (2), 1136–1144. doi:10.1038/s41380-021-01334-4

Kluwe, F., Michelet, R., Mueller-Schoell, A., Maier, C., Klopp-Schulze, L., van Dyk, M., et al. (2021). Perspectives on model-informed precision dosing in the digital health era: Challenges, opportunities, and recommendations. *Clin. Pharmacol. Ther.* 109 (1), 29–36. doi:10.1002/cpt.2049

Koch, G., Pfister, M., Daunhawer, I., Wilbaux, M., Wellmann, S., and Vogt, J. E. (2020). Pharmacometrics and machine learning partner to advance clinical data analysis. *Clin. Pharmacol. Ther.* 107 (4), 926–933. doi:10.1002/cpt.1774

Li, W., Yin, Y., Quan, X., and Zhang, H. (2019). Gene expression value prediction based on XGBoost algorithm. *Front. Genet.* 10, 1077. doi:10.3389/fgene.2019.01077

Li, X., Xu, X., Xie, F., Xu, X., Sun, Y., Liu, X., et al. (2020). A time-phased machine learning model for real-time prediction of sepsis in critical care. *Crit. Care Med.* 48 (10), e884–e888. doi:10.1097/CCM.0000000000004494

Lin, W. W., Jiao, Z., Wang, C. L., Wang, H. Y., Ma, C. L., Huang, P. F., et al. (2015). Population pharmacokinetics of valproic acid in adult Chinese epileptic patients and its application in an individualized dosage regimen. *Ther. Drug Monit.* 37 (1), 76–83. doi:10.1097/FTD.0000000000000100

Liu, X. Q., Yin, Y. W., Wang, C. Y., Li, Z. R., Zhu, X., and Jiao, Z. (2021). How to handle the delayed or missed dose of rivaroxaban in patients with non-valvular atrial fibrillation: Model-informed remedial dosing. *Expert Rev. Clin. Pharmacol.* 14 (9), 1153–1163. doi:10.1080/17512433.2021.1937126

Lopez-Arevalo, I., Aldana-Bobadilla, E., Molina-Villegas, A., Galeana-Zapién, H., Muñiz-Sanchez, V., and Gausin-Valle, S. (2020). A memory-efficient encoding method for processing mixed-type data on machine learning. *Entropy (Basel)* 22 (12), 1391. doi:10.3390/e22121391

Lundberg, S. M., and Lee, S. I. (2017). A unified approach to interpreting model predictions. *Red. Hook. N. Y. U. S. A.*, 4768–4777. In proceedings of the 31st international conference on neural information processing systems (NIPS'17). Curran Associates Inc. Available at: https://dl.acm.org/doi/pdf/10.5555/3295222.3295230.

Lv, C., Lu, J., Jing, L., Liu, T. T., Chen, M., Zhang, R., et al. (2021). Systematic external evaluation of reported population pharmacokinetic models of vancomycin in Chinese children and adolescents. *J. Clin. Pharm. Ther.* 46 (3), 820–831. doi:10.1111/jcpt.13363

Ma, P., Liu, R., Gu, W., Dai, Q., Gan, Y., Cen, J., et al. (2022). Construction and interpretation of prediction model of teicoplanin trough concentration via machine learning. *Front. Med. (Lausanne).* 9, 808969. doi:10.3389/fmed.2022.808969

McComb, M., Bies, R., and Ramanathan, M. (2022). Machine learning in pharmacometrics: Opportunities and challenges. *Br. J. Clin. Pharmacol.* 88 (4), 1482–1499. doi:10.1111/bcp.14801

Methaneethorn, J. (2018). A systematic review of population pharmacokinetics of valproic acid. *Br. J. Clin. Pharmacol.* 84 (5), 816–834. doi:10.1111/bcp.13510

Methaneethorn, J. (2017). Population pharmacokinetics of valproic acid in patients with mania: Implication for individualized dosing regimens. *Clin. Ther.* 39 (6), 1171–1181. doi:10.1016/j.clinthera.2017.04.005

Meyer, A., Zverinski, D., Pfahringer, B., Kempfert, J., Kuehne, T., Sündermann, S. H., et al. (2018). Machine learning for real-time prediction of complications in critical care: A retrospective study. *Lancet Respir. Med.* 6 (12), 905–914. doi:10.1016/S2213-2600(18)30300-X

Mould, D. R., and Upton, R. N. (2013). Basic concepts in population modeling, simulation, and model-based drug development-part 2: Introduction to pharmacokinetic modeling methods. *CPT Pharmacometrics. Syst. Pharmacol.* 2 (4), e38. doi:10.1038/psp.2013.14

Ogami, C., Tsuji, Y., Seki, H., Kawano, H., To, H., Matsumoto, Y., et al. (2021). An artificial neural network-pharmacokinetic model and its interpretation using Shapley additive explanations. *CPT Pharmacometrics Syst. Pharmacol.* 10 (7), 760–768. doi:10.1002/psp4.12643

Radzi, S., Karim, M., Saripan, M. I., Rahman, M., Isa, I., and Ibahim, M. J. (2021). Hyperparameter tuning and pipeline optimization via grid Search method and tree-based autoML in breast cancer prediction. *J. Pers. Med.* 11 (10), 978. doi:10.3390/jpm11100978

Romoli, M., Mazzocchetti, P., D'Alonzo, R., Siliquini, S., Rinaldi, V. E., Verrotti, A., et al. (2019). Valproic acid and epilepsy: From molecular mechanisms to clinical evidences. *Curr. Neuropharmacol.* 17 (10), 926–946. doi:10.2174/1570159X17666181227165722

Shapley, L. S. (1953). A value for n-person games. *Contributions Theory Games* 2, 307–317. doi:10.1515/9781400881970-018

Sherwin, C. M., Kiang, T. K., Spigarelli, M. G., and Ensom, M. H. (2012). Fundamentals of population pharmacokinetic modelling: Validation methods. *Clin. Pharmacokinet.* 51 (9), 573–590. doi:10.1007/BF03261932

Sibieude, E., Khandelwal, A., Hesthaven, J. S., Girard, P., and Terranova, N. (2021). Fast screening of covariates in population models empowered by machine learning. *J. Pharmacokinet. Pharmacodyn.* 48 (4), 597–609. doi:10.1007/s10928-021-09757-w

Song, C., Li, X., Mao, P., Song, W., Liu, L., and Zhang, Y. (2022). Impact of CYP2C19 and CYP2C9 gene polymorphisms on sodium valproate plasma concentration in patients with epilepsy. *Eur. J. Hosp. Pharm.* 29 (4), 198–201. doi:10.1136/ejhpharm-2020-002367

Štrumbelj, E., and Kononenko, I. (2014). Explaining prediction models and individual predictions with feature contributions. *Knowl. Inf. Syst.* 41, 647–665. doi:10.1007/s10115-013-0679-x

Tang, B. H., Guan, Z., Allegaert, K., Wu, Y. E., Manolis, E., Leroux, S., et al. (2021). Drug clearance in neonates: A combination of population pharmacokinetic modelling and machine learning approaches to improve individual prediction. *Clin. Pharmacokinet.* 60 (11), 1435–1448. doi:10.1007/s40262-021-01033-x

Wang, C. Y., Jiao, Z., Ding, J. J., Yu, E. Q., and Zhu, G. X. (2020). Remedial dosing recommendations for delayed or missed doses of valproic acid in patients with epilepsy based on Monte Carlo simulations. *Epilepsy Behav.* 111, 107265. doi:10.1016/j.yebeh.2020.107265

Wang, S., Li, J., Song, M., Yan, P., Ju, X., Liu, J., et al. (2021). Effect of CYP2C19 polymorphisms on serum valproic level acid in Chinese Han patients with schizophrenia. *Sci. Rep.* 11 (1), 23150. doi:10.1038/s41598-021-02628-x

Woillard, J. B., Labriffe, M., Debord, J., and Marquet, P. (2021a). Tacrolimus exposure prediction using machine learning. *Clin. Pharmacol. Ther.* 110 (2), 361–369. doi:10.1002/cpt.2123

Woillard, J. B., Labriffe, M., Prémaud, A., and Marquet, P. (2021b). Estimation of drug exposure by machine learning based on simulations from published pharmacokinetic models: The example of tacrolimus. *Pharmacol. Res.* 167, 105578. doi:10.1016/j.phrs.2021.105578

Xu, S., Chen, Y., Zhao, M., Guo, Y., Wang, Z., and Zhao, L. (2018). Population pharmacokinetics of valproic acid in epileptic children: Effects of clinical and genetic factors. *Eur. J. Pharm. Sci.* 122, 170–178. doi:10.1016/j.ejps.2018.06.033

Yaman, E., and Subasi, A. (2019). Comparison of bagging and boosting ensemble machine learning methods for automated EMG signal classification. *Biomed. Res. Int.* 2019, 9152506. doi:10.1016/10.1155/2019/9152506

Yang, C., Chen, M., and Yuan, Q. (2021). The application of XGBoost and SHAP to examining the factors in freight truck-related crashes: An exploratory analysis. *Accid. Anal. Prev.* 158, 106153. doi:10.1016/j.aap.2021.106153

Zang, Y. N., Guo, W., Dong, F., Li, A. N., de Leon, J., and Ruan, C. J. (2022b). Published population pharmacokinetic models of valproic acid in adult patients: A systematic review and external validation in a Chinese sample of inpatients with bipolar disorder. *Expert Rev. Clin. Pharmacol.*, 1–15. doi:10.1080/17512433.2022.2075849

Zang, Y. N., Guo, W., Niu, M. X., Bao, S., Wang, Q., Wang, Y., et al. (2022a). Population pharmacokinetics of valproic acid in adult Chinese patients with bipolar disorder. *Eur. J. Clin. Pharmacol.* 78 (3), 405–418. doi:10.1007/s00228-021-03246-2

Zheng, P., Yu, Z., Li, L., Liu, S., Lou, Y., Hao, X., et al. (2021). Predicting blood concentration of tacrolimus in patients with autoimmune diseases using machine learning techniques based on real-world evidence. *Front. Pharmacol.* 12, 727245. doi:10.3389/fphar.2021.727245

Zhu, X., Huang, W., Lu, H., Wang, Z., Ni, X., Hu, J., et al. (2021a). A machine learning approach to personalized dose adjustment of lamotrigine using noninvasive clinical parameters. *Sci. Rep.* 11 (1), 5568. doi:10.1038/s41598-021-85157-x

Zhu, X., Xiao, T., Huang, S., Liu, S., Li, X., Shang, D., et al. (2021b). Case report: Predicting the range of lamotrigine concentration using pharmacokinetic models based on Monte Carlo simulation: A case study of antiepileptic drug-related leukopenia. *Front. Pharmacol.* 12, 706329. doi:10.3389/fphar.2021.706329

frontiers | Frontiers in Pharmacology

TYPE Original Research
PUBLISHED 09 November 2022
DOI 10.3389/fphar.2022.1025417

OPEN ACCESS

EDITED BY
Zinnia P. Parra-Guillen,
University of Navarra, Spain

REVIEWED BY
Gilbert Koch,
University Children's Hospital Basel, Switzerland
Nils Rosjat,
Cognitive Neuroscience (INM-3), Germany

*CORRESPONDENCE
Patrick D. Roberts,
rbertsp@amazon.com

SPECIALTY SECTION
This article was submitted to Translational Pharmacology, a section of the journal Frontiers in Pharmacology

RECEIVED 22 August 2022
ACCEPTED 04 October 2022
PUBLISHED 09 November 2022

CITATION
Roberts PD and Conour J (2022), Mechanistic modeling as an explanatory tool for clinical treatment of chronic catatonia.
Front. Pharmacol. 13:1025417.
doi: 10.3389/fphar.2022.1025417

Mechanistic modeling as an explanatory tool for clinical treatment of chronic catatonia

Patrick D. Roberts[1]* and James Conour[2]

[1]Amazon Web Services, Portland, OR, United States, [2]Cascadia Behavioral Healthcare, Portland, OR, United States

Mathematical modeling of neural systems is an effective means to integrate complex information about the brain into a numerical tool that can help explain observations. However, the use of neural models to inform clinical decisions has been limited. In this study, we use a simple model of brain circuitry, the Wilson-Cowan model, to predict changes in a clinical measure for catatonia, the Bush-Francis Catatonia Rating Scale, for use in clinical treatment of schizophrenia. This computational tool can then be used to better understand mechanisms of action for pharmaceutical treatments, and to fine-tune dosage in individual cases. We present the conditions of clinical care for a residential patient cohort, and describe methods for synthesizing data to demonstrated the functioning of the model. We then show that the model can be used to explain effect sizes of treatments and estimate outcomes for combinations of medications. We conclude with a demonstration of how this model could be personalized for individual patients to inform ongoing treatment protocols.

KEYWORDS

schizophrenia, Bush-Francis Catatonia Rating Scale, quantitative systems pharmacology, antipsychotic, benzodiazepine, lamotrigine, Wilson-Cowan

1 Introduction

The treatment of severe and persistent mental illness has been a central challenge for psychiatry. Individuals with the most debilitating forms of schizophrenia often derive limited benefit from medications. Additionally, the efficacy of pharmacologic treatments can be highly variable. A full response to a medical intervention may take weeks or months to materialize. Moreover, it can be difficult to accurately assess the impact of a specific medication. These challenges are compounded by the inconsistent history of care for many psychiatric patients and the significant amounts of polypharmacy they have been prescribed. Technical tools offer a promising augmentation to a psychiatrist's experience to design treatment plans and may help reduce the inconsistencies and refine treatment for individual cases.

Catatonia manifests as a cluster of symptoms including rituals, repetitive movements, perseveration, and withdrawal (Northoff 2002). There is common co-morbidity with both psychiatric and medical illnesses (Bhati et al. 2007) and catatonia is often not recognized in its chronic form because it can present subtly and idiosyncratically (Penland et al. 2006). In individuals with treatment resistant schizophrenia, chronic catatonic may be

quite common, and direct treatment of catatonic symptoms improves cognition (Wilcox and Reid Duffy 2015; Ungvari et al. 2005). For this reason, we have focussed on using the Bush-Francis Catatonia Rating Scale (BFCRS) (Bush et al. 1996) as a measure of symptoms and then model pharmacological mechanisms that explain how medications alleviate catatonic symptoms.

The data in this study is based on a cohort of schizophrenia patients admitted to Cascadia Behavioral Healthcare for residential care. The clinical practice in treating these patients has been to introduce a minimal set of medications with a known effect of reducing psychiatric symptoms. For patients admitted with a diagnosis of schizophrenia, antipsychotic medication was transitioned to clozapine (if possible), and augmented lamotrigine and a benzodiazepine based on functional status and safety. Lamotrigine has been previously observed to reduce symptoms in combination with clozapine (Gray and Risch, 2009; Tiihonen et al. 2003). Benzodiazepines have shown a strong therapeutic efficacy in reducing catatonia symptoms (Rosebush and Mazurek (2010); Northoff et al. 2004) and are considered a first-line treatment for acute or chronic catatonia (Ungvari et al. 2005). A significant reduction in catatonic symptoms, as measured by BFCRS, was observed in the clinic with this treatment along with a corresponding improvement in psychiatric symptoms. However, a mechanistic understanding of the action of this combination is desirable to improve treatments and seek new strategies for psychiatric disease maintenance.

1.1 Modeling as an explanatory tool

Physiological modeling of pharmacological systems can provide insight into mechanisms of therapeutic treatments by coupling molecular action to observable function. Explanatory models require a balance between biological detail and conceptional simplicity to express how specific treatments result in observed functional changes. The psychomotor abnormalities observed in catatonia can be conceptualized as a seizing of motor patterns on a time scale long enough to result in the clinical observations such as posturing and repetitive movements. Clinical and imaging studies have suggested that the physiological basis of catatonia symptoms are cortical in origin (Northoff et al. 2004; Hirjak et al. 2019) resulting from an over-excitation of circuitry and under-gating of movement termination. The effective treatments also support the concept of an imbalance of inhibition and excitation in cortical structures because targets of lamotrigine reduce pyramidal cell excitation (Poolos et al. 2002; Xie et al. 1995), and benzodiazepines increase inhibition (Miller et al. 1987).

A neural model describing interactions of excitatory and inhibitory neurons, with sufficient structure to couple medication actions, is the Wilson-Cowan model (Wilson and Cowan 1972). This model is interpreted as two interacting populations of cortical neurons where a single variable for each population represents the average spike rate (Figure 1A). The Wilson-Cowan model is mathematically well-understood (Cowan et al. 2016; Bressloff 2010; Benayoun et al. 2010; Buice et al. 2010; Negahbani et al. 2015) with dynamics that can display excitatory bursts and oscillations for different choices of parameters. For the purposes of the current study, we select a parameter range so that the dynamics represent two steady states of spiking activity, a high-rate and low-rate, in two basins separated by a barrier. The hight of the barrier is determined by the parameters of the model and determines the perturbation required to transition from the high-rate state to the low-rate state. The transition from the high-rate state to the low-rate state represents the termination of a cortical activity pattern. If the barrier is high then the system becomes "stuck" in a functional pattern and is interpreted to represent symptoms of catatonia such as postering or perseveration. Parameters of the model determine the synaptic coupling between populations of neurons and internal neural excitability, and these parameters are affected by medications.

In our model, we start with baseline parameter settings with a high barrier to represent catatonia, then calculate the changes in parameters based on the doses of medications in the clinical treatment. We show that the change in the barrier can be correlated with the change in BFCRS score to explain how each medication is impacting symptoms of catatonia. By using the model as a clinical guide to treatment, the clinician can conceptualize the physiological effects of a treatment as controlling cortical excitability to treat catatonia. This allows guidance beyond the safety and efficacy of individual medications to integrate polypharmacy into utilizing additive effects maximize positive outcomes.

2 Materials and methods

2.1 Data synthesis

Clinical data on BFCRS scores and daily medication dosages were collected and analyzed for clinical treatment purposes. For demonstration purposes, we synthesized surrogate data based on the statistics of the original data set (Conour, 2015). Using the *SVD* (Patki et al. 2016) python package, we constructed a Gaussian copula model based on the daily dosages of medications, and BFCRS scores before and after changes in medication for 12 individuals. The statistical reconstruction method ensured that no personal patient data is present in the published study. The copula model generated many spurious data samples with unrealistic medication doses because there were few individuals included in training the model. To eliminate spurious data, we added rules determined by JC to be unlikely under clinical conditions (see Data Selection

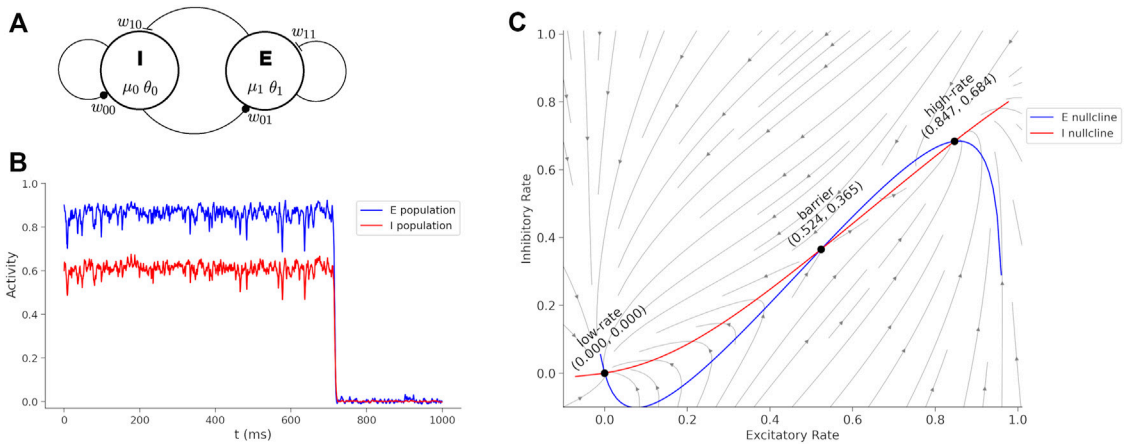

FIGURE 1
Wilson-Cowan model and dynamics. **(A)** Wilson-Cowan circuit with an inhibitory (I) and excitatory (E) neuron population. The model parameters associated with each circuit element are show. **(B)** Sustained activity eventually decays due to random perturbations drawn from a normal distribution with mean = 0 and standard deviation = 0.19. If the boundary is too high, then the sustained burst continues indefinitely. Treatments reduce the boundary between the states and transitions become more fluid and interpreted as a reduction of catatonia symptoms. **(C)** Phase plane of the Wilson-Cowan model with trajectories, nullclines and fixed points labeled.

Filter, Supplementary Data). The copula model generated 700 subjects and 58 subjects remained after filtering.

2.2 Wilson-Cowan model

The pharmaceutical treatments include three classes of medications: anticonvulsants, benzodiazepines, and antipsychotics. These medications operate *via* multiple mechanisms of action, and our approach couples their action to a model of cortical activity. In order to quantify the effects, we developed a two-state model of cortical dynamics that can predict how varying doses affect catatonic symptoms. We use a special case of the Wilson-Cowan equations:

$$\begin{aligned} \dot{x_0} &= -x_0 + F_0\left(w_{00}x_0 + w_{01}x_1\right) \\ \dot{x_1} &= -x_1 + F_1\left(w_{10}x_0 + w_{11}x_1\right) \end{aligned} \tag{1}$$

With the spike probability (rate) function:

$$F_a\left(x_a\right) = \frac{1}{1 + \exp\left[-\mu_a\left(x_a - \theta_a\right)\right]} \tag{2}$$

We interpret x_0 as the average rate of inhibitory interneurons (parvalbumin positive) and x_1 as the average rate of excitatory neurons (cortical pyramidal cells). The parameters of the model were initialized to express three fixed points, one stable fixed point representing a low spike rate, one stable fixed point representing a high spike rate, and a saddle point that is the barrier between the two states. The initial synaptic parameters were chosen to be: $w_{11} = 8.65$, $w_{10} = 4$, $w_{01} = 13$, and $w_{00} = 9$. The parameters for the rate function are $\mu_1 = 1.2$, $\theta_1 = 2.8$, $\mu_0 = 1.0$, and $\theta_0 = 4.0$. We modify these initial parameters to represent the effects of medications in the system, but the effects are small enough to restrict the model behavior to this special case of the Wilson-Cowan model with two stable, and one unstable, fixed points.

A simulation of the Wilson-Cowan equations (Eq. 1) is shown in Figure 1B. The rates are initialized near the high-rate fixed-point ($x_0 = 0.6$, $x_1 = 0.9$) and normally distributed (mean = 0 and standard deviation = 0.19) perturbation is injected into the each neural pool at each time-step to simulate noise. The high-rate state is unstable under perturbations and when noise is added, the system will spontaneously transition to the low-rate state. The duration of the time in the high-rate state can be interpreted as a form of working memory (Katori et al. 2011), but here we consider the duration as a phase of activity (Bagi et al. 2022) that can lead to perseveration when the barrier is too high and a large perturbation is required for a state transition. Medications act on parameters of the model to raise or lower the boundary and affect catatonia symptoms.

Figure 1C shows the phase plane for the initial parameters of (Eq. 1). The barrier (B) is calculated by a cumulative summation of the excitatory rate gradient ($\dot{x_1}$) along the x_0-nullcline ($\mathcal{N}_\mathcal{I}$) from the high-rate fixed point to the barrier fixed point,

$$B = \sum_{n \in \mathcal{N}_\mathcal{I}} \dot{x_1}\left(n\right) \tag{3}$$

where the sum is over a lattice of 100 evenly spaced points. The boundary as calculated here is proportional to the minimal perturbation necessary to transition out of the high-rate state basin, and will be compared with BFCRS score.

2.3 Coupling treatment doses to model parameters

Clinical doses were converted to changes in the model parameters through a series of calculations. First we approximated the pharmacokinetics of each medication (see Pharmacokinetic Parameters, Supplementary Data) to arrive at a concentration in the cerebrospinal fluid (CSF). Next we calculate the binding to a target, and finally approximate an effect on the model parameters (Spiros et al. 2010; Geerts et al. 2013). The following provides details of the pharmacokinetics and coupling for lamotrigine, lorazepam (and applies to other benzodiazepines according to their affinities), and antipsychotics.

After the effects of medications are calculated, the parameters of the Eq. 1, $\vec{p} = [\mu_0, \mu_1, \theta_0, \theta_1, w_{00}, w_{01}, w_{10}, w_{11}]$ are transformed to $\vec{p}\,' = [\mu_0, \mu_1', \theta_0', \theta_1', w_{00}', w_{01}', w_{10}', w_{11}']$ (only μ_0 is unaffected by any medication in this implementation). When the changes in model parameters are calculated, we multiply by an overall factor of $a \cdot \vec{p}\,'$, where $a = 0.35$ is an overall medication response factor. This response factor limits the dynamics of the system to maintain two stable fixed points separated by an unstable barrier fixed-point and ensure that the ground state of the system is the low-rate fixed point for all cases. The value of the response factor $a = 0.35$ was found experimentally for the range of doses and combinations of medications in the data. For the personalization demonstration, we replaced this single parameter with an independent value for each individual to calibrate the response to the medications for each subject.

2.3.1 Pharmacokinetics

After patients are admitted for care at Cascadia Behavioral Healthcare, they transition to the treatment over the course of several months. Their BFCRS scores are tested on admittance and after they stabilize on the new treatment, and daily variations in behavior are not measured. Therefore, we base our model on average daily concentrations in the blood and brain to predict the long-term changes in the BFCRS score. To compute the average CSF concentration, C_{ave}, we apply the following function to the clinical daily dose for the synthesized data:

$$C_{ave} = \frac{F \cdot D}{CL \cdot \tau \cdot K_p \cdot M} \tag{4}$$

where F is the bioavailability, D is the daily dose (mg), CL is the clearance (mg/hr), τ is the dose interval (hr), K_p is the brain/blood transport ratio, and M is the molecular weight to convert (g/mol) to (nM). A linear response of plasma concentration to dose has been observed in individual patients for two of the medications in treatments (clozapine and lamotrigine), suggesting that the use of linear pharmacokinetics is allowed in our model.

2.3.2 Lamotrigine

There are three targets of lamotrigine in cortical pyramidal cells, the Na^+-current (Xie et al. 1995), the I_h-current (Poolos et al. 2002), and glutamate release (Wang et al. 2001). The first two of these reduce the excitability of pyramidal cells and the third reduces the excitatory output of these neurons. We represent the reduction in excitability in model parameters as an increase in the threshold, θ_1. The reduction in excitatory synaptic out put is represented as a reduction in excitatory weights, w_{11} and w_{10}.

2.3.2.1 Na^+-current

Lamotrigine reduces Na^+-current by blocking in Na^+ channels in pyramidal cells (Xie et al. 1995). We calculate a change in Na^+-current, I_{Na}, with a binding equation following a calculated lamotrigine concentration, C_{LTG},

$$\Delta I_{Na} = 1 - \frac{C_{LTG}}{(C_{LTG} + K_C)^n} \tag{5}$$

where $K_C = 513$ uM, $n = 0.9$. To affect the rate in the model, we reduce θ_1 by calculating the effect, $E_{Na} = 1 - p_{Lam}(1 - \Delta I_{Na})$, where $p_{Lam} = 0.15$. The reduction in the Na current increases the threshold in excitatory neurons by multiplicative factor, $\theta_1' = \theta_1 / E_{Na}$, where the prime indicates the modified parameter.

2.3.2.2 I_h-current

Lamotrigine shifts the I-V activation curve of the I_h current (Poolos et al. 2002) and decreased evoked firing rate, $\Delta x_1 = 1 - 0.004 * C_{LTG}$, for $\Delta x_1 > 0$ and where C_{LTG} is the average concentration of lamotrigine in CSF. To represent this effect in our model parameters, we modify the threshold, θ_1, in pyramidal cells. The shift in based on the spike probability function linearized near threshold $F_1(x_1) = 1/2 + (\mu_1/4)(x_1 - \theta_1)$, so that θ_1 will be increased by the effect, $E_h = 1 - p_{Lam}(1 - \Delta x_1)$, where $p_{Lam} = 0.15$. The reduction in the Na current increases the threshold in excitatory neurons by, $\theta_1' = \theta_1 / E_h$.

2.3.2.3 Glutamate release

Lamotrigine reduces glutamate release from excitatory synapses proportionally to the concentration C_{LTG} (Wang et al. (2001)), $\Delta G = 1 - 0.004 * C_{LTG}$ for $\Delta G > 0$. The excitatory synaptic parameters, w_{11} and w_{10}, are affected by the effect, $E_{glu} = 1 - p_{Lam}(1 - \Delta G)$, where $p_{Lam} = 0.15$. The reduction in the Glutamate release decreases the excitatory synaptic parameters by, $w_{11}' = w_{11} E_{glu}$ and $w_{10}' = w_{10} E_{glu}$.

2.3.3 Benzodiazepines

Benzodiazepines such as lorazepam increase $GABA_A$ currents following binding at the BZD receptor site. The increase in $GABA_A$ synaptic current is represented in the model as an increase in the inhibitory synaptic weights, w_{01} and w_{00}. To calculate the receptor occupation we follow results reported in (Miller et al. 1987):

$$R_{BZD} = \frac{(C_{Lor})^A}{(C_{Lor})^A + B} \tag{6}$$

where $A = 1.4328$, $B = 73.89$ (ng/gm), and C_{Lor} is the average concentration of lorazepam in CSF. The inhibitory synaptic

parameters, w_{01} and w_{00}, are modified in the model by increasing the inhibitory synaptic parameters proportionally to the receptor occupation, $\Delta w'_{11} = w_{11}(1 + R_{BZD})$ and $w'_{10} = w_{10}(1 + R_{BZD})$. All other benzodiazepines are treated in the same manner to increase inhibitory synaptic parameters.

2.3.4 Antipsychotics

These medications bind competitively with endogenous neurotransmitters to specific receptors. We use an exact form of the competitive binding formula (Wang 1995):

$$\begin{aligned} a &= K_A + K_B + C_A + C_B - 1 \\ b &= K_B(C_A - 1) + K_A(C_B - 1) + K_A K_B \\ c &= -K_A K_B \\ \delta &= \arccos\left(\frac{-2a^3 + 9ab - 27c}{2\sqrt{(a^2 - 3b)^3}}\right) \\ R_{oc} &= C_A \frac{2\sqrt{a^2 - 3b}\cos(\theta/3) - a}{3K_A + (2\sqrt{a^2 - 3b}\cos(\theta/3) - a)} \end{aligned} \tag{7}$$

where K_A is the binding affinity of the endogenous neurotransmitter, C_A is the average concentration of the endogenous neurotransmitter, K_B is the binding affinity of the medication, and C_B is the average concentration of the medication. R_{oc} is the receptor occupation by the endogenous neurotransmitter and will be used to estimate the activation level of the receptor. In this study, endogenous levels of neurotransmitters were dopamine (tonic) = 37 mM, dopamine (burst) = 200 mM, serotonin = 3.9 mM, and acetylcholine = 10 mM (Dreyer et al. 2010; Paterson et al. 2010).

2.3.4.1 D1 activation effect

The endogenous concentration at dopamine synapses depend on the firing pattering so that simulations estimate (Dreyer et al. 2010) that tonic activity yields 37 ± 1.2 nM and bursts yield 100–300 nM. According to data in (Lapish et al. 2007), D1 activation decreases the slope parameter (μ_1) of the rate function in excitatory neurons, $\mu'_1 = \mu_1(1 - (R_{oc} - R_{con})/R_{con})$, where R_{con} is the control level. D1 activation decreases the threshold (θ_0) in inhibitory interneurons, $\theta'_0 = \theta_0(1 - (R_{oc} - R_{con})/R_{con})$. D1 activation increases w_{11}, and w_{10} because at low concentrations (< 50 uM) by acting preferentially on D1-like receptors to increase NMDA receptor-mediated transmission (Lee et al. 2002), and increases w_{01}, that we represent by $w'_{ab} = w_{ab}(1 + (R_{oc} - R_{con})/R_{con})$ where $(a, b) = (1, 1)$, $(1, 0)$, and $(0, 1)$.

2.3.4.2 D2 activation effect

At high concentrations (≥100 uM) DA activates D2-like receptors and suppress NMDA function (Kotecha et al. 2002), that we represent by decreasing w_{11} and w_{10}, that we represent by $w'_{ab} = w_{ab}(1 - (R_{oc} - R_{con})/R_{con})$ where $(a, b) = (1, 1)$ and $(1, 0)$. D2 also Increases the slope parameter (μ_1) of probability function in excitatory neurons (pyramidal cells (Lapish et al. 2007), $\mu'_1 = \mu_1(1 + (R_{oc} - R_{con})/R_{con})$.

2.3.4.3 5-HT1A activation effect

The effect of 5-HT1A receptor activation has been found to increase the spike threshold in excitatory neurons (pyramidal cells, (Foehring 1996), and we model the effect as a linear increase in the threshold of excitatory neurons, $\theta'_1 = \theta_1(1 + (R_{oc} - R_{con})/R_{con})$.

2.3.4.4 5-HT2A activation effect

The effect of 5-HT2A receptor activation has been found to decreases the spike threshold in excitatory neurons (pyramidal cells, (Carr et al. 2002), and we model the effect as a linear decrease in the threshold of excitatory neurons, $\theta'_1 = \theta_1(1 - (R_{oc} - R_{con})/R_{con})$.

2.3.4.5 M1 activation effect

The effect of M1 receptor activation has been found to decreases the spike threshold in excitatory neurons (pyramidal cells) (Perez-Rosello et al. 2005), and we model the effect as a linear decrease in the threshold of excitatory neurons, $\theta'_1 = \theta_1(1 - (R_{oc} - R_{con})/R_{con})$.

2.4 Statistical analysis

Statistical analysis was performed on simulated data and model results using python SciPy v1.5.4 statistical functions (Virtanen et al. 2020) and by direct calculations. The effect sizes comparing before and after treatment were calculated as the difference between means of the two groups divided by a standard deviation for the data. The associated p-value is calculated with the one-way ANOVA test. The relationship between the clinical BFCRS scores and the barrier in the model was measured with the Pearson correlation (r) using a linear regression analysis.

3 Results

3.1 Synthesized data

A summary of the synthesized dataset used in this study is shown in Figure 2, and the statistics of the medication combinations and dose ranges are consistent with the clinical patient data set. The mean BFCRS score before treatment is 17.3 ± 3.9 (std) and after treatment is 4.1 ± 2.8, resulting in an effect size of 2.7 ($p < 10^{-20}$) for the treatment (Figure 2A). The treatment results in a reduction in the BFCRS score for all subjects, with a minimum reduction of 9, and a maximum of 23.

In Figure 2B we show a histogram of the number of medications for each subject to demonstrate that the patients transition from a broad range of care to a more limited set of medications. The distribution of doses for medications upon admission (pre-treatment) and following stabilization of the

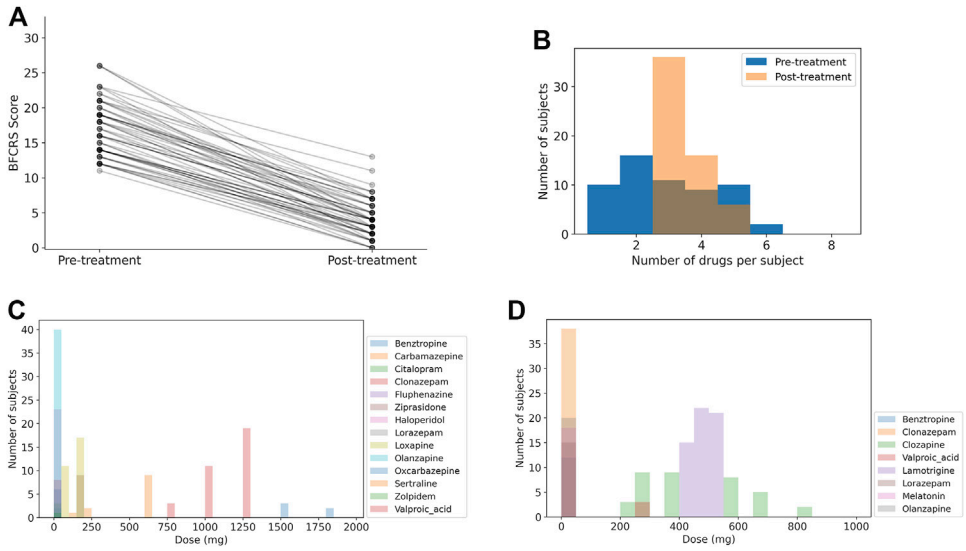

FIGURE 2
Summary of synthesized data. Note that the number of medications and distributions of doses is more restricted after treatment has stabilized. **(A)** BFCRS score for 58 synthesized data subjects before and after treatment. **(B)** Distribution of medication doses across all subjects before treatment. **(C)** Distribution of medication doses across all subjects after treatment. **(D)** Distribution of the number of medications for each subject before and after treatment.

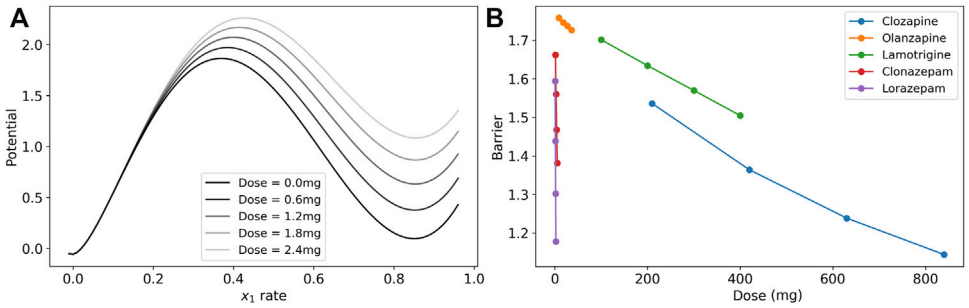

FIGURE 3
Dose response of the model barrier to medications. **(A)** Dose response of potential function (line integral of $\dot{x_1}$ in Eq. 1 on the x_0-nullcline) to show how the barrier becomes smaller with increasing doses of lorazepam. The two stable fixed points are where the excitatory rate is 0 and ~0.85. The peak of the barrier is the unstable fixed point where the excitatory rate is ~0.4. The vertical distance from the high-rate basin to the unstable peak is the barrier. **(B)** Dose response of model parameters for clozapine, olanzapine, lamotrigine, clonazepam, and lorazepam. The barrier between the high-rate state and the low-rate state for these medications is reduced in the treatment.

treatment (post-treatment) are shown in Figures 2C,D. Again, we see that the diversity of medications is reduced to focus treatment on catatonia symptoms with the minimal set of medications to simplify care.

3.2 Dose sensitivity

We visualize the change in the barrier in Figure 3A for the case of lorazepam. At the dose = 0.0 mg (black line), there are two minima in the potential of the model where the excitatory rate is zero and near 90%. The maximum near 40% is the unstable fixed point that is the boundary between the two states. As the dose increases (lighter gray lines) the depth of the higher-rate state decreases at a faster rate than the height of the unstable fixed point, and the depth of the potential well is reduced. This reduction in the depth (reduction of the boundary) is interpreted as a reduction of symptoms of catatonia because patients are less likely to become stuck in particular high-rate activity patterns.

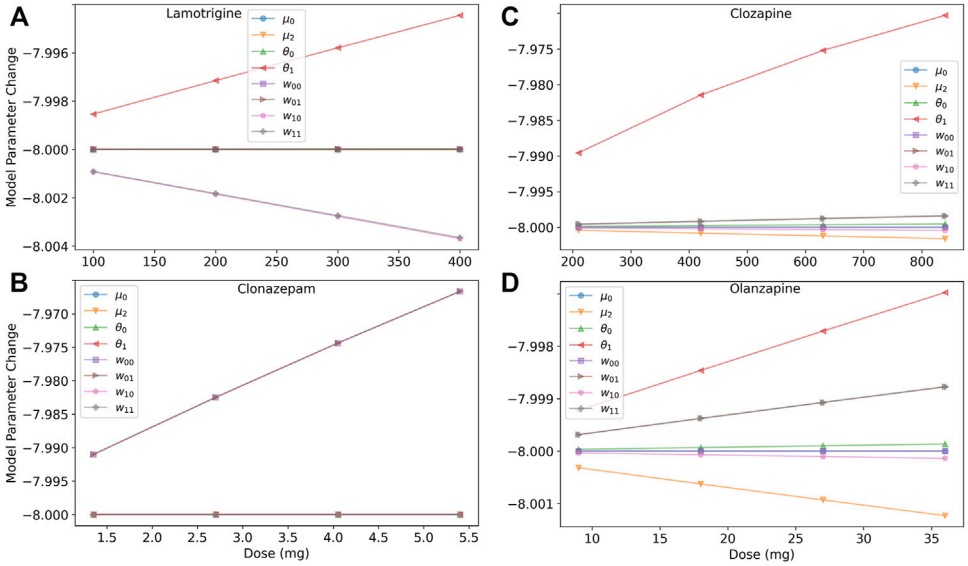

FIGURE 4
Dose response of model parameters for lamotrigine, clonazepam, clozapine, and olanzapine. **(A)** The dose response of the model's parameters for lamotrigine shows that the threshold of excitatory neurons (θ_1) increases with increasing dose leading to a decrease of the neurons' excitability. The excitatory synaptic parameters (w_{11} and w_{10}) decrease leading to a reduced excitation of the system. **(B)** The dose response of the model's parameters for clozapine shows that several parameters are affected, but the largest effect is an increase of the threshold in excitatory neurons (θ_1) due to blocking M1 and 5-HT2A receptors reducing the excitation of the system. **(C)** The dose response of the model's parameters for olanzapine shows less of a an increase in the threshold in excitatory neurons than clozapine, and a finer scale view of the other model parameters. **(D)** The dose response of the model's parameters for clonazepam show that only the inhibitory synaptic parameters are affected.

To illustrate the effects of each medication in the post-treatment cases, we calculated the model barrier height across the range of doses from the clinical data and tested the model for the change in the barrier for lamotrigine, two benzodiazepines, and two antipsychotics (Figure 3B). Each of the medication in the figure reduced the barrier in a nearly linear dose response in this range as demonstrated by a linear regression analysis that finds that $r^2 > 0.99$ ($p < 0.01$) in all cases except clozapine where $r^2 > 0.98$ ($p < 0.01$).

The three classes of medications, lamotrigine, benzodiazepines, and antipsychotics, affect the system through different mechanisms of action. Lamotrigine acts to reduce excitation by both reducing the excitability of the excitatory neuron population and reducing the excitatory synaptic weights. The benzodiazepines act through increasing the inhibitory synaptic weights to reduce the boundary between states.

The antipsychotics have more complicated mechanisms of action through dopamine, serotonin, and muscarinic receptors. We model two types of dopamine receptors, D1 and D2. In our model, D1 receptor activation decrease the excitability of the excitatory neuron population and increase the excitability of the inhibitory neuron population, both contributing to increasing barrier when D1 receptors are blocked by antipsychotics. However, D1 activation also increases excitatory synaptic transmission to have the opposite effect on the barrier by antipsychotics that block D1. The D2 receptor activation reduces excitatory synaptic transmission and increases the excitability of the excitatory neuron population leading to opposite effects. Activation of the two serotonin receptors included the model (5-HT1A and 5-HT2A) have opposite effects on the excitability of the excitatory neuron population, and M1 receptor activation increases their excitability. The affect of each antipsychotic depends on the affinity of the molecule to each receptor in competition with the background level of neurotransmitter, and we find that there is a net decrease in the barrier for increasing dose of both clozapine and olanizapine. Clozapine has a more mixed effect on several parameters with the largest effect on the threshold of excitatory neuron that reduces their overall excitability.

To help untangle the competing effects of the medications, we investigated the dose response of model parameters, as shown in Figure 4. Lamotrigine reduces excitability of excitatory neurons through the threshold by increasing θ_1, and reduces the excitatory synaptic weights, w_{10} and w_{11} (Figure 4A) The benzodiazepine (clonazepam, Figure 4B) has the simplest action and affects only the inhibitory synaptic weights (w_{00} and w_{01}) in the model. The increased inhibition in the system reduced the overall excitability, weakening the high-rate state and reducing the boundary. The antipsychotics affect multiple parameters

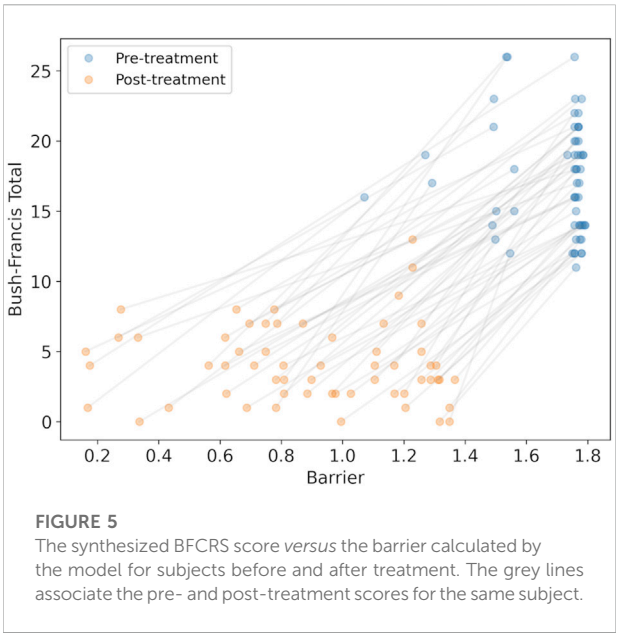

FIGURE 5
The synthesized BFCRS score *versus* the barrier calculated by the model for subjects before and after treatment. The grey lines associate the pre- and post-treatment scores for the same subject.

(Figures 4C,D), but the cumulative effect is to reduce barrier height. Clozapine has a stronger effect on the threshold θ_1 than olanzapine leading to a greater reduction of the barrier.

3.3 BFCRS clinical scale

We calculated the changes in the model parameter for each synthesized subject caused by medications at admission, and then after treatment was stabilized. With the modified parameters we could calculated the barrier between the high-rate state and the low-rate state to observe whether the barrier was reduced. A reduction in the barrier is interpreted as an improvement in catatonic symptoms. We find that the barrier was reduced in all cases (mean reduction 0.80 ± 0.32, with minimum reduction of 0.19), consistent with clinical observations. We could then compare the BFCRS clinical score with the barrier to visualize the effect of the treatment (Figure 5).

There is a clear reduction in the barrier (effect size = 2.14, $p < 10^{-20}$), consistent with the reduction in BFCRS score. However, there appears to be poor individual prediction by the model as observed in the even distribution of the changes across the subjects before and after treatment in Figure 5, and a linear regression results in $r^2 = 0.53$. To test the reliability of the model in predicting changes in individual cases, we compared the change in BFCRS score and barrier and found a correlation of $r^2 = 0.11$ ($p < 0.01$). We have confirmed that this is not due to lost correlations in our synthesized data, and may be attributed to individual differences between subjects in both their pre-treatment disease state and their response to the medications.

3.4 Combination efficacy

The combination of medications in the treatment has been clinically observed to be additive, and this observation can be explained by the parallel mechanisms of action. Lamotrigine and the benzodiazepines act on different sites, excitatory neurons and inhibitory synapses. Although the antipsychotics have some overlap with these parameters in the model, they act through different receptors. In the dynamic range of medication effects on the barrier size, the dose response is nearly linear, and we find an additive effect of the combination (Figure 6A). To relate the effect back to the clinic, we can use a linear mapping between the BFCRS score and the boundary to interpret the boundary as a BFCRS score and predict the effect of each medication and their combinations on the average subject. We calculate the mean BFCRS score and mean barrier for the population, before and after the treatment to obtain the mapping, and then plot the BFCRS score in Figure 6B.

3.5 Personalization

The model is good at predicting large changes in BFCRS score for the population as a whole, but more exact predictions of individuals should be possible with further parametrization. Ultimately, the model could then be used as a tool for informing clinical care and refining treatments. Because the model has few parameters to tune, then each subject could have a personalized model for use in the clinic. We personalized the model by calibrating the initial state with model parameters, and then adjusted the dose response parameter for each individual subject.

The first adjustment was to tune individual Wilson-Cowan model based on the initial BFCRS score for each patient. The barrier size can be adjusted in the Wilson-Cowan model so that patients with high BFCRS scores will have a corresponding model with a high barrier. We have attempted to tune the w_{01} model parameter to this end, but no clear result could be seen in the correlation of the outcomes to treatment. Further research will be needed to determine whether different model parameters need to be tuned to be more representative of the pathology underlying catatonia.

The second adjustment was to calibrate the individual dose response with model coupling parameters to the effect on BFCRS score. As patients are admitted to the residence, they transition their medication to the new regimen, and measures of the BFCRS score inform how each individual is affected by removing and adding medications. These changes in BFCRS score could be used to calibrate individual mechanisms and how they couple to model parameters. Such a tuning could create a model that will adapt along with the patient, and improves in its prediction power over time.

The results of these two modification are shown in Figure 7 where the new prediction of the barrier is compared with the

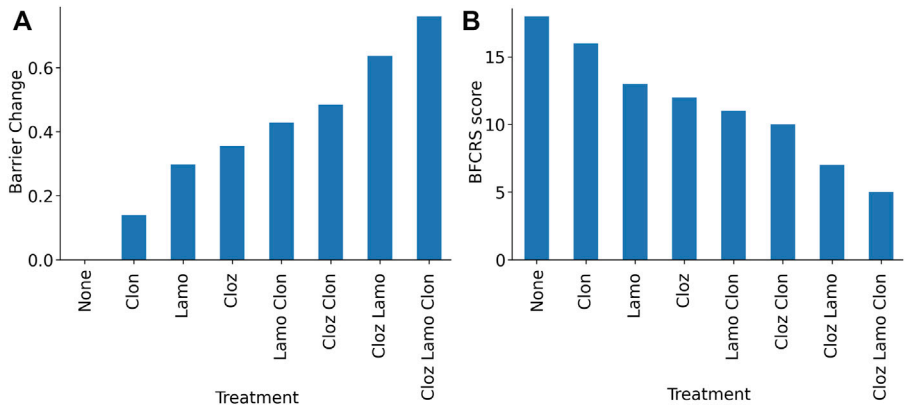

FIGURE 6
Model results for combinations of lamotrigine, clozapine, and clonazepam demonstrating the additive effects. **(A)** Barrier for combinations of medications in the treatment protocol. **(B)** Predicted BFCRS for combinations of medications in the treatment protocol.

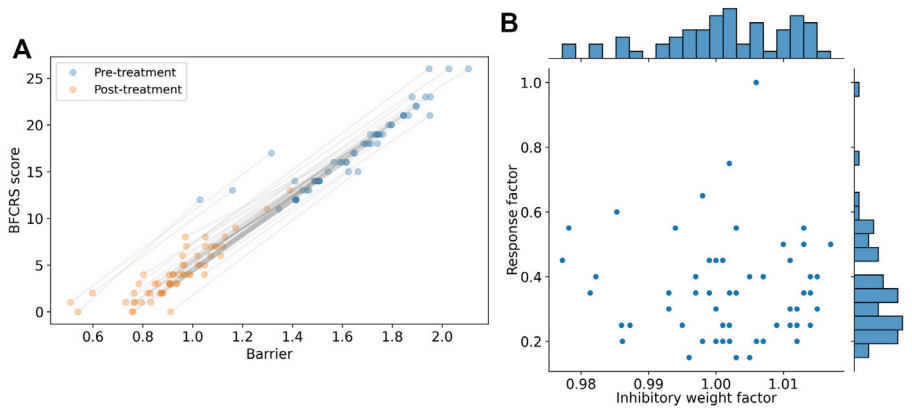

FIGURE 7
Demonstration of personalization potential of the model for individualized clinical predictions. **(A)** Personalized model prediction of barrier and the synthesized BFCRS score for subjects before and after treatment. The grey lines associate the pre- and post-treatment scores for the same subject. **(B)** Scatter plot and histograms of the parameters used for personalization (Inhibitory weight factor to modify w_{00} and the medication response factor). The scatter plot reveals no significant correlation between the personalization parameters ($r^2 = 0.001$ and $p > 0.7$).

BFCRS score. We find a higher correlation between the model barrier and the clinical score ($r^2 = 0.97$) and our comparison of the change in BFCRS score and barrier across individual yields a correlation of $r^2 = 0.92$ ($p < 10^{-30}$). These results give confidence that the effects predicted by the model can guide further changes in medication, and aid the psychiatrist in clinical decisions.

4 Discussion

The objective of this study was to demonstrate that a simple cortical model, with excitatory and inhibitory neural populations, is sufficiently descriptive to explain and predict clinical outcomes in schizophrenia patients with catatonia. The pharmaceutical coupling of the treatments to model parameters are based on known mechanisms of action in cortical neurons: pyramidal cells and parvalbumin positive inhibitory interneurons. We have demonstrated the utility of the model for explaining the observed clinical outcomes by tracing the action of medications to changes in the model dynamics by interpreting the change in the barrier between states as a change in a clinical measure, the BFCRS score. The model supports the clinical observation that the 3-medication combination, clozapine, lamotrigine, and a benzodiazepine, is additive, and explains how the pathways of action are independent on a mechanistic level. Finally, we took a first step at personalization of the model for individual subjects, with the goal of supporting individual clinical decisions with mechanistic explanations.

Augmenting psychiatric practice with a simple mechanistic model encourages a conceptual shift to a focus on reducing cortical excitability, either through reducing excitability of pyramidal neurons, or increasing inhibition. Each of the three medications are optimized on their own for safety and efficacy, but since they act on the excitability of the system through different mechanisms, they can have an additive effect on catatonic symptoms. Further use of this approach can suggest other means of controlling cortical excitability and inspire new treatment protocols.

Conceptualizing the action of this treatment as modifying excitability and connectivity of neuron populations also suggests mechanisms of observed clinical improvements. The clinical observation that reduced chronic catatonic features lead to meaningful improvements in social and cognitive function suggests that reducing the barrier represents a physical improvement in brain network connectivity and dynamical processing. Bursts of neural activity that control behavioral patterns become more flexible with a reduced barrier between states of excitation, and that flexibility leads to more fluid cognitive function and social behavior.

4.1 Extensions of the model

The model is based on cortical circuitry, in part because catatonia is thought to have a cortical origin. However, antipsychotics also target the striatum. Extending the model to include a cortical-striatum-thalamic loop would include additional dynamics that are presently missing. As yet, it is unknown if such an extension will add a precision that is visible in clinical usage, but this would be a rich area to explore.

One avenue to improve the model's predictions is to further personalize the model by individualizing the pharmacokinetics for each patient. When clozapine is administered, safety considerations require blood samples, and blood levels of clozapine have been recorded from many patients in this cohort. There is a wide variation in the dose response to blood serum concentration of clozapine, and these variations are not currently included in the model. We have tested the robustness of our results to ensure this observed variance does not affect the conclusions in this study, but clearly such an addition to the model will help to refine individual cases.

Clinically the BFCRS score can be low in lower functioning individuals and high in higher functioning individuals. There may be a correlation with changes in score and functional status for a population, but it is not yet clear with individual cases. Big changes can lead to little benefit sometimes, small changes can lead to large benefits. Additional neural circuitry in the model, such as a striatal-thalamic loop may help to explain a separation between BFCRS score and overall function. Such modification could be aided by analysis with a larger subject pool that may help to discern subgroups in responses to treatment.

Further clinical variables may provide new insights into how model outputs can be interpreted. Although the BFCRS score has provided a good clinical guidance for this cohort, the addition of either cognitive or motor measures could augment the model's interpretation. Furthermore, additional clinical measures could add constraints that require a more detailed model, such as adding a striatum, that the BFCRS score alone will not capture. Although further complications may degrade the causal interpretability because of added complex dynamics, there are likely parameter regions with simpler dynamics that may broaden the applicability to other symptoms of psychiatric disease.

Data availability statement

The datasets generated for this study can be found in the repo for Cascadia-Behavioral-Healthcare: https://github.com/pdroberts/cascadia-behavioral-healthcare.git.

Author contributions

JC was in charge of clinical care and worked with PR to synthesize data with statistics similar to clinical practice and observations. PR developed the model and visualizations and wrote the initial draft of the manuscript. Both authors contributed equally on planning and finalizing the manuscript.

Conflict of interest

Author PR was employed by the company Amazon Web Services. Author JC was employed by the company Cascadia Behavioral Healthcare. This research does not relate to PDR's position or activities at Amazon Web Services.

Publisher's note

Supplementary material

The Supplementary Material for this article can be found online at: https://www.frontiersin.org/articles/10.3389/fphar.2022.1025417/full#supplementary-material

References

Bagi, B., Brecht, M., and Sanguinetti-Scheck, J. I. (2022). Unsupervised discovery of behaviorally relevant brain states in rats playing hide-and-seek. *Curr. Biol.* 32, 2640–2653. doi:10.1016/j.cub.2022.04.068

Benayoun, M., Cowan, J. D., van Drongelen, W., and Wallace, E. (2010). Avalanches in a stochastic model of spiking neurons. *PLoS Comput. Biol.* 6, e1000846. doi:10.1371/journal.pcbi.1000846

Bhati, M. T., Datto, C. J., and O'Reardon, J. P. (2007). Clinical manifestations, diagnosis, and empirical treatments for catatonia. *Psychiatry.* 4, 46–52.

Bressloff, P. C. (2010). Metastable states and quasicycles in a stochastic Wilson-cowan model of neuronal population dynamics. *Phys. Rev. E Stat. Nonlin. Soft Matter Phys.* 82, 051903. doi:10.1103/PhysRevE.82.051903

Buice, M. A., Cowan, J. D., and Chow, C. C. (2010). Systematic fluctuation expansion for neural network activity equations. *Neural Comput.* 22, 377–426. doi:10.1162/neco.2009.02-09-960

Bush, G., Fink, M., Petrides, G., Dowling, F., and Francis, A. (1996). Catatonia. i. rating scale and standardized examination. *Acta Psychiatr. Scand.* 93, 129–136. doi:10.1111/j.1600-0447.1996.tb09814.x

Carr, D. B., Cooper, D. C., Ulrich, S. L., Spruston, N., and Surmeier, D. J. (2002). Serotonin receptor activation inhibits sodium current and dendritic excitability in prefrontal cortex via a protein kinase c-dependent mechanism. *J. Neurosci.* 22, 6846–6855. doi:10.1523/JNEUROSCI.22-16-06846.2002

Conour, J. (2015). *Compositions and methods for the treatment of catatonia.* US Patent 9,066,949.

Cowan, J. D., Neuman, J., and van Drongelen, W. (2016). Wilson–cowan equations for neocortical dynamics. *J. Math. Neurosci.* 6, 1–24. doi:10.1186/s13408-015-0034-5

Dreyer, J. K., Herrik, K. F., Berg, R. W., and Hounsgaard, J. D. (2010). Influence of phasic and tonic dopamine release on receptor activation. *J. Neurosci.* 30, 14273–14283. doi:10.1523/JNEUROSCI.1894-10.2010

Foehring, R. C. (1996). Serotonin modulates n-and p-type calcium currents in neocortical pyramidal neurons via a membrane-delimited pathway. *J. Neurophysiol.* 75, 648–659. doi:10.1152/jn.1996.75.2.648

Geerts, H., Roberts, P., and Spiros, A. (2013). A quantitative system pharmacology computer model for cognitive deficits in schizophrenia. *CPT. Pharmacometrics Syst. Pharmacol.* 2, e36–e38. doi:10.1038/psp.2013.12

Gray, J. A., and Risch, S. C. (2009). When clozapine is not enough: Augment with lamotrigine? *Curr. Psychiatry* 8, 40–47.

Hirjak, D., Kubera, K. M., Northoff, G., Fritze, S., Bertolino, A. L., Topor, C. E., et al. (2019). Cortical contributions to distinct symptom dimensions of catatonia. *Schizophr. Bull.* 45, 1184–1194. doi:10.1093/schbul/sby192

Katori, Y., Sakamoto, K., Saito, N., Tanji, J., Mushiake, H., and Aihara, K. (2011). Representational switching by dynamical reorganization of attractor structure in a network model of the prefrontal cortex. *PLoS Comput. Biol.* 7, e1002266. doi:10.1371/journal.pcbi.1002266

Kotecha, S. A., Oak, J. N., Jackson, M. F., Perez, Y., Orser, B. A., Van Tol, H. H., et al. (2002). A D2 class dopamine receptor transactivates a receptor tyrosine kinase to inhibit NMDA receptor transmission. *Neuron* 35, 1111–1122. doi:10.1016/s0896-6273(02)00859-0

Lapish, C. C., Kroener, S., Durstewitz, D., Lavin, A., and Seamans, J. K. (2007). The ability of the mesocortical dopamine system to operate in distinct temporal modes. *Psychopharmacology* 191, 609–625. doi:10.1007/s00213-006-0527-8

Lee, F. J., Xue, S., Pei, L., Vukusic, B., Chéry, N., Wang, Y., et al. (2002). Dual regulation of nmda receptor functions by direct protein-protein interactions with the dopamine d1 receptor. *Cell* 111, 219–230. doi:10.1016/s0092-8674(02)00962-5

Miller, L. G., Greenblatt, D. J., Paul, S. M., and Shader, R. I. (1987). Benzodiazepine receptor occupancy *in vivo*: Correlation with brain concentrations and pharmacodynamic actions. *J. Pharmacol. Exp. Ther.* 240, 516–522.

Negahbani, E., Steyn-Ross, D. A., Steyn-Ross, M. L., Wilson, M. T., and Sleigh, J. W. (2015). Noise-induced precursors of state transitions in the stochastic Wilson–cowan model. *J. Math. Neurosci.* 5, 9–27. doi:10.1186/s13408-015-0021-x

Northoff, G., Kötter, R., Baumgart, F., Danos, P., Boeker, H., Kaulisch, T., et al. (2004). Orbitofrontal cortical dysfunction in akinetic catatonia: A functional magnetic resonance imaging study during negative emotional stimulation. *Schizophr. Bull.* 30, 405–427. doi:10.1093/oxfordjournals.schbul.a007088

Northoff, G. (2002). What catatonia can tell us about "top-down modulation": A neuropsychiatric hypothesis. *Behav. Brain Sci.* 25, 555–577. doi:10.1017/s0140525x02000109

Paterson, L. M., Tyacke, R. J., Nutt, D. J., and Knudsen, G. M. (2010). Measuring endogenous 5-ht release by emission tomography: Promises and pitfalls. *J. Cereb. Blood Flow. Metab.* 30, 1682–1706. doi:10.1038/jcbfm.2010.104

Patki, N., Wedge, R., and Veeramachaneni, K. (2016). "The synthetic data vault," in *2016 IEEE international conference on data science and advanced analytics (DSAA)* (New Jersey, United States: IEEE), 399–410.

Penland, H. R., Weder, N., and Tampi, R. R. (2006). The catatonic dilemma expanded. *Ann. Gen. Psychiatry* 5, 14. doi:10.1186/1744-859X-5-14

Perez-Rosello, T., Figueroa, A., Salgado, H., Vilchis, C., Tecuapetla, F., Guzman, J. N., et al. (2005). Cholinergic control of firing pattern and neurotransmission in rat neostriatal projection neurons: Role of cav2. 1 and cav2. 2 ca2+ channels. *J. Neurophysiol.* 93, 2507–2519. doi:10.1152/jn.00853.2004

Poolos, N. P., Migliore, M., and Johnston, D. (2002). Pharmacological upregulation of h-channels reduces the excitability of pyramidal neuron dendrites. *Nat. Neurosci.* 5, 767–774. doi:10.1038/nn891

Rosebush, P. I., and Mazurek, M. F. (2010). Catatonia and its treatment. *Schizophr. Bull.* 36, 239–242. doi:10.1093/schbul/sbp141

Roth, B., and Lopez, E. (2006). Psychoactive drug screening program Ki database. Available at: https://kidbdev.med.unc.edu/databases/downloadki.html.

Spiros, A., Carr, R., and Geerts, H. (2010). Not all partial dopamine d2 receptor agonists are the same in treating schizophrenia. exploring the effects of bifeprunox and aripiprazole using a computer model of a primate striatal dopaminergic synapse. *Neuropsychiatr. Dis. Treat.* 6, 589–603. doi:10.2147/NDT.S12460

Tiihonen, J., Hallikainen, T., Ryynänen, O.-P., Repo-Tiihonen, E., Kotilainen, I., Eronen, M., et al. (2003). Lamotrigine in treatment-resistant schizophrenia: A randomized placebo-controlled crossover trial. *Biol. Psychiatry* 54, 1241–1248. doi:10.1016/s0006-3223(03)00524-9

Ungvari, G. S., Leung, S. K., Ng, F. S., Cheung, H.-K., and Leung, T. (2005). Schizophrenia with prominent catatonic features ('catatonic schizophrenia'): I. Demographic and clinical correlates in the chronic phase. *Prog. Neuropsychopharmacol. Biol. Psychiatry* 29, 27–38. doi:10.1016/j.pnpbp.2004.08.007

Virtanen, P., Gommers, R., Oliphant, T. E., Haberland, M., Reddy, T., Cournapeau, D., et al. (2020). SciPy 1.0: Fundamental algorithms for scientific computing in Python. *Nat. Methods* 17, 261–272. doi:10.1038/s41592-019-0686-2

Wang, S.-J., Sihra, T. S., and Gean, P.-W. (2001). Lamotrigine inhibition of glutamate release from isolated cerebrocortical nerve terminals (synaptosomes) by suppression of voltage-activated calcium channel activity. *Neuroreport* 12, 2255–2258. doi:10.1097/00001756-200107200-00042

Wang, Z.-X. (1995). An exact mathematical expression for describing competitive binding of two different ligands to a protein molecule. *FEBS Lett.* 360, 111–114. doi:10.1016/0014-5793(95)00062-e

Wilcox, J. A., and Reid Duffy, P. (2015). The syndrome of catatonia. *Behav. Sci.* 5, 576–588. doi:10.3390/bs5040576

Wilson, H. R., and Cowan, J. D. (1972). Excitatory and inhibitory interactions in localized populations of model neurons. *Biophys. J.* 12, 1–24. doi:10.1016/S0006-3495(72)86068-5

Xie, X., Lancaster, B., Peakman, T., and Garthwaite, J. (1995). Interaction of the antiepileptic drug lamotrigine with recombinant rat brain type iia na+ channels and with native na+ channels in rat hippocampal neurones. *Pflugers Arch.* 430, 437–446. doi:10.1007/BF00373920

frontiers | Frontiers in Pharmacology

TYPE Original Research
PUBLISHED 12 January 2023
DOI 10.3389/fphar.2022.1090554

OPEN ACCESS

EDITED BY
Victor Mangas Sanjuan,
University of Valencia, Spain

REVIEWED BY
Francine Johansson Azeredo,
University of Florida, United States
Leyanis Rodriguez Vera,
University of Florida, United States

*CORRESPONDENCE
Robin Michelet,
robin.michelet@fu-berlin.de

SPECIALTY SECTION
This article was submitted to Translational Pharmacology, a section of the journal Frontiers in Pharmacology

RECEIVED 05 November 2022
ACCEPTED 23 December 2022
PUBLISHED 12 January 2023

CITATION
Michelet R, Bindellini D, Melin J, Neumann U, Blankenstein O, Huisinga W, Johnson TN, Whitaker MJ, Ross R and Kloft C (2023), Insights in the maturational processes influencing hydrocortisone pharmacokinetics in congenital adrenal hyperplasia patients using a middle-out approach.
Front. Pharmacol. 13:1090554.
doi: 10.3389/fphar.2022.1090554

Insights in the maturational processes influencing hydrocortisone pharmacokinetics in congenital adrenal hyperplasia patients using a middle-out approach

Robin Michelet[1]*, Davide Bindellini[1,2], Johanna Melin[1,2], Uta Neumann[3], Oliver Blankenstein[3], Wilhelm Huisinga[4], Trevor N. Johnson[5], Martin J. Whitaker[6], Richard Ross[6,7] and Charlotte Kloft[1]

[1]Department of Clinical Pharmacy and Biochemistry, Institute of Pharmacy, Freie Universitaet Berlin, Berlin, Germany, [2]Graduate Research Training Program, Berlin, Germany, [3]Clinic for Pediatric Endocrinology and Diabetology, Charité-Universitätsmedizin, Berlin, Germany, [4]Institute of Mathematics, Universität Potsdam, Potsdam, Germany, [5]Certara UK Limited, Simcyp Division, Sheffield, United Kingdom, [6]Department of Oncology and Metabolism, University of Sheffield, Sheffield, United Kingdom, [7]Diurnal Limited, Cardiff, United Kingdom

Introduction: Hydrocortisone is the standard of care in cortisol replacement therapy for congenital adrenal hyperplasia patients. Challenges in mimicking cortisol circadian rhythm and dosing individualization can be overcome by the support of mathematical modelling. Previously, a non-linear mixed-effects (NLME) model was developed based on clinical hydrocortisone pharmacokinetic (PK) pediatric and adult data. Additionally, a physiologically-based pharmacokinetic (PBPK) model was developed for adults and a pediatric model was obtained using maturation functions for relevant processes. In this work, a middle-out approach was applied. The aim was to investigate whether PBPK-derived maturation functions could provide a better description of hydrocortisone PK inter-individual variability when implemented in the NLME framework, with the goal of providing better individual predictions towards precision dosing at the patient level.

Methods: Hydrocortisone PK data from 24 adrenal insufficiency pediatric patients and 30 adult healthy volunteers were used for NLME model development, while the PBPK model and maturation functions of clearance and cortisol binding globulin (CBG) were developed based on previous studies published in the literature.

Results: Clearance (CL) estimates from both approaches were similar for children older than 1 year (CL/F increasing from around 150 L/h to 500 L/h), while CBG concentrations differed across the whole age range (CBG_{NLME} stable around 0.5 μM vs. steady increase from 0.35 to 0.8 μM for CBG_{PBPK}). PBPK-derived maturation functions were subsequently included in the NLME model. After inclusion of the maturation functions, none, a part of, or all parameters were re-estimated. However, the inclusion of CL and/or CBG maturation functions in the NLME model did not result in improved model performance for the CL maturation function (ΔOFV > −15.36) and the re-estimation of parameters using the CBG maturation function most often led to unstable models or individual CL prediction bias.

Discussion: Three explanations for the observed discrepancies could be postulated, i) non-considered maturation of processes such as absorption or first-pass effect, ii) lack of patients between 1 and 12 months, iii) lack of correction of PBPK CL maturation functions derived from urinary concentration ratio data for the renal function relative to adults. These should be investigated in the future to determine how NLME and PBPK methods can work towards deriving insights into pediatric hydrocortisone PK.

KEYWORDS

hydrocortisone, congenital adrenal hyperplasia, population pharmacokinetics, middle-out approach, pediatrics, physiologically-based pharmacokinetics (PBPK), non-linear mixed effects modelling (NLME), maturation

1 Introduction

Congenital adrenal hyperplasia (CAH), a disease which leads to very low to no cortisol synthesis, is the commonest cause of adrenal deficiency in childhood. Patients have an increased morbidity and mortality in adult life that may in part relate to suboptimal glucocorticoid therapy in their early years of life (Finkielstain et al., 2012; Han et al., 2014; Bancos et al., 2015; Bornstein et al., 2016). Lifelong glucocorticoid replacement therapy with hydrocortisone is standard of care for CAH patients and personalized replacement therapy through precision medicine is essential in optimizing care (Merke and Bornstein, 2005; Hindmarsh, 2009; Kamoun et al., 2013). Hydrocortisone, which is chemically the same as endogenous cortisol, is administered multiple times per day due to its short terminal half-life and to approximate the physiological cortisol circadian rhythm (Knutson et al., 1997; Hindmarsh and Charmandari, 2015). Therefore, treating pediatricians are constantly faced with the risk of over- and under-dosing their patients, which may lead to complications of excess steroid therapy (Falhammar et al., 2014) and adrenal crisis (El-Maouche et al., 2018), respectively.

Mathematical models to investigate and quantify the sources of intra- and inter-individual variability (IIV) in pharmacokinetics (PK) and pharmacodynamics (PD) of drugs can help to support the choice of the right dose at the right time for the right patient in the form of model-informed precision dosing (Kluwe et al., 2020). This approach would be of value in helping optimize and individualize hydrocortisone replacement in neonates, infants and older children with CAH. To do this, a mathematical model needs to be able to describe the underlying processes in sufficient detail to capture the succinct parts while still being able to quantify and explain sources of variability to apply model predictions at the individual level. For the individualization of hydrocortisone treatment in (especially young) children, this means foremost an acceptable characterization of the PK of this endogenous compound across the pediatric age range.

Recently, both non-linear mixed effects (NLME) modelling of clinical data (the so-called 'top-down' approach) and physiologically-based pharmacokinetic (PBPK) modelling (the so-called 'bottom-up' approach) were applied to describe the PK of hydrocortisone (Melin et al., 2017; Michelet et al., 2020; Bonner et al., 2021). In the first approach, the authors were able to use clinical pediatric hydrocortisone PK data from CAH patients in combination with adult data to inform an NLME model quantifying the IIV in hydrocortisone PK across the pediatric age range (Melin et al., 2017), which was then optimized and used to simulate possible optimized dosing regimens (Michelet et al., 2020). However, the available clinical data was too sparse to quantify an impact of age on the PK parameters after taking body weight into consideration. In the second approach, a PBPK model was developed and qualified for hydrocortisone PK in adults, which was then combined with ontogeny functions obtained from literature data for the relevant processes to obtain a pediatric PBPK model (Bonner et al., 2021). These ontogeny functions focused on the maturation of 5α-reductase, 11-β hydroxysteroid dehydrogenase 2 (11-βHSD2), and cortisol binding globulin (CBG), known to be influential on hydrocortisone PK (Hadjian et al., 1975; Walker and Seckl, 2003; Wudy et al., 2007). A third approach to describe PK variability based on both aforementioned approaches, the so-called 'middle-out' approach was recently applied in pediatric PK modeling as combining the 'best-of-two-worlds' but has thus far not been applied to pediatric hydrocortisone PK (Tsamandouras et al., 2013; Michelet et al., 2018a; Michelet et al., 2018b; Germovsek et al., 2018). The benefit of this approach would be that the physiological insights coming from a PBPK approach could be implemented within the hierarchical variability quantification framework of an NLME approach, allowing for individual predictions of hydrocortisone PK and the application of stochastic simulations for evaluation of personalized dosing strategies.

In this manuscript, we investigated whether using such a middle-out approach by implementing the PBPK-derived insights regarding maturation of hydrocortisone PK processes into an NLME-framework based on available clinical data could better describe the interindividual variability of hydrocortisone PK, paving the way for model-based precision medicine dosing of hydrocortisone, particularly in pediatric CAH patients.

2 Methods

2.1 Patient characteristics and study design

The patient populations used in this work has been described elsewhere (Melin et al., 2017; Melin et al., 2020; Michelet et al., 2020). In short, for the pediatric patients, cortisol concentrations were collected in an open label, phase 3, single center clinical trial conducted at the Institute of Experimental Paediatric Endocrinology at Charité-Universitätsmedizin Berlin, CVK, Berlin (EudraCT number: 2014–002265-30). Written informed consent was given by parents/guardian and the study was approved by the relevant independent ethics committee (Ethics committee of Berlin, No. 14/0517- EK 12). Paediatric patients with adrenal insufficiency (23 with congenital adrenal hyperplasia and 1 with hypopituitarism) aged from birth to 6 years were included. One dose of individualized hydrocortisone granules (Alkindi®, Diurnal Europe B.V., Netherlands), corresponding to the individual standard morning dose (1–4 mg) was administered in the morning upon arrival to

10.3389/fphar.2022.1090554

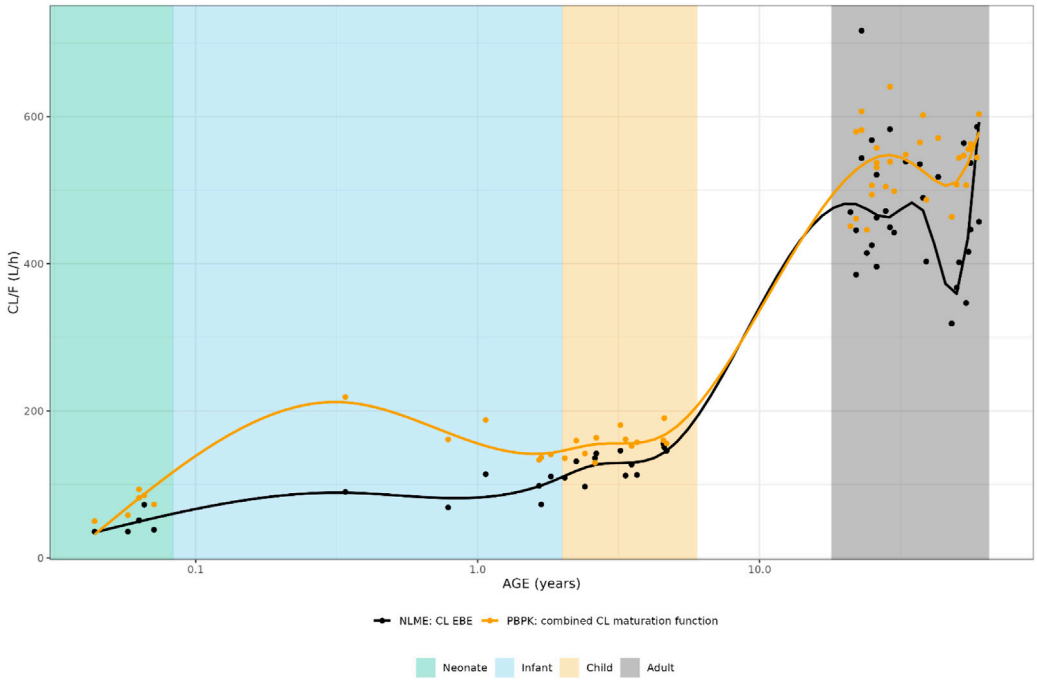

FIGURE 1
Comparison of individual apparent hydrocortisone clearance for neonates, infants, children and adults after administration of a pediatric formulation of hydrocortisone. The closed circles represent the individual values taking body weight (non-linear mixed effects model) or body weight and age (maturation function) into account. The lines represent Loess smoothers through the individual values. Age shown on a logarithmic scale.

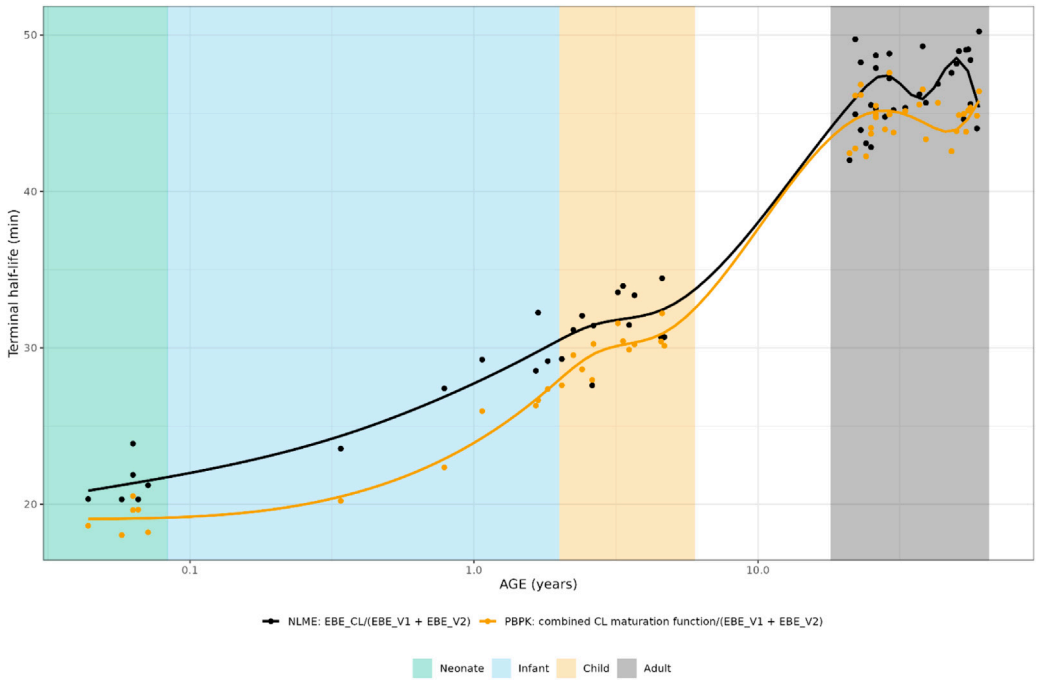

FIGURE 2
Comparison of individual hydrocortisone terminal half-life for neonates, infants, children and adults after administration of a pediatric formulation of hydrocortisone. The closed circles represent the individual values taking body weight (non-linear mixed effects model) or body weight and age (maturation function) into account. The lines represent Loess smoothers through the individual values. Age shown on a logarithmic scale.

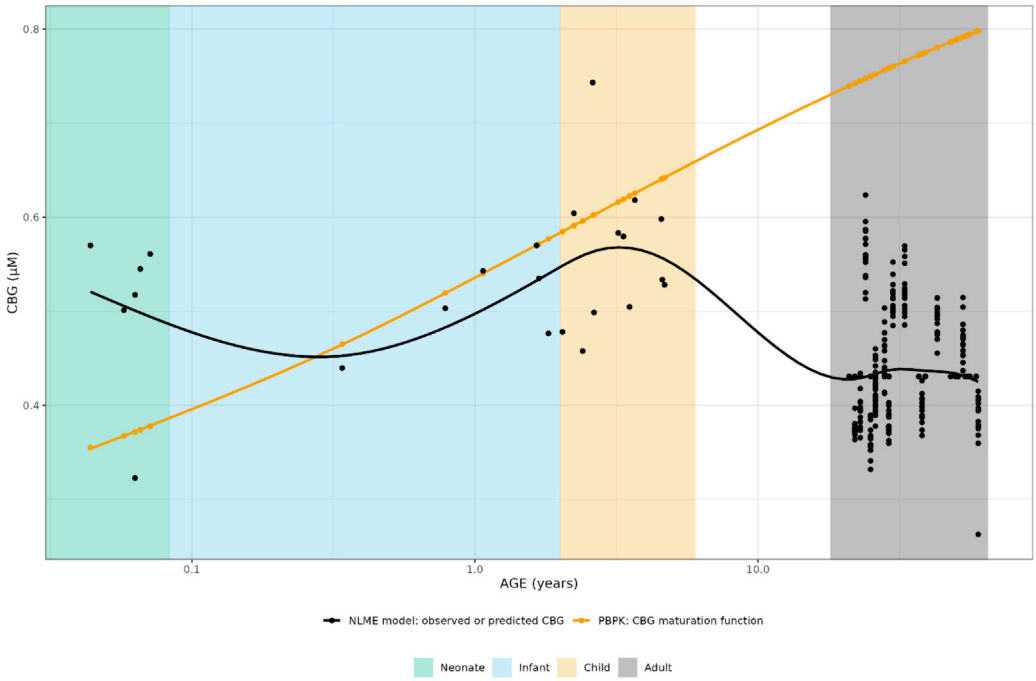

FIGURE 3
Comparison of individual cortisol-binding globulin concentrations for neonates, infants, children and adults. The closed circles represent the individual values taking body weight (non-linear mixed effects model) or body weight and age (maturation function) into account. The lines represent Loess smoothers through the individual values. Age shown on a logarithmic scale.

the clinic after at least 2 h fasting. Patients were not allowed to eat within 60 min post-dose (30 min for children below 1 year). All patients underwent plasma sampling prior to dose, 1 and 4 h post-dose. Three additional samples were retrieved per patient in cohort 1 (1–6 years), every individual was randomized into one of four groups ($n = 3$) in which two extra samples were taken after approximately 30, 45, 90, 120, 150, and/or 180 min and for all an extra sample around the expected minimum concentration (T_{min}) was taken.

For the adult healthy volunteers, data from two independent crossover studies (Infacort-001 and Infacort-002; EudraCT Number: 2013–000260-28 and EudraCT Number: 2013–000259-42) were included. For the arms considered in this work, healthy males between 18 and 60 years were included and received either single morning oral doses of 0.5, 2, 5, and 10 mg of individualized hydrocortisone granules (study 1, $n = 16$) or a single dose of 20 mg individualized hydrocortisone granules (study 2, $n = 14$). For both groups, dexamethasone (1 mg) was administered to suppress the endogenous cortisol synthesis. In study 1, plasma samples were taken at pre-dose and 0.5, 1, 1.5, 2.5, 3, 3.5, 4, 4.5, 5, 5.5, 6, 6.5, 7, 7.5, 8, 9, 10, 11, and 12 h post-dose and cortisol total concentrations were measured. In study 2, total cortisol and CBG were measured in plasma pre-dose, and 0.25, 0.5, 0.75, 1, 1.25, 1.5, 2, 2.5, 3, 4, 5, 6, 8, 10, and 12 h post-dose/period start.

2.2 Modelling approaches

2.2.1 Non-linear mixed-effects model

The previously developed NLME model was a semi-mechanistic model based on adult total and unbound hydrocortisone concentrations, allometrically scaled to the pediatric population. The model was further optimized based on the aforementioned data derived from a clinical trial using a pediatric formulation of hydrocortisone that allows accurate dosing in neonates, infants and children with adrenal insufficiency. Using the pediatric body weight and CBG, the semi-mechanistic PK model established on adult data could relatively well predict the observed pediatric observations. However, observed pre-dose concentrations in the pediatric CAH patients were often much higher than predicted by the cortisol baseline based on dexamethasone-suppressed adults. This discrepancy was hypothesized to result from the not-considered maturation of the enzyme 11-βHSD2, causing cyclic resynthesis from cortisone to cortisol (Martinerie et al., 2012). However, estimating the parameters of a semi-mechanistic PK model including maturation of this enzyme was not supported by the sparse pediatric data set, so an allometrically scaled model with separate baselines based on the adult and pediatric datasets was proposed as final model, resulting in good parameter precision for both fixed-effect and variability parameters. In this model, neonates had a lower and more variable relative clearance (CL per kg body weight) than infants, young children and adults, which can potentially be explained by the lower activity of 11-βHSD2 (converting cortisol to cortisone) (Martinerie et al., 2012) and 5α-reductase (irreversible metabolism of cortisol to 5α-DHF (allodihydrocortisol)) (Thigpen et al., 1993) in this age group. Conversely, relative CL in infants was predicted to be more variable than in children and adults, potentially due to the high activity of 5α-reductase in infants relative to their body size and incomplete maturation processes.

2.2.2 Physiologically-based pharmacokinetic model

The previously developed PBPK model (Bonner et al., 2021) was constructed as follows: published adult studies describing the PK of

TABLE 1 Parameter estimates, objective function value (OFV) and condition number (CN) from the middle-out models exploring the inclusion of a maturation function for cortisol clearance (CL).

Model	Base model	CL-maturation, no re-estimation run 0	CL-maturation, PK-estimation run 1	CL-maturation, MAT-estimation run 2	CL-maturation, re-estimation all' run 3
Parameter	Value (rse, %)	Value (rse, %)	Value (rse, %)	Value (rse, %)	Value (rse, %)
CL [L/h]	410 (8.1)	409 (-)	325 (ND)	409 (-)	484 (ND)
V2 [L]	10.6 (9.4)	10.6 (-)	10.4 (ND)	10.6 (-)	10.6 (ND)
Q [L/h]	160 (17.9)	160 (-)	147 (ND)	160 (-)	162 (ND)
V3 [L]	124 (16.3)	124 (-)	122 (ND)	124 (-)	127 (ND)
Km [nmol]	4,810 (21.2)	4,810 (-)	5,190 (ND)	4,810 (-)	4,830 (ND)
Vmax [nmol/h]	21,600 (11.0)	21,600 (-)	21,500 (ND)	21,600 (-)	21,600 (ND)
BASEAdult	15.4 (6.33)	15.4 (-)	15.4 (6.33)	15.4 (-)	15.4 (ND)
BASEChild	13.3 (1.94)	13.3 (-)	13.3 (1.94)	13.3 (-)	13.3 (ND)
IIVCL (CV%)	19.2 (17.8)	19.2 (-)	22.9 (ND)	17.2 (ND)	17.3 (ND)
IIV_{Km} (CV%)	45.6 (36.3)	45.6 (-)	40.7 (ND)	43.0 (ND)	42.9 (ND)
IIV_{Vmax} (CV%)	43.7 (16.7)	43.7 (-)	42.9 (ND)	43.0 (ND)	43.0 (ND)
IIV_{BASE} (CV%)	33.5 (22.3)	33.5 (-)	33.5 (ND)	33.5 (ND)	33.5 (ND)
IIV_{BIO} (CV%)	34.9 (19.3)	34.9 (-)	36.5 (ND)	35.2 (ND)	35.2 (ND)
$BASE_{1,5A}$		0.05 (-)	0.05 (-)	0.04 (ND)	0.003 (ND)
$MAX_{1,5A}$		14.8 (-)	14.8 (-)	3.24 (ND)	2.54 (ND)
$HILL_{5A}$		1.17 (-)	1.17 (-)	1.45 (ND)	1.66 (ND)
$TM_{50,5A}$		0.17 (-)	0.17 (-)	0.04 (ND)	0.04 (ND)
$BASE_{2,5A}$		1.56 (-)	1.56 (-)	1.51 (ND)	1.10 (ND)
$MAX_{2,5A}$		9.22 (-)	9.22 (-)	51.1 (ND)	310 (ND)
DEC_{5A}		1.78 (-)	1.78 (-)	59.8 (ND)	110 (ND)
$INFP_{5A}$		0.16 (-)	0.16 (-)	0.29 (ND)	0.29 (ND)
$BASE_{11B}$		0.02 (-)	0.02 (-)	0.01 (ND)	0.002 (ND)
MAX_{11B}		1.52 (-)	1.52 (-)	0.58 (ND)	0.50 (ND)
$HILL_{11B}$		0.15 (-)	0.15 (-)	143 (ND)	173 (ND)
$TM_{50,11B}$		0.27 (-)	0.27 (-)	4.05 (ND)	4.38 (ND)
Residual variability (CV%)	14.5 (8.0)	14.5 (-)	14.5 (ND)	14.5 (ND)	14.5 (ND)
Condition number	155.6	NA	ND	ND	ND
OFV	-3,907.90	-3,838.94	-3,894.65	-3,917.12	-3,917.24

CL: Apparent clearance, V2: apparent central volume of distribution, Q: apparent intercompartmental clearance, V3: peripheral volume of distribution, K_m: amount in depot compartment resulting in half of V_{max}, V_{max}: maximum absorption rate, $BASE_{Adult}$: cortisol baseline of dexamethasone suppressed healthy adults, $BASE_{Child}$: cortisol baseline of children with baseline measurement BLOQ, IIV: interindividual variability, $BASE_{1,5A}$: 5-alpha reductase activity at birth, $MAX_{1,5A}$: maximum 5-alpha reductase activity during first 3 months of life, $HILL_{5A}$, hill factor for the 5-alpha reductase ontogeny function during the first 3 months of life, $TM_{50,5A}$: age at which half of $MAX_{1,5A}$ is reached, $BASE_{2,5A}$, 5-alpha reductase activity at 3 months of age, $MAX_{2,5A}$: maximum 5-alpha reductase activity after first 3 months of life, DEC_{5A}: 5-alpha reductase activity decay rate, $INFP_{5A}$: inflection point of the 5-alpha reductase activity ontogeny function, $BASE_{11B}$: 11-β hydroxysteroid dehydrogenase 2 activity at birth, MAX_{11B}: maximum 11-β hydroxysteroid dehydrogenase 2 activity during life, $HILL_{11B}$: hill factor for the 11-β hydroxysteroid dehydrogenase 2 ontogeny function, $TM_{50,11B}$: age at which half of MAX_{11B} is reached. Parameters were allometrically scaled using a body weight of 70 kg and residual variability was estimated as additive error on a log scale.

intravenous (IV) hydrocortisone (Toothaker and Welling, 1982; Derendorf et al., 1991) were used to establish the initial drug parameters for distribution and elimination. The volume of distribution was described using a minimal PBPK model, this is akin to a 2-compartmental PK model plus liver compartment, this model also allowed the simulation of changing fraction unbound (f_u) on volume of distribution. The f_u was simulated based on binding to both albumin and CBG, protein reference values and dissociation constants are detailed in the original publication (Bonner et al., 2021). Cortisol elimination input intrinsic clearance values for 11-βHSD2,

10.3389/fphar.2022.1090554

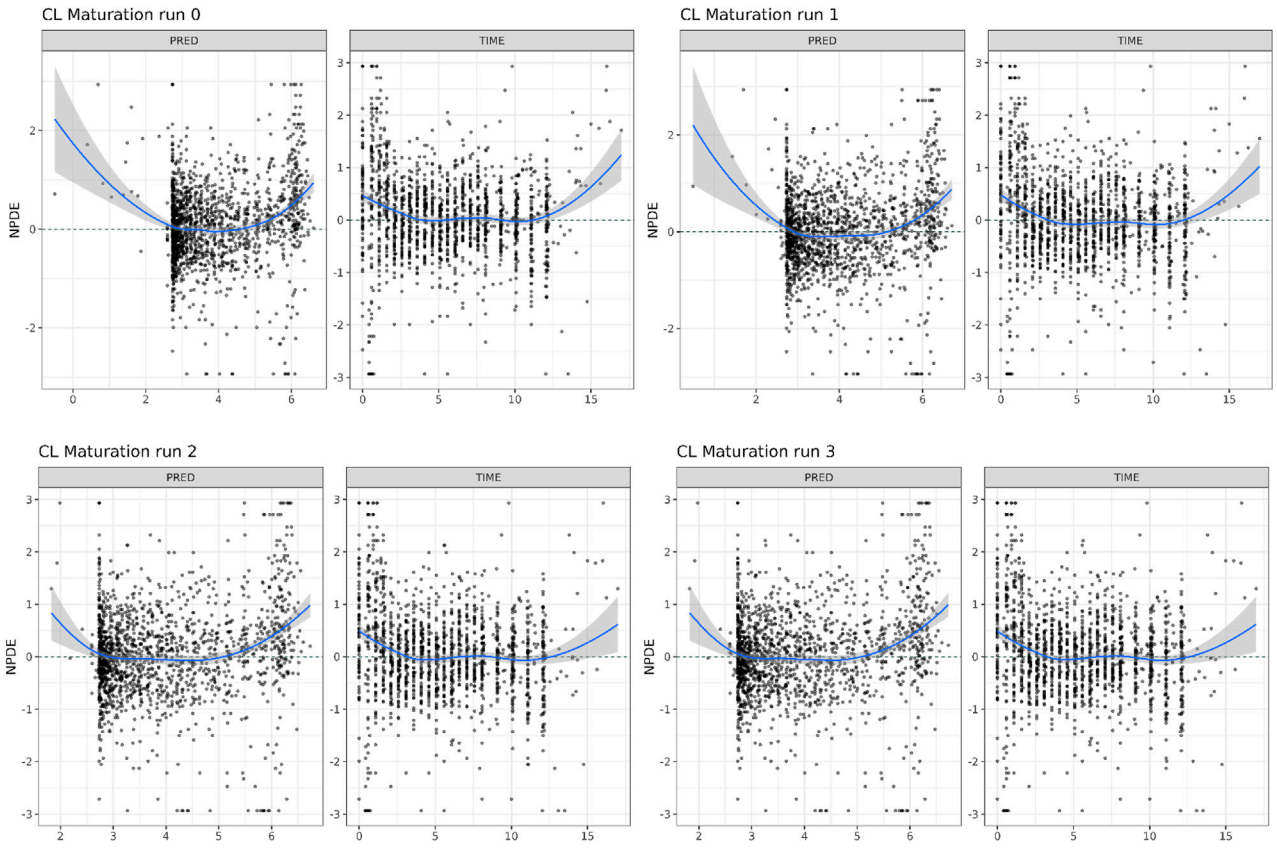

FIGURE 4
Normalized Distribution Prediction Errors (NPDE) of the 4 middle-out models incorporating the PBPK-derived clearance maturation function. Run 0: no re-estimation of parameters, run 1: re-estimation of NLME-derived PK parameters, run 2: re-estimation of PBPK-derived clearance maturation function, run 3: re-estimation of all parameters.

5α-reductase, CYP3A4 and additional CL (lumped 20β-oxoreductase and 5β-reductase pathways) were calculated using a retrograde model based on an IV clearance of 20 L/h and the literature derived fraction eliminated by each pathway of 30, 31.5, 2.5%, and 36%, respectively, Data from published studies describing immediate-release oral hydrocortisone PK (Toothaker et al., 1982; Derendorf et al., 1991) were then used to establish the absorption model parameters for the immediate-release formulations of hydrocortisone, and to provide further verification of the model. Once developed, clinical studies of the immediate-release multi-particulate formulation in adults (Infacort-001 and Infacort-002) were used to verify the final model before performing simulations in the paediatric population.

The Sim-Paediatric population was used for the latter which considers the relevant developmental physiology including the ontogeny of albumin and CYP3A4 expression (Johnson et al., 2006). For this study, further information was included on the ontogeny of CBG (meta-analysis of multiple sources including (Hadjian et al., 1975)), 11-βHSD2 and 5α-reductase. The ontogeny of 11β-HSD2 was derived based on urinary cortisone to cortisol ratios (Rogers et al., 2014), and that for 5α-reductase from urinary allo-tetrahydrocortisol/tetrahydrocortisol ratios (meta-analysis of multiple sources including (Wudy et al., 2007), equations are below. The final model was able to capture the majority of clinical data for the ages 2 to 4.7, 0.3 to 1.8, and 0.044–0.071 years within the 5th and 95th percentiles for the simulations.

2.2.3 Middle-out approach

As the maturation of different enzymatic processes was already hypothesized during the development of the NLME model, and formalized during the development of the PBPK model, the next step was to implement the PBPK-derived maturation functions into the NLME model. For this, the maturation of the CL and plasma-protein binding related processes identified in the PBPK model were considered: 5α-reductase (Equation ((1), (1) and (2)1-βHSD2 (Eq. 3) and CBG (Eq. (4)). Similar as in the PBPK model, CYP3A4-related metabolism was assumed to mature rapidly from birth onwards and, due to its contribution to the metabolism of 2.5%, assumed to have a negligible impact on the total CL (Kearns et al., 2003; Hines, 2007).

$$\mathbf{5\alpha-reductase}\left(\mathbf{0-0.25\,y}\right)=\mathbf{0.05}+\left(\frac{\left(\mathbf{14.82-0.05}\right)*\boldsymbol{AGE}^{\mathbf{1.17}}}{\mathbf{0.17}^{\mathbf{1.17}}+\boldsymbol{AGE}^{\mathbf{1.17}}}\right) \quad (1)$$

$$\mathbf{5\alpha-reductase}\left(\mathbf{>0.25\,y}\right)=\mathbf{1.56}+\left(\mathbf{9.22}*\mathbf{e}^{-\mathbf{1.78}*\left(\boldsymbol{AGE}-\mathbf{0.16}\right)}\right) \quad (2)$$

$$\mathbf{11-\beta HSD2}=\mathbf{0.02}+\left(\frac{\left(\mathbf{1.52-0.02}\right)*\boldsymbol{AGE}^{\mathbf{0.15}}}{\mathbf{0.27}^{\mathbf{0.15}}+\boldsymbol{AGE}^{\mathbf{0.15}}}\right) \quad (3)$$

10.3389/fphar.2022.1090554

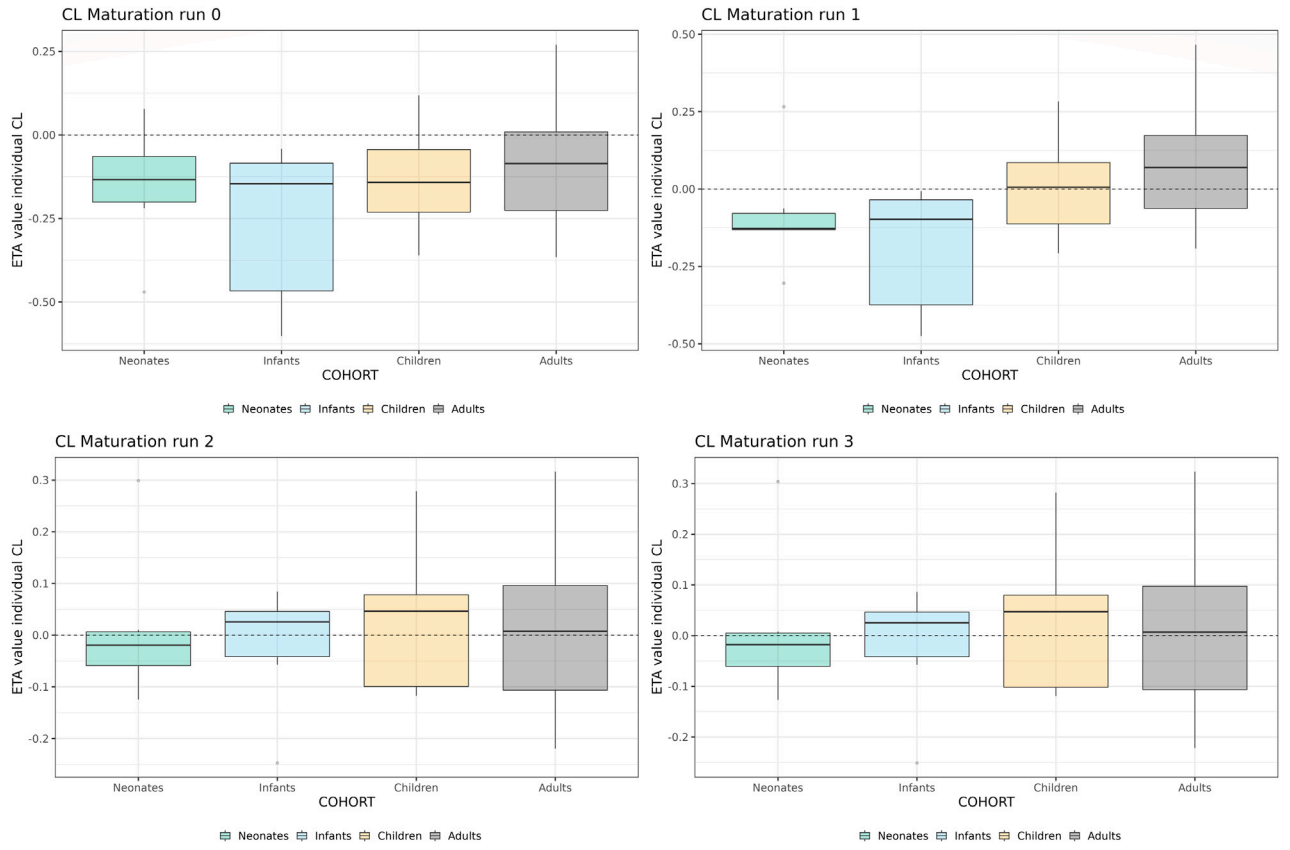

FIGURE 5
Individual clearance parameter estimates (empirical Bayes estimate) for the 4 middle-out models incorporating the PBPK-derived clearance maturation function. Run 0: no re-estimation of parameters, run 1: re-estimation of NLME-derived PK parameters, run 2: re-estimation of NLME-derived PK parameters, run 2: re-estimation of PBPK-derived clearance maturation function, run 3: re-estimation of all parameters. The dotted line depicts the clearance for a typical individual (i.e. without variability).

The PBPK-derived maturation functions for the binding to CBG was considered as it was originally derived (Bonner et al., 2021):

$$CBG\ (\mu M) = 0.195 + \left(\frac{(0.993 - 0.195) * AGE^{0.348}}{2.33^{0.348} + AGE^{0.348}}\right) \quad (4)$$

Further details regarding Equations 1–4 can be found in the original work describing the development of the hydrocortisone PBPK model (Bonner et al., 2021).

The PBPK-derived maturation functions for the metabolic enzymes were combined in a CL maturation function Eq. 5 following their proportional impact on the overall hydrocortisone CL based on the PBPK-derived contribution to the metabolism: 30% for 5α-reductase, 30% for 11-βHSD2 and 40% for other processes assumed not to undergo relevant maturation (Bonner et al., 2021).

$$CL_{ratio\frac{pediatric}{adult}}(AGE) = 30\% * 5\alpha - reductase_{AGE} + 30\% * 11 - \beta HSD2_{AGE} + 40\% \quad (5)$$

In order to investigate the utility of these maturation functions in the middle-out NLME framework, a step-wise approach was taken.

1) Comparison of maturation function-derived CL and CBG concentration to NLME-derived empirical Bayes estimates (EBE): CL_{EBE} and CBG_{EBE}.
2) Implementation of CL or CBG maturation functions in NLME model and re-estimation of none, parts of and full model. The procedure was performed for both maturation functions separately and then for both together.
3) Implementation of best-performing maturation functions into NLME model.

For step 1, CL_{EBE} were compared to CL values derived from PBPK maturation function Eq. 5. For this, the age-dependent CL-ratio calculated by the maturation function was multiplied with the adult population CL/F value estimated by the NLME model and corrected for body weight using allometric scaling as shown in Eq. 6.

$$CL_{PBPK} = CL_{NLME,adult} * CL_{ratio\frac{pediatric}{adult}}(AGE) * \left(\frac{BW\,(kg)}{70\,kg}\right)^{0.75} \quad (6)$$

To lessen the impact of allometric scaling assumptions and bioavailability, the elimination half-lives, defined as Eq. 7 for a two-compartmental model, were also calculated and compared.

$$t_{\frac{1}{2},\beta} = \frac{\ln\,(2)}{0.5 * \left(\frac{Q}{V_1} + \frac{Q}{V_2} + \frac{CL}{V_1} - \sqrt{\left(\frac{Q}{V_1} + \frac{Q}{V_2} + \frac{CL}{V_1}\right)^2 - 4 * \frac{Q}{V_2} * \frac{CL}{V_1}}\right)} \quad (7)$$

In step 2), PBPK-derived maturation functions were included in the NLME model separately and then both at the same time. Under all three

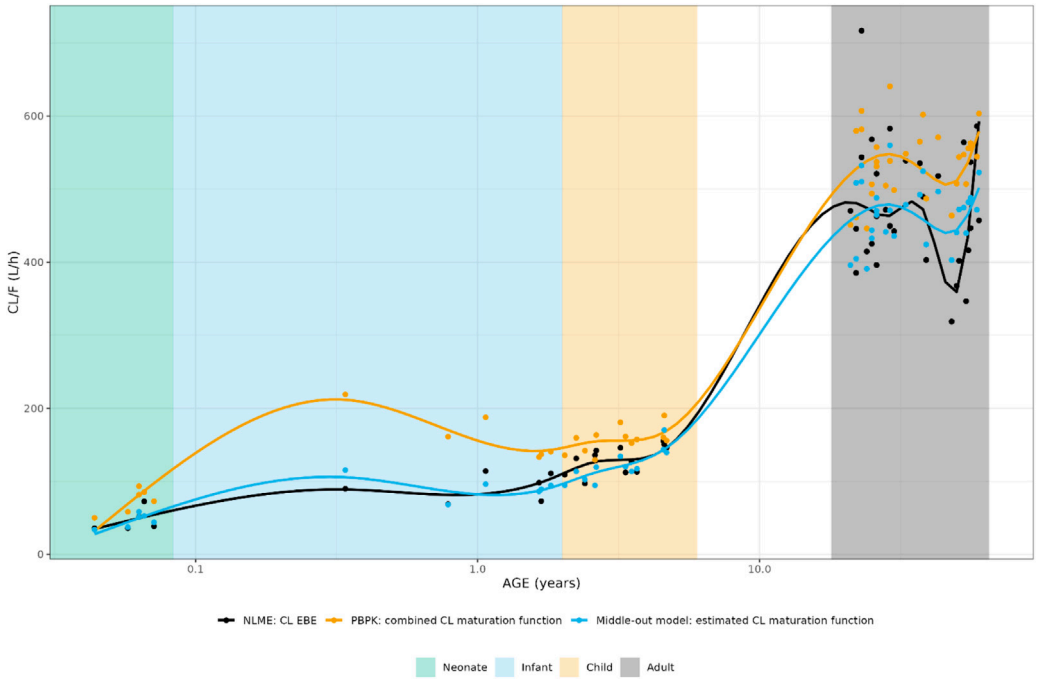

FIGURE 6
Comparison of individual apparent hydrocortisone clearance for neonates, infants, children and adults after administration of a pediatric formulation of cortisol using the NLME, PBPK or middle-out model (run 2). The closed circles and the lines represent the individual values and Loess smoothers through them. Age shown on a logarithmic scale.

scenarios, model performance was evaluated following one of four estimation steps. First, the parameters from the NLME model and the PBPK-derived maturation functions were not re-estimated and the model was evaluated as such. Second, the NLME-derived PK parameters were re-estimated while keeping the PBPK-derived maturation parameters fixed. Third, the PBPK-derived maturation parameters were re-estimated while keeping the NLME-derived PK parameters fixed. Fourth and final, all parameters were re-estimated based on the clinical dataset.

In general, model evaluation was performed based on predictive performance assessed by goodness-of-fit (GOF) plots and model stability assessed by condition number and parameter precision. Significant differences in model fit were defined as the difference in objective function value (OFV) being larger than $3.84^{*}n_{\text{parameters estimated}}$ ($p < 0.05$). To avoid bias in residuals calculated based on the M3 method, distributions of Normalized Prediction Distribution Errors (NPDEs (Brendel et al., 2006)) rather than Conditionally Weighted Residuals (CWRES) as a function of time and population prediction were used to judge the model fit (Jaber et al., 2021). Individual clearance estimates using empirical Bayes estimates were plotted as a function of age group to investigate introduction of age-dependent bias into the model. All estimations were performed using the FOCE + I algorithm.

2.3 Software

Data handling and management were performed using R/RStudio (version 4.0.1/1.3.1056), as well as data visualization. Modelling activities in the middle-out NLME framework were performed using NONMEM (version 7.5.0) and Pearl speaks NONMEM (PsN, version 5.0.0).

3 Results

3.1 Comparison of individual parameters derived by PBPK and NLME approach

The individually predicted CL and elimination half-lives are presented in Figure 1 and Figure 2. A relatively large overlap could be observed for children and adults older than 1 year. However, for children younger than 1-year substantial discrepancies in predicted elimination processes between the approaches were shown, possibly indicating the relevance of maturational processes in this age range.

For CBG, the PBPK-derived concentrations could be directly compared to the NLME derived ones. The NLME model was parametrized in a way that when a CBG measurement was available for an individual, this measurement was used in the model. When such a measurement was not available, the mean CBG concentration (22.4 μg/mL/0.431 μM) from an earlier developed CBG binding model was used (Melin et al., 2019), which was only the case for 16 adult individuals.

As can be seen in Figure 3, the PBPK-derived maturation in CBG concentrations was not represented in the NLME-based approach, resulting in a discrepancy over almost the entire age range.

TABLE 2 Parameter estimates, objective function value (OFV) and condition number (CN) from the middle-out models exploring the inclusion of a maturation function for cortisol binding globulin (CBG).

Model	Base model	CBG-maturation, no re-estimation	CBG-maturation, PK-estimation	CBG-maturation, MAT-estimation	CBG-maturation, re-estimation all
Parameter	Value (rse, %)	Value (rse, %)	Value (rse, %)	Value (rse, %)	Value (rse, %)
CL [L/h]	410 (8.1)	409 (-)	612 (1.90)	409 (-)	995 (13.3)
V2 [L]	10.6 (9.4)	10.6 (-)	10.4 (12.3)	10.6 (-)	13.6 (9.27)
Q [L/h]	160 (17.9)	160 (-)	147 (21.5)	160 (-)	422 (22.0)
V3 [L]	124 (16.3)	124 (-)	122 (24.4)	124 (-)	348 (18.4)
Km [nmol]	4,810 (21.2)	4,810 (-)	5,190 (1.66)	4,810 (-)	8,820 (25.1)
Vmax [nmol/h]	21,600 (11.0)	21,600 (-)	21,500 (0.03)	21,600 (-)	32,800 (14.9)
BASEAdult	15.4 (6.33)	15.4 (-)	15.4 (6.38)	15.4 (-)	15.6 (6.54)
BASEChild	13.3 (1.94)	13.3 (-)	13.3 (1.27)	13.3 (-)	13.3 (2.82)
IIVCL (CV%)	19.2 (17.8)	19.2 (-)	22.9 (72.5)	23.2 (18.9)	22.4 (19.0)
IIVKm (CV%)	45.6 (36.3)	45.6 (-)	40.7 (51.5)	51.3 (24.0)	46.4 (33.7)
IIV_{Vmax} (CV%)	43.7 (16.7)	43.7 (-)	42.9 (23.8)	42.9 (14.5)	40.0 (17.8)
IIV_{BASE} (CV%)	33.5 (22.3)	33.5 (-)	33.5 (22.0)	33.6 (22.4)	33.6 (22.2)
IIV_{BIO} (CV%)	34.9 (19.3)	34.9 (-)	36.5 (20.4)	42.1 (18.4)	31.9 (17.2)
$BASE_{CBG}$		0.20 (-)	0.05 (-)	0.456 (23.3)	1.83 (26.0)
MAX_{CBG}		0.99 (-)	14.8 (-)	0.643 (8.29)	0.71 (36.0)
$TM_{50,CBG}$		2.33 (-)	1.17 (-)	0.76 (113)	0.0233 0)
$HILL_{CBG}$		0.35 (-)	0.17 (-)	0.142 (251)	0.191 (45.8)
Residual variability (CV%)	14.5 (8.0)	14.5 (-)	14.5 (8.0)	14.2 (7.32)	14.0 (7.71)
CN	155.6	NA	$1.19 * 10^8$	217.5	846.6
OFV	-3,907.90	-3,934.75	-4,003.41	-3,961.00	-4,041.86

CL: Apparent clearance, V2: apparent central volume of distribution, Q: apparent intercompartmental clearance, V3: peripheral volume of distribution, K_m: amount in depot compartment resulting in half of V_{max}, V_{max}: maximum absorption rate, $BASE_{Adult}$: cortisol baseline of dexamethasone suppressed healthy adults, $BASE_{Child}$: cortisol baseline of children with baseline measurement BLOQ, IIV: interindividual variability, $BASE_{CBG}$: CBG, concentration at birth, MAX_{CBG}: maximum CBG, concentration, $TM_{50,CBG}$: age at which half of MAX_{CBG}, is reached; $HILL_{CBG}$, hill factor for the CBG, ontogeny function. Parameters were allometrically scaled using a body weight of 70 kg and residual variability was estimated as additive error on a log scale.

3.2 Implementation of CL or CBG maturation functions in NLME model

To investigate whether the discrepancies in individual parameters between the NLME and PBPK approach had a significant impact on the description of the observed clinical data and as such could provide a possibility for model improvement using a middle-out approach, the implementation of the PBPK-derived maturation functions within the NLME modelling framework was carried out.

3.2.1 Implementation of CL maturation

In Table 1, the parameter estimates of the implemented CL maturation functions within the NLME model are show. Inclusion of the maturation function without re-estimation of any parameter but including fitting of the individual profiles using empirical Bayes estimates (option MAXEVAL = 0 in NONMEM) resulted in a significantly worse fit as indicated by the OFV (ΔOFV = 34.48). Estimation of the PK parameters while keeping the maturation function constant also resulted in a worse fit (ΔOFV = 13.25) and in an unstable model as indicated by failure in convergence of the covariance matrix. Estimating the parameters of the maturation function alone or together with the PK parameters resulted in a non-significant improvement of the fit (ΔOFV = −9.22 > -15.36 for run 2 and −9.34 > −46.08 for run 3), also indicating by the NPDE distributions in Figure 4.

In Figure 5, the individual variance estimates for CL are shown as a function of age group. Here, the distribution of the empirical Bayes estimates per individual in order to describe the observed data *post hoc*

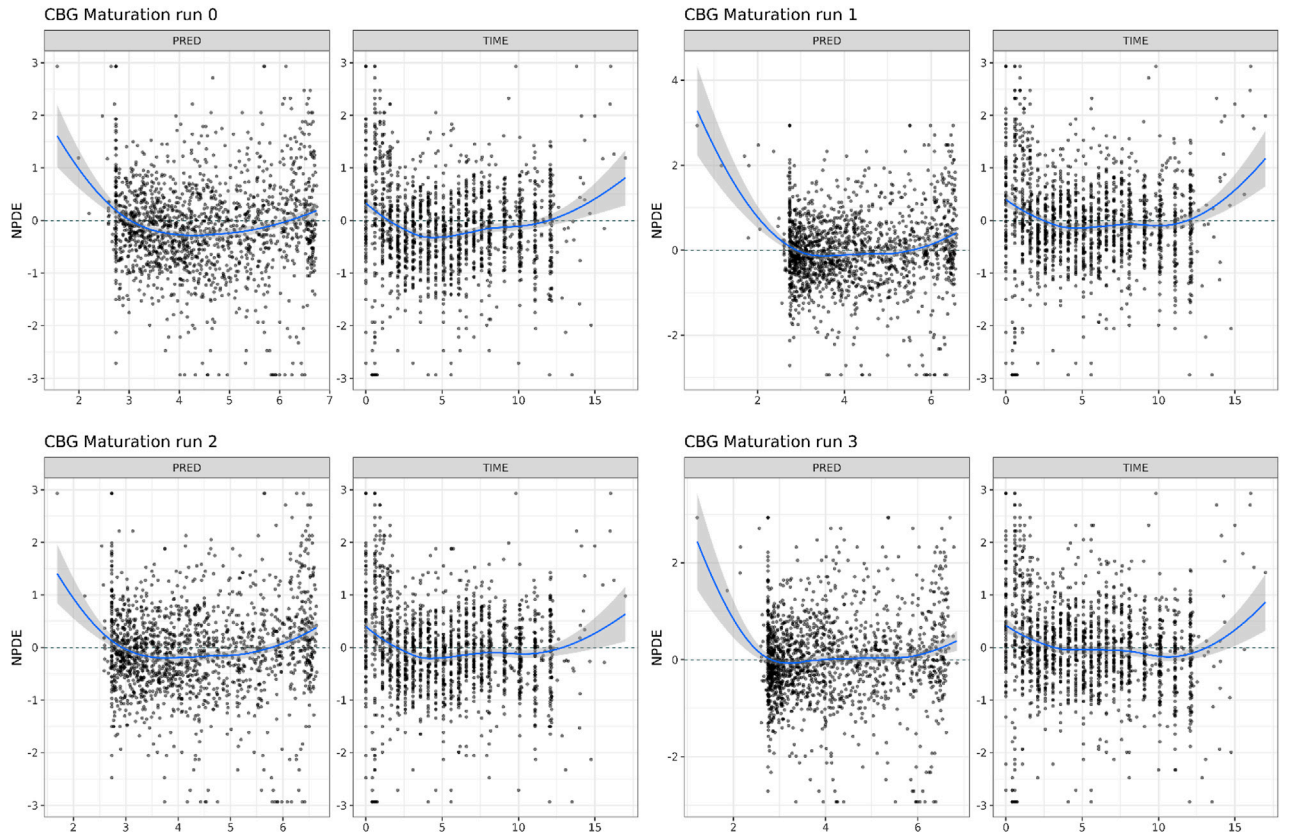

FIGURE 7
Normalized Distribution Prediction Errors (NPDE) of the 4 middle-out models incorporating the PBPK-derived cortisol-binding globulin (CBG) maturation function. Run 0: no re-estimation of parameters, run 1: re-estimation of NLME-derived PK parameters, run 2: re-estimation of PBPK-derived CBG maturation function, run 3: re-estimation of all parameters.

is shown. The centering of these distributions around 0 indicates an unbiased CL estimation. Inclusion of the maturation function without re-estimation induces an age-dependent bias in the CL estimation resulting in a skewed distribution of these individual estimates, which is only resolved by estimation of the maturation function parameters. In Figure 6, the CL maturation function based on only the PBPK model, only the NLME model and the estimated maturation function within the NLME framework are shown. Here it can be seen that estimation of the maturation function given the clinical datasets approaches the individual CL estimates as a function of age as fitted by the NLME model without maturation function.

3.2.2 Implementation of CBG maturation

In Table 2, the parameter estimates of the implemented CBG maturation functions within the NLME model are show. Inclusion of the maturation function without re-estimation of any parameter but including fitting of the individual profiles using empirical Bayes estimates (option MAXEVAL = 0 in NONMEM) resulted in a significantly better fit as indicated by the OFV (ΔOFV = −26.85 < 15.36). Estimation of the PK parameters while keeping the maturation function constant also resulted in a better fit (ΔOFV = −95.51 < 15.36) but in an unstable model as indicated by the very large condition number ($1.19 * 10^8 > 1000$) and the imprecision of some of the IIV-related parameters becoming high (IIV CL = 72.5% > 50%). Estimating the parameters of the maturation function alone or together with the PK parameters resulted in a significant improvement of the fit (ΔOFV = −53.1 < −15.36 for run 2 and −133.96 < −15.36 for run 3).

As indicated by the NPDE distributions in Figure 7 and the individual variance estimates for CL in Figure 8, the inclusion of a maturation function for CBG results in a biased estimate of the neonatal PK. Estimation of the maturation function alone resolves this bias at the cost of a biased adult CL. As can be seen in Figure 9, estimation of the maturation function alone using the clinical data approaches moves the CBG maturation function towards the individual CBG estimates as a function of age as fitted by the NLME model without maturation function. Estimation of all parameters simultaneously leads to a better-fitting stable model, using a strongly deviating maturation function (Figure 9) and CL-estimate (Table 2), and an underprediction of neonatal CL (Figure 8).

3.3 Implementation of best-performing maturation functions into NLME model

Ultimately, the inclusion of CL and/or CBG PBPK-derived maturation functions resulted in similar, or worse, model

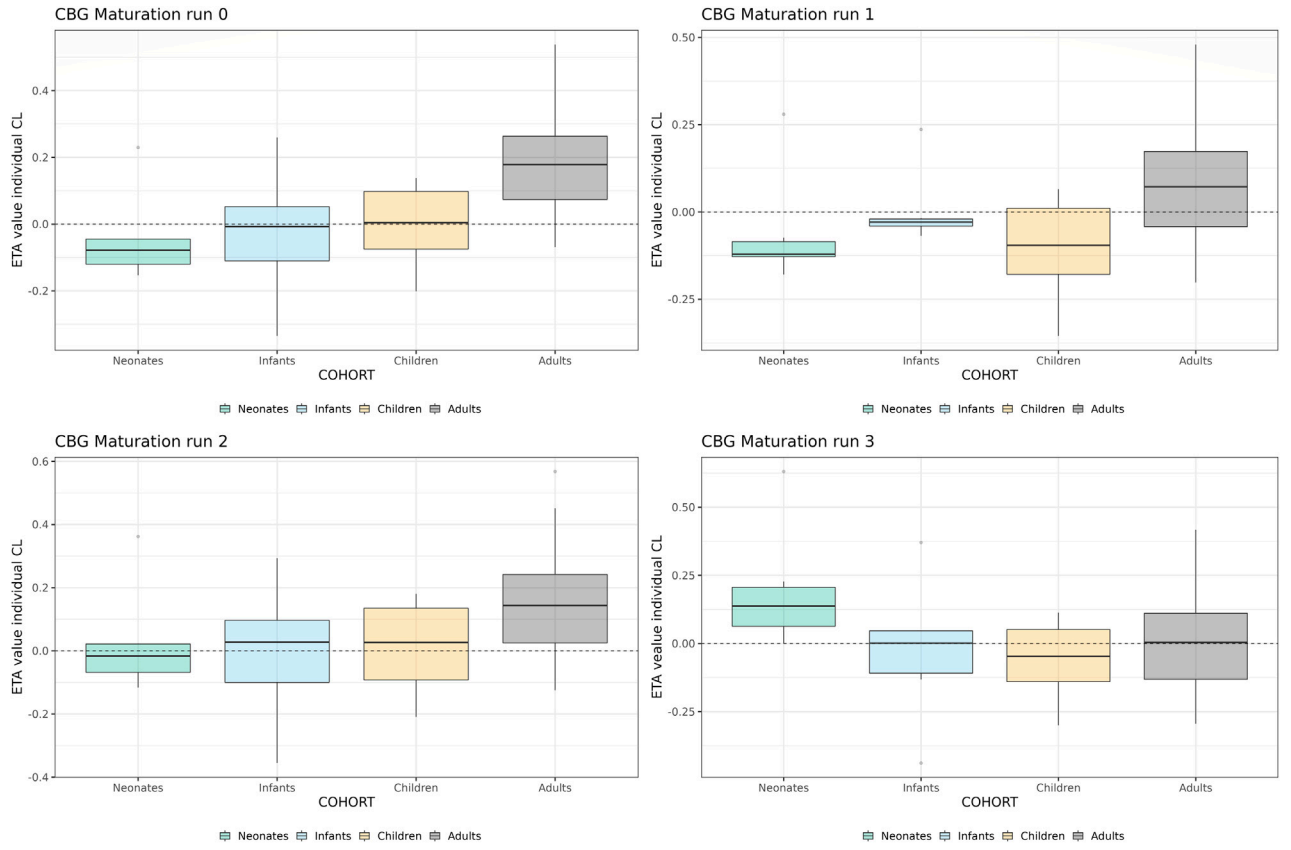

FIGURE 8
Individual clearance parameter estimates (empirical Bayes estimate) for the 4 middle-out models incorporating the PBPK-derived cortisol-binding globulin (CBG) maturation function. Run 0: no re-estimation of parameters, run 1: re-estimation of NLME-derived PK parameters, run 2: re-estimation of NLME-derived PK parameters, run 2: re-estimation of PBPK-derived CBG maturation function, run 3: re-estimation of all parameters. The dotted line depicts the clearance for a typical individual (i.e. without variability).

performance and the re-estimation of parameters most often led to unstable models or unrealistic parameter estimates.

4 Discussion

In this work, the maturation of different processes contributing to the PK of hydrocortisone were investigated using a middle-out approach, combining insights from clinical data analyzed using NLME modelling with ontogeny data from a PBPK model. As a first step, the conclusions of both techniques were compared to each other, showing significant differences between the two approaches. Indeed, the maturation of hydrocortisone CL was predicted differently between the two models for children between 1 month and 1 year of age but similar for the rest of the pediatric age range. For the maturation of CBG, NLME approaches predicted that no significant maturation takes place over the entire pediatric age range (Melin et al., 2017; Melin et al., 2019) while a PBPK approach showed an increase in CBG concentration from birth to adulthood (Bonner et al., 2021).

The insights from PBPK, based on an extensive review of the literature sources available at the time, were implemented in an NLME framework based on the model fitted to clinical data (Melin et al., 2017; Michelet et al., 2020) and interrogated for their potential to describe hydrocortisone PK data over the pediatric age range. Inclusion of the CL maturation function did not result in a significantly better description of the clinical data, and re-estimation of the maturation function parameters was not supported by the data. For the maturation of CBG, a better description of the clinical data was suggested by the fit, but only when the maturation function was either 1) re-estimated to approximate a stable CBG concentration over the entire age range or 2) estimated to be a decreasing function from birth on combined with a deviating PK model. Furthermore, large differences in parameter values were observed between the different re-estimation steps, indicating a discrepancy between the modeling approaches or their underlying data.

As neither the CL nor the CBG maturation function could show convincing improvements in the description of the clinical pediatric dataset, their implementation together in an optimal middle-out model was not successful. Several reasons can be proposed for this mismatch between the NLME and PBPK approach. First, a PBPK model includes maturational processes in a mechanistic way, modulating only the processes which are governed by the enzyme of which the maturation is considered. An NLME model, in contrast, lumps processes together into empirical compartments which consists of an arbitrary number of the abovementioned processes. A straightforward example of this is the maturation of the first-pass effect and bioavailability, which would be considered in a carefully

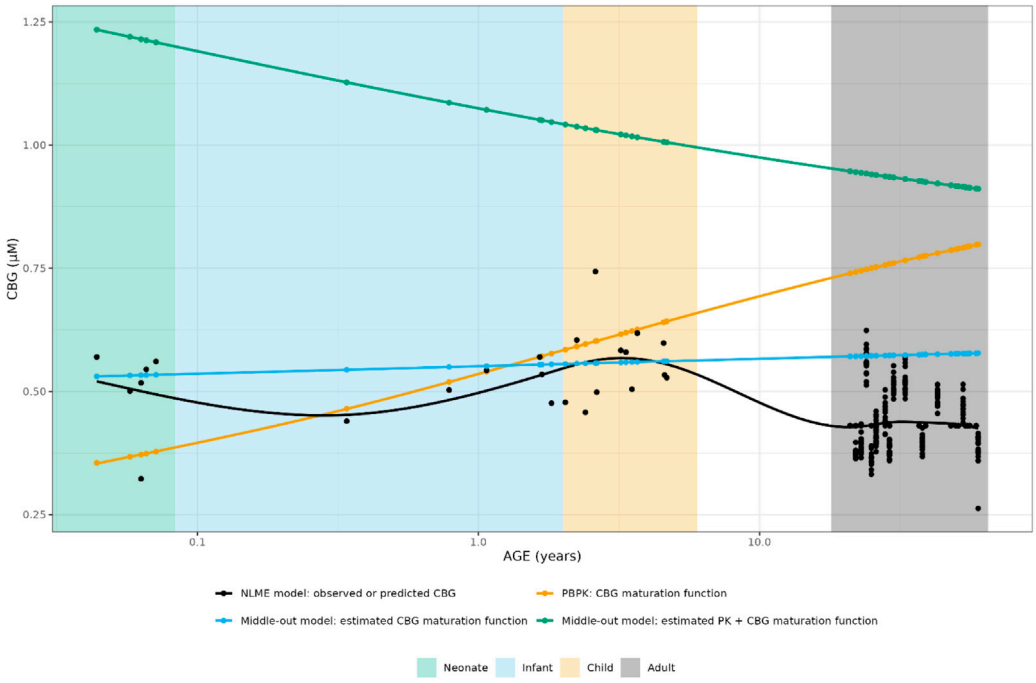

FIGURE 9
Comparison of individual cortisol-binding globulin concentrations for neonates, infants, children and adults using the NLME, PBPK or middle-out model (CBG-run 2 and run 3). The closed circles and the lines represent the individual values and Loess smoothers through them. Age shown on a logarithmic scale.

constructed PBPK model, but is not taken into account in the maturation function of apparent CL (CL/F) in the NLME/middle-out approach. Mechanistic investigation of the processes governing the first pass processes of hydrocortisone PK would considerably help to elucidate the maturation of bioavailability and absorption of hydrocortisone in the pediatric population. In the current study, all data was derived from individualized hydrocortisone granules which are immediate release. However, a modified-release formulation would have a more profound effect on bioavailability and absorption, which would need to be characterized in order to update the underlying structural PK model.

Second, the current findings are dependent on the nature of clinical data which is available for hydrocortisone PK in CAH pediatric patients. Our current clinical dataset is collected from clinical trials, where different cohorts were selected, for regulatory and ethical reasons, based on distinct age cut-offs. These cohorts were defined as neonates (0–1 month), infants (1 month–2 years) and children (2–6 years). In general it is difficult to recruit such young children, especially for a rare disease, into the clinical trials and hence the overall numbers of pediatric patients is low. This is further compounded by, when children are recruited into the trial, they are often recruited towards the upper end of these age groups–this is particularly evident for the infant cohort where there are more patients towards 2 years of age, resulting in a lack of data between 1 month and 12 months of age. This makes the discrepancies between the PBPK and NLME approach challenging to validate with the current dataset, because there is a large gap in the data where, potentially, the most scientific interest lies in the maturation functions of enzymes with early age.

Although the implementation of the PPBK-derived maturation functions into the NLME framework show potential for better description of the PK of hydrocortisone in children, clinical data available to date do not support them formally. Thus, more PK data in young infants would be very beneficial to further develop and refine these modelling approaches. This sparsity of infant data also puts into question the typical staggered approach of pediatric clinical trials (although it is acknowledged that this needs to be balanced by the regulatory and ethical requirements of running the clinical trial with pediatric patients), as these age cut-offs will more likely recruit older children per cohort (Manolis et al., 2011). Indeed, our new insigh can contribute to the concrete design of next clinical trial.

Third, the maturation functions derived in the PBPK framework also contain uncertainty. Both the 11-βHSD2 and 5α-reductase maturation functions were derived from data on the ratio of urinary concentrations, which might need to be corrected for the renal function relative to adults. This correction was applied before to quantify the maturation of CYP2D6 and CYP3A4 in the first year of life (Johnson et al., 2008). Refitting the maturation functions for the metabolic enzymes on the metabolic ratios considering relative renal function might be a first step towards closing the gap between the two approaches depicted in this work. The maturation function for CBG was fitted on very variable data, with a lack of data for children over 12 months of age, indicating the need for further confirmation of this maturation function.

In this investigation the prior information of the PBPK-derived maturation function was either taken at value or re-estimated, i.e., it was taken as an uninformative or informative prior. Given more information about the relevant age ranges as described above, Bayesian approaches could be applied to explore the space of models in between the extreme solutions presented in this work. Furthermore, the impact of the explored models on dosing recommendations was outside the scope of this work, but could be explored once the gap between the two approaches depicted in this work is closed. Indeed, an adequate description of HC interindividual

variability as a function of age would directly impact personalized dosing, moving from body-weight based dosing to age- and body-weight dosing (Melin et al., 2020).

5 Conclusion

The maturation of different PK processes impacts the treatment of pediatric CAH patients with hydrocortisone. In current population NLME PK and PK/PD models, often only body weight is considered as covariate to explain the impact of age on hydrocortisone PK. In this work, insights of a PBPK modelling approach into maturation of hydrocortisone CL *via* 5α-reductase and 11-βHSD2 and cortisol binding *via* CBG were introduced in a NLME model fitted to pediatric clinical data. The discrepancies between the approaches show the importance of applying multidisciplinary methodologies in the analysis of pediatric data and of the balanced collection of clinical data across the pediatric age range. Lastly, further investigation of the maturation of 5α-reductase and 11-βHSD2 between 1 month and 12 months of age, and the maturation of CBG across the entire age range, is warranted for further development of these modelling approaches.

Data availability statement

The data analyzed in this study is subject to the following licenses/restrictions: Sharing of the clinical data analyzed in this work can be discussed upon reasonable request to the authors. Requests to access these datasets should be directed to r.j.ross@sheffield.ac.uk.

Ethics statement

The studies involving human participants were reviewed and approved by Ethics committee of Berlin, No. 14/0517- EK 12. Written informed consent to participate in this study was provided by the participantsandapos; legal guardian/next of kin.

Author contributions

RM, RR, MJW, and TNJ contributed to conception and design of the model-based analysis. UN and OB designed and carried out the clinical study on which the model-based analysis is based. JM, RM, and TNJ developed first iterations of the models on which the analysis is based. RM and DB performed the model-based analysis. RM and DB wrote the first draft of the manuscript. RM, DB, RR, MJW, and TNJ wrote sections of the manuscript. WH and CK provided supervision of the work and input in the analysis plan. All authors contributed to manuscript revision, read, and approved the submitted version.

Acknowledgments

We acknowledge support by the Open Access Publication Initiative of Freie Universität Berlin.

Conflict of interest

RM, MJW and DB have nothing to declare. JM is currently working at AstraZeneca in Gothenburg, Sweden. CK and WH report grants from an industry consortium (AbbVie Deutschland GmbH and Co. KG, AstraZeneca, Boehringer Ingelheim Pharma GmbH and Co. KG, Grünenthal GmbH, F. Hoffmann-La Roche Ltd., Merck KGaA and SANOFI) for the PharMetrX PhD program. CK reports an additional grant from the Innovative Medicines Initiative-Joint Undertaking ('DDMoRe'), grants from the Federal Ministry of Education and Research within the Joint Programming Initiative on Antimicrobial Resistance Initiative (JPIAMR) and from the European Commission within in the Horizon 2020 framework programme ("FAIR"), all outside the submitted work. CK reports a grant from Diurnal Ltd. UN and OB report a fee for presentation and UN grants from Diurnal Ltd., RR is Director of Diurnal Limited. TNJ is an employee of employee of Certara UK Limited.

The remaining author declares that the research was conducted in the absence of any commercial or financial relationships that could be construed as a potential conflict of interest.

Publisher's note

References

Bancos, I., Hahner, S., Tomlinson, J., and Arlt, W. (2015). Diagnosis and management of adrenal insufficiency. *Lancet Diabetes Endocrinol.* 3 (3), 216–226. doi:10.1016/S2213-8587(14)70142-1

Bonner, J. J., Burt, H., Johnson, T. N., Whitaker, M. J., Porter, J., and Ross, R. J. (2021). Development and verification of an endogenous PBPK model to inform hydrocortisone replacement dosing in children and adults with cortisol deficiency. *Eur. J. Pharm. Sci.* 165, 105913. doi:10.1016/j.ejps.2021.105913

Bornstein, S. R., Allolio, B., Arlt, W., Barthel, A., Don-Wauchope, A., Hammer, G. D., et al. (2016). Diagnosis and treatment of primary adrenal insufficiency: An endocrine society clinical practice guideline. *J. Clin. Endocrinol. Metab.* 101, 364–389. doi:10.1210/jc.2015-1710

Brendel, K., Comets, E., Laffont, C., Laveille, C., and Mentré, F. (2006). Metrics for external model evaluation with an application to the population pharmacokinetics of gliclazide. *Pharm. Res.* 23 (9), 2036–2049. doi:10.1007/s11095-006-9067-5

Derendorf, H., Mollmann, H., Barth, J., Mollmann, C., Tunn, S., and Krieg, M. (1991). Pharmacokinetics and oral bioavailability of hydrocortisone. *J. Clin. Pharm.* 31 (5), 473–476. doi:10.1002/j.1552-4604.1991.tb01906.x

El-Maouche, D., Hargreaves, C. J., Sinaii, N., Mallappa, A., Veeraraghavan, P., and Merke, D. P. (2018). Longitudinal assessment of illnesses, stress dosing, and illness sequelae in patients with congenital adrenal hyperplasia. *J. Clin. Endocrinol. Metab. [Internet* 103 (6), 2336–2345. doi:10.1210/jc.2018-00208

Falhammar, H., Frisén, L., Norrby, C., Hirschberg, A. L., Almqvist, C., Nordenskjöld, A., et al. (2014). Increased mortality in patients with congenital adrenal hyperplasia due to 21-hydroxylase deficiency. *J. Clin. Endocrinol. Metab.* 99 (12), E2715–E2721. doi:10.1210/jc.2014-2957

Finkielstain, G. P., Kim, M. S., Sinaii, N., Nishitani, M., van Ryzin, C., Hill, S. C., et al. (2012). Clinical characteristics of a cohort of 244 patients with congenital adrenal hyperplasia. *J. Clin. Endocrinol. Metab.* 97 (12), 4429–4438. doi:10.1210/jc.2012-2102

Germovsek, E., Barker, C. I. S., Sharland, M., and Standing, J. F. (2018). Pharmacokinetic–pharmacodynamic modeling in pediatric drug development, and the importance of standardized scaling of clearance. *Clin. Pharmacokinet.* 58, 39–52. doi:10.1007/s40262-018-0659-0

Hadjian, A. J., Chedin, M., Cochet, C., and Chambaz, E. M. (1975). Cortisol binding to proteins in plasma in the human neonate and infant. *Pediat Res.* 9, 40–45. doi:10.1203/00006450-197501000-00008

Han, T. S., Conway, G. S., Willis, D. S., Krone, N., Rees, D. A., Stimson, R. H., et al. (2014). Relationship between final height and health outcomes in adults with congenital adrenal hyperplasia: United Kingdom congenital adrenal hyperplasia adult study executive (CaHASE). *J. Clin. Endocrinol. Metab.* 99 (8), E1547–E1555. doi:10.1210/jc.2014-1486

Hindmarsh, P. C., and Charmandari, E. (2015). Variation in absorption and half-life of hydrocortisone influence plasma cortisol concentrations. *Clin. Endocrinol. (Oxf) [Internet]* 82 (4), 557–561. doi:10.1111/cen.12653

Hindmarsh, P. C. (2009). Management of the child with congenital adrenal hyperplasia. *Best. Pract. Res. Clin. Endocrinol. Metab.* 23 (2), 193–208. doi:10.1016/j.beem.2008.10.010

Hines, R. N. (2007). Ontogeny of human hepatic cytochromes P450. *J. Biochem. Mol. Toxicol.* 21, 169–175. doi:10.1002/jbt.20179

Jaber, M. M., Cheng, S., and Brundage, R. C. (2021). Evaluation of bias in weighted residual calculations when handling below the limit of quantification data using Beal's M3 method. *CPT Pharmacometrics Syst. Pharmacol.* 10, 275. doi:10.1002/psp4.12616

Johnson, T. N., Rostami-Hodjegan, A., and Tucker, G. T. (2006). Prediction of the clearance of eleven drugs and associated variability in neonates, infants and children. *Clin. Pharmacokinet. [Internet]* 45 (9), 931–956. doi:10.2165/00003088-200645090-00005

Johnson, T. N., Tucker, G. T., and Rostami-Hodjegan, A. (2008). Development of CYP2D6 and CYP3A4 in the first year of life. *Clin. Pharmacol. Ther.* 83, 670–671. doi:10.1038/sj.clpt.6100327

Kamoun, M., Feki, M., Sfar, M., and Abid, M. (2013). Congenital adrenal hyperplasia: Treatment and outcomes. *Indian J. Endocrinol. Metab.* 17, 14. doi:10.4103/2230-8210.119491

Kearns, G. L., Abdel-Rahman, S. M., Alander, S. W., Blowey, D. L., Leeder, J. S., Kauffman, R. E., et al. (2003). Developmental Pharmacology — drug disposition, action, and therapy in infants and children. *N. Engl. J. Med.* 349 (12), 1157–1167. doi:10.1056/NEJMra035092

Kluwe, F., Michelet, R., Mueller-Schoell, A., Maier, C., Klopp-Schulze, L., van Dyk, M., et al. (2020). Perspectives on model-informed precision dosing in the digital health era: Challenges, opportunities, and recommendations. *Clin. Pharmacol. Ther.* 109, 29–36. doi:10.1002/cpt.2049

Knutson, U., Dahlgreen, J., Marcus, C., Rosberg, S., Bronnegard, M., and Stierna, P. (1997). Circadian cortisol rhythms in healthy boys and girls: Relationships with age, growth, body composition, and pubertal development. *J. Clin. Endocrinol. Metabolism* 82 (2), 536. doi:10.1210/jcem.82.2.3769

Manolis, E., Osman, T. E., Herold, R., Koenig, F., Tomasi, P., Vamvakas, S., et al. (2011). Role of modeling and simulation in pediatric investigation plans. *Paediatr. Anaesth.* 21 (3), 214–221. doi:10.1111/j.1460-9592.2011.03523.x

Martinerie, L., Pussard, E., Meduri, G., Delezoide, A. L., Boileau, P., and Lombès, M. (2012). "Lack of renal 11 beta-hydroxysteroid dehydrogenase type 2 at birth, a targeted temporal window for neonatal glucocorticoid action in human and mice," in *PLoS one*. Editor O. Baud, 7, e31949. doi:10.1371/journal.pone.0031949

Melin, J., Parra-Guillen, Z. P., Hartung, N., Huisinga, W., Ross, R. J., Whitaker, M. J., et al. (2017). Predicting cortisol exposure from paediatric hydrocortisone formulation using a semi-mechanistic pharmacokinetic model established in healthy adults. *Clin. Pharmacokinet.* 57, 515–527. doi:10.1007/s40262-017-0575-8

Melin, J., Hartung, N., Parra-Guillen, Z. P., Whitaker, M. J., Ross, R. J., and Kloft, C. (2019). The circadian rhythm of corticosteroid-binding globulin has little impact on cortisol exposure after hydrocortisone dosing. *Clin. Endocrinol. (Oxf).* 91 (1), 33–40. doi:10.1111/cen.13969

Melin, J., Parra-Guillen, Z. P., Michelet, R., Truong, T., Huisinga, W., Hartung, N., et al. (2020). Pharmacokinetic/pharmacodynamic evaluation of hydrocortisone therapy in pediatric patients with congenital adrenal hyperplasia. *J. Clin. Endocrinol. Metab.* 105 (4), e1729–e1740. doi:10.1210/clinem/dgaa071/5735214

Merke, D. P., and Bornstein, S. R. (2005). Congenital adrenal hyperplasia. *Lancet* 365, 2125–2136. doi:10.1016/S0140-6736(05)66736-0

Michelet, R., van Bocxlaer, J., Allegaert, K., and Vermeulen, A. (2018). The use of PBPK modeling across the pediatric age range using propofol as a case. *J. Pharmacokinet. Pharmacodyn.* 45, 765–785. doi:10.1007/s10928-018-9607-8

Michelet, R., van Bocxlaer, J., and Vermeulen, A. (2018). PBPK in preterm and term neonates: A review. *Curr. Pharm. Des.* 23, 5943–5954. doi:10.2174/1381612823666171009143840

Michelet, R., Melin, J., Parra-Guillen, Z. P., Neumann, U., Whitaker, M. J., Stachanow, V., et al. (2020). Paediatric population pharmacokinetic modelling to assess hydrocortisone replacement dosing regimens in young children. *Eur. J. Endocrinol.* 183, 357–368. doi:10.1530/EJE-20-0231

Rogers, S. L., Hughes, B. A., Jones, C. A., Freedman, L., Smart, K., Taylor, N., et al. (2014). Diminished 11β-hydroxysteroid dehydrogenase type 2 activity is associated with decreased weight and weight gain across the first year of life. *J. Clin. Endocrinol. Metab.* 99, E821–E831. doi:10.1210/jc.2013-3254

Thigpen, A. E., Silver, R. I., Guileyardo, J. M., Casey, M. L., McConnell, J. D., and Russell, D. W. (1993). Tissue distribution and ontogeny of steroid 5 alpha-reductase isozyme expression. *J. Clin. Investigation* 92 (2), 903–910. doi:10.1172/JCI116665

Toothaker, R. D., Craig, W. A., and Welling, P. G. (1982). Effect of dose size on the pharmacokinetics of oral hydrocortisone suspension. *J. Pharm. Sci.* 71 (10), 1182–1185. doi:10.1002/jps.2600711029

Toothaker, R. D., and Welling, P. G. (1982). Effect of dose size on the pharmacokinetics of intravenous hydrocortisone during endogenous hydrocortisone suppression. *J. Pharmacokinet. Biopharm.* 10 (2), 147–156. doi:10.1007/BF01062332

Tsamandouras, N., Rostami-Hodjegan, A., and Aarons, L. (2013). Combining the "bottom-up" and "top-down" approaches in pharmacokinetic modelling: Fitting PBPK models to observed clinical data. *Br. J. Clin. Pharmacol.* 79, 0–16. doi:10.1111/bcp.12234

Walker, B. R., and Seckl, J. R. (2003). "Cortisol metabolism," in *International textbook of obesity*, 241–268. doi:10.1002/0470846739.ch18

Wudy, S. A., Hartmann, M. F., and Remer, T. (2007). Sexual dimorphism in cortisol secretion starts after age 10 in healthy children: Urinary cortisol metabolite excretion rates during growth. *Am. J. Physiol. Endocrinol. Metab.* 293, E970–E976. doi:10.1152/ajpendo.00495.2006

frontiers | Frontiers in Pharmacology

TYPE Perspective
PUBLISHED 17 February 2023
DOI 10.3389/fphar.2022.1094281

OPEN ACCESS

EDITED BY
Zinnia P. Parra-Guillen,
University of Navarra, Spain

REVIEWED BY
Nadia Terranova,
Merck, Switzerland

*CORRESPONDENCE
Benjamin Ribba,
benjamin.ribba@roche.com

SPECIALTY SECTION
This article was submitted to Translational Pharmacology, a section of the journal Frontiers in Pharmacology

RECEIVED 09 November 2022
ACCEPTED 12 December 2022
PUBLISHED 17 February 2023

CITATION
Ribba B (2023), Reinforcement learning as an innovative model-based approach: Examples from precision dosing, digital health and computational psychiatry. *Front. Pharmacol.* 13:1094281. doi: 10.3389/fphar.2022.1094281

Reinforcement learning as an innovative model-based approach: Examples from precision dosing, digital health and computational psychiatry

Benjamin Ribba*

Roche Pharma Research and Early Development (pRED), F. Hoffmann-La Roche Ltd, Basel, Switzerland

Model-based approaches are instrumental for successful drug development and use. Anchored within pharmacological principles, through mathematical modeling they contribute to the quantification of drug response variability and enables precision dosing. Reinforcement learning (RL)—a set of computational methods addressing optimization problems as a continuous learning process—shows relevance for precision dosing with high flexibility for dosing rule adaptation and for coping with high dimensional efficacy and/or safety markers, constituting a relevant approach to take advantage of data from digital health technologies. RL can also support contributions to the successful development of digital health applications, recognized as key players of the future healthcare systems, in particular for reducing the burden of non-communicable diseases to society. RL is also pivotal in computational psychiatry—a way to characterize mental dysfunctions in terms of aberrant brain computations—and represents an innovative modeling approach forpsychiatric indications such as depression or substance abuse disorders for which digital therapeutics are foreseen as promising modalities.

KEYWORDS

pharmacometrics, digital health, reinforcement learning, precision dosing, computational psychiatry

1 Reinforcement learning for precision dosing

Precision dosing, or the ability to identify and deliver the right dose and schedule (i.e. the dose and schedule with highest likelihood of maximizing efficacy and minimizing toxicity), is critical for public health and society. Precision dosing is not only important for marketed drugs to reduce the consequences of imprecise dosing in terms of costs and adverse events; but also for therapeutics in development to reduce attrition, often related to the challenge of precisely characterizing the therapeutic window due to a suboptimal understanding of drug-response variability. Achieving the benefit to society of precision dosing requires the identification of the main drivers of response variability, as early as possible in the drug development process, and the deployment into clinical practice

through an infrastructure designed for real-time dosing decisions in patients (Maxfield and Zineh, 2021; Peck, 2021).

Model-based approaches to clinical pharmacology, also known as clinical pharmacometrics (PMX) play a critical role in precision dosing. First, they contribute to the identification of the determinants of response variability through quantitative analysis of pharmacokinetic (PK) and pharmacodynamics (PD) relationships, and second, they constitute a central part of the infrastructure providing a simulation engine, predicting individual patient's response to a dose, and from which optimal dosing is identified through reverse engineering. Often this reverse engineering comprises two steps: first the PMX model's individual parameters are calculated through Bayesian inference, i.e. through the calculation of the mode of posterior distribution (maximum a posteriori or MAP); second, an optimal dosing scheduling is calculated, often *via* an heuristic approach through simulating various feasible dosing scenarios on inferred individuals model's instances.

Many examples exist in literature describing relevant PKPD models for precision dosing. For instance, in oncology, a model describing the time course of neutrophils following chemotherapy treatment is an ideal candidate for optimizing chemotherapy delivery (see (Friberg et al., 2002) as an example). Studies have also reported clinical investigations of model-based precision dosing approaches. For instance, the clinical study "MODEL1" was a phase I/II trial and a clear clinical attempt of a personalized dosing regimen of docetaxel and epirubicin patients with metastatic breast cancer and was shown to lead to improved efficacy-toxicity balance (Henin et al., 2016).

Reinforcement learning (RL) was also used for precision dosing. Still in oncology, Maier et al. extended the classical framework of model-driven precision dosing with RL coupled or not with data assimilation techniques (Maier et al., 2021). Previously, RL applications—although without clinical confirmation—were developed for brain tumors (Yauney and Shah, 2018) based on a model of tumor size response to chemotherapy (Ribba et al., 2012). We have recently evaluated the performance of RL algorithms for precision dosing of propofol for general anesthesia and for which a meta-analysis showed that the monitoring of the bispectral index (BIS)—a PD endpoint—contributes to reduce the amount of propofol given and the incidence of adverse reactions (Wang et al., 2021). In (Ribba et al., 2022), we performed a theoretical analysis of propofol precision dosing confronting RL to hallmarks of clinical pharmacology problems during drug development, i.e. the low number of patients and tested dosing regimen, the incomplete understanding of the drivers of response and the presence of high variability in the data.

While RL does not present as a universal solution for all types of precision dosing problems, it is an interesting modeling paradigm worth exploring. In comparison to the way PMX traditionally addresses precision dosing, RL presents several advantages. First, the possibility to take into account high dimensional PKPD variables while classical model-based approaches are often limited to a low number of variables (plasma concentration and one endpoint). In doing so, it represents an opportunity for the integration of digital health data such as from wearable devices or digital health technologies in general. Second, the definition of the precision dosing policy in a dynamic and adaptable manner through the continuous learning of the algorithm through real and simulated experience (data). RL is an approach by which both the underlying model and the optimal dosing rules are learnt simultaneously while for classical approaches, these represent two sequential steps: in other words, the consequence of the dose does not influence the model structure. Recently, studies have been published illustrating methodologies for adapting PKPD model structures through data assimilation (Lu et al., 2021; Bram et al., 2022). While high dosing frequency is not a prerequisite condition for the applicability of RL to precision dosing, this approach is well suited when the solution space of dosing is large, making heuristic approaches to find optimal dosing solutions inadequate. In our example on propofol, dosing could happen every 5 s so over a short period of 2 min, the space of solutions to explore when considering dichotomous dosing even is greater than 16 million possibilities.

RL is at the crossroads between two scientific fields. First, the field of learning by trial and error that started with the study of the psychology of animal learning and second, the field of optimal control (Sutton and Barto, 2018). RL are often formally described with Markov Decision Process or MDP which includes all important features a learning agent should have, namely, being able to sense the environment, being able to take action and have clarity on the goal. In RL, a learning agent takes an action and, as a result, transitions from one state to another. After each action taken, the interaction between the agent and its environment produces a reward. The goal of the RL problem is to map actions to situations (state), i.e. knowing which actions to take in each state to maximize the accumulated reward. As long as the optimization problem can be formulated within the MDP framework, RL can be applied and its efficiency explored.

For precision dosing of propofol, the state can be represented by a table, an approach also called tabular solution methods. In the next two sections, the state will be defined by a continuous function. The reward was determined based on the value reached by the BIS as a direct consequence of the action taken: the closer the BIS to the target, the higher the reward. Finally, given the theoretical study, the true PKPD model (linking the dose application to BIS) was used as an experience (data) generator. The left column of Table 1 summarizes the characteristics of the application of RL to the propofol precision dosing problem.

The minimal set of RL characteristics makes it a very flexible paradigm, suitable for a large variety of problems. Herein, we will in fact illustrate this flexibility by illustrating how this framework

TABLE 1 Main characteristics of RL algorithm implementation to the precision dosing of pharmacological interventions (left column); the precision dosing of digital intervention (middle column); and computational psychiatry (right column). While there are multiple similarities between the precision dosing of pharmacological and digital interventions, the application of RL in computational psychiatry shows as a paradigm shift. RL computational machinery is not deployed as a technical approach to address the optimal control problem of precision dosing but is fitted to (cognitive task) data assuming the algorithm itself presents mechanistic similarities with how brain's participants functioned during the task.

	Precision dosing of a pharmacological intervention	Precision dosing of a digital intervention	Computation psychiatry
Study case [References]	Optimal dosing of propofol administration (Ribba et al., 2022)	Just-in-time-adaptive-intervention for HeartSteps, mobile app aimed at reducing physical inactivity (Liao et al., 2020)	Population analysis of signal-detection task in anhedonic subjects (Huys et al., 2013)
Type of RL solution	Tabular	Continuous	
State	*Is directly linked to the state of the patient*		*Is linked to the situation the participant to the task is presented with and based on which an action must taken*
	PK drivers and/or PD endpoint such as the BIS	Contextual drivers (e.g. weather conditions, time of the day) and patient-related status derived from wearable device equipment	Belief of the correctness (weight) of each stimuli present in the task
Action	Dose or not	Dose (walking suggestion message) or not	Participant's answer choice
Reward	*Defined to enable the algorithm converging to the optimal dosing solution*		*Corresponds to whether the answer is correct or wrong*
	Simple function of BIS leading to high reward when actual BIS is close to its target	Step count in the 30 min window after each decision time	Automatically derived from the answer as per task design and setup
Use of simulated experience?	*Yes*		*No*
	The true underlying PKPD model is used	Linear model assimilating real data	No need for simulated experience, RL algorithm is mapped to the trial-by-trial data
Algorithm	Temporal difference Q-learning	Thomson Sampling	Temporal difference Q-learning
Free parameters	*Used to calibrate model of patient's response to dosing event*		*Used to calibrate RL algorithm*
	Parameters of the PKPD model	Parameters of the linear model for reward prediction under alternative dosing scenarios	Learning rate and reward sensitivity parameter

can be viewed as a bridge between a priori distinct areas such as precision dosing of pharmacological drugs, digital health and computational psychiatry.

In the appendix, we propose to demystify how RL algorithms—such as temporal difference Q-learning, repeatedly mentioned here—work, taking a simple illustration from video gaming.

2 Reinforcement learning in digital health

For several years, many reports have indicated the key importance of digital health for reducing the burden to society of non-communicable diseases such as cardiovascular, diabetes, cancer or psychiatric diseases, in part due to the aging of the population and—paradoxically—the success of pharmacologically-based interventions in increasing life expectancy while being affected by pathological conditions (Fleisch et al., 2021). Prevention and interventions targeting lifestyle are essential tools to address this societal challenge of ever-growing importance as our healthcare systems risk collapse under cost pressure.

In 2008, it was estimated that physical inactivity causes 6% of the burden of coronary heart disease, 7% of type II diabetes, 10% of breast cancer and 10% of colon cancer and overall the cause of more than 5.3 million of the 57 million deaths which occurred that year (Lee et al., 2012). In that study, the authors also estimated that with 25% reduction of physical inactivity, 1.3 million of deaths could be averted every year. Given the constant increase of smartphone coverage worldwide, it is natural to think of mobile health technologies to support healthy lifestyle habits and prevention. The thinktank Metaforum from KU Leuven dedicated its position paper 17 on the use of wearables and mobile technologies for collecting information on individual behavior and physical status—combined with data from individual's environment—to personalize recommendations (interventions) bringing the subject to adopt a healthier lifestyle (Claes, 2022).

When the intervention is intended to have a therapeutic benefit, it falls in the field of digital therapeutics when associated with demonstration of clinical effectiveness and approved by regulatory bodies (Sverdlov et al., 2018). This point of junction

between digital health applications and pharmacological drugs represents a ground for attempting to reframe PMX—a recognized key player in the development of the latter—as a key support to the development of the former, in particular when it comes to precision dosing for digital health.

The precision dosing of digital therapeutics overlaps with the concept of just-in-time adaptive intervention or JITAI (Nahum-Shani et al., 2018). In the mobile technology literature, JITAI has been primarily considered as a critical topic for increasing adherence and retention of users; but within a therapeutic perspective, it should encompass both the topic of adherence and retention to the therapeutic modality and the topic of its optimal dosing in order to maximize clinical benefit. For clarity, these two different learning problems should be distinguished as many existing applications focus primarily on the first one. For example, a growing number of mobile applications developed under the concept of virtual coaching aim to optimize the design of the interventions (time and content, e.g. messages sent by the app to the users with the form of a prompt appearing on a locked screen) to incite the user to take actions. HeartSteps was designed to encourage user to increase their physical activity and where content delivery, such as tailored walking suggestion messages, is optimized with an RL algorithm (Liao et al., 2020). Here, RL is used to address the first learning problem: How to deliver the content so that the user is doing what is recommended. We each need different forms of prompting and potentially different forms of exercise to increase our physical activity. Overall, this problem is similar to that of adherence to a pharmacological regimen. But a second problem is: what is the right dose of the desired intervention? In other words: How many steps is optimal for each patient? This is the usual precision dosing problem for drugs and there is a clear opportunity for digital health applications to extend the domain of application of JITAIs to that problem as well.

One of the particularly interesting aspects of the research on RL algorithms for HeartSteps is that, beyond the innovative nature of the work purely related to the design of personalized interventions, it also includes ways to objectively evaluate its efficiency. An experimental design called micro-randomized trial (MRT) is proposed as a framework to evaluate the effectiveness of personalized *versus* non-personalized interventions (Klasnja et al., 2015; Qian et al., 2022). The principle of MRT is to randomize the interventions multiple times for each subject. Statistical approaches have been studied to leverage MRT-derived data in order to inform treatment effects and the response variability (Qian et al., 2020). In the theoretical propofol example described in the previous section, we used the true PKPD model to simulate experience. In the real-life RL application of HeartSteps, the authors had the objective to design a method for learning quickly and for accommodating noisy data (Liao et al., 2020). To address these points, the authors used a simulation engine to enhance data collected from real experience and this simulation engine was built with simple linear models. Precisely, the authors modeled the difference in reward function under alternative dosing options with low dimensional linear models, which features were selected based on retrospective analysis of previous HeartSteps data and based on experts' guidance. The precision dosing problem was addressed using posterior sampling *via* Thompson-Sampling, identified as performant in balancing exploration and exploitation (Russo and Van Roy, 2014; Russo et al., 2018). The definition of the state was based on several individual's features including contextual information or sensor data from wearable devices while the reward was defined as the step counts within 30 min after the "dosing" event. The middle column of Table 1 summarizes the main characteristic of RL application to this problem.

3 Reinforcement learning in computational psychiatry

Like mechanistic modelling, computational psychiatry refers to a systems approach aimed at integrating underlying pathophysiological processes. However, while mechanistic modelling efforts typically use multiscale biological processes as building blocks, some models that fall within the remit of computational psychiatry (such as RL) use different types of building blocks, and in particular brain cognitive processes.

Model-based approaches have shown relevance for addressing major challenges in neuroscience (see (Conrado et al., 2020) for an example for Alzheimer disease). Quantitative systems pharmacology and mechanistic-based multiscale modelling are, in particular, associated with major hopes while acknowledging significant challenges such as the lack of quantitative and validated biomarkers, the subjective nature of clinical endpoints and the high selectivity of drug candidates not reflecting the complex interactions of different brain circuits (Geerts et al., 2020; Bloomingdale et al., 2021). These challenges are equally valid for attempting to address psychiatric conditions. This can partly explain the efficiency of non-pharmacological interventions, such as targeted psychotherapy approaches, recognized as one of the most precise and powerful approaches (Insel and Cuthbert, 2015).

The efficiency of such interventions is a testimony of how the brain's intrinsic plasticity can alter neural circuits. Some (discursive) disease models—with a focus on systems dimensions–propose new perspectives in the understanding of such conditions. For instance, it has been reported that emotion-cognition interactions gone awry can lead to anxiety and depression conditions; with anxious individuals displaying attentional-bias toward threatening stimuli and have difficulty disengaging from it (Crocker et al., 2013). Further data-driven understanding—at the systems level—is key to increase the likelihood of success of such non-pharmacological interventions, as it is equally the case for research and development of pharmaceutical compounds (Pao and Nagel,

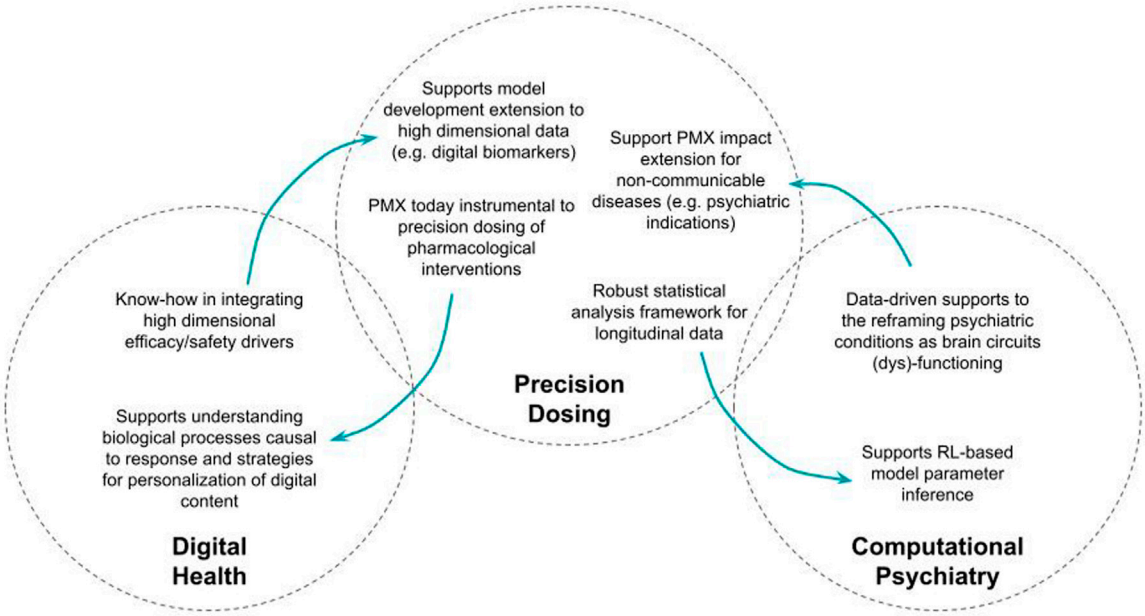

FIGURE 1
Illustration of the mutual benefits of increased permeability between model-based approaches to precision dosing and digital health, on one hand, and computational psychiatry on the other hand.

2022). Such data-driven understanding can be integrated in the design of relevant non-pharmacological interventions, with some of them known to be amenable to digital delivery through, for instance, digital therapeutics (Jacobson et al., 2022).

A precision medicine initiative—precision psychiatry—has been initiated for psychiatric indications, such as major depression or substance abuse disorder, constituting a major part of non-communicable diseases (Insel and Cuthbert, 2015). The core idea of precision psychiatry lies in the reframing the diagnosis and care of affected subjects by moving away from a symptom-based to a data-driven categorization through a focus on system dimension *via* integration of data from cognitive, affective and social neuroscience, overall shifting the way to characterize these conditions in terms of brain circuits (dys-)functioning. This concept materialized in proposing the Research Domain Criteria (RDoc) in 2010 (Insel et al., 2010) as a framework for research in pathophysiology of psychiatric conditions.

Integrating into a multiscale modelling framework, data from cognitive, affective and social neuroscience is an objective of computational psychiatry, defined as a way to characterize mental dysfunction in terms of aberrant computation in the brain (Montague et al., 2012). Not surprisingly, by its mimicking of human and animal learning processes, RL plays a key role in computational psychiatry. RL in computational psychiatry proposes to map brain functioning in an algorithmic language offering then the possibility to explore, through simulations, the dysfunctioning of these processes as well as the theoretical benefit of interventional strategies. Two examples will be further developed here and the readers can refer to (Seriès, 2020) for an overview of more computational psychiatry methods, models and study cases.

In a RL framework, actions by the learner are chosen according to their value function, which holds the expected accumulated reward. The value function is updated through experience using feedback from the environment to the action taken. This update is also called temporal difference. An analogy has been drawn between this temporal difference and reward-error signals carried by dopamine in decision-making. Temporal difference reinforcement learning algorithms learn by estimating a value function based on temporal differences. The learning stops as this different converges to zero (see Supplementary Material for further details). Such a framework can be used to reframe addiction as a decision-making process gone awry. Based on the observation that addictive drugs produce a transient increase in dopamine through neuropharmacological mechanisms, the proposed model assumes that an addictive drug produces a positive temporal difference independent of the value function so that the action of taking drug will be always preferred over other actions (Redish, 2004). This model provides a tool to explore the efficiency of public health strategies. For instance, the model proposes some hypotheses to explain the incomplete success of strategies based on offering money as an alternate choice from drug intake.

RL models are used for the analysis of data of cognitive tasks and in particular tasks related to decision-making. Instead of focusing on the summary statistics of such tests (e.g, total number

of errors), RL-based approaches allow for the integration of trial-by-trial data similarly to what model-based approaches typically do—with longitudinal data analysis—to better decipher response variability *via* the characterization of PK and PD processes. In the same way, trial-by-trial data can be leveraged to estimate RL-model based parameters which, in turn, can be compared to clinical endpoints such as measures of symptom severity to disentangle the role of brain circuit mechanisms overall contributing to a better understanding of response variability. RL for cognitive testing data in psychiatric populations is a complete paradigm change with respect to its application for precision dosing problems. While–in the two previous examples—RL was used to solve the problem of optimal dosing, now the RL algorithm is mapped to neuro-cognitive processes. Quantitatively characterizing these processes for each patient (estimating parameters from RL algorithms) is proposed as a methodology for extracting relevant information towards disease characterization and thus, response variability.

In (Huys et al., 2013), the authors use RL models to analyse population data of a behavioural test (signal-detection task) to study aspects of anhedonia—a core symptom of depression—related to reward learning. The authors proposed a RL model based on Q-learning update integrating two parameters: the classical learning rate and a parameter related to reward sensitivity modulating the percentage of the reward value actually contributes to the update of the Q value function. By performing a correlation analysis of the inferred parameters with anhedonic depression questionnaire, the authors found a negative correlation between the reward sensitivity but no correlation with the learning rate. Overall, these results led to the conclusion that the sensitivity to the reward and not the learning rate could be the main driver explaining why in anhedonic individuals, reward has less impact than in non-anhedonic individuals. Unravelling these two mechanisms is important for the planning of successful digital, behavioural and pharmacological strategies. The right column in Table 1 depicts the summary characteristics of RL applied to that study.

4 Conclusion

In this perspective, we have illustrated the flexibility of RL framework throughout the described applications in precision dosing, digital health and computational psychiatry and with that have demonstrated the benefit for the modeling community to become familiar with these approaches. The contrary is also true, and the field of precision digital therapeutics and computational psychiatry can benefit much from a proximity to the PMX community.

First, PMX methods could make RL even better. The field of computational psychiatry could benefit from input from the PMX community when it comes to statistical aspects related to parameters inference and clinical endpoint modelling. Two areas for which PMX has adopted as its state-of-the-art, population approach (with powerful algorithms such as stochastic approximation expectation-maximization algorithm (Lavielle, 2014)) and joint modelling respectively.

Second, the field of digital health should benefit from what constitutes one of the essential objectives of model-based drug development approaches, namely: elucidating response variability. It is particularly important for the successful development of digital therapeutic interventions to know how to characterize the efficacy and safety profiles and to know how to develop personalization strategies based on this understanding. The fact that it is about digital interventions should not prevent developers from prioritizing research in understanding underlying causal biological and (patho)-physiological processes of response, which will always be a key factor of successful therapy development, either pharmacological or not. Figure 1 proposes an illustration of these mutual benefits.

5 Legend

Table 1: Main characteristics of RL algorithm implementation to the precision dosing of pharmacological interventions (left column); the precision dosing of digital intervention (middle column); and computational psychiatry (right column). While there are multiple similarities between the precision dosing of pharmacological and digital interventions, the application of RL in computational psychiatry shows as a paradigm shift. RL computational machinery is not deployed as a technical approach to address the optimal control problem of precision dosing but is fitted to (cognitive task) data assuming the algorithm itself present mechanistic similarities with how brain's participants functioned during the task.

Data availability statement

The original contributions presented in the study are included in the article/Supplementary Material, further inquiries can be directed to the corresponding author.

Author contributions

BR: manuscript writing.

Acknowledgments

The author wishes to acknowledge Lucy Hutchinson, Richard Peck and Denis Engelmann for providing inputs on the drat manuscript.

Conflict of interest

The author is employed by F. Hoffmann La Roche Ltd.

Publisher's note

All claims expressed in this article are solely those of the authors and do not necessarily represent those of their affiliated organizations, or those of the publisher, the editors and the reviewers. Any product that may be evaluated in this article, or claim that may be made by its manufacturer, is not guaranteed or endorsed by the publisher.

Supplementary material

The Supplementary Material for this article can be found online at: https://www.frontiersin.org/articles/10.3389/fphar.2022.1094281/full#supplementary-material

References

Bloomingdale, P., Karelina, T., Cirit, M., Muldoon, S. F., Baker, J., McCarty, W. J., et al. (2021). Quantitative systems pharmacology in neuroscience: Novel methodologies and technologies. *CPT Pharmacometrics Syst. Pharmacol.* 10 (5), 412–419. doi:10.1002/psp4.12607

Bram, D. S., Parrott, N., Hutchinson, L., and Steiert, B. (2022). Introduction of an artificial neural network-based method for concentration-time predictions. *CPT Pharmacometrics Syst. Pharmacol.* 11 (6), 745–754. doi:10.1002/psp4.12786

Claes, S. (2022), Mobile health revolution in healthcare: Are we ready? Metaforum position paper 17 2019 [cited 2022 October 10]; Available at: https://www.kuleuven.be/metaforum/visie-en-debatteksten/2019-mobile-health-revolution-in-healthcare.

Conrado, D. J., Duvvuri, S., Geerts, H., Burton, J., Biesdorf, C., Ahamadi, M., et al. (2020). Challenges in alzheimer's disease drug discovery and development: The role of modeling, simulation, and open data. *Clin. Pharmacol. Ther.* 107 (4), 796–805. doi:10.1002/cpt.1782

Crocker, L. D., Heller, W., Warren, S. L., O'Hare, A. J., Infantolino, Z. P., and Miller, G. A. (2013). Relationships among cognition, emotion, and motivation: Implications for intervention and neuroplasticity in psychopathology. *Front. Hum. Neurosci.* 7, 261. doi:10.3389/fnhum.2013.00261

Fleisch, E., Franz, C., and Herrmann, A. (2021). *The digital pill*.

Friberg, L. E., Henningsson, A., Maas, H., Nguyen, L., and Karlsson, M. O. (2002). Model of chemotherapy-induced myelosuppression with parameter consistency across drugs. *J. Clin. Oncol.* 20 (24), 4713–4721. doi:10.1200/JCO.2002.02.140

Geerts, H., Wikswo, J., van der Graaf, P. H., Bai, J. P. F., Gaiteri, C., Bennett, D., et al. (2020). Quantitative systems pharmacology for neuroscience drug discovery and development: Current status, opportunities, and challenges. *CPT Pharmacometrics Syst. Pharmacol.* 9 (1), 5–20. doi:10.1002/psp4.12478

Henin, E., Meille, C., Barbolosi, D., You, B., Guitton, J., Iliadis, A., et al. (2016). Revisiting dosing regimen using PK/PD modeling: The MODEL1 phase I/II trial of docetaxel plus epirubicin in metastatic breast cancer patients. *Breast Cancer Res. Treat.* 156 (2), 331–341. doi:10.1007/s10549-016-3760-9

Huys, Q. J., Pizzagalli, D. A., Bogdan, R., and Dayan, P. (2013). Mapping anhedonia onto reinforcement learning: A behavioural meta-analysis. *Biol. Mood Anxiety Disord.* 3 (1), 12. doi:10.1186/2045-5380-3-12

Insel, T., Cuthbert, B., Garvey, M., Heinssen, R., Pine, D. S., Quinn, K., et al. (2010). Research domain criteria (RDoC): Toward a new classification framework for research on mental disorders. *Am. J. Psychiatry* 167 (7), 748–751. doi:10.1176/appi.ajp.2010.09091379

Insel, T. R., and Cuthbert, B. N. (2015). Medicine. Brain disorders? Precisely. *Science* 348 (6234), 499–500. doi:10.1126/science.aab2358

Jacobson, N. C., Kowatsch, T., and Marsch, L. A. (2022). *Digital therapeutics for mental health and addiction: The state of the science and vision for the future*. San Diego, CA: Academic Press, 270.

Klasnja, P., Hekler, E. B., Shiffman, S., Boruvka, A., Almirall, D., Tewari, A., et al. (2015). Microrandomized trials: An experimental design for developing just-in-time adaptive interventions. *Health Psychol.* 34S, 1220–1228. doi:10.1037/hea0000305

Lavielle, M. (2014). *Mixed effects models for the population approach: Models, tasks, methods and tools*. 1st edition. Chapman and Hall/CRC.

Lee, I. M., Shiroma, E. J., Lobelo, F., Puska, P., Blair, S. N., Katzmarzyk, P. T., et al. (2012). Effect of physical inactivity on major non-communicable diseases worldwide: An analysis of burden of disease and life expectancy. *Lancet* 380 (9838), 219–229. doi:10.1016/S0140-6736(12)61031-9

Liao, P., Greenewald, K., Klasnja, P., and Murphy, S. (2020). Personalized HeartSteps: A reinforcement learning algorithm for optimizing physical activity. *Proc. ACM Interact. Mob. Wearable Ubiquitous Technol.* 4 (1), 18. doi:10.1145/3381007

Lu, J., Deng, K., Zhang, X., Liu, G., and Guan, Y. (2021). Neural-ODE for pharmacokinetics modeling and its advantage to alternative machine learning models in predicting new dosing regimens. *iScience* 24 (7), 102804. doi:10.1016/j.isci.2021.102804

Maier, C., Hartung, N., Kloft, C., Huisinga, W., and de Wiljes, J. (2021). Reinforcement learning and Bayesian data assimilation for model-informed precision dosing in oncology. *CPT Pharmacometrics Syst. Pharmacol.* 10 (3), 241–254. doi:10.1002/psp4.12588

Maxfield, K., and Zineh, I. (2021). Precision dosing: A clinical and public health imperative. *JAMA* 325 (15), 1505–1506. doi:10.1001/jama.2021.1004

Montague, P. R., Dolan, R. J., Friston, K. J., and Dayan, P. (2012). Computational psychiatry. *Trends Cogn. Sci.* 16 (1), 72–80. doi:10.1016/j.tics.2011.11.018

Nahum-Shani, I., Smith, S. N., Spring, B. J., Collins, L. M., Witkiewitz, K., Tewari, A., et al. (2018). Just-in-Time adaptive interventions (JITAIs) in mobile health: Key components and design principles for ongoing health behavior support. *Ann. Behav. Med.* 52 (6), 446–462. doi:10.1007/s12160-016-9830-8

Pao, W., and Nagel, Y. A. (2022). Paradigms for the development of transformative medicines-lessons from the EGFR story. *Ann. Oncol.* 33 (5), 556–560. doi:10.1016/j.annonc.2022.02.005

Peck, R. W. (2021). Precision dosing: An industry perspective. *Clin. Pharmacol. Ther.* 109 (1), 47–50.

Qian, T., Klasnja, P., and Murphy, S. A. (2020). Linear mixed models with endogenous covariates: Modeling sequential treatment effects with application to a mobile health study. *Stat. Sci.* 35 (3), 375–390. doi:10.1214/19-sts720

Qian, T., Walton, A. E., Collins, L. M., Klasnja, P., Lanza, S. T., Nahum-Shani, I., et al. (2022). The microrandomized trial for developing digital interventions: Experimental design and data analysis considerations. *Psychol. Methods* 27, 874–894. doi:10.1037/met0000283

Redish, A. D. (2004). Addiction as a computational process gone awry. *Science* 306 (5703), 1944–1947. doi:10.1126/science.1102384

Ribba, B., et al. (2022). *Model enhanced reinforcement learning to enable precision dosing: A theoretical case study with dosing of propofol*. CPT Pharmacometrics Syst Pharmacol.

Ribba, B., Kaloshi, G., Peyre, M., Ricard, D., Calvez, V., Tod, M., et al. (2012). A tumor growth inhibition model for low-grade glioma treated with chemotherapy or radiotherapy. *Clin. Cancer Res.* 18 (18), 5071–5080. doi:10.1158/1078-0432.CCR-12-0084

Russo, D. J., Van Roy, B., Kazerouni, A., Osband, I., and Wen, Z. (2018). A tutorial on Thompson sampling. *Found. Trends® Mach. Learn.* 11 (1), 1–96. doi:10.1561/2200000070

Russo, D., and Van Roy, B. (2014). Learning to optimize via posterior sampling. *Math. Operations Res.* 39 (4), 1221–1243. doi:10.1287/moor.2014.0650

Seriès, P. E. (2020). *Computational psychiatry*. The MIT Press.

Sutton, R., and Barto, A. (2018). *Reinforcement learning: An introduction*. Second edition.

Sverdlov, O., van Dam, J., Hannesdottir, K., and Thornton-Wells, T. (2018). Digital therapeutics: An integral component of digital innovation in drug development. *Clin. Pharmacol. Ther.* 104 (1), 72–80. doi:10.1002/cpt.1036

Wang, D., Song, Z., Zhang, C., and Chen, P. (2021). Bispectral index monitoring of the clinical effects of propofol closed-loop target-controlled infusion: Systematic review and meta-analysis of randomized controlled trials. *Med. Baltim.* 100 (4), e23930. doi:10.1097/MD.0000000000023930

Yauney, G., and Shah, P. (2018). "Reinforcement learning with action-derived rewards for chemotherapy and clinical trial dosing regimen selection," in Proceedings of the 3rd Machine Learning for Healthcare Conference (PMLR: Proceedings of Machine Learning Research), 161–226. D.-V. Finale, et al., Editors.

frontiers | Frontiers in Pharmacology

TYPE Perspective
PUBLISHED 08 March 2023
DOI 10.3389/fphar.2022.1058220

OPEN ACCESS

EDITED BY
Victor Mangas Sanjuan,
University of Valencia, Spain

REVIEWED BY
Sherwin Sy,
University of Florida, United States

*CORRESPONDENCE
Benjamin Ribba,
benjamin.ribba@roche.com

SPECIALTY SECTION
This article was submitted to Translational Pharmacology,
a section of the journal
Frontiers in Pharmacology

RECEIVED 30 September 2022
ACCEPTED 01 December 2022
PUBLISHED 08 March 2023

CITATION
Ribba B, Roller A, Helms H-J, Stern M and Bleul C (2023), Circulating tumor DNA: Opportunities and challenges for pharmacometric approaches.
Front. Pharmacol. 13:1058220.
doi: 10.3389/fphar.2022.1058220

Circulating tumor DNA: Opportunities and challenges for pharmacometric approaches

Benjamin Ribba*, Andreas Roller, Hans-Joachim Helms, Martin Stern and Conrad Bleul

Roche Pharma Research and Early Development, Roche Innovation Center Basel, F. Hoffman-La Roche Ltd, Basel, Switzerland

To support further development of model-informed drug development approaches leveraging circulating tumor DNA (ctDNA), we performed an exploratory analysis of the relationships between treatment-induced changes to ctDNA levels, clinical response and tumor size dynamics in patients with cancer treated with checkpoint inhibitors and targeted therapies. This analysis highlights opportunities for pharmacometrics approaches such as for optimizing sampling design strategies. It also highlights challenges related to the nature of the data and associated variability overall emphasizing the importance of mechanistic modeling studies of the underlying biology of ctDNA processes such as shedding, release and clearance and their relationships with tumor size dynamic and treatment effects.

KEYWORDS

early clinical development, cancer immunotherapies, circulating tumor DNA (ctDNA), clinical efficacy, modeling and simulation

Introduction

Predicting long-term clinical benefit of anti-cancer drugs is notoriously difficult. Nevertheless, such predictions can play a key role in reducing the attrition rate of anti-cancer molecules in late phase clinical trials (Hutchinson and Kirk, 2011). Recently, circulating tumor DNA (deoxyribonucleic acid) or ctDNA, which can be collected longitudinally, has been shown to hold additional predictive power to imaging-based markers of response (Cescon et al., 2020). Pharmacometric (PMX) approaches can take the advantage of longitudinal measurements as demonstrated with tumor growth modeling approaches and, as such, represent an opportunity for ctDNA to inform new molecular entity (NME) clinical trial development with respect to identification of clinically most promising compounds, optimal sampling design, combination partners, and precision dosing.

In this perspective, through the exploratory analysis of ctDNA data from nearly 500 cancer patients treated with checkpoint inhibitors and targeted therapies, we dissect the relationships between on-treatment ctDNA change over time from baseline and overall survival, clinical response, and tumor size dynamics. We believe this effort is a required first step for the further successful development of model-based approaches. The analysis also sheds light on interconnected challenges related to the specific nature of the data, associated variability, and complexity of underlying biology of ctDNA processes such as shedding, release, and clearance (Avanzini et al., 2020) and their relationships with tumor size dynamics and treatment effects (see Figure 1A).

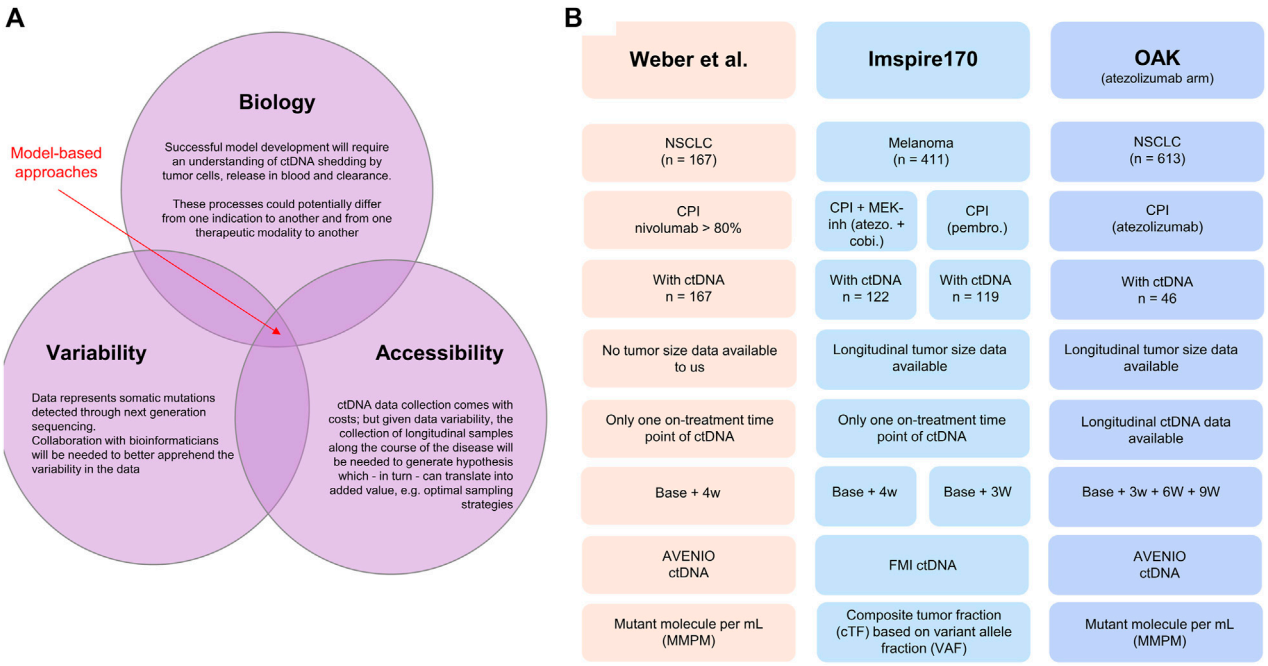

FIGURE 1
(A) Illustration of the interconnected challenges inherent to the successful development of a model-based approach for leveraging longitudinal ctDNA to support early clinical decision-making in oncology, namely, the access to highly longitudinal samples and the understanding of disease biology and bioinformatic nature of the data. **(B)** Database description: Weber et al. (2021) clinical study published in 2021. The dataset was shared with the authors without further obligations according to the policy of the Journal of Clinical Oncology Precision Oncology and according to the local patient-level sharing privacy rules. The dataset is composed of 167 patients with non-small cell lung cancer. The ctDNA sample collection was performed between 2015 and 2018. The Roche AVENIO assay was used for ctDNA measurements and reported as (average) mutant molecules per milliliter measured consistently at two time points (baseline, i.e., cycle 1 1 and 28 days in median, SD = 10 days). For 15 patients, the ctDNA value at both baseline and on treatment was recorded 0, making the calculation of change from baseline impossible. These patients were removed from the analysis. Patients suffered from stage IIIB (13.2%) or stage IV (86.8%) NSCLC; all were treated with checkpoint inhibitors (nivolumab for more than 80%). The overall response rate was 26.3% (n = 44), and the mean treatment duration was 13 cycles. Anonymized patient-level survival data were available. IMspire170: Roche sponsored study on patients with melanoma (Gogas et al., 2021) Data consisted of 411 patients, of which 209 patients were treated with the checkpoint inhibitor atezolizumab with the tyrosine kinase (MEK-) inhibitor cobimetinib and 202 patients with pembrolizumab. ctDNA measurements were reported as a ctDNA tumor fraction (cTF) based on aneuploidy and variant allele fraction (VAF) and were available for 241 patients (122 in the group treated with atezolizumab and cobimetinib and 119 in the group treated with pembrolizumab). Two time points were available: baseline (cycle 1 day 1) and cycle 2 day 1 (corresponding to 21 days for the pembrolizumab cohort and 28 days for the atezolizumab/cobimetinib cohort). Tumor size (sum of longest diameters) was available longitudinally for 409 patients out of the 411 patients. Patient-level survival data were available. OAK: Roche sponsored the study on non-small cell lung cancer patients treated with the checkpoint inhibitor atezolizumab or chemotherapy docetaxel (Rittmeyer et al., 2017). The study included 1,225 patients. ctDNA data were available for a subset only (n = 94). Our analysis included only the data from the atezolizumab arm (n = 613 and 46 with ctDNA data). The data from the chemotherapy arm were only used for developing the ctDNA time course model with the treatment arm regarded as a covariate. The Roche AVENIO assay was performed for ctDNA measurements and reported as mutant molecules per milliliter, and data at four time points were available: cycle 1 (baseline), cycle 2 (around 21 days), cycle 3 (around 42 days), and cycle 4 (around 63 days). These data were used for longitudinal modeling using the Stein et al. model. OAK ctDNA data analysis has been already published (Zou et al., 2021).

Problem statement

Traditionally, the rate of "best overall response" gives an indication of patients' early response to treatment based on repeatedly quantifying the size of one or several cancer lesions by radiographic imaging. The overall response rate (ORR) is the percentage of patients achieving a complete or partial response through RECIST 1.1 at any time of the treatment (Ruchalski et al., 2021). Observing a high ORR in early clinical studies is encouraging and often ungates further studies and investment. A low ORR, on the contrary, could amongst others, indicate an absence of efficacy and can support the decision to stop development of an experimental treatment. However, the correlation between ORR and long-term clinical benefit is limited, in particular for cancer immunotherapy which does not act directly by killing tumor cells but rather stimulates an anti-tumor response (Gerwing et al., 2019; Goulart et al., 2022). For tebentafusp, a T-cell bispecific cancer immunotherapy approved recently for the treatment of metastatic uveal melanoma, approval was based on the observed improvement of overall survival in a randomized phase III trial. Early clinical trials had shown many patients remaining on trial for a long time in stable disease, however, with a radiological response rate (RR) of only 12% (Carvajal et al., 2022). Such a low response rate could have led many drug developers to stop the development of what is, in reality, an efficacious medicine. This example indicates that while RR could be associated with high specificity for identification of drugs that convey a survival benefit, sensitivity might be low. As a consequence, complementing RR information with data that can hold predictive potential is key for decision-making in oncology development where decisions to invest in large and costly confirmatory clinical trials typically relies on the results of previously conducted clinical studies (phase I - II) with a limited number of patients (Cannarile et al., 2021).

The PMX community has been, for many years, contributing to the question of how to improve early decision-making. It proposes to leverage the time course of tumor size instead of relying on a categorical score (RECIST 1.1) derived from the comparison of the sum of the longest diameters (SLD) between baseline from up to five measurable target lesions and one given time point (the one at which the best response is observed) (Yates and Cheung, 2021). As such, PMX approaches are ideally positioned to integrate informative data collected longitudinally. In fact, efforts to complement the existing state-of-the-art tumor size kinetic models with other relevant biomarkers have been an important area of research for many years (Netterberg et al., 2020).

Liquid biopsies enabling the measurement of ctDNA have emerged as a promising technology to overcome some of the limitations discussed previously (Zhang et al., 2020). When tumor cells die from apoptosis or necrosis, their DNA is shed and released into circulating blood (Heitzer et al., 2020). Technologies such as next-generation sequencing (NGS) can detect somatic mutations and quantify ctDNA in terms of variant allele frequency (VAF, ratio between the number of mutated- and wild-type DNA copies) or mutant tumor molecules per milliliter of plasma (MMPM) (Bos et al., 2021). Numerous studies have now been published on the potential of ctDNA for screening or for characterizing disease biology (Cheng et al., 2016). Another application with a lot of potential with respect to the opinions discussed previously is the use of ctDNA as a measure of disease burden and with this, as a predictor of long-term clinical benefit (Bratman et al., 2020). In the aforementioned example of tebentafusp, ctDNA change from baseline within 9 weeks following treatment start was associated with long-term clinical benefit. It was also reported that the degree of ctDNA reduction correlated with overall survival and that this association was largely independent from the radiological response categorization (Shoushtari et al., 2021).

Circulating tumor DNA and overall survival

To better understand the potential of model-based approaches to explore ctDNA data, we built a dataset composed of 454 patients from three published clinical studies (Rittmeyer et al., 2017; Gogas et al., 2021; Weber et al., 2021). Two studies focused on non-small cell lung cancer (n = 213 patients in total: 167 in one study and 46 in another) and one on melanoma (n = 241). The studies involved different types of treatment: immunotherapy with a checkpoint inhibitor (CPI: atezolizumab, nivolumab, pembrolizumab, durvalumab, and ipilimumab) alone (n = 332, pooling data from three studies) or in combination with targeted therapy (atezolizumab + cobimetinib) (n = 122, from one study). Indication, treatment, and sampling design of ctDNA and technology for its quantification were different between the studies. A summary of the analyzed dataset is illustrated in Figure 1B.

Based on the data from Weber et al. (2021), which were shared with us without further obligations according to the policy of the Journal of Clinical Oncology Precision Oncology, we show in Figure 2A Kaplan–Meier curves of patients' overall survival as a function of early change in ctDNA. We selected the commonly used 50% ctDNA reduction from baseline as the cut-off (Nabet et al., 2020; Weber et al., 2021; Zou et al., 2021). The two curves separate, and the patients who achieve a 50% ctDNA reduction have a larger probability to live longer than those who do not. We calculated hazard ratios using varying cut-offs of ctDNA change from baseline and showed that a higher degree of ctDNA decrease is associated with a lower hazard ratio (i.e., longer survival), similar to what has been reported for tebentafusp (Figure 2A, inset).

To further evaluate the impact of ctDNA dynamics on the long-term clinical outcome (e.g., overall survival), we used the same dataset to perform a simulation study using RECIST 1.1 response criteria as a comparator. For RECIST, we defined response as complete response (CR) or partial response (PR). For ctDNA, we kept the commonly used threshold of 50% drop at week 4 from baseline. We generated overall survival data using exponential distribution parameterized with the observed hazard rates and performed simulations with a virtual population of 10,000 patients, varying the percentage of responders in the population from 10 to 90%, plotted corresponding Kaplan–Meier curves, and derived median survival time as a function of percentage of response for both ctDNA and RECIST 1.1 (Figure 2B). Finally, we selected a landmark of 6 months and calculated survival at this time point. We found that with 10% of responders in terms of ctDNA, 62% of patients would be alive at 6 months (56% when response is defined by RECIST 1.1), while 90% of responders would translate into a survival for 81% of patients at the landmark (89% with RECIST 1.1). From these data, we evaluate that 10% more ctDNA responders would translate into 1–2 months of survival benefit. It is interesting to note that the increase in the median survival time as a function of the percentage of responders is greater with RECIST 1.1 than it is for ctDNA (Figure 2B, inset).

To evaluate if ctDNA holds predictivity independent of RECIST 1.1, we performed a multivariate Cox proportional hazard model regression. Hazard ratios (HRs) were estimated to be 0.12 and 0.6 for RECIST 1.1 and ctDNA, respectively. The lower HR obtained for RECIST 1.1 is consistent with what is observed in the inset of Figure 2B. In this model, no dependency could be detected supporting the hypothesis of the independent predictive value of ctDNA. In addition to that, the difference in the time of assessment of RECIST 1.1 and ctDNA could contribute to the difference in the parameter estimates. Best overall response (BOR) by RECIST 1.1 can be taken at any time with first tumor size assessment typically occurring at week 6, while ctDNA data were taken at week 4 in this dataset. Overall, these findings are in line with the high sensitivity/low specificity of RECIST 1.1-based criteria as discussed previously.

Circulating tumor DNA and clinical response

We further looked into potential relationships between ctDNA change and overall response with waterfall plots of ctDNA change colored by BOR (Figure 2C). Given the presence of large variation in the data, it is common to represent ctDNA change from baseline in terms of (base 10) logarithmic change. We see a clustering of best responses (lighter colors) within the negative ctDNA change from baseline, i.e., reduction. The rate of RECIST 1.1 responders (complete or partial response) was 35% (28/79) in patients with ctDNA decrease from baseline. Among the 73 patients with ctDNA increase, less patients were RECIST 1.1 responders (22%; 16/73). This clustering was observed consistently in the two other datasets. For patients treated with OAK (atezolizumab arm), 37% (7/19) of patients with ctDNA decrease were RECIST 1.1 responders, compared to only 11% (2/18) for patients with ctDNA increase. In IMspire170 (both arms

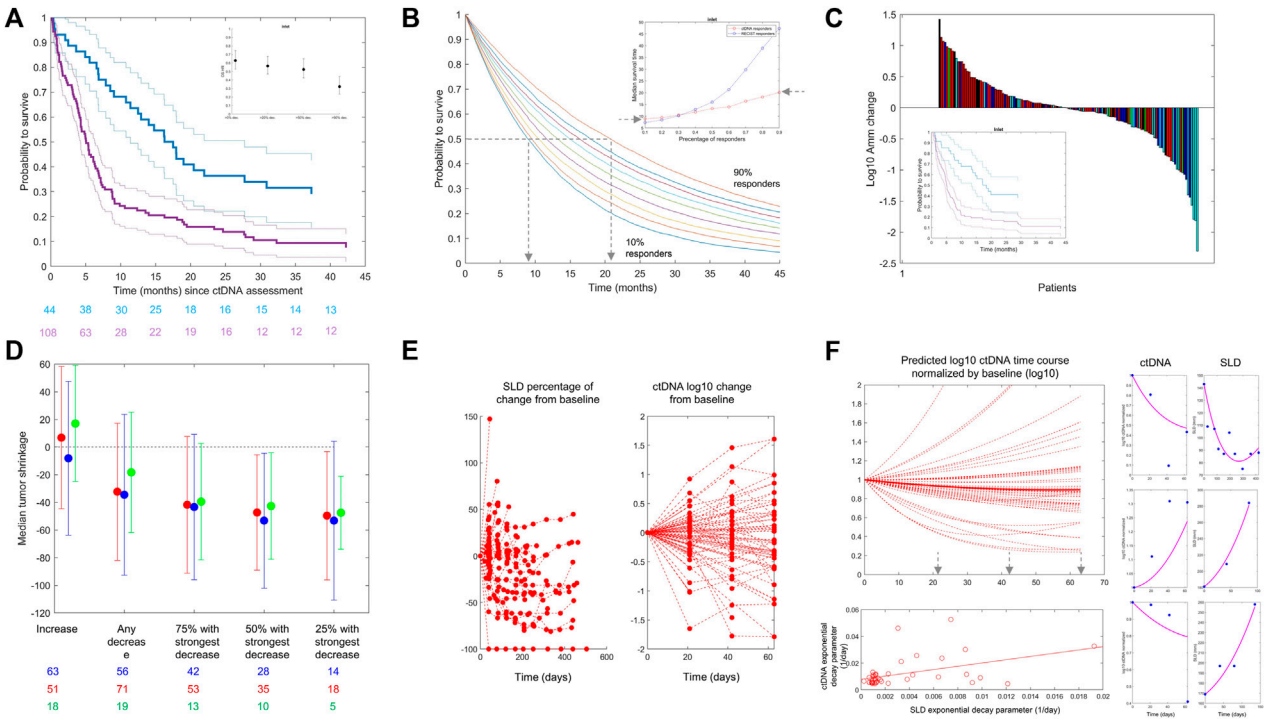

FIGURE 2
(A) From the Weber et al. dataset. Kaplan–Meier estimates of overall survival stratified by ctDNA change on treatment *versus* baseline: decrease >50% (blue line) *versus* all other patients (purple line). Confidence intervals are shown with thin lines. A: Data from Weber et al., NSCLC patients treated with CPI. The inset graphic shows the evolution of OS HR when reducing the ctDNA decrease cut-off (from left to right). The chosen cut-off values (20, 50, and 90% ctDNA reduction) represent approximately the observed quartiles of ctDNA reductions. More reduction is associated with better HR. **(B)** Kaplan–Meier (KM) curves are simulated using the exponential distribution parameterized according to the observed hazard rates of responders in terms of ctDNA drop from the Weber et al. dataset. Each colored line is a KM curve for a given percentage of responders from 10 to 90%. The inset shows the evolution of the median survival time (time at which half of the population is still alive) as a function of the percentage of responders for both ctDNA (red) and RECIST 1.1 (blue). **(C)** From the Weber et al. dataset. Waterfall plots of ctDNA colored by best overall response following RECIST 1.1 categorization. Complete response (green), partial response (cyan), stable disease (blue), and progressive disease (red) are shown. The inset shows Kaplan–Meier curves using ctDNA decrease less (purple) or more (blue) than 50% (like in panel **(A)**) in the patients within the same RECIST 1.1 category "stable disease." **(D)** Median tumor change (*y*-axis) in patient subgroups defined by the ctDNA decrease cut-off (*x*-axis) for atezolizumab + cobimetinib (red) and pembrolizumab (blue) for patients with melanoma in IMspire170 and atezolizumab for patients with NSCLC in OAK (green). The length of the error bars corresponds to ± 1 SD. **(E)** OAK data: Tumor size (left) and ctDNA (right) change from baseline over time. **(F)** Left/top: Model-based predictions of ctDNA time course in patients with NSCLC treated with atezolizumab (OAK study) using the Stein et al. model, omitting the baseline term and using individual parameter estimates. Left/bottom: Scatter plot of predicted exponential decay for ctDNA *versus* same parameter for tumor size (dots) (see equation 1). The line is a least square regression. Right: Individual fits for the joined ctDNA–SLD model proposed in equation (2). The model can fit data when ctDNA and SLD time courses are positively correlated (top) or negatively correlated (bottom). We here report individual fits as illustration only. The model can fit different types of profiles although parameters of the model were not estimated with sufficient precision to use this model for any predictive purpose.

together), 53% (125/238) of the patients experienced a decrease in ctDNA. Among them, 52% (65/125) had a complete or partial response compared to 32% (36/113) of patients who had ctDNA increased or unchanged.

Also, similar to tebentafusp and other reported data, ctDNA provides more granularity than overall response assessed through RECIST 1.1 because in patients from the same response categories (stable disease), a cut-off of ctDNA change can still separate patients in terms of survival benefit (inset of Figure 2C).

Circulating tumor DNA and tumor size change

The previous analysis was further extended by looking into potential relationships between ctDNA change and quantitative tumor size change (rather than the RECIST 1.1 response category) in the studies where longitudinal tumor size data were available to us (i.e., OAK and IMspire170). We calculated the maximal change in the sum of the longest diameters each patient experienced across the whole time window of tumor size data collection. This value can be negative (in case of tumor size shrinkage) or positive (in case of tumor size increase). We show in Figure 2D the result of the analysis for IMspire170 (atezolizumab + cobimetinib (red) and pembrolizumab (blue)) and OAK atezolizumab datasets (green points). There was a relationship between the magnitude of ctDNA decrease (*x*-axis) taken at a fixed time point and the maximum tumor size change. The stronger the early ctDNA drop, the more the tumor shrinkage observed.

To try to elucidate the relationships between ctDNA data and tumor size, we jointly looked at the SLD and ctDNA time courses in the OAK dataset for which we had several time point measurements of ctDNA. Consistently at all cycles, we found that the majority of patients with

ctDNA decrease have an early (week 6) tumor size decrease: 50% [(11/22) at cycle 2 (week 3), 63% (12/19) at cycle 3 (week 6), and 65% (11/17) at cycle 4 (week 9)]. The majority of patients with ctDNA increase have an early tumor size increase [62% (13/21), 65% (11/17), and 64% (9/14) at cycles 2, 3, and 4, respectively], altogether suggesting a link between early ctDNA and tumor size change.

Optimal sampling strategy and the challenge of variability

Circulating tumor DNA data collection and quantification come at a significant cost (burden for patients, for study operations, and financially). Therefore, designing methods for optimal sampling of ctDNA is important.

We used an empirical approach where we modeled the ctDNA time course using a bi-exponential model classically used to capture tumor size dynamics, also called the Stein model (Stein et al., 2011):

$$y = y_0 \cdot \left(exp\left(-k_s \cdot t\right) + exp\left(k_g \cdot t\right) - 1\right),$$

where k_s is the decay parameter, k_g is the regrowth parameter, and y_0 is the initial value which was not estimated but fixed to the observed baseline value.

All ctDNA data were expressed in terms of (average) mutant molecule per ml (MMPM) and log(base 10)-transformed. Monolix (version 2021 R1, Lixoft SAS, a Simulation Plus company) was used to estimate the two parameters of the structural model and parameter(s) of a constant error model within a population framework, allowing to estimate variability in these parameters in the population. All population parameters were estimated with a low or moderate standard error [RSE]: 30.1% and 27.4% for the growth and decay rate fixed effect, respectively; 25% and 20% for the inter-individual variability random effects; and less than 5% for the residual error model parameter.

With this model, we reproduced the predicted time course of ctDNA in patients treated with atezolizumab (Figure 2F, top left). For patients with a decrease in ctDNA, we identified the time at which the ctDNA time course achieved its nadir following the idea that this would be the theoretical time at which the ctDNA measures hold the highest information. The result of this analysis shows that 21 days or cycle 2 might be too early for informative ctDNA measurements as the majority of the simulated patients had their ctDNA nadir beyond cycle 4, i.e., 9 weeks.

However, large inter-individual variability parameters were estimated, specifically for both decay and growth rates with an estimate close to 100% (assessed through the standard deviation of the random effects). These parameters were estimated with reasonable precision, which overall indicates the high degree of inter- and intra-individual variability (see Appendix for further details).

It is important to highlight that the nature of the data themselves, being a summarized statistics based on a number of alleles which most likely change from one time point to the other (not the same allele will contribute to the final data readout), may have a large contribution to the observed time course variability. Given the identified variability, the collection of longitudinal sampling of ctDNA along the course of the disease is needed to generate hypotheses on the optimal sampling strategy. This also appears important given that optimal strategies should not be "one size fits all"—as different drugs and mechanisms of action could be associated with different optimal sampling times.

Joint modeling of ctDNA and tumor size time course and the challenge of biological complexity

When we applied the model by Stein et al. (Stein et al., 2011) to the SLD time course, which was independent of the ctDNA data, we found that the resulting parameter governing the decay slightly correlated with the same parameter for ctDNA (Figure 2F bottom left) (r = 0.45), supporting the hypothesis of the presence of a mechanical link between ctDNA and tumor size.

To follow up, we tested a simple joint model of ctDNA and SLD time course encoding the correlation between the two decay phenomena:

$$SLD(t) = SLD_0 \cdot \left(exp\left(-k_{sT} \cdot t\right) + exp\left(k_{gT} \cdot t\right) - 1\right),$$
$$ctDNA(t) = ctDNA_0 \cdot \left(exp\left(-\zeta \cdot k_{sT} \cdot t\right) + exp\left(k_g \cdot t\right) - 1\right),$$

where SLD denotes the sum of the longest diameter and SLD_0 its baseline value. k_{gT} is the SLD growth parameter and k_{sT} is the decay rate which we found again in the equation for ctDNA. The parameter ζ links the time course dynamics of SLD and ctDNA data. For data fitting, the population parameters were all fixed to values obtained when fitting ctDNA and SLD data independently (see Appendix for further details). Only the parameter ζ and its variability were estimated. Consistent with the hypothesis of the mechanical link between the two observations, its population value was 1.94 (RSE of 37%) and variability was 0.86 (RSE of 35%).

This model could reproduce patients' ctDNA and SLD data through its flexibility to capture both expected (Figure 2F, right side top and middle row) and unexpected profiles (bottom row), i.e., ctDNA increase and SLD decrease, or the contrary. We believe that the ability of such a model to reproduce patient-level data is an additional support to the hypothesis of a link between ctDNA and SLD time course in the case of the checkpoint inhibitor and should be viewed as an incentive for the development of further modeling attempts.

However, proper joint modeling of ctDNA and SLD time course will require an understanding of ctDNA shedding by tumor cells, ctDNA release into blood, and clearance. These processes could potentially differ from one indication to another and from one therapeutic modality to another. Some mechanistic modeling efforts have been already undertaken. For example, Avanzini et al. (2020) modeled the mechanisms of ctDNA shedding and release into circulation; they assumed that ctDNA is shed by dying tumor cells with a certain shedding probability and that the half-life of ctDNA in circulation is around 30 min.

Conclusion

In many recent studies, ctDNA has shown potential to be used as a powerful biomarker for long-term clinical benefit of patients receiving anti-cancer treatment. ctDNA has obvious advantages over other techniques such as imaging; it is less invasive and time-consuming and can theoretically provide a high quality estimate of the total tumor burden, while imaging-based techniques focus on a limited number of

identified target lesions. Moreover, it could become less costly as technology evolves.

From this perspective, we have compiled a large dataset of patients (~500 patients) with varying tumor indications (non-small-cell lung carcinoma (NSCLC) and melanoma), treatments (CPI ± targeted therapy) and ctDNA panels (AVENIO and FMI), and sampling times (longitudinal and static).

Our objective was neither to provide a holistic introduction to ctDNA and associated technology nor to showcase a sophisticated ctDNA data modeling framework. Clearly, much work remains to be conducted to improve such models and what we reported should serve as an introduction to this problem. Rather, through statistical and empirical modeling of this dataset, we wish to contribute to familiarize the PMX community with the opportunity that ctDNA modeling can represent the early clinical development of anti-cancer therapeutic agents and raise awareness of potential challenges.

The presented analysis also sheds some light on the challenges to be expected when it comes to using ctDNA data for decision-making. First, we need to consider the nature of the data and their associated variability: coming from bioinformatic readout, modelers will need to closely work with bioinformaticians to effectively model the data. Then, the accessibility to longitudinal data should be taken into account notwithstanding the cost of these measurements. Longitudinal assessments should offer the opportunity of a better understanding given the potentially high level of variability in the data. This should lead to more precise mathematical formulation of the underlying biological processes which contributes to increase the quality of modeling readouts, reduces variability, and in turn contributes to optimal sampling strategies given an underlying hypothesis between ctDNA shedding/release, treatment action, and tumor dynamics.

In conclusion, our analysis, in agreement with published literature, makes ctDNA an ideal candidate—based on its predictive potential—for integration within a pharmacometric framework to complement the current state-of-the-art tumor growth kinetic models.

By focusing efforts on promoting collection of longitudinal data, understanding of underlying biology and the nature of the data and their variability, there is hope for the development of successful modeling frameworks jointly describing ctDNA, tumor size, and long-term clinical benefit, which overall can significantly contribute to answering key questions around early identification of most promising compounds and precision dosing.

Data availability statement

The data analyzed in this study is subjected to the following licenses/restrictions: summary data have been already published. Raw data are not public. Requests to access these datasets should be directed to Weber, S., et al., Dynamic Changes of Circulating Tumor DNA Predict Clinical Outcome in Patients With Advanced Non-Small-Cell Lung Cancer Treated With Immune Checkpoint Inhibitors. JCO Precis Oncol, 2021. 5: p. 1540-1553; Zou, W., et al., ctDNA Predicts Overall Survival in Patients With NSCLC Treated With PD-L1 Blockade or With Chemotherapy. JCO Precis Oncol, 2021. 5: p. 827-838; Gogas, H., et al., Cobimetinib plus atezolizumab in BRAF(V600) wild-type melanoma: primary results from the randomized phase III IMspire170 study. Ann Oncol, 2021. 323): p. 384-394.

Ethics statement

The manuscript contains a meta-analysis of data generated in previously published clinical trials. The studies involving human participants were reviewed and approved. All protocols were IRB approved at the respective study sites. The patients/participants provided their written informed consent to participate in the studies.

Author contributions

BR: design study, data analysis, and manuscript writing; AR: design study; HH: design study and data analysis; MS: design study and manuscript writing; CB: design study.

Acknowledgments

The authors wish to express their gratitude to René Bruno, Matts Kaagedal, Philippe Pierillas, Zoe-June Assaf, Barzin Nabet, Wei Zou, Vaios Karanikas, and Daniel Watterkamp for their scientific inputs in the design of this research and their careful review of the manuscript. They also wish to thank Harry Groen and his team for sharing the Weber et al. dataset without further obligations.

Conflict of interest

All authors were employed by F. Hoffmann La Roche Ltd. at the time of the analysis and manuscript writing.

Publisher's note

Supplementary material

The Supplementary Material for this article can be found online at: https://www.frontiersin.org/articles/10.3389/fphar.2022.1058220/full#supplementary-material

References

Avanzini, S., Kurtz, D. M., Chabon, J. J., Moding, E. J., Hori, S. S., Gambhir, S. S., et al. (2020). A mathematical model of ctDNA shedding predicts tumor detection size. *Sci. Adv.* 6 (50), eabc4308. doi:10.1126/sciadv.abc4308

Bos, M. K., Nasserinejad, K., Jansen, M. P. H. M., Angus, L., Atmodimedjo, P. N., de Jonge, E., et al. (2021). Comparison of variant allele frequency and number of mutant molecules as units of measurement for circulating tumor DNA. *Mol. Oncol.* 15 (1), 57–66. doi:10.1002/1878-0261.12827

Bratman, S. V., Yang, S. Y. C., Iafolla, M. A. J., Liu, Z., Hansen, A. R., Bedard, P. L., et al. (2020). Personalized circulating tumor DNA analysis as a predictive biomarker in solid tumor patients treated with pembrolizumab. *Nat. Cancer* 1 (9), 873–881. doi:10.1038/s43018-020-0096-5

Cannarile, M. A., Gomes, B., Canamero, M., Reis, B., Byrd, A., Charo, J., et al. (2021). Biomarker technologies to support early clinical immuno-oncology development: Advances and interpretation. *Clin. Cancer Res.* 27 (15), 4147–4159. doi:10.1158/1078-0432.CCR-20-2345

Carvajal, R. D., Nathan, P., Sacco, J. J., Orloff, M., Hernandez-Aya, L. F., Yang, J., et al. (2022). Phase I study of safety, tolerability, and efficacy of tebentafusp using a step-up dosing regimen and expansion in patients with metastatic uveal melanoma. *J. Clin. Oncol.* 40 (17), 1939–1948. doi:10.1200/JCO.21.01805

Cescon, D. W., Bratman, S. V., Chan, S. M., and Siu, L. L. (2020). Circulating tumor DNA and liquid biopsy in oncology. *Nat. Cancer* 1 (3), 276–290. doi:10.1038/s43018-020-0043-5

Cheng, F., Su, L., and Qian, C. (2016). Circulating tumor DNA: A promising biomarker in the liquid biopsy of cancer. *Oncotarget* 7 (30), 48832–48841. doi:10.18632/oncotarget.9453

Gerwing, M., Herrmann, K., Helfen, A., Schliemann, C., Berdel, W. E., Eisenblatter, M., et al. (2019). The beginning of the end for conventional RECIST - novel therapies require novel imaging approaches. *Nat. Rev. Clin. Oncol.* 16 (7), 442–458. doi:10.1038/s41571-019-0169-5

Gogas, H., Dreno, B., Larkin, J., Demidov, L., Stroyakovskiy, D., Eroglu, Z., et al. (2021). Cobimetinib plus atezolizumab in BRAF(V600) wild-type melanoma: Primary results from the randomized phase III IMspire170 study. *Ann. Oncol.* 32 (3), 384–394. doi:10.1016/j.annonc.2020.12.004

Goulart, B. H. L., Mushti, S., Chatterjee, S., Larkins, E. A., Donoghue, M. B., Tang, S., et al. (2022). Association of progression-free survival and overall response rate with overall survival in first-line randomized trials of immune checkpoint inhibitor–based regimens for metastatic non–small cell lung cancer (NSCLC): An FDA pooled analysis. *J. Clin. Oncol.* 40 (16), 9029. doi:10.1200/jco.2022.40.16_suppl.9029

Heitzer, E., Auinger, L., and Speicher, M. R. (2020). Cell-Free DNA and apoptosis: How dead cells inform about the living. *Trends Mol. Med.* 26 (5), 519–528. doi:10.1016/j.molmed.2020.01.012

Hutchinson, L., and Kirk, R. (2011). High drug attrition rates--where are we going wrong? *Nat. Rev. Clin. Oncol.* 8 (4), 189–190. doi:10.1038/nrclinonc.2011.34

Nabet, B. Y., Esfahani, M. S., Moding, E. J., Hamilton, E. G., Chabon, J. J., Rizvi, H., et al. (2020). Noninvasive early identification of therapeutic benefit from immune checkpoint inhibition. *Cell* 183 (2), 363–376. doi:10.1016/j.cell.2020.09.001

Netterberg, I., Karlsson, M. O., Terstappen, L. W. M. M., Koopman, M., Punt, C. J. A., and Friberg, L. E. (2020). Comparing circulating tumor cell counts with dynamic tumor size changes as predictor of overall survival: A quantitative modeling framework. *Clin. Cancer Res.* 26 (18), 4892–4900. doi:10.1158/1078-0432.CCR-19-2570

Rittmeyer, A., Barlesi, F., Waterkamp, D., Park, K., Ciardiello, F., von Pawel, J., et al. (2017). Atezolizumab versus docetaxel in patients with previously treated non-small-cell lung cancer (OAK): A phase 3, open-label, multicentre randomised controlled trial. *Lancet* 389 (10066), 255–265. doi:10.1016/S0140-6736(16)32517-X

Ruchalski, K., Braschi-Amirfarzan, M., Douek, M., Sai, V., Gutierrez, A., Dewan, R., et al. (2021). A primer on RECIST 1.1 for oncologic imaging in clinical drug trials. *Radiol. Imaging Cancer* 3 (3), e210008. doi:10.1148/rycan.2021210008

Shoushtari, A. N., Collins, L., Espinosa, E., Sethi, H., Stanhope, S., Abdullah, S., et al. (2021). 1757O Early reduction in ctDNA, regardless of best RECIST response, is associated with overall survival (OS) on tebentafusp in previously treated metastatic uveal melanoma (mUM) patients. *Ann. Oncol.* 32, S1210. doi:10.1016/j.annonc.2021.08.1702

Stein, W. D., Gulley, J. L., Schlom, J., Madan, R. A., Dahut, W., Figg, W. D., et al. (2011). Tumor regression and growth rates determined in five intramural NCI prostate cancer trials: The growth rate constant as an indicator of therapeutic efficacy. *Clin. Cancer Res.* 17 (4), 907–917. doi:10.1158/1078-0432.CCR-10-1762

Weber, S., van der Leest, P., Donker, H. C., Schlange, T., Timens, W., Tamminga, M., et al. (2021). Dynamic changes of circulating tumor DNA Predict clinical outcome in patients with advanced non-small-cell lung cancer treated with immune checkpoint inhibitors. *JCO Precis. Oncol.* 5, 1540–1553. doi:10.1200/PO.21.00182

Yates, J. W. T., and Cheung, S. Y. A. (2021). A meta-analysis of tumour response and relapse kinetics based on 34, 881 patients: A question of cancer type, treatment and line of treatment. *Eur. J. Cancer* 150, 42–52. doi:10.1016/j.ejca.2021.03.027

Zhang, Q., Luo, J., Wu, S., Si, H., Gao, C., Xu, W., et al. (2020). Prognostic and predictive impact of circulating tumor DNA in patients with advanced cancers treated with immune checkpoint blockade. *Cancer Discov.* 10 (12), 1842–1853. doi:10.1158/2159-8290.CD-20-0047

Zou, W., Yaung, S. J., Fuhlbruck, F., Ballinger, M., Peters, E., Palma, J. F., et al. (2021). ctDNA predicts overall survival in patients with NSCLC treated with PD-L1 blockade or with chemotherapy. *JCO Precis. Oncol.* 5, 827–838. doi:10.1200/PO.21.00057

frontiers | Frontiers in Pharmacology

TYPE Original Research
PUBLISHED 20 June 2023
DOI 10.3389/fphar.2023.1163432

OPEN ACCESS

EDITED BY
Zinnia P. Parra-Guillen,
University of Navarra, Spain

REVIEWED BY
Antje-Christine Walz,
3T Biosciences, United States
Blerta Shtylla,
Pfizer, United States
Lena Elisabeth Friberg,
Uppsala University, Sweden

*CORRESPONDENCE
Samira Anbari,
smeybod1@jhmi.edu

RECEIVED 10 February 2023
ACCEPTED 06 June 2023
PUBLISHED 20 June 2023

CITATION
Anbari S, Wang H, Zhang Y, Wang J, Pilvankar M, Nickaeen M, Hansel S and Popel AS (2023), Using quantitative systems pharmacology modeling to optimize combination therapy of anti-PD-L1 checkpoint inhibitor and T cell engager.
Front. Pharmacol. 14:1163432.
doi: 10.3389/fphar.2023.1163432

Using quantitative systems pharmacology modeling to optimize combination therapy of anti-PD-L1 checkpoint inhibitor and T cell engager

Samira Anbari[1]*, Hanwen Wang[1], Yu Zhang[1], Jun Wang[2], Minu Pilvankar[2], Masoud Nickaeen[2], Steven Hansel[2] and Aleksander S. Popel[1,3]

[1]Department of Biomedical Engineering, Johns Hopkins University School of Medicine, Baltimore, MD, United States, [2]Biotherapeutics Discovery Research, Boehringer Ingelheim Pharmaceuticals Inc., Ridgefield, CT, United States, [3]Department of Oncology, Sidney Kimmel Cancer Center, Johns Hopkins University School of Medicine, Baltimore, MD, United States

Although immune checkpoint blockade therapies have shown evidence of clinical effectiveness in many types of cancer, the outcome of clinical trials shows that very few patients with colorectal cancer benefit from treatments with checkpoint inhibitors. Bispecific T cell engagers (TCEs) are gaining popularity because they can improve patients' immunological responses by promoting T cell activation. The possibility of combining TCEs with checkpoint inhibitors to increase tumor response and patient survival has been highlighted by preclinical and clinical outcomes. However, identifying predictive biomarkers and optimal dose regimens for individual patients to benefit from combination therapy remains one of the main challenges. In this article, we describe a modular quantitative systems pharmacology (QSP) platform for immuno-oncology that includes specific processes of immune-cancer cell interactions and was created based on published data on colorectal cancer. We generated a virtual patient cohort with the model to conduct *in silico* virtual clinical trials for combination therapy of a PD-L1 checkpoint inhibitor (atezolizumab) and a bispecific T cell engager (cibisatamab). Using the model calibrated against the clinical trials, we conducted several virtual clinical trials to compare various doses and schedules of administration for two drugs with the goal of therapy optimization. Moreover, we quantified the score of drug synergy for these two drugs to further study the role of the combination therapy.

KEYWORDS

immune-oncology, quantitative systems pharmacology (QSP), immune checkpoint inhibitor, bispecific T cell engager, virtual clinical trial, dose optimization

1 Introduction

Colorectal cancer (CRC) is the third most frequent cause of cancer-related death worldwide (Bray et al., 2018). Surgery, chemotherapy, and radiotherapy—also used in combination—have historically been the standard treatments for colorectal cancer. Unfortunately, these treatments have a lot of adverse consequences since they are non-specific and cytotoxic to all cells, including healthy cells (Johdi and Sukor, 2020). In recent

years, cancer immunotherapy as a more effective alternative approach has changed the area of cancer treatments (Morrissey et al., 2016; Golshani and Zhang, 2018).

Immune checkpoint blockade therapies, including anti-PD-L1 and anti-PD-1, have raised a lot of attention and have shown a significant increase in the survival rate of patients with multiple solid tumor types (Alsaab et al., 2017; Popovic, Jaffee, and Zaidi, 2018; Sharma and Allison, 2020; Sharma et al., 2021). Nonetheless, the results of clinical trials show that only a small number of patients with metastatic CRC (mCRC) benefit from checkpoint inhibitors (Hegde and Chen, 2020). For example, the IMblaze370 study failed to improve overall response in the PD-L1 inhibitor atezolizumab monotherapy or even in combination therapy with the MEK inhibitor cobimetinib when compared with regorafenib in previously treated mCRC patients (Eng et al., 2019). It is essential, however, to keep looking into the role of checkpoint inhibitors, particularly in combination with other immunotherapy methods for the treatment of colorectal cancer.

The T cell bispecific antibody, cibisatamab (CEA-TCB), is a novel immunotherapy agent that guides T cells to tumor cells that express the carcinoembryonic antigen (CEA) glycoprotein at the cell surface regardless of their T cell receptor specificity (Bacac et al., 2016; Lehmann et al., 2016; Gonzalez et al., 2019). Numerous colorectal tumors exhibit an overexpression of CEA on their cell surfaces, making cibisatamab a prospective candidate for the treatment of colorectal cancer. Cibisatamab (RO6958688; RG7802) has been used in monotherapy and in combination with atezolizumab (anti-PD-L1) in clinical trials (NCT02324257, NCT02650713). The results from these trials have shown promising outcomes for the treatment of CRC with bispecific antibodies in solid tumors (Tabernero et al., 2017).

Although the combination therapy of bispecific antibody with PD-L1 inhibitors in solid tumors has shown significant promise, there may be drawbacks down the road, including the inability to pinpoint the cause of side effects, drug-drug interactions, cumulative side effects, and greater costs. As a result, optimization of dose and sequence for these combination therapies can be beneficial to reduce the potential risk of combination therapies and enhance the advantages.

Moreover, identifying the combination therapies with synergistic effects, which enable dose reduction of individual drugs and increase their efficacy, is desirable in clinical studies specially for bispecific antibodies that show toxic behavior at higher doses. Several synergy quantification methods have been proposed to assess drug combination performance (Chou, 2010; Meyer et al., 2020). The majority of synergy metric approaches are based on either Loewe Additivity (LA) principle (Loewe, 1953) or Bliss Independence (BI) method (BLISS, 1939; Berenbaum, 1978; Greco et al., 1995). More recently, a synergy framework called multi-dimensional synergy of combinations (MuSyC) has been introduced (Meyer et al., 2019), which was used in this study to quantify the synergy of combination therapy with atezolizumab and cibisatamab. This method's key benefit is its ability to distinguish between synergetic potency and synergistic efficacy.

In this study, we have extended our previously developed QSP model of T cell engager (TCE) and anti-PD-L1 antibody in CRC (Ma et al., 2020a; Ma et al., 2020b) by incorporating the dynamics of helper T cells (Th) and myeloid-derived suppressor cells (MDSCs) from our study of triple-negative breast cancer (TNBC) (Wang et al., 2021) and modified the binding dynamics of TCE to fit the *in vitro* data of cibisatamab (Vyver et al., 2021). Using this model, we aim to optimize the dose and sequence of cibisatamab and atezolizumab and investigate their synergistic behavior in combination therapy.

2 Materials and methods

2.1 Model structure

The current QSP model is modified from our previously published QSP platforms (Ma et al., 2020a; Wang et al., 2021) built using SimBiology toolbox in MATLAB (MathWorks, Natick, MA). The model is composed of four compartments, which includes central, peripheral, tumor and tumor-draining lymph node compartments. The model consists of connected modules that describe the dynamics of molecular and cellular interactions associated with different species shown in Figure 1. In summary, the model simulates the dynamics of naïve $CD4^+$ and $CD8^+$ T cells, taking into account their trafficking between the central, peripheral, and lymph node compartments, as well as their proliferation in the peripheral and lymph node compartments. A small number of cancer cells are initially incorporated into the tumor compartment, and their dynamics is modeled using a logistic growth approach. Cancer cell death, or apoptosis, is modeled as a first-order reaction, which results in the release of tumor-associated neo-antigens and self-antigens into the tumor compartment.

The model considers the uptake of tumor-derived neo-antigens and self-antigens by antigen-presenting cells (APCs), their subsequent maturation, and their migration to the tumor-draining lymph node compartment. The detailed mechanisms of antigen processing and presentation, including the cleavage of proteins into peptides, binding of peptides to MHC molecules, and transport to the cell surface, are all incorporated into the model. The activation of naïve T cells is dependent on the extent of T cell receptor ligation by peptide-MHC on APCs, and is implemented as a Hill function. Following activation, Tregs, cytotoxic T cells, and helper T cells infiltrate into the tumor. Tumor-infiltrating cytotoxic T cells kill cancer cells, and their rate of killing depends on the ratio of cytotoxic T cells and cancer cells. This process also results in the enhanced release of tumor-associated antigens. However, the model assumes that tumor-infiltrating cytotoxic T cells and helper T cells become exhausted by the interaction of PD-1 with ligands on cancer cells and the action of Tregs.

The model also includes the secretion of CCL2 by cancer cells, which is assumed to mediate the recruitment of myeloid-derived suppressor cells (MDSCs) into the tumor compartment. MDSCs are assumed to release arginase-I (Arg-I) and nitric oxide (NO), which inhibit the cytotoxic activity of T cells. TGF-β and Arg-I facilitate the trans-differentiation of helper T cells to Tregs in the tumor.

Finally, the model incorporates the pharmacokinetics and pharmacodynamics of two antibodies: the anti-PD-L1 antibody atezolizumab and the T cell engager antibody cibisatamab. Both antibodies are directly administered into the central compartment. The pharmacokinetics of the antibodies incorporates their clearance from the central compartment, their transport between the central and peripheral/tumor compartments, and their transport from the tumor to the tumor-draining lymph node compartment. The

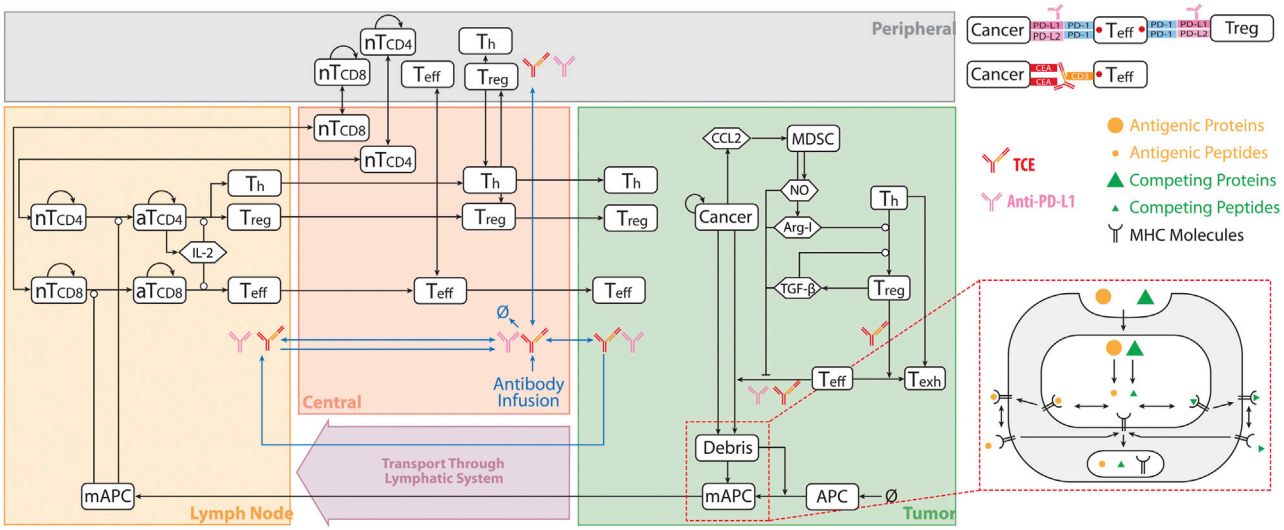

FIGURE 1
QSP Model Diagram. The model is divided into of four compartments: central, peripheral, tumor, and tumor-draining lymph node, which describe cycles of immune activation in lymph nodes, T cell trafficking to the tumor, killing of cancer cells, immune evasion, and antigen release and lymphatic transport. nT, naïve T cell; aT, activated T cell; NO, nitric oxide; Arg-I, arginase I; Treg, regulatory T cell; Teff, effector T cell; Th, helper T cell; Texh, exhausted T cell; MDSC, myeloid derived suppresser cells; mAPC, mature antigen presenting cell. Cytokine degradation and cellular clearance were omitted in the diagram. Modified from (Ma et al., 2020b; Wang et al., 2021).

pharmacodynamics of the anti-PD-L1 antibody is modeled by its binding to the PD-L1 on cancer cells and regulatory T cells, which blocks the interactions of PD-1 with PD-L1. The subsequent reduction in the amount of ligand-bound PD-1 decreases the inhibitory action of PD-1 on T cell-mediated killing of cancer cells, which is also modeled as a Hill function. The bispecific T cell engager can bind to CD3 on T cells and CEA on cancer cells, leading to the formation of CEA_TCE_CD3 molecule and enhanced cancer killing by Teff cells. The details on TCE binding module and the equations describing pharmacokinetic of both cibisatamab and atezolizumab are elaborated in the Supplementary Material.

In this study, dynamics of T cells, APCs, tumor-specific neoantigens and tumor-associated self-antigens, immune checkpoints, MDSCs are adapted from (Wang et al., 2021). The tumor growth dynamics with a logistic growth rate and TCE model with binding modifications are based on (Ma et al., 2020b) with modified hill function coefficient of T cell activation fitted to *in vitro* data of cibisatamab, Figure 2. The modules have a total of 131 ordinary differential equations (ODEs), 27 algebraic equations (i.e., repeated assignment rules), 211 parameters, and were created using MATLAB scripts. The online Supplementary Tables S2–S7 include complete listings of model parameters, reactions, algebraic equations, and cellular and molecular species, as well as details on each module.

2.2 Virtual patient generation and virtual clinical trial

To create a virtual patient cohort that resembles the clinical population, a subset of model parameters is varied (Supplementary Table S7) while others remain at the baseline level (Supplementary Table S4). Both the baseline values and ranges of selected parameters are based on experimental and clinical data, where available (see Supplementary Table S4 notes for references). However, the distributions of some parameters are not currently available. For those parameters, we have estimated their ranges such that the 95% confidence interval of simulated ORR rate would correspond to the results of the clinical trial (percentage of PR/CR) per RECIST, for each therapy. The model is first initialized with a small number of cells before performing a virtual clinical trial. Using Latin Hypercube Sampling (LHS), the values of selected parameters are randomly generated based on the calibrated parameter distributions, with each parameter set representing a potential virtual patient. If the tumor is able to reach the desired initial tumor size, which corresponds to the pre-treatment tumor size in actual clinical trials and varies among patients, the simulation will proceed to estimate the response to therapy. To avoid generating implausible patients due to uncertainty in parameter ranges, the following physiological parameters were used to screen VPs: tumor diameter, T cell density in the blood, and Teff to Treg ratio.

2.3 Statistical analysis

Latin Hypercube Sampling (LHS) and Partial Rank Correlation Coefficient (PRCC) methods are used to perform global uncertainty and sensitivity analyses (Marino et al., 2008) to investigate the effects of varied parameter values on model observations. The virtual patient population is resampled using bootstrap sampling in order to compare model predictions and clinical data. The 95 percentile confidence intervals and bootstrap median are then computed for comparison between model predictions and clinical results. Statistical analyses are carried out via MATLAB 2020a (MathWorks, Natick, MA).

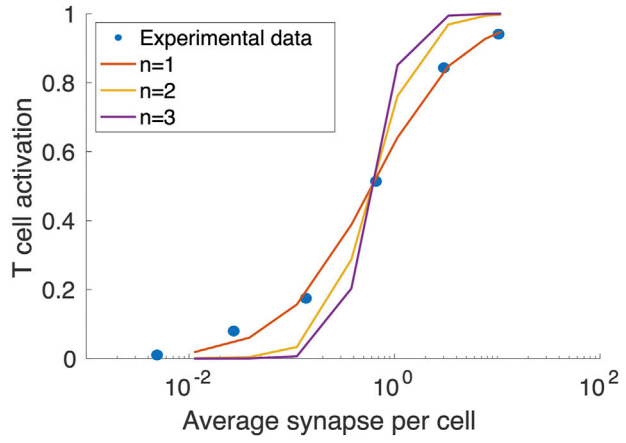

FIGURE 2
Fitting the Hill function coefficient (n) of T cell activation to concentration on synapse formed per T cells. The blue circles are extracted from (Vyver et al., 2021).

2.4 Drug synergy quantification

Using the MuSyC technique (Meyer et al., 2019), the synergy of combination therapy is evaluated for the median behavior of simulated virtual patients. In summary, two parameters representing synergistic potency, α, and synergistic efficacy, β, are quantified for a two-dimensional space representative of response to two targeted drugs. The parameter α measures how the presence of another drug affects the effective dose of one drug. When two drugs have synergistic potency ($\log(\alpha) > 0$), the EC50 value decreases due to the addition of the other drug, corresponding to an increase in potency. The percent increase in the effect of a drug combination over the most effective single drug is referred to as the parameter β. For example, in the case of synergistic efficacy ($\beta > 0$), the maximum effect (E_{max}) of combined drugs is greater than the maximum effect of the individual drugs.

3 Results

3.1 In silico virtual clinical trial of atezolizumab and cibisatamab

For this study, a virtual cohort of 500 patients was created by LHS method, and those who did not reach the desired initial tumor size or with implausible parameter values were regarded as non-patients and excluded from the virtual trial. Filtered virtual patients (VPs) were used for estimating overall response rate (ORR) of colorectal cancer in mono- and combination therapy using atezolizumab and cibisatamab. It is important to note that the same VPs were used in all the cases. The parameters with no experimentally reported values (Supplementary Table S4) were fitted to the outcome of clinical trials NCT02324257 and NCT02650713, with 60 mg cibisatamab QW as a monotherapy treatment and 60 mg cibisatamab QW plus 1200 mg atezolizumab Q3W for combination therapy (Tabernero et al., 2017). The ORRs were calculated for VPs following RECIST 1.1 (Eisenhauer et al., 2009) after 400 days, as summarized in Table 1. In order to compare the simulation results with the actual clinical trials, we have calculated 95% percentile bootstrap confidence intervals (95% CI) of the ORRs by randomly sampling 31 VPs 10,000 times in cibisatamab monotherapy and 25 VPs 10,000 times in combination therapy. MATLAB's "bootci" function was used for calculation of 95% CI and, the number of selected VPs was chosen based on number of patients in NCT02324257 (31 patients, cibisatamab monotherapy) and NCT02650713 (25 patients, combination therapy). Since the result of atezolizumab was not reported in these trials, the result of atezolizumab monotherapy from the IMblaze370 (NCT02788279) trial with a 2% (95% CI: 0.3–7.8) response rate was used to calibrate the model and compare with the clinical trial results (Eng et al., 2019). Similar to cibisatamab monotherapy, we have randomly sampled 31 patients for calculation of CI in the case of atezolizumab monotherapy.

In order to visualize the dynamics of individual virtual patients and compare different treatments, we plotted the rate of response for all treatment cases as spider plots, showing both the individual variabilities of patients by randomly selecting 100 VPs in Figure 3A, and the median behavior of the virtual population in Figure 3B. In addition, the best overall response is demonstrated by waterfall plots, as shown in Figure 3C.

To determine the strength of the correlation between parameters and tumor volume, global uncertainty and sensitivity analysis was performed using PRCC (Figure 4). Tumor volume was significantly positively associated with initial tumor diameter and tumor growth rate in both cibisatamab monotherapy and combination therapy. Moreover, in both cases, neo-antigen specific T cell clones (TCC) were highly negatively associated with tumor volume. To further explore the results, we plot the time profile of tumor size and T cell densities in the tumor compartment in Figure 5. As shown in this figure, the median tumor size is significantly lower in responders, while Teff cell density, Treg cell density and their ratio are higher in responders as expected. Moreover, initial values of Teff cell density is strongly correlated with responder/non-responder status, suggesting that pre-treatment values of Teff density is a predictive biomarker in monotherapies and combination therapy.

TABLE 1 Overall Response Rate of 60 mg cibisatamab monotherapy, 1200 mg atezolizumab monotherapy and their combination therapy.

Treatment	Simulated ORR (%)	95% CI	Clinical ORR	References
Cibisatamab	8.2	0%–22.6%	6%	Tabernero et al. (2017)
Atezolizumab	3.4	0%–12.9%	2% (IMblaze370 trial)	Eng et al. (2019)
Combination Therapy	11.1	0%–28%	12%	Tabernero et al. (2017)

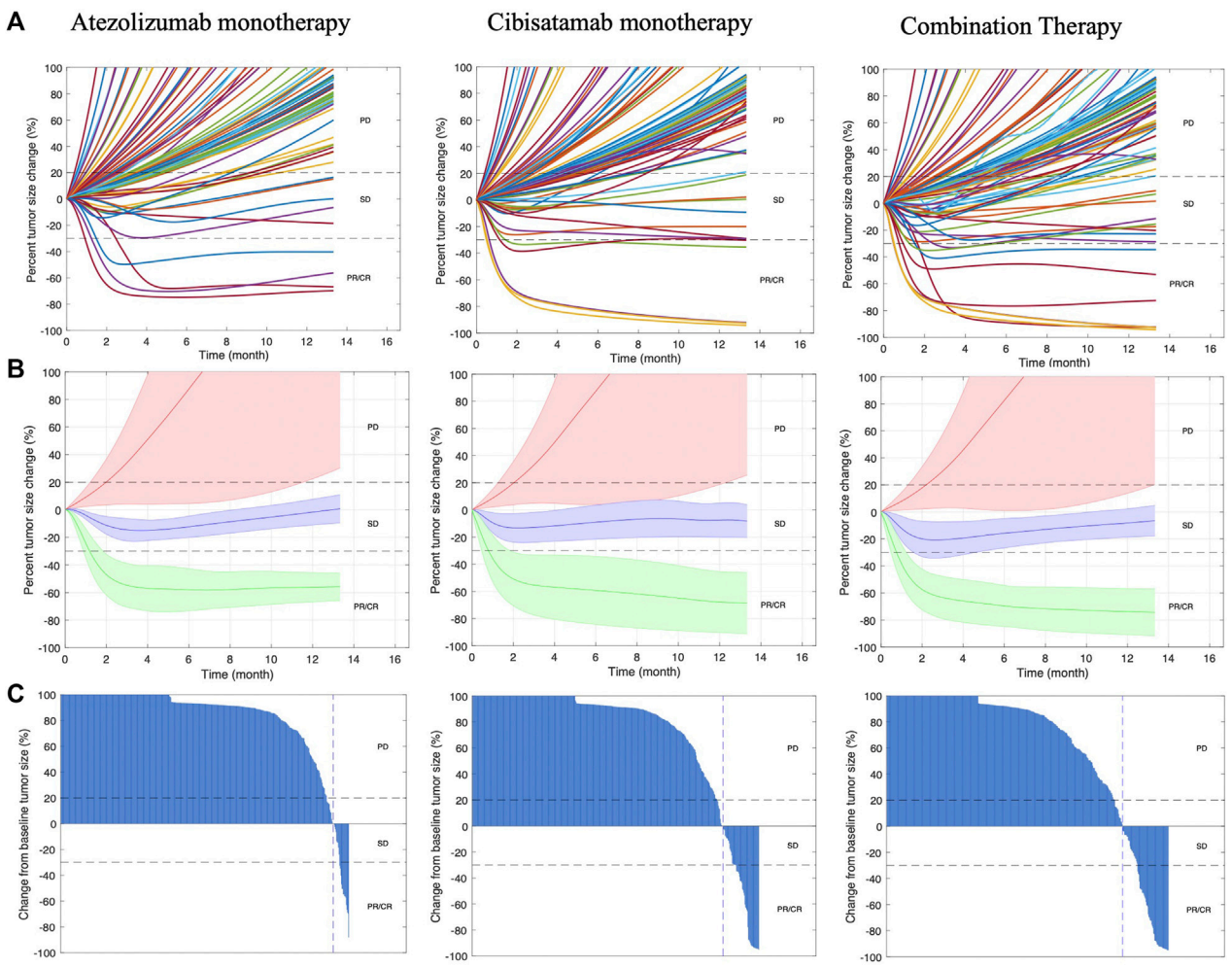

FIGURE 3
Rate of response in model-predicted tumor diameter of **(A)** 100 randomly selected virtual patients; **(B)** all VPs. Solid line represents the median and shaded area stands for the median absolute error (mad); **(C)** best overall response represented by waterfall plots for all VPs. Response is assessed by RECIST 1.1. CR, complete response; PR, partial response; SD, stable disease; PD, progressive disease.

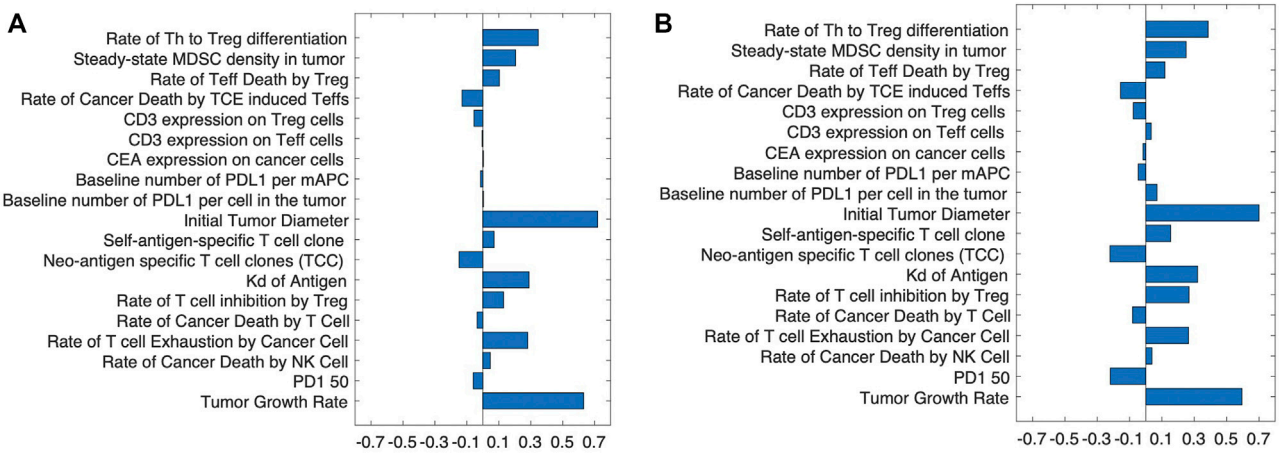

FIGURE 4
The partial rank correlation coefficient, PRCC, between input parameters and tumor volume after treatment with **(A)** cibisatamab monotherapy and **(B)** combination therapy.

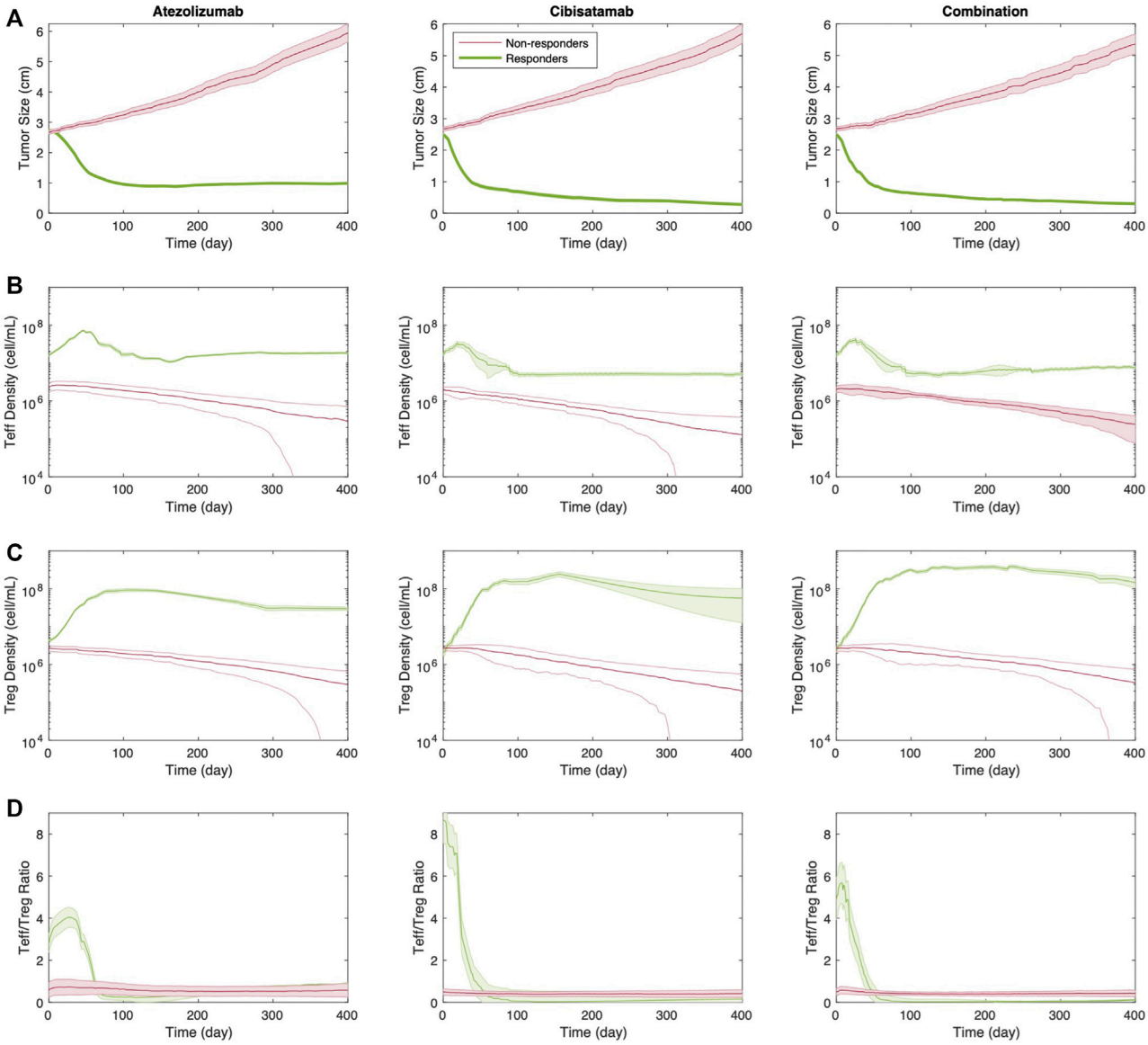

FIGURE 5
Time profile of **(A)** tumor size; **(B)** Teff cell density; **(C)** Treg cell density; and **(D)** Teff to Treg cells ratio for responders vs. non-responders in monotherapies and combination therapy. Thick line represents the median and shaded area stands for the standard error.

3.2 Optimization of dose regimen of combination therapy with atezolizumab and cibisatamab by sequential therapy simulations

At the next step, we aim to investigate the possibility of dosage optimization using the current QSP platform, which has been validated by its efficacy prediction of the combination therapy with atezolizumab and cibisatamab. To this end, we conducted 40 different virtual clinical trials, using the same VPs from above, with various cibisatamab and atezolizumab doses and schedules. We have kept the dose and frequency of atezolizumab the same for all the cases, 1,200 mg Q3W, since this is an established dose in clinical trials of colorectal cancer (Tapia Rico et al., 2018). Atezolizumab administration was simulated starting on day 1, week 2 or week 3 after reaching initial tumor diameter, in combination with cibisatamab. Cibisatamab dose size and schedule were selected in the range of 0–100 mg and QW-Q3W, respectively. These selected dose sizes and schedules are in agreement with the ranges used in clinical trials. The median tumor volume at week 8 (the time of first follow up in clinical trial after treatment) and ORR for each combination at the end of treatment are reported in Figure 6. We aimed to determine whether treatment outcomes differed between early in treatment results and end-point results. To achieve this, we primarily measured the median tumor volume, as the overall response rate (ORR) may not fully reflect individual patient dynamics until the end of the treatment.

Overall, by considering both ORR and median tumor volume, the result shows that concurrent combination therapy has slightly better response compared to sequential therapies.

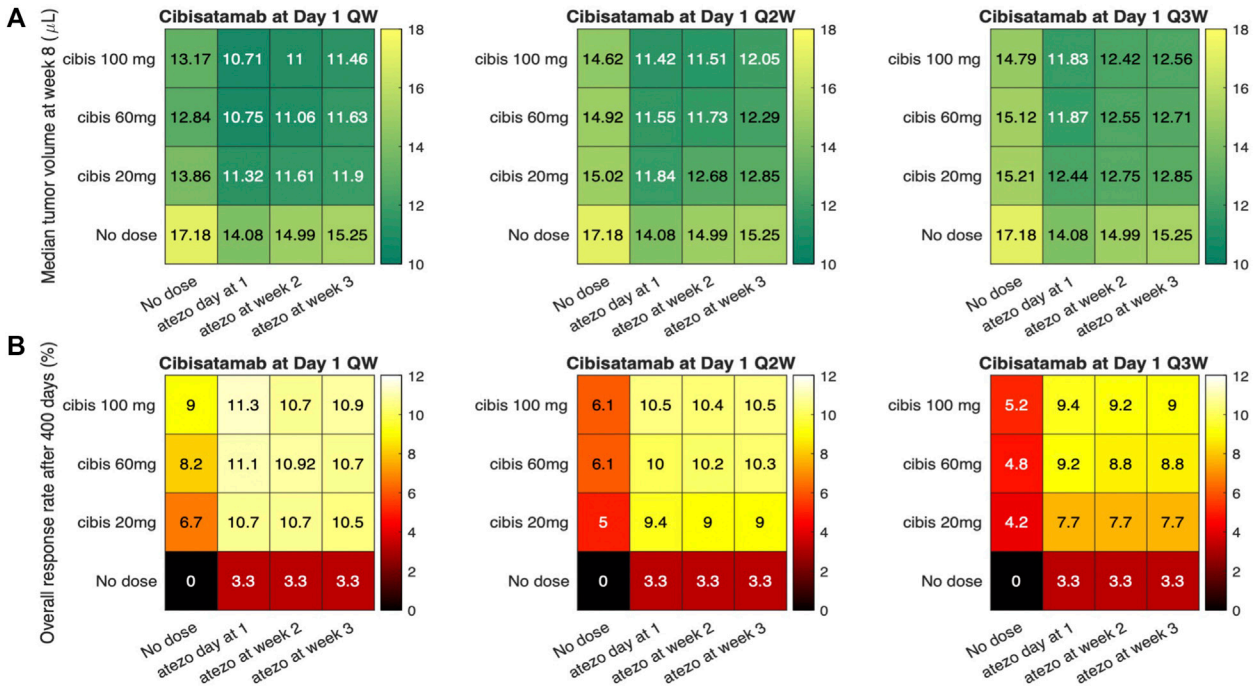

FIGURE 6
Simulations of sequential therapies using various atezolizumab and cibisatamab dose and schedule. **(A)** represents the median tumor volume after 8 weeks; and **(B)** Overall response rate for each dose regimen.

Although the highest efficacy is observed for weekly administration of cibisatamab, which is the same frequency used in clinical trials, the result of simulation shows that biweekly (Q2W) and triweekly (Q3W) administration of cibisatamab can have similar efficacy, which may be beneficial to reduce the toxicity associated with bispecific antibodies.

3.3 Quantification of drug synergy

Next, we used the QSP model to quantify the synergy of combination therapy with atezolizumab and cibisatamab. 25 different simulations were conducted for various combinations of drugs concentration, with cibisatamab in the range of 0–80 mg and atezolizumab within the range of 0–1600 mg for the same VPs in each simulation. For each combination, the ratio of final tumor size to tumor size at the conditions with no drug at the end of 400 days, was calculated as the metric of response. Then, a two-dimensional heatmap was plotted for the results, Figure 7. Quantification of the synergy using multidimensional synergy of combinations (MuSyC) technique suggests a small synergistic efficacy β_{obs} = 0.072, as well as a small synergistic potency log (α_2) = 0.064.

4 Discussion

TCEs have become an important part of the therapeutic research strategy to treat cancer (Dahlén et al., 2018; Zhou et al., 2021). They enable a powerful mode of action by activating T cells through the creation of artificial immune synapses (Morcos et al., 2020). Explorative preclinical and emerging clinical data indicate a potential for enhanced efficacy and reduced systemic toxicity. However, TCEs are a complex modality with challenges to overcome in early clinical trials, including the selection of relevant starting doses. “Dosing strategy plays a crucial role in determining the therapeutic window of TCEs because of the desire to maximize therapeutic efficacy in the context of known mechanism-related adverse events, such as cytokine release syndrome (CRS) and neurological adverse events” (Betts and van der Graaf, 2020). Moreover, other drug combinations with T cell engagers have been a promising approach to treat cancers. While comprehensive drug combination tests are effective for identifying novel synergistic drug combinations, measuring all possible combinations is challenging due to the size of potential therapeutic agents and cell lines. Mechanistic modeling approaches like quantitative system pharmacology (QSP) models are powerful tools that can be used to integrate diverse data to predict/refine clinical dosing regimens and design trials to optimize efficacy (Jafarnejad et al., 2019; Hosseini et al., 2020; Sové et al., 2020; Sové et al., 2022; Wang et al., 2022). Modeling can be used to guide rational decision making, to inform precision medicine strategies, and to increase overall efficiency of the oncology clinical development process (Betts and van der Graaf, 2020; Gibbs et al., 2020).

In this study, we extend our previously developed QSP platform (Ma et al., 2020a) to study the combination therapy of an immune

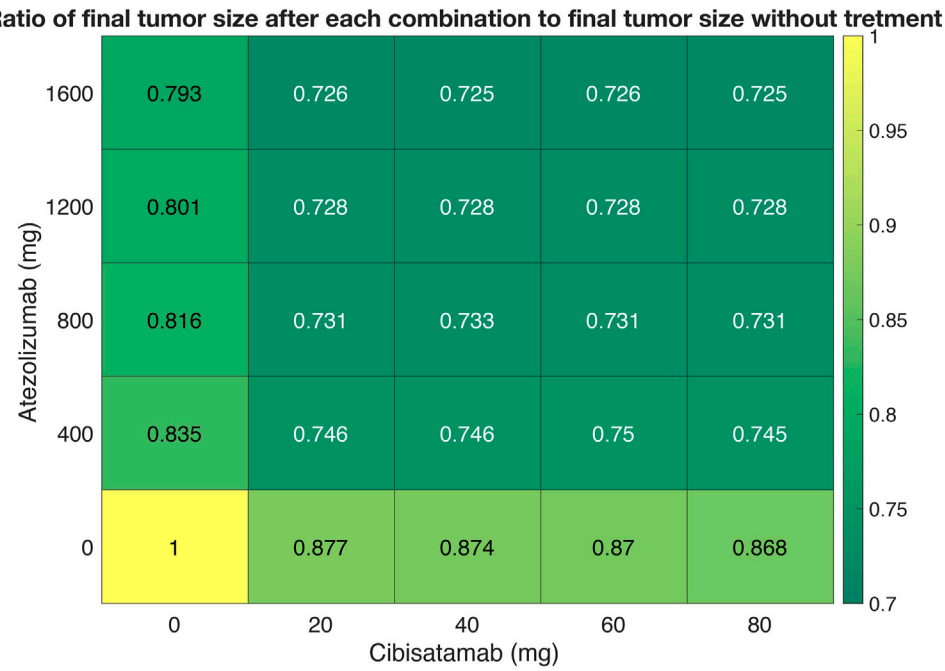

FIGURE 7
A dose-response heatmap for atezolizumab within the range of 0–1600 mg and cibisatamab in the range of 0–80 mg.

checkpoint inhibitor, atezolizumab, and a T cell engager, cibisatamab. Following recent developments in kinetic modeling of bispecific antibodies (Vauquelin and Charlton, 2013; Schropp et al., 2019), we simplified the binding of cibisatamab to CEA, by considering one binding arm with a newly added parameter to account for the avidity of cibisatamab and thus modifying the binding affinity between the second target and cibisatamab bound to the first target. We calibrated the model by fitting the model to the experimental data of level of T cell activation as a function of average synapse per cell from (Vyver et al., 2021). We have also adopted the dynamics of T cells, helper T cells, APCs, tumor-specific neoantigens and tumor-associated self-antigens, immune checkpoints and MDSCs from our study of TNBC (Wang et al., 2021).

Using the model calibrated against clinical data, we performed a series of *in silico* clinical trials to investigate the optimal dose schedule of atezolizumab and cibisatamab for colorectal cancer. The results suggest that concurrent combinations result in higher ORRs (and smaller tumor size) than sequential combinations. Although the highest efficacy is observed for weekly administration of cibisatamab, which is the same frequency used in clinical trial, the results of simulations show that biweekly (Q2W) and triweekly (Q3W) administration of cibisatamab can have similar efficacy to weekly with potentially less toxicity and adverse events associate with CRS in T cell engagers (Yu and Wang, 2019).

To investigate how the presence of one drug would affect the efficacy and potency of the other drug in combination therapy, we investigated the drug synergy quantification using MuSyC method developed by (Meyer et al., 2019). The results of our simulations showed insignificant synergy of potency and efficacy for combination therapy of atezolizumab and cibisatamab. This could be due to the fact that these two drugs have independent mechanisms of action. In this study, we have used the ratio of tumor size at the end of simulation following treatment to tumor size at the end of the simulation with no treatment as the metric of response. However, other metrics like ORR, duration of response or T cell densities might be other potential metrics to further investigate the drug synergy in combination therapy. Moreover, the drug synergy quantification based on these traditional statistical models may lack high power and accuracy measurement due to small data size. In future, and with availability of additional data the machine learning techniques of drug synergy quantifications may bring many advantages, including high accuracy, ability to model non-linear effects, and robustness to parameter assumptions (Preuer and Lewis, 2018; Liu and Xie, 2021; Zhang et al., 2021; Tang and Gottlieb, 2022).

One of the major challenges in QSP models is the parameter estimations due to high complexity of the models. Generation of virtual patients with the goal of establishing a reliable and effective algorithm is an ongoing research in the field of pharmacology modeling (Allen et al., 2016; Rieger et al., 2018). In this study, most of the parameters are estimated using experimental data for colorectal cancer and validated by comparing the results to response rate of patients in clinical trial. However, the importance of some parameters like the rate of Teff suppression by activated Tregs due to bispecific T cell engagers and their influence on the result of combination therapy remains to be explored.

Here, we used QSP modeling to perform *in silico* clinical trials of atezolizumab and cibisatamab to study optimization of dose and schedule in combination therapy and drug synergy quantification. This model can be extended to study other bispecific T cell engagers and immune checkpoint inhibitors in colorectal and other cancers if sufficient data for parameter recalibration and model validation are available. Also, the QSP approach can be used in model-informed drug

design (MIDD) and design of clinical trials and provide regulatory assistance (Azer et al., 2021; Bai et al., 2021).

Data availability statement

The datasets presented in this study can be found in online repositories. The names of the repository/repositories and accession number(s) can be found in the article/Supplementary Material. The model code and MATLAB script used in this study are available at http://dx.doi.org/10.17632/crk9tmnmb7.1.

Author contributions

SA, SH, and AP designed the project; AP and SH directed the project; SA and HW built and modified the model; SA, HW, and YZ contributed analysis tools; SA performed all simulations, collected the data, did all analysis and drafted the manuscript; SA, HW, YZ, MP, MN, JW, SH, and AP revised the manuscript critically; All authors contributed to the article and approved the submitted version.

Funding

This work was supported by a grant from Boehringer Ingelheim Pharmaceuticals, Inc. and in part by NIH grants R01CA138264 and U01CA212007.

Conflict of interest

Authors JW, MP, MN and SH are employed by Boehringer Ingelheim. These authors had the following involvement with the study: discussion of study design and results of computer simulations, and editing the manuscript.

The remaining authors declare that the research was conducted in the absence of any commercial or financial relationships that could be construed as a potential conflict of interest.

Publisher's note

Supplementary material

The Supplementary Material for this article can be found online at: https://www.frontiersin.org/articles/10.3389/fphar.2023.1163432/full#supplementary-material

References

Allen, R. J., Rieger, T. R., and Musante, C. J. (2016). Efficient generation and selection of virtual populations in quantitative systems pharmacology models. *CPT Pharmacometrics Syst. Pharmacol.* 5 (3), 140–146. doi:10.1002/psp4.12063

Alsaab, H. O., Samaresh Sau, R. A., Tatiparti, K., Bhise, K., Kashaw, S. K., and Iyer, A. K. (2017). PD-1 and PD-L1 checkpoint signaling inhibition for cancer immunotherapy: Mechanism, combinations, and clinical outcome. *Front. Pharmacol.* 8, 1–15. doi:10.3389/fphar.2017.00561

Azer, K., Kaddi, C. D., Jeffrey, S., Barrett, J., McQuade, S. T., Merrill, N. J., et al. (2021). History and future perspectives on the discipline of quantitative systems pharmacology modeling and its applications. *Front. Physiology* 12, 637999. doi:10.3389/fphys.2021.637999

Bacac, M., Fauti, T., Sam, J., Colombetti, S., Weinzierl, T., Ouaret, D., et al. (2016). A novel carcinoembryonic antigen T-cell bispecific antibody (CEA TCB) for the treatment of solid tumors. *Clin. Cancer Res.* 22 (13), 3286–3297. doi:10.1158/1078-0432.CCR-15-1696

Bai, J. P. F., Earp, J. C., Florian, J., Madabushi, R., Strauss, D. G., Wang, Y., et al. (2021). Quantitative systems pharmacology: Landscape analysis of regulatory submissions to the US food and drug administration. *CPT Pharmacometrics Syst. Pharmacol.* 10 (12), 1479–1484. doi:10.1002/psp4.12709

Berenbaum, M. C. (1978). A method for testing for synergy with any number of agents. *J. Infect. Dis.* 137 (2), 122–130. doi:10.1093/infdis/137.2.122

Betts, A., and van der Graaf, P. H. (2020). Mechanistic quantitative pharmacology strategies for the early clinical development of bispecific antibodies in oncology. *Clin. Pharmacol. Ther.* 108 (3), 528–541. doi:10.1002/cpt.1961

Bliss, C. I. (1939). The toxicity of poisons applied jointly. *Ann. Appl. Biol.* 26 (3), 585–615. doi:10.1111/j.1744-7348.1939.tb06990.x

Bray, F., Ferlay, J., Soerjomataram, I., Siegel, R. L., Torre, L. A., and Jemal, A. (2018). Global cancer statistics 2018: GLOBOCAN estimates of incidence and mortality worldwide for 36 cancers in 185 countries. *CA A Cancer J. Clin.* 68 (6), 394–424. doi:10.3322/caac.21492

Chou, T. C. (2010). Drug combination studies and their synergy quantification using the chou-talalay method. *Cancer Res.* 70 (2), 440–446. doi:10.1158/0008-5472.CAN-09-1947

Dahlén, E., Veitonmäki, N., and Norlén, P. (2018). Bispecific antibodies in cancer immunotherapy. *Ther. Adv. Vaccines Immunother.* 6 (1), 3–17. doi:10.1177/2515135518763280

Eisenhauer, E. A., Therasse, P., Bogaerts, J., Schwartz, L. H., Sargent, D., Ford, R., et al. (2009). New response evaluation criteria in solid tumours: Revised RECIST guideline (version 1.1). *Eur. J. Cancer* 45 (2), 228–247. doi:10.1016/j.ejca.2008.10.026

Eng, C., Kim, T. W., Bendell, J., Argilés, G., Tebbutt, N. C., Di Bartolomeo, M., et al. (2019). Atezolizumab with or without cobimetinib versus regorafenib in previously treated metastatic colorectal cancer (IMblaze370): A multicentre, open-label, phase 3, randomised, controlled trial. *Lancet Oncol.* 20 (6), 849–861. doi:10.1016/S1470-2045(19)30027-0

Gibbs, J. P., Yuraszeck, T., Biesdorf, C., Xu, Y., and Kasichayanula, S. (2020). Informing development of bispecific antibodies using physiologically based pharmacokinetic-pharmacodynamic models: Current capabilities and future opportunities. *J. Clin. Pharmacol.* 60 (S1), S132–S146. doi:10.1002/jcph.1706

Golshani, G., and Zhang, Y. (2018). Advances in immunotherapy for colorectal cancer: A review. *Ther. Adv. Vaccines* 9 (6), 259–261. doi:10.1177/https

Gonzalez, E., Semmianikova, M., Griffiths, B., Khan, K. H., Barber, L. J., Woolston, A., et al. (2019). CEA expression patterns determine response and resistance to the CEA-TCB bispecific immunotherapy antibody in colorectal cancer patient derived organoids. *J. Clin. Oncol.* 37 (4), 535. doi:10.1200/jco.2019.37.4_suppl.535

Greco, W. R., Bravo, G., and Parsons, J. C. (1995). The search for synergy: A critical review from a response surface perspective. *Surf. Perspect.* 47 (2), 331–385.

Hegde, P. S., and Chen, D. S. (2020). Top 10 challenges in cancer immunotherapy. *Immunity* 52 (1), 17–35. doi:10.1016/j.immuni.2019.12.011

Hosseini, I., Gadkar, K., Stefanich, E., Chung Li, C., Sun, L. L., Ramanujan, S., et al. (2020). Mitigating the risk of cytokine release syndrome in a phase I trial of CD20/CD3 bispecific antibody mosunetuzumab in NHL: Impact of translational system modeling. *Npj Syst. Biol. Appl.* 6 (1), 28. doi:10.1038/s41540-020-00145-7

Jafarnejad, M., Gong, C., Gabrielson, E., Bartelink, I. H., Vicini, P., Wang, B., et al. (2019). A computational model of neoadjuvant PD-1 inhibition in non-small cell lung cancer. *AAPS J.* 21 (5), 79. doi:10.1208/s12248-019-0350-x

Johdi, N. A., and Sukor, N. F. (2020). Colorectal cancer immunotherapy: Options and strategies. *Front. Immunol.* 11, 1624–1718. doi:10.3389/fimmu.2020.01624

Lehmann, S., Perera, R., Grimm, H. P., Sam, J., Colombetti, S., Fauti, T., et al. (2016). *In vivo* fluorescence imaging of the activity of CEA TCB, a novel T-cell bispecific antibody, reveals highly specific tumor targeting and fast induction of T-cell-mediated tumor killing. *Clin. Cancer Res.* 22 (17), 4417–4427. doi:10.1158/1078-0432.CCR-15-2622

Liu, Q., and Xie, L. (2021). TranSynergy: Mechanism-Driven interpretable deep neural network for the synergistic prediction and pathway deconvolution of drug combinations. *PLoS Comput. Biol.* 17 (2), 86533. doi:10.1371/JOURNAL.PCBI.1008653

Loewe, S. (1953). The problem of synergism and antagonism of combined drugs. *Arzneimittelforschung* 3, 285–290.

Ma, H., Wang, H., Sove, R. J., Jafarnejad, M., Tsai, C. H., Wang, J., et al. (2020a). A quantitative systems pharmacology model of T cell engager applied to solid tumor. *AAPS J.* 22 (4), 85–16. doi:10.1208/s12248-020-00450-3

Ma, H., Wang, H., Sové, R. J., Wang, J., Craig, G., and Aleksander, S. (2020b). Combination therapy with T cell engager and PD-L1 blockade enhances the antitumor potency of T cells as predicted by a QSP model. *J. Immunother. Cancer* 8 (2), 001141–1211. doi:10.1136/jitc-2020-001141

Marino, S., Hogue, I. B., Ray, C. J., and Kirschner, D. E. (2008). A methodology for performing global uncertainty and sensitivity analysis in systems biology. *J. Theor. Biol.* 254 (1), 178–196. doi:10.1016/j.jtbi.2008.04.011

Meyer, C. T., Wooten, D. J., Lopez, C. F., and Quaranta, V. (2020). Charting the fragmented landscape of drug synergy. *Trends Pharmacol. Sci.* 41 (4), 266–280. doi:10.1016/j.tips.2020.01.011

Meyer, C. T., Wooten, D. J., Paudel, B. B., Bauer, J., Hardeman, K. N., Westover, D., et al. (2019). Quantifying drug combination synergy along potency and efficacy axes. *Cell. Syst.* 8 (2), 97–108. doi:10.1016/j.cels.2019.01.003

Morcos, P. N., Li, J., Hosseini, I., and Chung, C. L. (2020). Quantitative clinical pharmacology of T-cell engaging bispecifics: Current perspectives and opportunities. *Clin. Transl. Sci.* 14, 75–85. doi:10.1111/cts.12877

Morrissey, K., Yuraszeck, T., Li, C. C., Zhang, Y., and Kasichayanula, S. (2016). Immunotherapy and novel combinations in oncology: Current landscape, challenges, and opportunities. *Clin. Transl. Sci.* 9 (2), 89–104. doi:10.1111/cts.12391

Popovic, A., Jaffee, E. M., and Zaidi, N. (2018). Emerging strategies for combination checkpoint modulators in cancer immunotherapy. *J. Clin. Investigation* 128 (8), 3209–3218. doi:10.1172/JCI120775

Preuer, K., Lewis, R. P. I., Hochreiter, S., Bulusu, K. C., and Klambauer, G. (2018). Sepp hochreiter, andreas bender, krishna C. Bulusu, and günter klambauer. *Bioinformatics* 34 (9), 1538–1546. doi:10.1093/bioinformatics/btx806

Rieger, T. R., Allen, R. J., Bystricky, L., Chen, Y., and Cui, Y. (2018). Improving the generation and selection of virtual populations in quantitative systems pharmacology models. *Prog. Biophysics Mol. Biol.* 139, 15–22. doi:10.1016/j.pbiomolbio.2018.06.002

Schropp, J., Khot, A., Shah, D. K., and Koch, G. (2019). Target-mediated drug disposition model for bispecific antibodies: Properties, approximation, and optimal dosing strategy. *CPT Pharmacometrics Syst. Pharmacol.* 8 (3), 177–187. doi:10.1002/psp4.12369

Sharma, P., and Allison, J. P. (2020). Dissecting the mechanisms of immune checkpoint therapy. *Nat. Rev. Immunol.* 20 (2), 75–76. doi:10.1038/s41577-020-0275-8

Sharma, P., Siddiqui, B. A., Anandhan, S., Yadav, S. S., Subudhi, S. K., Gao, J., et al. (2021). The next decade of immune checkpoint therapy. *Cancer Discov.* 11 (4), 838–857. doi:10.1158/2159-8290.CD-20-1680

Sové, R. J., Jafarnejad, M., Zhao, C., Wang, H., Ma, H., and Popel, A. S. (2020). QSP-IO: A quantitative systems pharmacology toolbox for mechanistic multiscale modeling for immuno-oncology applications. *CPT Pharmacometrics Syst. Pharmacol.* 9 (9), 484–497. doi:10.1002/psp4.12546

Sové, R. J., Verma, B. K., Wang, H., Ho, W. J., Yarchoan, M., and Popel, A. S. (2022). Virtual clinical trials of anti-PD-1 and anti-CTLA-4 immunotherapy in advanced hepatocellular carcinoma using a quantitative systems pharmacology model. *J. Immunother. Cancer* 10 (11), e005414–14. doi:10.1136/jitc-2022-005414

Tabernero, J., Melero, I., Ros, W., Argiles, G., Marabelle, A., Rodriguez-Ruiz, M. E., et al. (2017). Phase ia and ib studies of the novel carcinoembryonic antigen (CEA) T-cell bispecific (CEA CD3 TCB) antibody as a single agent and in combination with atezolizumab: Preliminary efficacy and safety in patients with metastatic colorectal cancer (MCRC). *J. Clin. Oncol.* 35 (15), 3002. doi:10.1200/JCO.2017.35.15_suppl.3002

Tang, Y. C., and Gottlieb, A. (2022). SynPathy: Predicting drug synergy through drug-associated pathways using deep learning. *Mol. Cancer Res.* 20 (5), 762–769. doi:10.1158/1541-7786.MCR-21-0735

Tapia Rico, G., and TimothyPrice, J. (2018). Atezolizumab for the treatment of colorectal cancer: The latest evidence and clinical potential. *Expert Opin. Biol. Ther.* 18 (4), 449–457. doi:10.1080/14712598.2018.1444024

Vauquelin, G., and Charlton, S. J. (2013). Exploring avidity: Understanding the potential gains in functional affinity and target residence time of bivalent and heterobivalent ligands. *Br. J. Pharmacol.* 168 (8), 1771–1785. doi:10.1111/bph.12106

Vyver, A. J. V., Weinzierl, T., Eigenmann, M. J., Frances, N., Herter, S., Buser, R. B., et al. (2021). Predicting tumor killing and T-cell activation by t-cell bispecific antibodies as a function of target expression: Combining *in vitro* experiments with systems modeling. *Mol. Cancer Ther.* 20 (2), 357–366. doi:10.1158/1535-7163.MCT-20-0269

Wang, H., Ma, H., Sové, R. J., Emens, L. A., and Aleksander, S. P. (2021). Quantitative systems pharmacology model predictions for efficacy of atezolizumab and nab-paclitaxel in triple-negative breast cancer. *Negat. Breast Cancer* 9, 002100. doi:10.1136/jitc-2020-002100

Wang, H., Zhao, C., CesarSanta-Maria, A., Emens, L. A., and Popel, A. S. (2022). Dynamics of tumor-associated macrophages in a quantitative systems pharmacology model of immunotherapy in triple-negative breast cancer. *IScience* 25 (8), 104702. doi:10.1016/j.isci.2022.104702

Yu, L., and Wang, J. (2019). T cell-redirecting bispecific antibodies in cancer immunotherapy: Recent advances. *J. Cancer Res. Clin. Oncol.* 145 (4), 941–956. doi:10.1007/s00432-019-02867-6

Zhang, T., Zhang, L., Payne, P., and Fuhai, L. (2021). Synergistic drug combination prediction by integrating multiomics data in deep learning models. *Methods Mol. Biol.* 2194, 223–238. doi:10.1007/978-1-0716-0849-4_12

Zhou, S., Liu, M., Ren, F., Meng, X., and Yu, J. (2021). The landscape of bispecific T cell engager in cancer treatment. *Biomark. Res.* 9 (1), 38–23. doi:10.1186/s40364-021-00294-9

Frontiers in Pharmacology

Explores the interactions between chemicals and living beings

The most cited journal in its field, which advances access to pharmacological discoveries to prevent and treat human disease.

Discover the latest Research Topics

See more →

Frontiers

Avenue du Tribunal-Fédéral 34
1005 Lausanne, Switzerland
frontiersin.org

Contact us

+41 (0)21 510 17 00
frontiersin.org/about/contact